

©2015

JON A. MACKEY

ALL RIGHTS RESERVED

THERMOELECTRIC ENERGY CONVERSION: ADVANCED
THERMOELECTRIC ANALYSIS AND MATERIALS DEVELOPMENT

A Dissertation

Presented to

The Graduate Faculty of The University of Akron

In Partial Fulfillment

of the Requirements for the Degree

Doctor of Philosophy

Jon A. Mackey

May, 2015

THERMOELECTRIC ENERGY CONVERSION: ADVANCED
THERMOELECTRIC ANALYSIS AND MATERIALS DEVELOPMENT

Jon A. Mackey

Dissertation

Approved:

Accepted:

Advisor
Dr. Celal Batur

Department Chair
Dr. Sergio Felicelli

Committee Member
Dr. Alp Sehirlioglu

Dean of the College
Dr. George Haritos

Committee Member
Dr. Minel Braun

Interim Dean of the Graduate School
Dr. Rex Ramsier

Committee Member
Dr. Guo-Xiang Wang

Date

Committee Member
Dr. Jerry Young

Committee Member
Dr. Bob Veillette

ABSTRACT

Thermoelectric materials exhibit a significant coupling between thermal and electrical transport. Devices made from thermoelectric materials can convert between thermal and electrical energy. System reliability is extremely high but widespread use of the technology is hindered by low conversion efficiency. To increase the practicality of thermoelectric devices improvements are required in both (i) device design and (ii) thermoelectric materials.

Advanced thermoelectric analysis developed in this work provides general guidelines for device design by introducing a new set of design factors. The new analytic factors include Device Design Factor, Fin Factor, Inductance Factor, and Thermal Diffusivity Factor. The advanced analysis is applied to two material systems developed in this work. The first system investigated was a composite of WSi_2 precipitates in a Si/Ge matrix. The composite was investigated through both solidification techniques and powder processing. The system has a 30% higher figure of merit, a material parameter relating to conversion efficiency, than traditional zone-leveled Si/Ge. The second system investigated was a novel quaternary $\text{Co}_x\text{Ni}_{4-x}\text{Sb}_{12-y}\text{Sn}_y$ skutterudite. The system was found to achieve both n- and p-type conduction with tuning of the Co level.

ACKNOWLEDGEMENTS

I would first like to thank Professor Alp Sehrioglu from Case Western Reserve University for supporting this work and my graduate studies both financially and academically. Alp has provided many helpful comments and guidance over the course of the last four years. I would next like to thank Dr. Fredrick Dynys for assisting in the technical work of this study. Fredrick has helped to guide a large portion of the experimental research in this work at NASA Glenn Research Center. I would like to thank my advisor Professor Celal Batur and all of my committee members at The University of Akron for their time and effort in reviewing this work.

I would also like to thank Ben Kowalski, Serene Farmer, Dereck Johnson, Richard Rogers, Terry Mccue, Elahe Farghadany, Tom Sabo, and Ray Babuder from NASA Glenn Research Center and Case Western Reserve University as well as Sabah Bux and Jean-Pierre Fleurial from NASA JPL for their technical assistance and insightful conversations throughout this work. I thank Ali Sayir from the Air Force Office of Scientific Research, for guidance with general research topics and some advice on thermoelectrics. The spark plasma sintering equipment used in this work was generously provided by Mike Cinibulk from the Air Force Research Laboratories at Wright-Patterson Air Force Base. Assistance with spark plasma sintering

was provided by Charles Cooke. Finally, I would like to thank my friends and family for their support in this work. The author also gratefully acknowledges funding sources NASA/USRA 04555-004, NASA cooperative agreement NNX08AB43A, AFOSR FA9550-09-1-0312, and the NASA Radioisotope Power System program.

TABLE OF CONTENTS

	Page
LIST OF TABLES	x
LIST OF FIGURES	xii
CHAPTER	
I. INTRODUCTION	1
1.1 Introduction to Thermoelectricity	1
1.2 Scope of Work	4
II. LITERATURE REVIEW	9
2.1 Introduction	9
2.2 Thermoelectric Devices	9
2.3 Thermoelectric Analysis	14
2.4 Thermoelectric Materials	19
2.5 Couple Segmentation and Staging	29
III. REVIEW OF THERMOELECTRIC ANALYSIS	31
3.1 Introduction	31
3.2 Figure of Merit	31
3.3 Thermoelectric Transport	43
3.4 Summary	53

IV. ADVANCED THERMOELECTRIC ANALYSIS	54
4.1 Introduction	54
4.2 Motivation for Advanced Analysis	54
4.3 Problem Statement	55
4.4 Cylindrical Coordinates	58
4.5 Variable Boundary Conditions	61
4.6 Lateral Heat Transfer	69
4.7 Comparison of Variable Boundary Conditions and Lateral Heat . . .	74
4.8 Variable Material Properties	77
4.9 Transient Operation	80
4.10 Conclusion	89
V. COUPLE DESIGN EMPLOYING ADVANCED ANALYSIS	90
5.1 Introduction	90
5.2 $\text{WSi}_2\text{-Si}_{1-x}\text{Ge}_x$ Couple Design	90
5.3 Skutterudite Couple Design	95
5.4 Conclusion	99
VI. EXPERIMENTAL PROCEDURE	100
6.1 Introduction	100
6.2 Materials Synthesis	100
6.3 Chemical and Structure Analysis	106
6.4 Transport Property Characterization	109

6.5	Conclusion	112
VII. MEASUREMENT UNCERTAINTY ANALYSIS		114
7.1	Introduction	114
7.2	Measurement Definition	114
7.3	Uncertainty Sources	118
7.4	Cold-Finger Modeling using FEA	125
7.5	Uncertainty Analysis Example	134
7.6	Conclusion	139
VIII. $\text{WSi}_2\text{-Si}_{1-x}\text{Ge}_x$ COMPOSITES: PROCESSING AND THERMOELECTRIC PROPERTIES		141
8.1	Introduction	141
8.2	System Background	141
8.3	Solidification Processing	142
8.4	Solidification Thermoelectric Properties	152
8.5	Powder Processing	163
8.6	Powder Processed Thermoelectric Properties	179
8.7	Influence of Oxygen Contamination	194
8.8	Conclusion	196
IX. $\text{Co}_x\text{Ni}_{4-x}\text{Sb}_{12-y}\text{Sn}_y$ QUATERNARY SKUTTERUDITE SYSTEM: PROCESSING AND THERMOELECTRIC PROPERTIES		199
9.1	Introduction	199
9.2	System Background	199
9.3	$\text{Co}_x\text{Ni}_{4-x}\text{Sb}_{12-y}\text{Sn}_y$ Processing	206

9.4	$\text{Co}_x\text{Ni}_{4-x}\text{Sb}_{12-y}\text{Sn}_y$ Thermoelectric Properties	221
9.5	Conclusion	230
X.	CONCLUSIONS AND FUTURE WORK	232
10.1	Advanced Thermoelectric Design	232
10.2	Measurement Uncertainty	233
10.3	$\text{WSi}_2\text{-Si/Ge}$ System	234
10.4	$\text{Co}_x\text{Ni}_{4-x}\text{Sb}_{12-y}\text{Sn}_y$ Skutterudite System	235
	BIBLIOGRAPHY	236
	APPENDICES	254
	APPENDIX A. DEVICE DESIGN AND TESTING	255
	APPENDIX B. UNCERTAINTY ANALYSIS DETAILS	260

LIST OF TABLES

Table	Page
4.1 Comparison of simplified boundary condition to numerical solution of actual condition.	67
4.2 Comparison of couple parameters demonstrating the importance of considering several factors.	75
5.1 Temperature averaged material properties (300 – 950 °C)	91
5.2 W/Si/Ge couple design	93
5.3 W/Si/Ge couple design summary	94
5.4 Temperature averaged material properties (20 – 250 °C)	95
5.5 $\text{Co}_x\text{Ni}_{4-x}\text{Sb}_{12-y}\text{Sn}_y$ couple design	96
5.6 $\text{Co}_x\text{Ni}_{4-x}\text{Sb}_{12-y}\text{Sn}_y$ couple design summary	98
6.1 Summary of samples and testing supporting the dissertation.	113
7.1 Sources of resistivity uncertainty	119
7.2 Sources of Seebeck uncertainty	123
8.1 Nominal compositions of the specimens studied	145
8.2 Calculated thermal conductivity of $\text{WSi}_2\text{-Si/Ge}$ samples	159
8.3 Nominal compositions and processing details of powder processed W/Si/Ge	166
8.4 Sintering schedule	167
8.5 Strain rate of six samples demonstrating the influence of W	176

8.6	Oxygen level of $\text{WSi}_2\text{-Si}_{1-x}\text{Ge}_x$ composites using different processing conditions.	195
9.1	Summary of $\text{Co}_x\text{Ni}_{4-x}\text{Sb}_{12-y}\text{Sn}_y$ skutterudite samples and room temperature properties.	209
9.2	Summary of $\text{A}_z\text{Co}_2\text{Ni}_2\text{Sb}_8\text{Sn}_4$ skutterudite samples and room temperature properties.	210
9.3	Electron probe microanalysis (EPMA) of skutterudite samples	216

LIST OF FIGURES

Figure	Page
1.1 Flow chart outlining the organization of the dissertation.	6
1.2 Flow chart outlining the contributions developed in the dissertation. . .	8
2.1 Typical TE device composed of n- and p-type thermoelements, metallic electrodes, and hot and cold ceramic heat spreaders.	10
2.2 An open circuit conductor composed of two materials A and B with an arbitrary temperature profile. Conductor is subject to zero electrical current flux (eJ_N).	16
2.3 Isothermal junction ($\nabla T = 0$) between two conductors composed of materials A and B. Electrical charge flux (eJ_N) is conserved in the junction but heat (q'') may be either released or absorbed.	18
2.4 Figure of merit of several common TE systems, data extracted from several sources.	21
2.5 ASM International (1996) phase diagram of the Si/Ge binary system. .	22
2.6 Crystal structure and range of possible skutterudites, adapted from reference.	27
2.7 ASM International (1996) phase diagram of the Co/Sb binary system. .	28
2.8 a) Segmented TE couple b) cascaded TE couple.	30

3.1	A thermoelectric couple configured for electrical power generation. Two legs (A and B) are connected thermally in parallel between thermal reservoirs T_H and T_C and electrically in series with load resistance R . Geometric parameters of legs include A cross-sectional area and L leg length. Material properties include σ electrical conductivity, S Seebeck coefficient, and k thermal conductivity. Electrical dependant parameters include ϕ voltage and I electrical current. The spatial x coordinate originates at the hot shoe of the legs.	38
3.2	Energy transport in a one-dimensional thermoelectric conductor.	39
3.3	Contour map of conversion efficiency over a space of X and Y parameters, a clear design point exists. Values are calculated using properties typical of a Si/Ge couple found on NASA's radioisotope thermoelectric generators.	42
3.4	Trends in Seebeck coefficient, electrical conductivity, and thermal conductivity as a function of carrier density.	52
4.1	A thermoelectric couple configured for electrical power generation. Two legs (a and b) are connected thermally in parallel between thermal reservoirs T_{∞_h} and T_{∞_c} and electrically in series with load resistance R . Heat transfer coefficients in the hot and cold shoes are denoted \bar{h}_h and \bar{h}_c and the leg side convection coefficient h corresponds to side ambient temperature T_{∞} . Geometric parameters of legs include A cross-sectional area and L leg length. Material properties include σ electrical conductivity, S Seebeck coefficient, and k thermal conductivity. Electrical dependant parameters include ϕ voltage and I electrical current. The spatial x coordinate originates at the hot shoe of the legs.	56
4.2	Schematic of a cylindrical couple, highlighting the geometric parameters of interest: leg width w , and inner/ outer radius r_i and r_o	59
4.3	Device Design Factor as a function of leg length for a range of heat transfer coefficients.	65
4.4	Typical temperature profiles for a range of ambient temperatures, with $X=1$ and $Y=1$ for convenience.	70
4.5	Max conversion efficiency for a range of property slopes, for fixed average properties. a) Thermal conductivity, b) Seebeck coefficient, c) Electrical resistivity.	79

4.6	Transient thermoelectric couple introducing the density ρ , specific heat c_p , and electrical inductance H	81
4.7	A study on hot shoe temperature of three different geometrically and electrically similar couples under On/Off heat flux cycles; parameter of study is the Thermal Diffusivity Factor Γ . Inset is the applied hot shoe heat flux.	85
4.8	Cycle efficiency of a transient couple as a function of the thermal diffusivity parameter Γ	86
4.9	Hot shoe temperature due to a sinusoidal heat flux, displaying a transient startup and a periodic steady state.	87
4.10	Left) Power amplitude versus Inductance Factor β with power versus time curves inset. Right) Power amplitude versus frequency with power versus time curves inset.	88
6.1	Temperature profile along the pull direction of the vertical Bridgman furnace used for this study. Red line indicates a solidifying temperature of $900^\circ C$ at which a thermal gradient can be calculated. The white arrow in the picture indicates the pull direction.	102
6.2	Picture of the MBRAUN glovebox (Left) and PM100 planetary mill (Right) used for this study.	103
6.3	Powder being pressed in graphite dies: cold pressed die (Left) and die mounted with insulation for SPS run (Right).	105
7.1	Potentiometric configuration for Seebeck coefficient or electrical resistivity measurement. Samples cut to the shape of a rectangular prism or cylinder are held in place by electrodes, top and bottom, while two probe thermocouples make contact on a single face of the sample.	115
7.2	Examples of possible sample uniformity challenges. (Center) an ideal sample, (Left and Right) practical samples shown with exaggerated draft angles.	120
7.3	Demonstration of the cold-finger effect leading to an under-estimated temperature difference.	126
7.4	Sample temperature profiles for three ambient temperatures.	128
7.5	Temperature contour of sample and probes, demonstrating the cold-finger effect.	130

7.6	Sample temperature profiles for three ambient temperatures.	131
7.7	(Left) voltage versus current plots used to measure electrical resistivity. (Right) voltage versus temperature difference plots used to measure Seebeck coefficient. Data measured on a 2 at% P doped 80/20 Si/Ge sample.	135
7.8	Uncertainty in electrical resistivity (Left) and Seebeck coefficient (Right) due to several sources. Data measured on a 2 at% P doped 80/20 Si/Ge sample.	137
7.9	Electrical resistivity and Seebeck coefficient data (Left) and power factor (Right) with uncertainty. Data measured on a 2 at% P doped 80/20 Si/Ge sample.	139
8.1	Back-scattered SEM images (A and B) with EDS chemical maps (Right) of Ge, Si, and W. Large WSi_2 precipitates (white faceted precipitates) are in an inhomogeneous Si/Ge matrix.	146
8.2	Pattern for Sample 3, $\text{Si}_{89.8}\text{Ge}_{9.3}\text{W}_{0.9}$ (top), and $\text{Si}_{90}\text{Ge}_{10}$ (bottom), addition of W component forms WSi_2 second phase with no shift in Si/Ge reflections.	147
8.3	Electrical resistivity of three comparable samples prepared using BN or SiO_2 crucibles. Trend indicates un-intentional doping resulting from the BN crucible.	149
8.4	Composition for ingots prepared in BN and SiO_2 crucibles as determined by ICP and Nitrogen determination. Samples are not intentionally doped.	150
8.5	Arrhenius plot of electrical conductivity of several W/Si/Ge samples. Closed symbols represent 0.8 at% W, open symbols 3 at% W. Included are published values for RTG and nano-structured $\text{Si}_{80}\text{Ge}_{20}$ alloys.	152
8.6	Seebeck coefficient of several W/Si/Ge samples. Closed symbols represent 0.8 at% W, open symbols 3 at% W. Included are published values for RTG and nano-structured $\text{Si}_{80}\text{Ge}_{20}$ alloys.	155
8.7	A) Total thermal conductivity of several W/Si/Ge samples. B) Calculated lattice thermal conductivity component. Closed symbols represent 0.8 at% W, open symbols 3 at% W. Included are published values for RTG and nano-structured $\text{Si}_{80}\text{Ge}_{20}$ alloys.	156

8.8	Schematic diagram of Si/Ge matrix with silicide precipitate. Repeating unit highlighted to the right to outline the geometric parameters x and d	161
8.9	Figure of merit (ZT) of several W/Si/Ge samples. Closed symbols represent 0.8 at% W, open symbols 3 at% W. Included are published values for RTG and nano-structured $\text{Si}_{80}\text{Ge}_{20}$ alloys.	163
8.10	A set of typical powder processed W/Si/Ge samples. Pellets have 1" diameter.	168
8.11	a) Milled powder after the first MA procedure, b) BSE image of sintered pellet of powder shown in 1a, c) Milled powder after the second three-step MA procedure, d) BSE image of sintered pellet of powder shown in 1c. All micrographs are shown for sample 9 (Si/Ge at% 90/10, WSi_2 2 vf%, P Doped); scale bars 15 μm	169
8.12	WSi_2 precipitate size distribution histogram and precipitate count mask for sample 1 (a and b, 2 vf% WSi_2) and sample 7 (c and d, 5 vf% WSi_2). Count mask scale bars are 10 μm	170
8.13	BET average particle size versus milling time (Top). DLS particle size distributions for three different milling times (Bottom).	173
8.14	XRD for sample 9 (Si/Ge at% 90/10, WSi_2 1.9 vf%, P Doped). Mixed powder after the second step of milling (Bottom), MA powder after the third step of milling and before sintering (Top). Si (*) and Ge (+) reflections coalesce into a single broad reflection, while W (^) reflections broaden.	175
8.15	Oxygen content of six samples compared against a sample prepared by solidification techniques.	178
8.16	Hall carrier density (Top) and Hall mobility (Bottom) of samples 5 and 6 versus temperature.	180
8.17	Electrical resistivity of n-type sample 9 (filled squares) and p-type sample 10 (open squares) upon the first heating and cooling cycle after densification.	183
8.18	Dopant stability of samples 2, 3, 5, and 6 (n-type filled shapes, p-type open shapes). Samples annealed at 700 °C with room temperature carrier density measured after quenching.	184

8.19	Seebeck coefficient (Left) and electrical resistivity (Right) of samples with constant WSi_2 volume fraction. Including: sample 1 (filled triangle), sample 5 (filled square), sample 6 (open square), sample 9 (filled circle), and sample 10 (open circle). Included are two published nano Si/Ge data sets (with no silicide precipitates) from Joshi et al. (solid line), and Wang et al. (dashed line).	186
8.20	Seebeck coefficient (Left) and electrical resistivity (Right) of samples with constant Si/Ge ratio. Including: sample 2 (filled diamond), sample 3 (open diamond), sample 4 (filled circle), sample 5 (filled square), sample 6 (open square), sample 7 (filled triangle). Included are two published nano Si/Ge data sets from Joshi et al. (solid line), and Wang et al. (dashed line).	187
8.21	Total thermal conductivity (Left) and lattice thermal conductivity (Right) of samples with constant WSi_2 volume fraction. Including: sample 1 (filled triangle), sample 5 (filled square), sample 6 (open square), sample 9 (filled circle), and sample 10 (open circle). Included are two published nano Si/Ge data sets from Joshi et al. (solid line), and Wang et al. (dashed line).	190
8.22	Total thermal conductivity (Left) and lattice thermal conductivity (Right) of samples with constant Si/Ge ratio. Including: sample 2 (filled diamond), sample 3 (open diamond), sample 4 (filled circle), sample 5 (filled square), sample 6 (open square), sample 7 (filled triangle). Included are two published nano Si/Ge data sets from Joshi et al. (solid line), and Wang et al. (dashed line).	191
8.23	Figure of merit of samples with constant WSi_2 volume fraction (Left) and constant Si/Ge ratio (Right). Included are two published nano Si/Ge data sets (with no silicide precipitates) from Joshi et al. (solid black line), and Wang et al. (dashed black line), and Si/Ge RTG data (dot-dash brown line and dotted brown line).	193
8.24	Micrographs of a) air loaded and b) argon loaded samples. White phase is WSi_2 , black phase is SiO_2 , gray phase is $\text{Si}_{1-x}\text{Ge}_x$. c) oxygen (green) and tungsten (red) EDS chemical maps on an EBSD grain boundary map of a sample loaded in air.	196
8.25	Study on loading powders in 'Air' compared to 'Argon'. a) Electrical resistivity and Seebeck coefficient b) Thermal conductivity including electrical and lattice components.	197
9.1	A) Ingot of Ni/Bi/Ge melt (25 mm diameter). B) Cross-section view of ingot showing phase segregation of Bi and Ni_xGe phases.	201

9.2	Secondary electron SEM micrograph of microwave sintered sample showing heterogeneous phases and porosity. Inset) cross-section view of sample.	203
9.3	XRD of milling study on Ni/Sb/Ge system, milling interval between selected profiles was 1-3 hours. Bottom profile (milling time 2 hours) contains Sb (^), Ge (o), and Ni (#) phases. Top profile (milling time 19 hours) contains Sb (^), NiSb (*), and Ge (o) phases.	205
9.4	Backscattered SEM micrograph of cold pressed and sintered sample showing heterogeneous phases and porosity. Inset) cross-section view of sample.	206
9.5	Backscattered electron and EDS chemical map of the solidified ingot of sample 1 ($\text{Ni}_4\text{Sb}_8\text{Sn}_4$).	208
9.6	Backscattered electron micrographs a) near the crucible wall and b) toward the center of the ingot of sample 3 ($\text{Co}_{0.5}\text{Ni}_{3.5}\text{Sb}_7\text{Sn}_5$).	208
9.7	Milling study of phase change calculated from XRD taken at intervals during milling: a) sample 1 $\text{Ni}_4\text{Sb}_8\text{Sn}_4$ nominal, b) sample 4 $\text{Co}_1\text{Ni}_3\text{Sb}_7\text{Sn}_5$ nominal.	212
9.8	Typical hot pressed skutterudite ingots, 1/2" diameter by 1" tall. Shown cut for electrical measurement (rectangular prism) and thermal measurement (disk).	214
9.9	Microstructure and XRD Rietveld refinement on three hot pressed samples. a) and b) sample 1 c) and d) sample 2 e) and f) sample 4.	215
9.10	Summary of data presented in Table 9.1 with skutterudite lattice parameter and phase quantity (wt%) for a) Co (x) study and b) Sn (y) study. Dashed lines are added to guide the eye.	217
9.11	Annealing of sample 6 displaying increased porosity and decomposition to the Ni_3Sn_4 phase. a) As sintered sample, b) after 200 °C anneal for 72 hours, c) after 400 °C anneal for 72 hours	218
9.12	a) Resistivity versus temperature and b) Seebeck coefficient versus temperature for sample 8 displaying repeatable hysteresis loops on heating and cooling curves.	219
9.13	Seebeck coefficient at 40 °C and 200 °C as a function of testing cycle count. Shown for a) sample 7 and b) sample 8, sample 7 trend is typical of samples 1-7.	220

9.14	(a and c) Resistivity versus temperature and (b and d) Seebeck coefficient versus temperature for samples 2-6 (a and b) and samples 6-8 (c and d).	222
9.15	Room temperature and 200 °C resistivity and Seebeck coefficient for Co (x) level (a and b) and Sn (y) level (c and d) in $\text{Co}_x\text{Ni}_{4-x}\text{Sb}_{12-y}\text{Sn}_y$ system.	223
9.16	(a and c) Thermal conductivity versus temperature and (b and d) material figure of merit versus temperature for samples 2-6 (a and b) and samples 6-8 (c and d). Total thermal conductivity shown with solid symbols, calculated lattice thermal conductivity shown with open symbols.	226
9.17	Room temperature and 200 °C total thermal conductivity and material figure of merit for Co (x) level (a and b) and Sn (y) level (c and d) in $\text{Co}_x\text{Ni}_{4-x}\text{Sb}_{12-y}\text{Sn}_y$ system	227
9.18	Room temperature hall mobilities and hall carrier densities of several skutterudites. Samples in this work are shown with stars.	228
9.19	Predicted figure of merit as a function of carrier density, as calculated from a single parabolic band model. Sample 2 ($\text{Ni}_4\text{Sb}_7\text{Sn}_5$) and Sample 6 ($\text{Co}_2\text{Ni}_2\text{Sb}_7\text{Sn}_5$) calculated at 400K.	229
9.20	Thermoelectric properties of samples 7, 9-13. a) Electrical resistivity, b) Seebeck coefficient, and c) total thermal conductivity.	230
A.1	Fabrication and testing of a two-couple device, a) hot and cold shoes painted with Pt ink b) two n- and two p-type legs mounted to shoes and electrodes c) complete device d) device mounted in test rig.	256
A.2	Top) Voltage versus current plot of device under three different thermal conditions, Bottom) Voltage, Power, and Current as a function of test load.	258
A.3	Thevenin resistance, open circuit voltage, and maximum power as a function of test time during an endurance test in air.	259

CHAPTER I

INTRODUCTION

1.1 Introduction to Thermoelectricity

Thermoelectric materials are a class of materials which exhibit a significant coupling between thermal and electrical transport. This coupling of thermal and electrical energy can be exploited to serve as a solid state heat pump or heat engine. Unlike conventional heat engines and pumps thermoelectric devices require no traditional working fluids, mechanical components, moving parts, or closed loop cycles. During operation thermoelectric devices produce no vibrations, noise, or torque making them an ideal power source for precise scientific equipment, whose measurements could be altered by noise or vibrations created from other power sources. Classically, thermoelectric devices have found applications in a range of NASA spacecraft for power generation as a part of the radioisotope power system (RPS) in the form of radioisotope thermoelectric generators (RTG). The Voyager missions launched in 1977 are continuing to operate with a Multi-Hundred Watt Radioisotope Thermoelectric Generator (MHW-RTG), proving the extreme reliability of thermoelectric devices [1]. Additional probes including the Galileo mission to Jupiter (1987 launch, mission successfully completed), the Ulysses solar mission (1990 launch, mission suc-

cessfully completed), Cassini Saturn orbital mission (1997 launch, mission ongoing), and the New Horizons mission to Pluto and Kuiper Belt (2006 launch, mission ongoing) have demonstrated the reliability of thermoelectric technology with years of continued operation, without any maintenance. These probes were powered by the NASA General Purpose Heat Source Radioisotope Thermoelectric Generator (GPHS RTG). The GPHS RTG had a beginning of mission (BOM) specification of 285 W electrical, but in practice was capable of producing more than 300 W electrical power from 4410 W thermal power, representing a conversion efficiency of approximately 6% [1]. In total, between NASA and the Department of Defense, the United States has launched 45 RTG [2]. Recently the Curiosity Mars Science Laboratory has utilized thermoelectric technology to provide power for scientific equipment and locomotive power [3].

Continued use of thermoelectric systems for spacecraft requires improved conversion efficiency and increased specific power. This must be accomplished by increasing probe power without increasing weight and without additional rare plutonium-238 fuel. Improvements in thermoelectric devices are required to reduce the use of fuel to compete with alternative power supply choices such as sterling engines [4, 5], thermoacoustic engines [6, 7], or photovoltaic conversion systems [8]. In recent years alternative power supply choices have made advancements in both conversion efficiency and specific power, but thermoelectric devices continue to provide the most reliable option due to the absence of moving parts and working fluids. Additionally,

unlike photovoltaic systems thermoelectric generators are able to operate in both dark and dusty environments.

Thermoelectric devices are increasingly being considered for applications other than space. For terrestrial applications economic and environmental factors become significant. For instance the cost per Watt ratio of a device and production volume can serve as deciding factors in the selection of a material system. Thus in addition to enhancing conversion efficiency emphasis must be put on economically viable materials and fabrication processes through consideration of factors such as abundance, toxicity, availability, and ease of scale-up to production level. These governing requirements drive a need to design new thermoelectric materials from readily available materials while maximizing the conversion efficiency.

Driven by the need to improve fuel economy the automotive industry is investigating thermoelectric devices for both refrigeration and power generation. Local HVAC cooling of an automobile is possible with the use of thermoelectric elements mounted directly in the seat; this method of cooling can potentially consume less power as compared to cooling the entire space of the car. Additionally, several auto manufacturers are considering thermoelectric power generation systems to be mounted in the exhaust system or directly in the tires [9]. Thermoelectric devices in the exhaust system can recover some of the 40% of energy wasted as hot exhaust gas, and reduce the direct engine load of the alternator [10]. Several exhaust based thermoelectric generators have been designed with working prototypes both bench-top tested and field tested and achieved power outputs on the order of 300

W electrical [11]. Aside from automotive applications the aerospace industry has considered thermoelectric devices for power generation. Thermoelectric devices offer the potential to provide the aerospace industry with local low power scavenging to enable wireless smart sensors [12, 13]. An aircraft engine is well suited for thermoelectric devices thanks to the large range of temperature gradients resulting from cold ambient surroundings and a hot thermal engine. Additionally, a number of military applications could benefit from the silent operation of thermoelectric devices. Power supplies for Naval submarines or stealth unmanned vehicles could gain from the silent and vibrationless operation of thermoelectric devices.

1.2 Scope of Work

This dissertation is split into two main parts (i) Analysis, covering the thermodynamic analysis, heat transfer, and solid-state transport of thermoelectric devices, and (ii) Experimental Development, covering the development of two new thermoelectric material systems. Increasing the efficiency of thermoelectric generators requires advancements in both the design of devices as well as the materials used. The materials developed in this work are used in the design portion of the dissertation. The scope of the work is outlined in the flowchart of Figure 1.1. Part I Analysis (Chapters 3, 4, and 5) provides a review of previously established thermoelectric analysis and introduces a new advanced set of analysis techniques. These advanced techniques are applied to the materials which are introduced in the second half of the work. Part II Experimental (Chapters 6, 7, 8, and 9) introduces the development of two new ther-

thermoelectric material systems in addition to providing a detailed uncertainty analysis for measured properties. Due to the lack of high temperature measurement standards in the thermoelectric community the uncertainty analysis completed serves to allow data comparison between labs. The two material systems investigated in this work use the measurement uncertainty analysis to report all measured properties. The Analysis and Experimental parts of this dissertation are connected through Chapter 5, where the advanced thermoelectric modeling is applied to the two material systems of this work.

The dissertation is composed of nine main chapters and includes work previously published by the author in peer-reviewed journals [14–16], conference proceedings [17], and additional unpublished work. Chapters 1 and 2 provide an introduction and review published literature on thermoelectric devices, thermoelectric analysis, and thermoelectric materials. Chapter 3 provides a more detailed account of thermoelectric analysis, leading into the need for more advanced analysis techniques.

This work focuses on four main topics critical to the advancement of thermoelectric technology. (i) Advanced analytic modeling of a thermoelectric couple; Chapter 4 introduces several complicating factors into a thermodynamic model of thermoelectric devices that are solved analytically. The physics uncovered in this section is applicable to all thermoelectric materials including the materials developed in this work as described in later chapters. These were the materials employed in case studies of device design as described in Chapter 5. Some of the original work

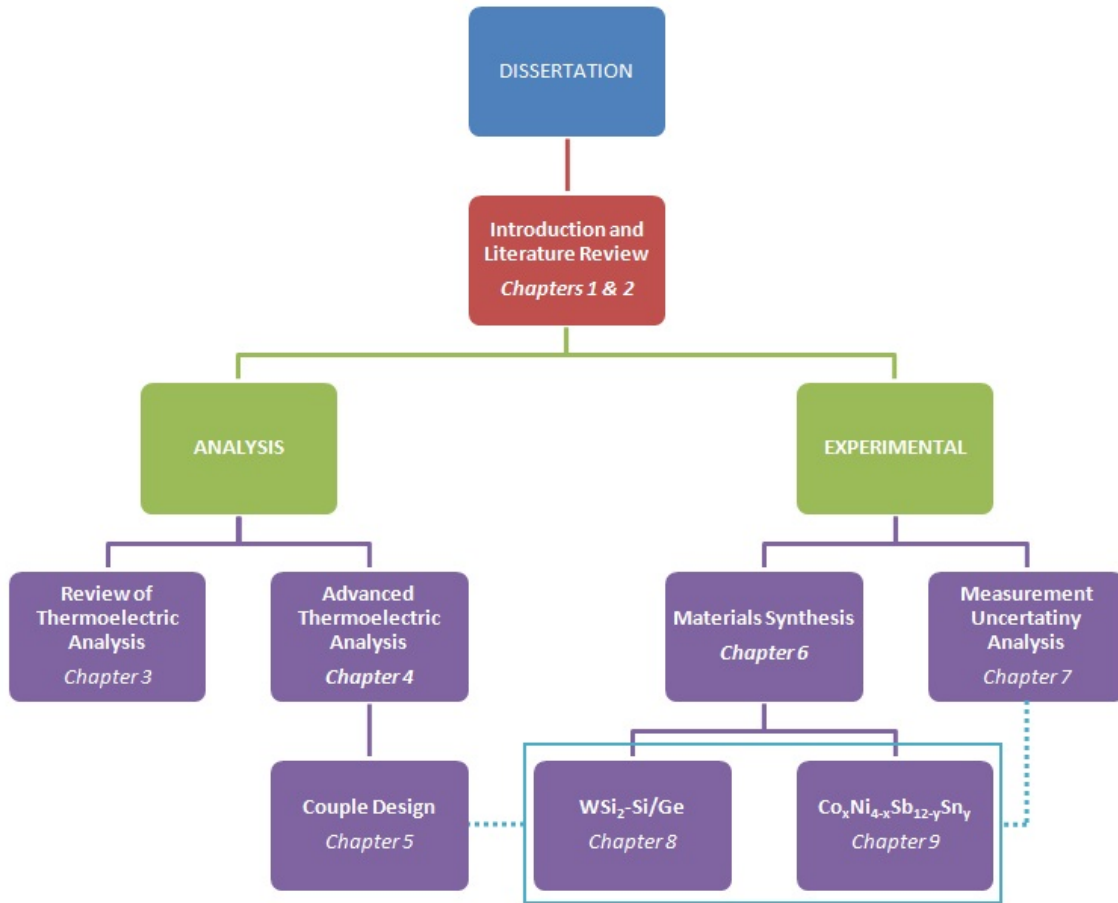


Figure 1.1: Flow chart outlining the organization of the dissertation.

presented in Chapter 4 has been published in reference [14], the remainder is being compiled for a future publication.

Chapter 6 introduces the processing and characterization techniques used in this work leading into the experimental portion of the work. (ii) Detailed uncertainty analysis of the measured properties is the second main focus topic; Chapter 7 introduces an uncertainty analysis of a measurement configuration common to the thermoelectric community. The analysis goes beyond a simple statistical calculation

and employs the finite element method along with error propagation theory to estimate the true uncertainty of the critical measurement data. The original work on uncertainty analysis has been published in reference [15]. (iii) Development of a tungsten silicide (WSi_2) in silicon germanium (Si/Ge) nano-structured composite is the third focus topic; Chapter 8 introduces the processing and thermoelectric properties of this improved Si/Ge based system. The classic Si/Ge system is a proven high temperature thermoelectric material, which benefits from the nano-structured composite form investigated within this work. Composition-structure-property relations were studied on the system with a focus on thermoelectric properties. The original solidification work of this section has been published in reference [16], with the powder processing work submitted for publication to *Acta Materialia*. (iv) Development of a novel medium temperature quaternary skutterudite system $\text{Co}_x\text{Ni}_{4-x}\text{Sb}_{12-y}\text{Sn}_y$ is the final focus topic; Chapter 9 introduces the processing and thermoelectric properties of the new skutterudite system. Effects of composition and structure were investigated on thermoelectric properties. The original work of this section has been published in reference [17], with the remaining work to be published as a future article. Finally, Chapter 10 provides a summary and future work. Additional information concerning details of the uncertainty analysis and device testing can be found in Appendices at the end of the dissertation.

The topics covered in this dissertation advance thermoelectric technology by applying an interdisciplinary approach to the field. The contributions of the dissertation are outlined in Figure 1.2. The topics investigated include fundamental

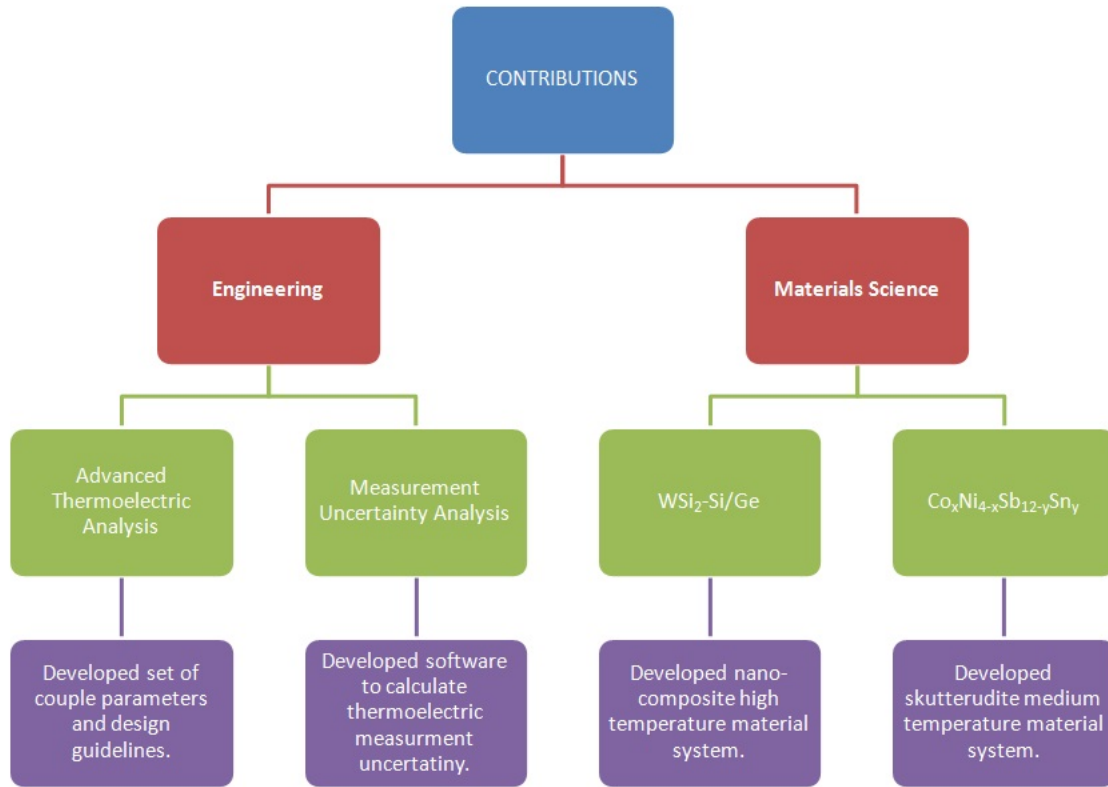


Figure 1.2: Flow chart outlining the contributions developed in the dissertation.

mathematical modeling, engineering based measurement uncertainty analysis, and material science focused materials development. The modeling employs mathematical techniques not commonly used in the thermoelectric community. The uncertainty characterization includes both measurement characterization and numerical heat transfer analysis to provide a critical uncertainty. The new material systems of the work add to the ensemble of thermoelectric materials available to the community, covering both a medium and high temperature range between the two systems.

CHAPTER II

LITERATURE REVIEW

2.1 Introduction

This chapter will introduce the background of (i) thermoelectric devices, (ii) thermoelectric analysis, (iii) common thermoelectric material systems, and (iv) segmented and cascaded couples which provides a link between the two material systems investigated in this work.

2.2 Thermoelectric Devices

Work in thermoelectric (TE) materials dates back to the work of Thomas Johann Seebeck in 1821 [18, 19] and Jean Peltier in 1833 [19, 20]. Rayleigh first considered the use of the Seebeck coefficient for electric power generation in 1885 [19]. Widespread use of TE devices was not possible until the development of semiconductor based materials, such as bismuth telluride, lead telluride, and silicon germanium [13, 21]. Today TE devices are used as heat engines to convert between thermal and electrical energy, as heat pumps for refrigeration, and as thermal energy sensors. They are used widely across military, aerospace, and commercial sectors with a large amount of research driven by the use of TE devices in spacecraft power systems.

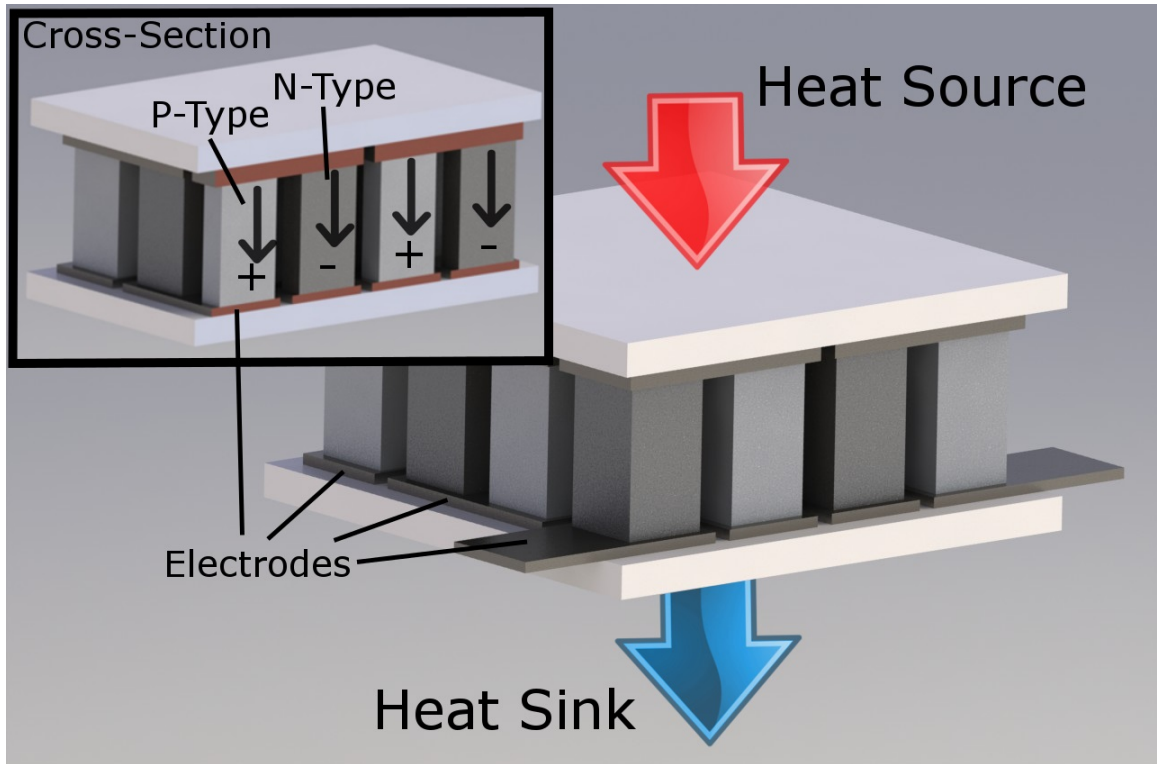


Figure 2.1: Typical TE device composed of n- and p-type thermoelements, metallic electrodes, and hot and cold ceramic heat spreaders.

Typically TE devices are composed of n- and p-type semiconductor TE legs arranged electrically in series and thermally in parallel, see Figure 2.1. The legs are connected electrically with metallic interconnections and are mounted on electrically insulating ceramic heat spreaders. When an electrical current is driven through the device heat is pumped between the two ceramic plates and the device can be used for refrigeration. Alternatively, if heat is allowed to transfer through the device, from some heat source to a sink, an electrical current is generated which can be used as an electrical power source.

TE coolers generally have a low coefficient of performance, but their reliability, small size, absence of moving parts, and absence of working fluids makes them ideal for a number of niche applications in military, space, aerospace, and commercial industry. The absence of a working fluid makes TE devices a friendly option for cooling electronics, where leaking fluids could be damaging. They have been used both for local cooling of microelectronics and general cooling of larger components. Micromachining techniques make it possible to build TE coolers directly into electronic components and boards, especially laser diodes. In addition to electronics, TEs have found cooling applications in personnel garments, portable refrigerators, wine coolers, helmet refrigerators, and automobile seat coolers [21].

TE power generation has been limited to military and space applications due to low conversion efficiency. Commercial applications are currently being investigated, such as automotive or diesel exhaust heat power generation, but systems still need to demonstrate economic viability. Prototype automotive power generation modules have demonstrated power outputs on the order of 300 W electrical [11]. TE devices are also being considered for low power scavenging, on the order of microwatt or milliwatt. Wireless sensors, which require a low power source such as a battery, are becoming more common in commercial and aerospace industries. Since TE modules provide continuous power without the need for maintenance, they can replace batteries in sensors. Low power TE devices can be configured to operate on natural thermal gradients which can exist in the location of the sensor [21]. The largest and most established use of TE power generation is in spacecraft. Both the

Department of Defence and NASA have launched craft powered by radioisotope TE generators (RTG). Since servicing spacecraft after launch is nearly impossible the reliability factor of a TE power system outweighs cost and efficiency concerns. The United States has launched over 45 RTGs with an excellent record of success [2]. The RTG program uses a Pt-238 core to generate the required constant heat flux, the ambient cold of space is used as the heat sink for the RTG. NASA has developed a number of RTG systems including the Systems for Nuclear Auxiliary Power RTG (SNAP-RTG), Multi-Hundred Watt RTG (MHW-RTG), and General Purpose Heat Source RTG (GPHS-RTG). The MHW-RTG on the Voyager spacecraft has been continuously operating since 1977, and the mission continues to this day [2].

The fuel source, Pt-238, used in spacecraft RTG systems is extremely rare in the enriched form. A limited supply of enriched fuel exists due to the shutdown of enrichment facilities, meaning that the space program is limited in the number of craft. To conserve fuel higher conversion efficiency is required of future RTG systems, so that less fuel may be consumed by each craft. Current conversion efficiencies are around 5% for GPHS-RTG [1]. As a possible replacement to the low conversion efficiency RTG systems NASA has investigated Stirling engines.

Robert Stirling patented the Stirling engine in 1816 [5]. The Stirling engine is a closed loop heat engine in which the working fluid is displaced from the hot and cold portions of the engine by manipulating the fluid boundaries by means of a power and displacer piston [4]. Unlike the isentropic expansion and compression of the ideal Carnot cycle the Stirling cycle undergoes a constant volume process. Stirling engines

have demonstrated higher conversion efficiency than RTG systems around 25% [4], and they can be designed to work with the same fuel source as RTG. However, the Stirling engine contains a number of moving parts, gaskets, and working fluids and therefore cannot compete with RTG systems in terms of reliability.

Another competitor to TE power generation is photovoltaic (PV) conversion. PV systems provide direct conversion of sunlight into electrical energy by the photoelectric effect. As sunlight strikes a PV cell, energy is absorbed into electrons in the material, raising their energy level to free them and cause a voltage potential in the cell. Similar to TE technology the investigation of new semiconductor materials has enhanced PV conversion efficiency. PV technology can be easily integrated into many systems including building rooftop arrays, large scale power plants, and spacecraft. The free source of sunlight makes PV technology a strong candidate for renewable energy, as no fuel is required. As a drawback of PV, the availability of sunlight is not always reliable or controllable. For terrestrial applications weather and day/night cycles make it difficult to balance loads and power source in a large scale grid, especially with increasing reliance on PV [8]. In spacecraft applications such as probes which visit locations without a reliable source of sunlight, or probes which work in dusty environments, PV is not a reliable power choice. PV cells also suffer from losses in conversion efficiency and long-term damage due to excess temperature as a result of incident radiation, further reducing their reliability factor [22]. Hybrid PV-TE devices have been proposed, in which the excess thermal energy generated in the PV system is used to operate a TE system [23–25]. PV-TE systems result in

enhancement in conversion efficiency compared to either PV or TE systems alone. As an alternative approach TE systems can be used for active cooling on PV systems, the systems can be designed to keep the PV system operating within the ideal temperature range [22, 25].

2.3 Thermoelectric Analysis

To guide TE material and device design several metrics must be considered including conversion efficiency, power density, cost per Watt ratio, and specific power. The guiding metric depends on application. For space applications the need to conserve fuel and reduce craft weight places conversion efficiency and specific power at the top of the list. For commercial applications the economic cost per Watt ratio may dominate. For military or aerospace applications with confined space the power density may be most critical. In nearly all applications the conversion efficiency, defined as the ratio of electrical power to thermal power, plays a large role in TE effectiveness. The calculation of conversion efficiency of a TE device was first completed in 1911 by E. Altenkirch [26] then was revised to the form recognized today in 1957 by Abram Ioffe [27]. The details of the derivation for TE conversion efficiency are outlined in Chapter 3, and have been investigated in a number of works [26–30]. The conversion efficiency of a power generation TE and the coefficient of performance of a refrigeration TE device both depend on the Carnot efficiency of the engine and a dimensionless term named the thermoelectric figure-of-merit or ZT . The conversion

efficiency of a TE device increases with increasing ZT. The ZT is simply composed of temperature T and three material properties as,

$$ZT_{Material} = \frac{S^2\sigma T}{k}. \quad (2.1)$$

The material properties of interest are the Seebeck coefficient S , electrical conductivity σ , and thermal conductivity k . The electrical and thermal conductivity of a material are well studied for a number of different materials but the Seebeck coefficient and two other TE properties (Peltier coefficient and Thomson coefficient) are unique to TE materials. In material design it becomes critical to develop materials with high Seebeck coefficient and electrical conductivity while having a low thermal conductivity. Performance of TE devices have been investigated by a number of different groups using both analytical [26–40] and numerical techniques [41–47]. Work in accounting for the commonly neglected Thomson heat and other variable material properties has been performed by Sherman et al. [29], Yamashita [31], Min and Rowe [32], Huang et al. [40], and Sandoz-Rosado et al. [42]. Work on transient couples has been performed by Gou et al. [45], Meng et al. [43], D. Crane [46], Nguyen et al. [47], and Alata et al. [38]. Chapter 4 will introduce another analysis of both variable material properties and transient operation but the solution is setup to be more generally applicable than the treatments referenced above.

To better understand TE phenomenon consider the material properties Seebeck coefficient, Peltier coefficient, and Thomson coefficient. The Seebeck coefficient is the principle material property which leads to the operation of a thermocouple, first

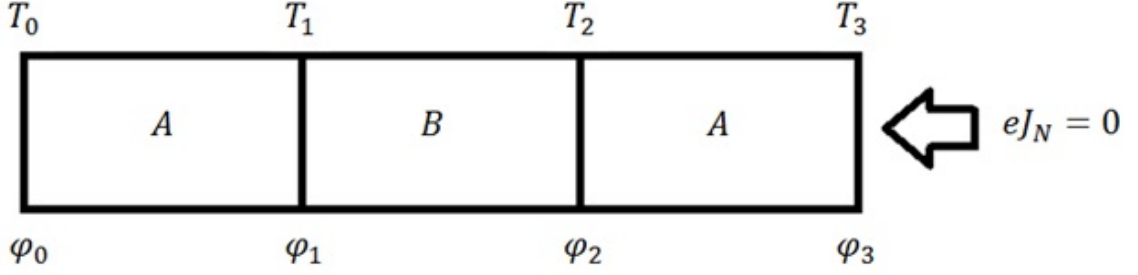


Figure 2.2: An open circuit conductor composed of two materials A and B with an arbitrary temperature profile. Conductor is subject to zero electrical current flux (eJ_N).

observed in 1821 by Thomas Johann Seebeck [18, 19]. Consider Figure 2.2, an open circuit conductor composed of two materials A and B under an arbitrary temperature profile. The temperature gradient results in an electrical potential in the conductor, forming the basis of the thermocouple as a temperature measurement device. By definition, equation 2.2, the voltage difference ($d\phi$) between any two points, 1 and 2, can be expressed in terms of the Seebeck coefficient (S) and temperature (T using integration variable τ)

$$S = -\frac{d\phi}{dT}, \quad (2.2)$$

$$-\int_{T_1}^{T_2} S(\tau)d\tau = \int_{\phi_1}^{\phi_2} d\theta = \phi_1 - \phi_2. \quad (2.3)$$

For instance the electrical potential between the ends of the conductor shown in Figure 2.2 can be expressed in terms of the individual Seebeck coefficients of the A and B materials separately

$$\phi_3 - \phi_0 = - \int_{T_0}^{T_3} S(\tau) d\tau = - \left(\int_{T_0}^{T_1} S_A d\tau + \int_{T_1}^{T_2} S_B d\tau + \int_{T_2}^{T_3} S_A d\tau \right). \quad (2.4)$$

Now consider the case when T_0 and T_3 are equal, which could be practical for a thermocouple composed of materials A and B with the volt meter connected at locations 0 and 3

$$\begin{aligned} \phi_3 - \phi_0 &= - \left(\int_{T_0}^{T_1} S_A d\tau + \int_{T_2}^{T_0} S_A d\tau + \int_{T_1}^{T_2} S_B d\tau \right) \\ &= - \left(\int_{T_1}^{T_2} S_B d\tau - \int_{T_1}^{T_2} S_A d\tau \right) = - \int_{T_1}^{T_2} (S_B - S_A) d\tau. \end{aligned} \quad (2.5)$$

Equation 2.5 serves as the basis of thermocouple thermometry. If the temperature dependant Seebeck coefficient of materials A and B are known and the temperature T_2 is also known, by another thermometry technique, then the temperature T_1 can be determined from the voltage potential generated between points 0 and 3.

The Peltier coefficient, first observed in 1833 by Jean Peltier [19, 20], is the principle factor in thermoelectric refrigeration. Consider Figure 2.3 which shows an isothermal junction between two conductors A and B, through which both an electric current and heat flux passes. It is experimentally verifiable that as electrical current flows through the junction heat may be either released or absorbed depending on the materials A and B and the direction of the current flow. The release or absorption of heat at the junction depends on the difference of total internal energy flux (J_U) of the two conductors as

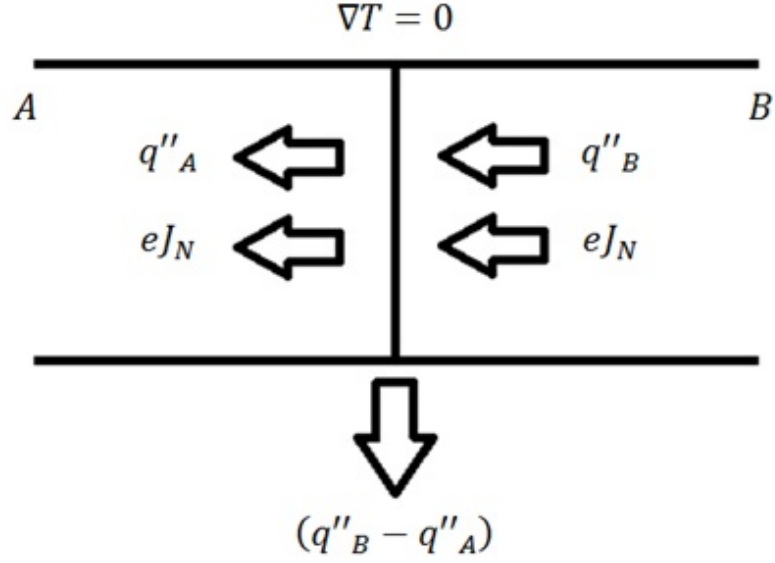


Figure 2.3: Isothermal junction ($\nabla T = 0$) between two conductors composed of materials A and B. Electrical charge flux (eJ_N) is conserved in the junction but heat (q'') may be either released or absorbed.

$$J_{U_B} - J_{U_A} = q''_B + eJ_N\phi_B - q''_A - eJ_N\phi_A = q''_B - q''_A, \quad (2.6)$$

where $\phi_{A,B}$ is the voltage potential in the two materials at the location of the junction. By definition of the Peltier coefficient, equation 2.7, we find the amount of heat released is proportional to the difference in Peltier coefficient of the two materials and the electrical current (eJ_N) passed through the junction, equation 2.8. Depending on the magnitude of the material's Peltier coefficients and the direction of the current density the heat could either be released or absorbed at the junction

$$\pi = \frac{q''}{eJ_N}, \quad (2.7)$$

$$J_{U_B} - J_{U_A} = (\pi_B - \pi_A)eJ_N. \quad (2.8)$$

Considering the temperature dependence of the Seebeck coefficient the third TE coefficient can be defined as,

$$\tau = \frac{dS}{dT}T. \quad (2.9)$$

The Thomson coefficient was first observed in 1854 by William Thomson (also known as Lord Kelvin) [48, 49]. It will be demonstrated in Chapter 3 that all three TE properties are simply different manifestations of the same TE phenomenon.

2.4 Thermoelectric Materials

Early TE materials were made of metals like iron, copper, zinc-antimony, and German silver (Cu60%-Ni20%-Zn20%) and were prone to mechanical failure, oxidation, and very low conversion efficiency [21, 50]. A wide range of TE materials have been studied since the space program's work in the 1960s. For the NASA radioisotope power system program (RPS) materials which have flown on craft include lead telluride (PbTe), tellurides of antimony germanium and silver known as the TAGS system (AgSbTe₂ – GeTe), lead tin telluride (PbSnTe), and silicon germanium (Si_{1-x}Ge_x) [2]. Commercialized TE materials include bismuth telluride (Bi₂Te₃), lead telluride (PbTe), and silicon germanium (SiGe) [21]. Additional TE systems being studied include Zintl (some example compounds include Yb₁₄MnSb₁₁, Sr₃GaSb₃,

Ca₅Al₂Sb₆) [51–56], Chalcogenides (Bi₂Te₃, Sb₂Te₃) [57–60], Skutterudites (CoSb₃, NiP₃, Ce_yFe_{4-x}Co_xSb₁₂) [17, 61–90], Clathrates (Sr₈Ga₁₆Ge₃₀, Ba₈In₁₆Sn₃₀) [58, 58, 59, 91], Half-Heuslers (TiNiSn, Zr_{0.4}Hf_{0.6}NiSn_{0.98}Sb_{0.02}) [58, 59, 92], silicides (MgSi₂, Re_xMn_{1-x}Si_{1.8}) [93–96], oxides (NaCo₂O₄, SrTiO₃) [58, 59, 97, 98], and polymers (PEDOT:PSS, Polyacetylene) [59, 99]. Each system has a unique operating temperature range due to the temperature dependence of figure of merit (ZT, see Eqn. 2.1), summary of which is shown in Figure 2.4 for some representative systems. In general, most materials have an increasing figure of merit up to some characteristic temperature, above which the properties drop off. In addition to selecting a material based on figure of merit alone several other temperature dependant factors can play a role. For instance some materials are known to have sublimation issues at high temperatures or others are subject to problems with solid-state phase change.

Two material systems are the focus of this work. These systems are the high temperature (600 – 1000 °C) Si/Ge system, which has flown on several NASA missions, and the moderate temperature (200 – 600 °C) skutterudite system.

2.4.1 Silicon Germanium

Silicon germanium is the most established high temperature system with much of the early work done for the RPS program during the 1960s and 1970s [100–114]. Both the GPHS RTG and the MHW RTG use Si/Ge legs doped to n- or p-type with phosphorous or boron, respectively. Several factors have made Si/Ge a successful system for deep space TEs. For instance the mechanical stability of the system,

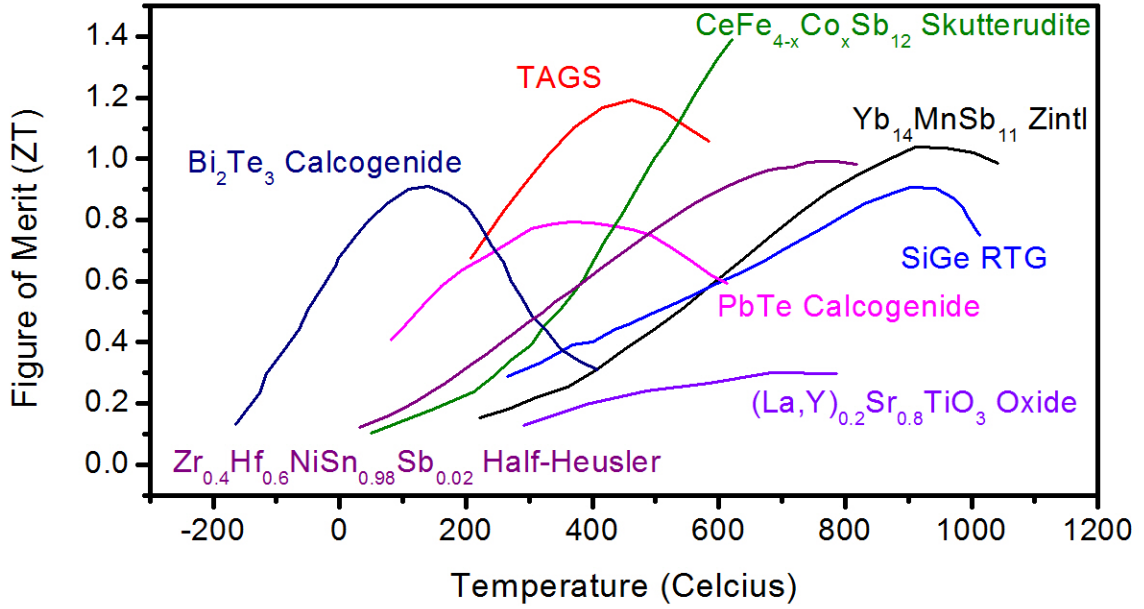


Figure 2.4: Figure of merit of several common TE systems, data extracted from several sources [51, 57, 92, 98].

as compared to other TE systems, makes it possible for the device to withstand the vibrations and acceleration of a rocket launch. The system is capable of withstanding a high hot shoe temperature, to nearly 1000°C . Since the conversion efficiency of a TE device is dependent on the Carnot efficiency a higher hot shoe temperature will be more efficient. Additionally, a higher hot shoe temperature allows for a higher specific power thanks to higher Stefan-Boltzmann radiation from the warmer cold shoe [1]. The system is relatively stable in either air or under vacuum without the need for complex inert gas systems [105]. Finally, the system has a reasonable range of figure of merit (peak ZT 0.5 for p-type, peak ZT 1.0 for n-type) over the temperature range required of the RTG program, although the advancement of TEs requires substantial improvements in figure of merit.

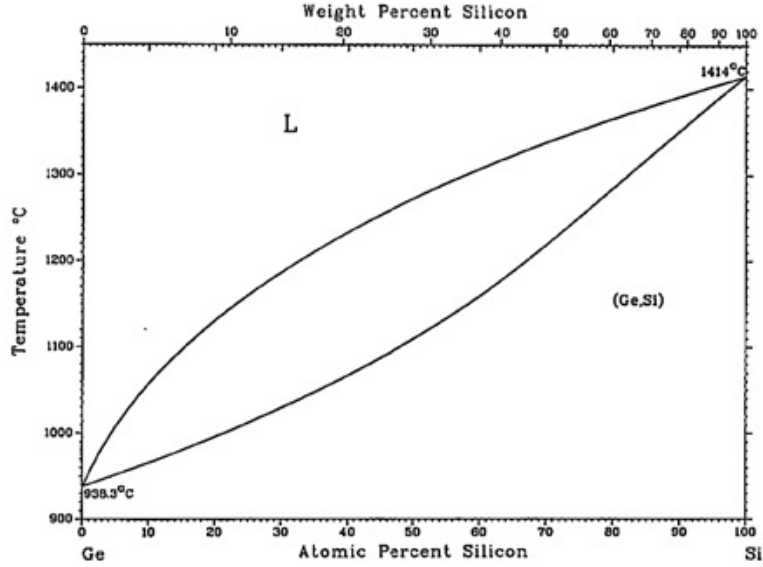


Figure 2.5: ASM International (1996) phase diagram of the Si/Ge binary system.

Much of the original work on the system was performed on solidified Si/Ge alloys [115]. The $\text{Si}_x\text{Ge}_{1-x}$ system has complete solid-state solubility over the entire 0-100% range (Fig. 2.5) and crystallizes in the cubic Fd-3m space group. The melting point of pure Si is 1414°C and the lattice parameter is 5.43 \AA [116]. The melting point of pure Ge is 938.3°C with lattice parameter 5.62 \AA [117]. For the range of $\text{Si}_x\text{Ge}_{1-x}$ alloys the melting temperature and lattice parameter fall between these two extremes. While the system theoretically has complete solubility, it is well known that Si/Ge is non-congruent in the melt, resulting in segregation of Si and Ge [106]. The segregation in melt processing is due to slow solid-state diffusion coefficients during cooling. To get a uniform Si/Ge distribution lengthy zone leveling is employed, which consists of passing the solidified ingot through a slow moving hot zone several times to get longer

diffusion times [103, 106]. The intrinsic carrier densities of $\text{Si}_x\text{Ge}_{1-x}$ alloys is too low for TE applications so electronically active dopants must be added to tune the n- and p-type carrier densities to the required levels of $10^{20} - 10^{21}$ carriers per cm^3 . Required carrier density levels are based on the carrier dependence of the electronic properties in ZT (see Fig. 3.4 later). Boron has one less valence electron than the $\text{Si}_x\text{Ge}_{1-x}$ alloy and accepts an electron, resulting in the creation of a hole and a p-type material. Phosphorous has one additional valence electron than the $\text{Si}_x\text{Ge}_{1-x}$ alloy and donates an electron, resulting in the creation of an n-type material. Phosphorous and Boron have limited solubility in Si/Ge and the solubility of Phosphorous is retrograde above 950°C [106]. As a result the dopant stability is a critical factor to consider in the Si/Ge system.

Lattice disorder introduced by the $\text{Si}_x\text{Ge}_{1-x}$ alloy introduces significant phonon scattering and greatly reduces the total thermal conductivity of Si/Ge from that of either pure Si or pure Ge. As a result the figure of merit of a $\text{Si}_x\text{Ge}_{1-x}$ alloy is greatly improved over that of either pure Si or Ge alone [101, 102]. Additional significant reductions in thermal conductivity result from the heavy doping levels in the form of impurity scattering of phonons. In general the $\text{Si}_x\text{Ge}_{1-x}$ system has optimal figure of merit performance in the range of x between 0.7 and 0.9 and with dopant levels less than 2 at% [103, 106].

In the early 1990s work in the Si/Ge system focused on studying the effect of grain size on the TE transport properties [118–120]. It was found that reducing the grain size to the range of 2-5 μm could introduce a grain boundary phonon scattering

mechanism. While the alloy scattering of the Si/Ge lattice disorder scatters short wavelength phonons the micron grain boundary scattering scatters the longer phonon wavelengths. Investigation of grain size effects on the figure of merit showed that the ZT was improved by 10% for 2-5 μm grains over that of large grain materials ($>170 \mu\text{m}$) [120].

The mid 1990s lead to resurgence in TE research as a result of the work of Dresselhaus, Hicks, and Chen with their work in nano-structuring [60, 121–127]. Nano-structuring of TE materials provides two potential improvements (i) an enhancement of the electrical power factor through low dimensionality and (ii) a reduction of lattice thermal conductivity by preferential scattering of phonons over electronic charge carriers. Low dimensional materials have the potential to benefit from an altered density of states from that assumed in 3D bulk (Eqn. 3.54). As a result it becomes possible to tune the Seebeck coefficient independent of the electrical conductivity and thereby increase the electronic power factor ($S^2\sigma$). This phenomena was experimentally verify for the first time with a 2D superlattice of PbTe quantum wells and $\text{Pb}_{1-x}\text{Eu}_x\text{Te}$ barriers [123, 125]. Phonon scattering by nano-structured interfaces was experimentally verified in a $\text{Bi}_2\text{Te}_3/\text{Sb}_2\text{Te}_3$ superlattice; it was shown that control of the interface spacing could preferentially scatter phonons over charge carriers leading to enhanced figure of merit [60].

In 2008 both n- and p-type Si/Ge were experimentally verified to have significant enhancement in figure of merit as a result of nano-sized grains, reducing thermal conductivity independent of electrical conductivity. Josh et al. reported

a figure of merit improvement of 90% for p-type nano-structured Si/Ge over traditional RTG values [128]. Wang et al. reported a 40% figure of merit improvement for n-type nano-structured Si/Ge over RTG [129]. While nano-sized grains have been shown to significantly improve TE properties there is potential for thermally induced grain growth to hinder the improvements. As an alternative approach, Mingo et al. proposed introduction of a thermally stable nano-precipitate into a Si/Ge matrix to reduce thermal conductivity [130]. The theoretical calculations showed that this method provides the possibility of tuning the phonon scattering while still retaining a thermally stable material. It was determined that an optimal precipitate size of 2-10 nm in a Si/Ge alloy would be required to maximize the reduction in thermal conductivity [130]. More recently, theoretical work has suggested that a broad range of length scales can further reduce thermal conductivity of a Si/Ge nano-composite over that of a narrow range [131]. Several groups have theoretically investigated the nano-particle in Si/Ge alloy approach with similar conclusions [130–135]. Experimental work on synthesizing nano-precipitates in Si/Ge alloys has been reported for the $\text{Si}_{80}\text{Ge}_{20}\text{B}_6\text{-Er}$ [136], $\text{Si}_{80}\text{Ge}_{20}\text{-CrSi}_2$ [137], and $\text{Si}_{92}\text{Ge}_8\text{-MoSi}_2$ [138] systems.

2.4.2 Skutterudite

Skutterudites have been a well studied class of TE materials which have shown promise as a high figure of merit material [61–65, 139, 140]. Skutterudites exhibit strong figure of merit, good mechanical properties, and can be relatively cheap compared to other TE materials. Skutterudites got their name from the mineral CoAs_3 ,

first mined in Skutterudite, Norway [61]. The binary skutterudite structure is represented by the chemical formula BX_3 where B is Co, Rh, Ir, Fe, Ni, Ru, or Pd and X is a pnictogen atom such as P, As, Sb, or Bi. The skutterudite system forms the cubic Im-3 space group with 32 atoms per unit cell shown in Figure 2.6. The crystal structure contains a transition metal framework (B, blue atoms, Wyckoff 8c position) with six planar pnictogen rings (X, yellow atoms, Wyckoff 24g) and two relatively large voids per unit cell (shown filled by red atoms in Figure 2.6 site A, Wyckoff 2a). A complete description of the crystal structure can be defined by a single lattice parameter, the y and z positional parameters of the pnictogen rings, and the occupancy of all sites. Typically only a partial occupancy of the filler 2a sites (A, red atoms) is thermodynamically stable, while the other sites are nearly full. Tuning of the electronic properties is typically controlled by substitutions on the transition metal or pnictogen ring sites, such that a solid solution of two elements often occupies each location. The skutterudite crystal structure can be viewed as a distortion on the cubic perovskite ruthenium oxide ReO_3 structure [61, 82].

A key advantage of the system is that the voids may be filled with electropositive atoms such as elements from the lanthanide series to serve as phonon scattering centers and greatly reduce the thermal conductivity. In this way, the skutterudite system fits the model of a phonon-glass electron-single-crystal (PGEC) framework. An ideal PGEC would have the low thermal conductivity of an amorphous glass and the high carrier mobility of a single crystal. These attributes would lead to a high TE figure of merit. The general formula for a filled skutterudite can be written as

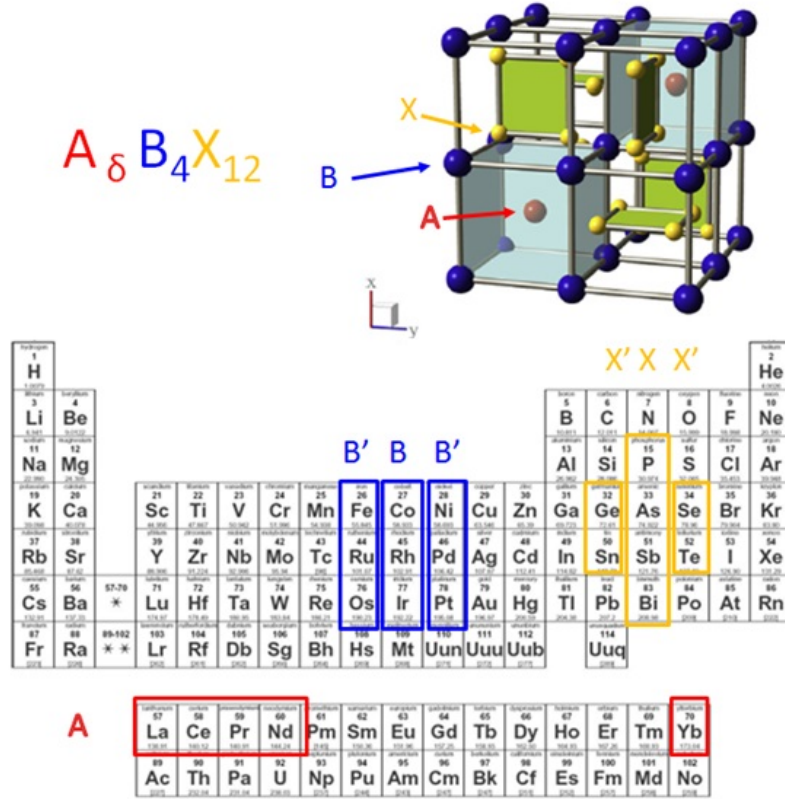


Figure 2.6: Crystal structure and range of possible skutterudites, adapted from reference [70].

AB_4X_{12} [82]. Filled skutterudites have experimentally been shown to have decreased lattice thermal conductivity leading to enhanced figure of merit over unfilled skutterudites [69–73, 87–89]. Each filler atom has a characteristic mass which leads to scattering of a specific frequency phonon. Therefore it is common to use several filler atoms, of notably different mass, to scatter a wide frequency range of phonons, this is called double or triple filling. Work in the skutterudite system has developed strong n-type skutterudites with peak ZT of 1.5 for double and triple filled samples such as $Ba_uLa_vYb_wCo_4Sb_{12}$ [66, 67]. P-type skutterudites are not as strong, with peak ZT

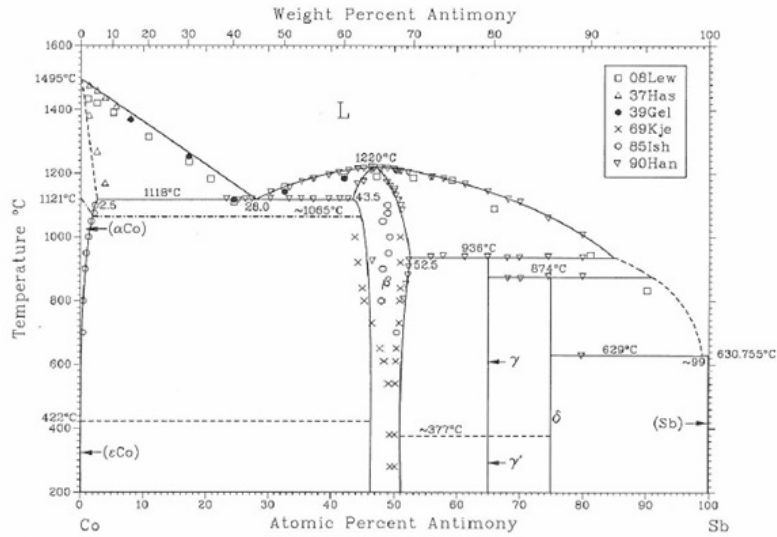


Figure 2.7: ASM International (1996) phase diagram of the Co/Sb binary system.

of 1.0 for filled samples $\text{Ce}_{0.28}\text{Fe}_{1.5}\text{Co}_{2.5}\text{Sb}_{12}$ [83, 84]. Due to the relatively low ZT values for p-type skutterudites current research has focused on finding new p-type skutterudites.

A number of skutterudites have been achieved in practice either from a peritectic reaction by way of incongruent melting, under hydrothermal conditions, or under high temperature and pressure [82]. Figure 2.7 shows the binary phase diagram of Co and Sb. At 75 at% Co and 874 °C the CoSb_3 skutterudite phase forms from a peritectic reaction of 66.7 at% Co γ phase and 90 at% Co liquid phase. The kinetically slow peritectic reaction of the skutterudite phase requires long processing times for melt derived samples and often includes notable levels of secondary phases.

In addition to filling schemes the skutterudite system has potential to be improved by introducing disorder on the pnictogen rings, which have been shown to carry a majority of thermal vibrations [68]. Disorder on the pnictogen rings can be introduced by making substitutions on the pnictogen site to form ternary skutterudites with the general formula $BX_{3-x}^I X_x^{II}$. Some ternary skutterudites include $\text{CoGe}_{1.5}\text{S}_{1.5}$ [74], $\text{CoGe}_{1.5}\text{Se}_{1.5}$ [74], $\text{IrGe}_{1.5}\text{S}_{1.5}$ [63], $\text{IrGe}_{1.5}\text{Se}_{1.5}$ [63], $\text{IrSn}_{1.5}\text{S}_{1.5}$ [63], $\text{RhGe}_{1.5}\text{S}_{1.5}$ [63], $\text{Co}_4\text{Ge}_6\text{Se}_6$ [75] and $\text{Ni}_4\text{Sb}_8\text{Sn}_4$ [77, 78]. Lists of potential ternary skutterudites can be found summarized in the works of Bauer et al. [76] and Fleurial et al. [65]. Additionally, similar to the Si/Ge system skutterudites can potentially be improved through nano-structuring.

2.5 Couple Segmentation and Staging

No single TE material displays strong figure of merit over the entire operating temperature of a practical device (Fig. 2.4). In order to get the largest conversion efficiency out of a device low, medium, and high temperature materials can either be segmented or cascaded into compound modules [13, 110, 141–143]. Segmentation of a TE couple consists of physically bonding two or more TE materials such that heat and electricity flow directly through both materials in a single couple. The design of the couple can be made such that each material is subjected to its optimal temperature range, thereby increasing the overall device efficiency. Cascaded, or staged, TE devices consist of two or more devices of a single material staged thermally in series. In this form each material is found in a separate couple. Figure 2.8 shows both

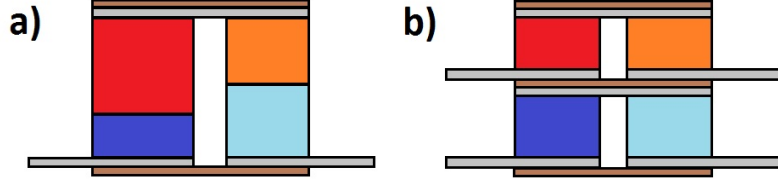


Figure 2.8: a) Segmented TE couple b) cascaded TE couple.

the segmented and staged configurations. Through these design techniques a high temperature system like Si/Ge can be made to compliment a medium temperature system like skutterudite.

The work of Snyder and Ursell [141] introduced the concept of a compatibility factor s in terms of ZT and Seebeck coefficient S as

$$s = \frac{\sqrt{1 + ZT} - 1}{ST}. \quad (2.10)$$

This intrinsic material parameter serves as a straight-forward design point for segmented couples. If two materials have comparable compatibility factors, then the couple will be improved by segmentation of the two material systems. Alternatively two material systems with greatly differing compatibility factors can suffer a reduction in conversion efficiency as a result of segmenting. For a cascaded TE device, if each stage is independently load balanced and temperatures are selected appropriately then the resulting conversion efficiency will always be improved over that of a single stage.

CHAPTER III

REVIEW OF THERMOELECTRIC ANALYSIS

3.1 Introduction

This chapter will introduce the fundamental analysis techniques commonly used to understand and design thermoelectric materials, couples, and devices. The methods introduced herein are well documented in a number of sources, referenced throughout. The chapter provides a greater depth into the analysis of thermoelectric materials than was provided briefly in Chapter 2. First, the critical design factor -figure of merit- will be derived as a result of irreversible thermodynamics, then the critical material properties found in figure of merit will be investigated from a perspective of solid-state transport. The chapter serves to gain a deeper understanding of the parameters and properties critical to thermoelectric devices.

3.2 Figure of Merit

The well known thermoelectric figure of merit guides materials development due to the relation between the figure of merit and the conversion efficiency of a couple. To gain a deeper understanding of the connection between figure of merit and conversion efficiency a classic approach of thermodynamics and heat transfer can be applied to

a simple thermoelectric couple. First, the governing thermoelectric equations can be derived from irreversible thermodynamics, then the governing equations can be applied to a thermoelectric couple.

To develop an understanding of thermoelectric phenomenon a thermoelectric conductor will be investigated as a conjugate two force/flux conductor, as studied by Onsager in 1931 [144, 145]. A domain may conduct an internal energy flux, denoted J_U , with an internal energy force proportional to $\nabla(1/T)$ as per an entropic view of the fundamental relation of thermodynamics [28]. Additionally, this domain may conduct electronic charge carriers, flux J_N , with a charge carrier force proportional to $\nabla(\xi/T)$, where the chemical potential of carriers is equal to the charge of each carrier (e) multiplied by the electrostatic potential (ϕ) acting on the carrier, such as $\xi = e\phi$ [28]. In a non-thermoelectric Fourier conductor or electrical conductor these two fluxes and forces would be independent of one another. The transport equations would be simply the standard Fourier's and Ohm's Laws, with a thermal conductivity and electrical conductivity coefficient relating the two force/flux relations. For a thermoelectric material both forces must be considered simultaneously, as well as the cross coupling of the two forces and fluxes. In the case of a one-dimensional thermoelectric domain the general transport must be considered as

$$J_U = L_{00} \frac{d}{dx} \left(\frac{1}{T} \right) + L_{01} \frac{d}{dx} \left(\frac{-e\phi}{T} \right), \quad (3.1)$$

$$J_N = L_{10} \frac{d}{dx} \left(\frac{1}{T} \right) + L_{11} \frac{d}{dx} \left(\frac{-e\phi}{T} \right). \quad (3.2)$$

The one-dimensional treatment is only meant to reduce unnecessary complexities; a full-dimensional study could similarly be carried out. The L_{ij} coefficients are the desired transport coefficients for a thermoelectric conductor. Traditionally we are more concerned with the heat flux, denoted q'' , rather than the total internal energy flux J_U . Expressing the fluxes in terms of the traditional terminology we can state

$$J_U = q'' + e\phi J_N. \quad (3.3)$$

Regrouping terms we obtain the force flux relation in terms of desired quantities as

$$J_N = (L_{10} - e\phi L_{11}) \frac{d}{dx} \left(\frac{1}{T} \right) + \frac{L_{11}}{T} \frac{d}{dx} (-e\phi), \quad (3.4)$$

$$q'' = (L_{00} - e\phi[L_{10} + L_{01}] + [e\phi]^2 L_{11}) \frac{d}{dx} \left(\frac{1}{T} \right) + \left(\frac{L_{01}}{T} - e\phi \frac{L_{11}}{T} \right) \frac{d}{dx} (-e\phi). \quad (3.5)$$

These expressions for the carrier flux and heat flux can be simplified by introducing a set of coefficients ℓ_{ij} to capture the coefficients in equations 3.4 and 3.5

$$J_N = \ell_{00} \frac{d}{dx} \left(\frac{1}{T} \right) + \frac{\ell_{01}}{T} \frac{d}{dx} (-e\phi), \quad (3.6)$$

$$q'' = \ell_{10} \frac{d}{dx} \left(\frac{1}{T} \right) + \frac{\ell_{11}}{T} \frac{d}{dx} (-e\phi). \quad (3.7)$$

Two useful experiments can be considered to help relate these unknown coefficients to experimentally measurable properties. Consider a one-dimensional conductor in an open circuit condition with a finite thermal gradient. In this case equation 3.8 can be applied to relate the thermal conductivity to the ℓ_{ij} coefficients by applying the open circuit condition to equations 3.6 and 3.7

$$q'' = -k \frac{dT}{dx}, \quad (3.8)$$

$$k = \frac{1}{T^2} \left(\ell_{10} - \frac{\ell_{00}\ell_{11}}{\ell_{01}} \right). \quad (3.9)$$

Additionally, the voltage established in this conductor can be measured as a result of the thermal gradient. This material property, the Seebeck coefficient (S), can be related to the ℓ_{ij} coefficients through the open circuit condition, equations 3.6 and 3.7, and the definition of Seebeck coefficient from equation 3.10

$$S = -\frac{d\phi}{dT}, \quad (3.10)$$

$$S = \frac{\ell_{00}}{eT\ell_{01}}. \quad (3.11)$$

Consider a second experiment of an isothermal conductor with a finite potential gradient. In this case Ohm's Law can be applied to relate electrical conductivity to ℓ_{ij} by applying an isothermal condition to equations 3.6 and 3.7

$$eJ_n = -\sigma \frac{d\phi}{dx}, \quad (3.12)$$

$$\sigma = \frac{e^2 \ell_{01}}{T}. \quad (3.13)$$

Additionally, the ratio of heat flux to electrical flux can be measured as a result of the potential gradient. This material property, the Peltier coefficient (π), can be related to the ℓ_{ij} coefficients through the isothermal condition, equations 3.6 and 3.7, and the definition of Peltier coefficient from equation 3.14

$$\pi = \frac{\dot{q}}{eJ_N}, \quad (3.14)$$

$$\pi = \frac{\ell_{11}}{e\ell_{01}}. \quad (3.15)$$

The four unknown ℓ_{ij} coefficients can be expressed in terms of the experimentally measurable material properties, temperature, and carrier charge as

$$\ell_{00} = \frac{S\sigma T^2}{e}, \quad (3.16)$$

$$\ell_{01} = \frac{\sigma T}{e^2}. \quad (3.17)$$

$$\ell_{10} = T^2(k + \sigma\pi S), \quad (3.18)$$

$$\ell_{11} = \frac{\pi\sigma T}{e}, \quad (3.19)$$

Onsager's reciprocity relation states the equivalence of the L_{01} and L_{10} coefficients as a result of the principle of microscopic reversibility [144, 145]. The definition of the modified coefficients ℓ_{ij} implies the equivalence of the ℓ_{00} and ℓ_{11} terms as well, which can be applied to equations 3.16 and 3.19 to prove the first Kelvin relation, an experimentally verifiable relation shown as

$$ST = \pi. \quad (3.20)$$

Introducing the material properties (Eqns. 3.18-3.17) into the ℓ_{ij} coefficients of equations 3.6 and 3.7 and applying the first Kelvin relation (Eqn. 3.20) a useful set of expressions for a thermoelectric conductor can be obtained as

$$eJ_N = -\sigma \frac{d\phi}{dx} - S\sigma \frac{dT}{dx}, \quad (3.21)$$

$$q'' = -S\sigma T \frac{d\phi}{dx} - (k + S^2\sigma T) \frac{dT}{dx}. \quad (3.22)$$

The rearrangement of equation 3.21 and 3.22 results in two useful expressions for a thermoelectric material

$$\frac{d\phi}{dx} = -S \frac{dT}{dx} - \frac{eJ_N}{\sigma}, \quad (3.23)$$

$$q'' = ST_e J_N - k \frac{dT}{dx}. \quad (3.24)$$

Equations. 3.21 and 3.24 now constitute Ohm's Law and Fourier's Law for a thermoelectric conductor, respectively. With these governing transport equations a practical application of thermoelectrics may be considered.

Figure 3.1 shows a typical construction for a thermoelectric couple in a power generation configuration. Thermoelectric legs are prepared from two different materials (subscripts A and B). The couple is a heat engine transferring heat from the hot thermal reservoir T_H to the cold reservoir T_C . Due to the coupled thermal and electrical nature of the materials involved an electrical potential is developed along with the thermal gradient. This induced electrical potential then induces a current I in the load resistance R . It becomes the design challenge to select the geometric parameters, cross-sectional area A and leg length L , and the material properties to optimize the conversion of heat to electrical power. In the steady-state case the critical material properties involved are σ the electrical conductivity, S Seebeck coefficient, and k thermal conductivity.

To evaluate the thermodynamic conversion efficiency of the thermoelectric couple consider Figure 3.2; a one-dimensional thermoelectric material with sides insulated to both thermal and electrical conduction which is broken into a finite control volume with cross-sectional area A and length Δx . Both the heat and electrical energy flux must be considered on entering and exiting from the control volume

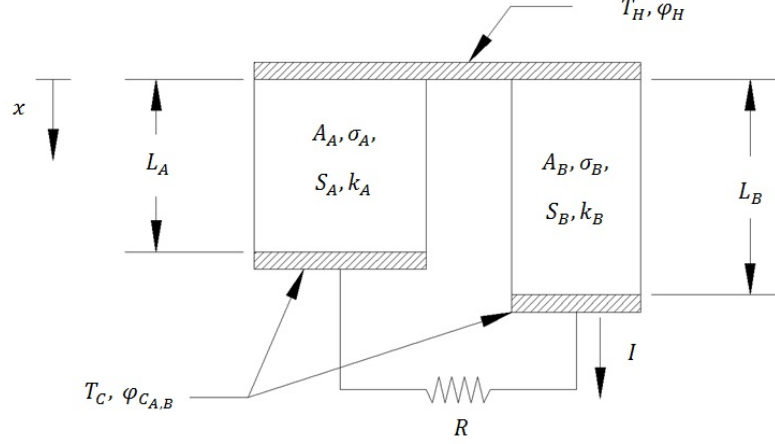


Figure 3.1: A thermoelectric couple configured for electrical power generation. Two legs (A and B) are connected thermally in parallel between thermal reservoirs T_H and T_C and electrically in series with load resistance R . Geometric parameters of legs include A cross-sectional area and L leg length. Material properties include σ electrical conductivity, S Seebeck coefficient, and k thermal conductivity. Electrical dependant parameters include ϕ voltage and I electrical current. The spatial x coordinate originates at the hot shoe of the legs.

$$q_x A - q_{x+\Delta x} A + e J_N \phi_x A - e J_N \phi_{x+\Delta x} A = 0. \quad (3.25)$$

In the limit of the length Δx approaching zero the energy balance results in the governing equation for a thermoelectric conductor

$$-\frac{dq}{dx} - e J_N \frac{d\phi}{dx} = 0. \quad (3.26)$$

Applying equations 3.23 and 3.24 to the terms in equation 3.26 and applying the derivatives results in

$$\frac{d}{dx} \left(-k \frac{dT}{dx} \right) + e J_N T \frac{dS}{dx} - \frac{(e J_N)^2}{\sigma} = 0. \quad (3.27)$$

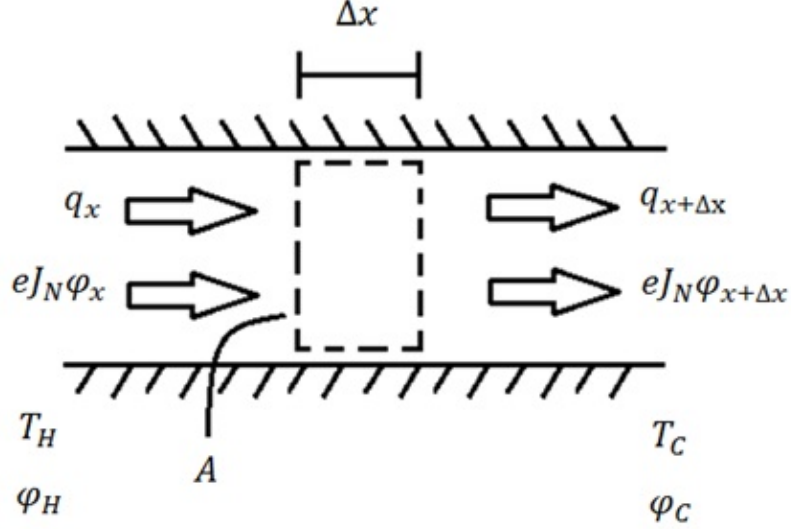


Figure 3.2: Energy transport in a one-dimensional thermoelectric conductor.

To clean up the second term in equation 3.27 consider a chain rule on the Seebeck coefficient and make use of the second Kelvin relation as the definition of the Thomson coefficient (Eqn. 3.28) [29]. The final result (Eqn. 3.29) governs the thermal energy in a one-dimensional thermoelectric conductor

$$\tau = \frac{dS}{dT}T, \quad (3.28)$$

$$\frac{d}{dx} \left(-k \frac{dT}{dx} \right) + eJ_N \tau \frac{dT}{dx} - \frac{(eJ_N)^2}{\sigma} = 0. \quad (3.29)$$

The first term of equation 3.29 accounts for thermal conduction, the second terms account for the Thomson heat and is proportional to the electrical current density, the third term accounts for Joule heating as a result of the current density squared.

A solution of the temperature gradient (Eqn. 3.31) in terms of the current can be obtained from equation 3.29 after application of (i) two thermal boundary conditions, (ii) a simplifying assumption of constant material properties (such that Thomson coefficient is zero per Equation 3.28), and (iii) the relation between electrical current and current density in each leg shown in equation 3.30 (per nomenclature defined in Figure 3.1).

$$I = -eJ_{N_A}A_A = eJ_{N_B}A_B, \quad (3.30)$$

$$\left. \frac{dT}{dx} \right|_{x=0} = \frac{I^2L}{2k\sigma A^2} - \frac{\Delta T}{L}. \quad (3.31)$$

As a result of the fixed temperature boundaries and electrical conditions in Figure 3.1 the electrical current in the circuit can be evaluated (Eqn. 3.32) from solution of equation 3.23 and an application of Ohm's law to the couple. The numerator is the open circuit voltage of the couple and the denominator represents the combined resistivity of the leg materials and the electrical load

$$I = \frac{(S_B - S_A)\Delta T}{R + \frac{L_A}{\sigma_A A_A} + \frac{L_B}{\sigma_B A_B}}. \quad (3.32)$$

The desired conversion efficiency can be expressed in terms of the electrical power out (Eqn. 3.33 numerator) and the thermal heat into the couple (Eqn. 3.33 denominator). The thermal heat in includes both the heat conducted away in each leg and the Peltier heat released in the junction as

$$\eta = \frac{I^2 R}{\dot{Q}_H} = \frac{I^2 R}{-k_A A_A \frac{dT_A}{dx}|_{x=0} - k_B A_B \frac{dT_B}{dx}|_{x=0} + (S_B - S_A) I T_H}. \quad (3.33)$$

Two dimensionless parameters can be introduced to simplify the analysis. The first X (Eqn. 3.34) is a geometric parameter which captures the ratio of the two leg's slenderness ratios; such that two legs with identical slenderness ratios will have an X value of 1, while a couple with one slender leg and one thick leg will have a non-unity X . The second parameter Y (Eqn. 3.35) is a ratio of the electrical load resistance to the couple resistance.

$$X = \frac{A_B L_A}{L_B A_A}, \quad (3.34)$$

$$Y = \frac{R}{\frac{L_A}{\sigma_A A_A} + \frac{L_B}{\sigma_B A_B}}. \quad (3.35)$$

Introduction of equations 3.31, 3.32, 3.34 and 3.35 into the conversion efficiency (Eqn. 3.33) and some manipulation result in the following conversion efficiency equation involving the traditional thermodynamic Carnot efficiency η_C as

$$\eta = \frac{\eta_C Y}{\frac{1}{T_H} \frac{\left(\frac{1}{\sigma_A} + \frac{1}{\sigma_B X}\right)(k_A + k_B X)}{(S_B - S_A)^2} (1 + Y)^2 + (1 + Y) - \frac{1}{2} \eta_C} \quad \text{with } \eta_C = \frac{\Delta T}{T_H}. \quad (3.36)$$

Figure 3.3 plots a typical range of conversion efficiencies for a space of X (Eqn. 3.34) and Y (Eqn. 3.35) coordinates. The figure was created using typical values of NASA's radioisotope thermoelectric generators with Si/Ge couples applied to equation 3.36 [14]. A clear optimum point exists in the contour space of Figure 3.3.

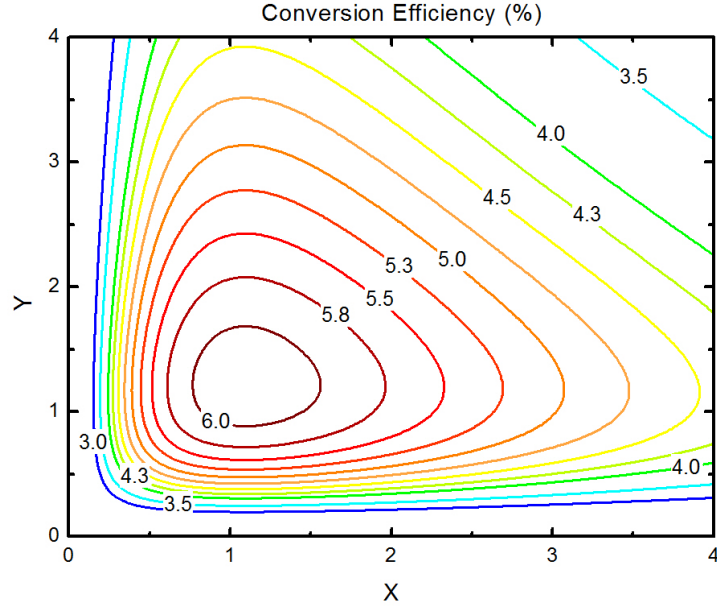


Figure 3.3: Contour map of conversion efficiency over a space of X and Y parameters, a clear design point exists. Values are calculated using properties typical of a Si/Ge couple found on NASA's radioisotope thermoelectric generators [14].

$$X_{opt} = \sqrt{\frac{k_A \sigma_A}{k_B \sigma_B}}, \quad (3.37)$$

$$Y_{opt} = \sqrt{1 + \frac{(S_B - S_A)^2}{\left(\frac{1}{\sigma_A} + \frac{1}{\sigma_B X}\right) (k_A + k_B X)} T_{avg}}. \quad (3.38)$$

A common term involving the material properties has occurred several times (see Eqn. 3.36 and 3.38), this term will be denoted as Z . The units of the Z term are inverse temperature.

$$Z(X) = \frac{(S_B - S_A)^2}{\left(\frac{1}{\sigma_A} + \frac{1}{\sigma_B X}\right) (k_A + k_B X)} \quad \text{with} \quad Z(X_{opt}) = \frac{(S_B - S_A)^2}{\left(\sqrt{\frac{k_A}{\sigma_A}} + \sqrt{\frac{k_B}{\sigma_B}}\right)^2}. \quad (3.39)$$

The Z term occurs in both Equations 3.36 and 3.38 multiplied by a representative temperature (either the hot shoe temperature or the couple average temperature). The conversion efficiency (Eqn. 3.36) is directly proportional to the Z term, such that a material design goal becomes to select materials with a large Z [27]. The Z term as defined involves material properties from both legs. In practice during material design only a single leg is investigated at a time, as a result a figure of merit (ZT) can be established as

$$ZT_{Material} = \frac{S^2\sigma T}{k}. \quad (3.40)$$

The majority of research in the thermoelectric community has focused on designing or searching for materials with a large figure of merit. The following section will investigate some of the details of this figure of merit from another perspective. The work of Chapter 4 will introduce a more advanced analysis which will incorporate a less restrictive couple as outlined classically here. Several of the assumptions of this chapter are too restrictive to apply in real application.

3.3 Thermoelectric Transport

Common thermoelectric materials are heavily doped semiconductors with transport properties similar to metals. The carrier densities of most thermoelectric materials are fairly temperature independent, until high temperatures activate bipolar conductors [146]. A simple model of the transport of thermoelectrics provides a guide for

material design without introducing unnecessary complexity. This section will investigate the material properties Seebeck coefficient, electrical conductivity, and thermal conductivity found in the figure of merit. Since design of thermoelectric materials requires high figure of merit it becomes useful to have an understanding of factors which govern material properties involved in the figure of merit. For instance, it is beneficial to understand the dependence of material properties on the charge carrier density, as will be shown as the main result of this section in Figure 3.4.

Consider the Boltzmann transport equation (Eqn. 3.41) to compliment the above derivation of equations 3.21 and 3.22 and to further investigate the material figure of merit [147].

$$\frac{\partial f}{\partial t} + \vec{V} \cdot \frac{\partial f}{\partial \vec{r}} + \vec{a} \cdot \frac{\partial f}{\partial \vec{V}} = \left(\frac{\partial f}{\partial t} \right)_{Coll.}, \quad (3.41)$$

where f is the distribution function, \vec{V} is the carrier velocity vector, \vec{a} is the carrier acceleration vector, \vec{r} is the position vector, and t is time. Considering the steady electron transport in a one-dimensional ($\vec{r} = (0, 0, z)$) isotropic metallic conductor, the relaxation time approximation may be applied to account for carrier collisions (*Coll.*)

$$\left(\frac{\partial f}{\partial t} \right)_{Coll.} = \frac{f_0 - f}{\tau}, \quad (3.42)$$

where f_0 is an equilibrium distribution function of carriers and τ is a relaxation time. The carrier velocity and acceleration can then be expressed by equations 3.43 and 3.44.

$$\vec{V} = (0, 0, V_z), \quad (3.43)$$

$$\vec{a} = (0, 0, \frac{-eE_z}{m^*}). \quad (3.44)$$

where V_z is the carrier velocity in the z-direction, e is the fundamental charge of the carrier, m^* is the effective carrier mass, and E_z is the electrical field in the z-direction. After applying the local equilibrium assumption and the chain rule equations 3.45 and 3.46 are obtained, note that temperature is not a function of velocity, and energy ($\varepsilon = \frac{1}{2}m^*V_z^2$ with reduced energy $\epsilon = \frac{\varepsilon}{k_bT}$ where k_b is the Boltzmann constant) is not a function of space at local equilibrium.

$$\frac{\partial f}{\partial V_z} = \frac{\partial f}{\partial \varepsilon} \frac{\partial \varepsilon}{\partial V_z} + \frac{\partial f}{\partial T} \frac{\partial T}{\partial V_z} = \frac{\partial f}{\partial \varepsilon} \frac{\partial \varepsilon}{\partial V_z} = \frac{\partial f_0}{\partial \varepsilon} \frac{\partial \varepsilon}{\partial V_z} = \frac{\partial f_0}{\partial \varepsilon} \frac{d}{dV_z} \left(\frac{1}{2}m^*V_z^2 \right) = m^*V_z \frac{\partial f_0}{\partial \varepsilon}, \quad (3.45)$$

$$\frac{\partial f}{\partial z} = \frac{\partial f}{\partial \varepsilon} \frac{\partial \varepsilon}{\partial z} + \frac{\partial f}{\partial T} \frac{\partial T}{\partial z} = \frac{\partial f}{\partial T} \frac{\partial T}{\partial z} = \frac{\partial f_0}{\partial T} \frac{\partial T}{\partial z}. \quad (3.46)$$

With the above assumptions we can find the electron distribution function for a continuum that is subject to a temperature gradient and electrical potential; found by

equating the left hand side of equation 3.41 with the right hand side of equation 3.42 and applying equations 3.45 and 3.46 as

$$f(\varepsilon, T) = f_0 + \tau \left(\frac{eE_z}{m^*} \frac{\partial f_0}{\partial \varepsilon} \frac{d\varepsilon}{dV_z} - V_z \frac{\partial f_0}{\partial T} \frac{dT}{dz} \right) = f_0 + \tau \left(eV_z E_z \frac{\partial f_0}{\partial \varepsilon} - V_z \frac{\partial f_0}{\partial T} \frac{dT}{dz} \right). \quad (3.47)$$

The expression for flux of a property Ψ across a surface with normal \vec{n} can be expressed in terms of the distribution function f as

$$\vec{\Psi} = \int \Psi f \vec{V} \cdot \vec{n} d\varepsilon. \quad (3.48)$$

Now expressions for the current density ($\Psi = -e$) and heat flux ($\Psi = \varepsilon - \xi$) in terms of temperature gradient and electric field can be obtained (where ξ is the electrochemical potential of carriers, with corresponding reduced electrochemical potential $\eta = \frac{\xi}{k_b T}$).

$$eJ_N = -e \int V_z f_0 d\varepsilon - e^2 E_z \int \tau V_z^2 \frac{\partial f_0}{\partial \varepsilon} d\varepsilon + e \frac{dT}{dz} \int \tau V_z^2 \frac{\partial f_0}{\partial T} d\varepsilon, \quad (3.49)$$

$$q'' = J_U - \xi J_N = \int V_z (\varepsilon - \xi) f_0 d\varepsilon + e E_z \int \tau V_z^2 (\varepsilon - \xi) \frac{\partial f_0}{\partial \varepsilon} d\varepsilon - \frac{dT}{dz} \int \tau V_z^2 (\varepsilon - \xi) \frac{\partial f_0}{\partial T} d\varepsilon. \quad (3.50)$$

Further evaluation of the above two expressions using the definition of the Fermi-Dirac (FD) distribution (Eqn. 3.51), introduces the density of states D . This results in equations 3.52 and 3.53 which now represent a transport model of the equations obtained from irreversible thermodynamics (Eqn. 3.21 and 3.22).

$$f_0(\varepsilon, T) = f_{FD}(\varepsilon, T)D(\varepsilon) = \frac{1}{e^{\frac{\varepsilon-\xi}{k_b T}} + 1} D(\varepsilon), \quad (3.51)$$

$$eJ_N = \frac{e^2}{3} \int \tau V^2 \frac{\partial f_{FD}}{\partial \varepsilon} D(\varepsilon) d\varepsilon \frac{d\phi}{dz} - \frac{e}{3T} \int \tau V^2 (\varepsilon - \xi) \frac{\partial f_{FD}}{\partial \varepsilon} D(\varepsilon) d\varepsilon \frac{dT}{dz}, \quad (3.52)$$

$$q'' = -\frac{e}{3} \int \tau V^2 (\varepsilon - \xi) \frac{\partial f_{FD}}{\partial \varepsilon} D(\varepsilon) d\varepsilon \frac{d\phi}{dz} + \frac{1}{3T} \int \tau V^2 (\varepsilon - \xi)^2 \frac{\partial f_{FD}}{\partial \varepsilon} D(\varepsilon) d\varepsilon \frac{dT}{dz}. \quad (3.53)$$

Comparing the coefficients on the electrostatic and thermal gradients of equations 3.52 and 3.21 allows for an expression of the Seebeck coefficient. Using the bulk solid density of states D for free electrons (Eqn. 3.54) a simplification of the Seebeck expression (Eqn. 3.55) is possible.

$$D(\varepsilon) = 4\pi \left(\frac{2m^*}{h^2} \right)^{3/2} \sqrt{\varepsilon}, \quad (3.54)$$

$$S = \frac{\frac{e}{3T} \int \tau V^2 (\varepsilon - \xi) \frac{\partial f_{FD}}{\partial \varepsilon} D(\varepsilon) d\varepsilon}{\frac{e^2}{3} \int \tau V^2 \frac{\partial f_{FD}}{\partial \varepsilon} D(\varepsilon) d\varepsilon} = \frac{k_b}{e} \left(\frac{\int \varepsilon^{3/2} (\varepsilon - \eta) \tau \frac{\partial f_{FD}}{\partial \varepsilon} d\varepsilon}{\int \varepsilon^{3/2} \tau \frac{\partial f_{FD}}{\partial \varepsilon} d\varepsilon} \right). \quad (3.55)$$

The Fermi-Dirac distribution of free electrons in a metal must be applied to further investigate the Seebeck coefficient. In the Fermi-Dirac distribution electrons are indistinguishable and only one electron is permitted per quantum state; the distribution follows (Eqn. 3.56). Additionally, a power law model is applied to the carrier relaxation time (Eqn. 3.57) which involves a fitting parameter λ which depends on

the scattering mechanism [146]. The Fermi integrals defined by equation 3.58 are introduced in equation 3.59 to simplify notation.

$$f_{FD}(\epsilon) = \frac{1}{e^{\epsilon-\eta} + 1}, \quad (3.56)$$

$$\tau = \tau_0 \epsilon^{\lambda-1/2}, \quad (3.57)$$

$$F_j(\eta) = \int_0^\infty f_{FD} \epsilon^j d\epsilon = \int_0^\infty \frac{\epsilon^j}{e^{\epsilon-\eta} + 1} d\epsilon, \quad (3.58)$$

$$S = \frac{k_b}{e} \left(\frac{(2 + \lambda)F_{\lambda+1}(\eta)}{(1 + \lambda)F_\lambda(\eta)} - \eta \right). \quad (3.59)$$

This expression of Seebeck coefficient is valid for a bulk solid with a single parabolic band. Involved in the relation is a temperature and chemical potential dependence within the Fermi integrals. To better understand the Seebeck coefficient, consider the carrier density of a material obtained from integrating the Fermi-Dirac distribution function and the density of states (Eqns. 3.56 and 3.54) as

$$n = \int f_{FD}(\epsilon)D(\epsilon)d\epsilon = 4\pi \left(\frac{2m^*k_bT}{h^2} \right)^{3/2} \int_0^\infty \frac{\sqrt{\epsilon}}{e^{\epsilon-\eta} + 1} d\epsilon = 4\pi \left(\frac{2m^*k_bT}{h^2} \right)^{3/2} F_{\frac{1}{2}}(\eta). \quad (3.60)$$

The Seebeck coefficient can be expressed in terms of this carrier density, a measurable material property, in the limit of a degenerate electron gas (large η) [146] as

$$S = (1 + \lambda) \frac{8\pi^2 k_b^2 T m^*}{3eh^2} \left(\frac{\pi}{3n} \right)^{2/3}. \quad (3.61)$$

From this simplified relation it becomes clear that a general trend of Seebeck coefficient is to increase with increasing temperature and to decrease with increasing carrier density (to be shown later in Fig. 3.4). While equation 3.61 involves several drastic simplifications it provides a simple means to calculate the carrier effective mass by measuring Seebeck coefficient and carrier density at temperature. As a more rigorous approach the carrier effective mass can be calculated from equations 3.59 and 3.60 in the same fashion, but this involves numerical estimation of Fermi integrals.

Comparing the coefficients on the electrostatic potential in equations 3.52 and 3.21 allows for an expression of the electrical conductivity which can be simplified with equations 3.54, 3.56, and 3.57 as

$$\sigma = -\frac{2e^2}{3m^*} \int \frac{\partial f_{FD}}{\partial \varepsilon} \tau \varepsilon D(\varepsilon) d\varepsilon = \frac{8\pi e^2 \tau_0}{3m^*} \left(\frac{2m^* k_b T}{h^2} \right)^{3/2} (1 + \lambda) F_\lambda(\eta). \quad (3.62)$$

For a scattering parameter of $\lambda = 1/2$ the electrical conductivity reduces to the Drude-Lorentz expression derived from kinetic theory of a free-electron model [147].

$$\sigma = \frac{ne^2 \tau_0}{m^*} = ne\mu \quad (3.63)$$

This simplified relation shows that the electrical conductivity is proportional to the carrier density n (later in Fig. 3.4), the carrier charge e , and the carrier mobility $\mu = \frac{e\tau_0}{m^*}$. Using the electrical conductivity, carrier density, calculated effective carrier mass

(found by solving Eqns. 3.61 and 3.60), and equation 3.63 the scattering parameter τ_0 can be calculated. Similar to the effective carrier mass the scattering parameter can also be calculated using numerical integration in equation 3.62. It should be noted that carrier scattering can arise from several interactions including carrier-carrier (c-c), carrier-phonon (c-p), carrier-defect (c-d), and carrier-boundary (c-b) phenomena. The result of all of these interactions adds according to Matthiessen's rule [147] as

$$\frac{1}{\tau} = \frac{1}{\tau_{c-c}} + \frac{1}{\tau_{c-p}} + \frac{1}{\tau_{c-d}} + \frac{1}{\tau_{c-b}}. \quad (3.64)$$

The thermal conductivity (k) of a thermoelectric is composed of two parts, a lattice contribution due to phonons and an electronic contribution due to charge carriers, $k = k_e + k_l$. Comparing the coefficient on thermal gradient in equation 3.53 to Fourier's Law, an expression for the electronic component of thermal conductivity can be obtained as

$$\begin{aligned} k_e &= -\frac{1}{3T} \int \tau V^2 (\epsilon - \xi)^2 \frac{\partial f_{FD}}{\partial \epsilon} D(\epsilon) d\epsilon \\ &= -4\pi \left(\frac{2m^* k_b T}{h^2} \right)^{3/2} \frac{2\tau_0}{3m^* T} \int \epsilon^{\lambda+1} (\epsilon - \eta)^2 \frac{\partial f_{FD}}{\partial \epsilon} d\epsilon. \end{aligned} \quad (3.65)$$

Simplifying the Fermi-Dirac distribution in equation 3.65 results in equation 3.66, which can also be derived directly from kinetic theory of electrons. The electronic component of thermal conductivity is proportional to the carrier density (later in Fig. 3.4) as

$$k_e = \frac{n\pi^2 k_b^2 T}{2m^*} \tau_0. \quad (3.66)$$

The lattice component of thermal conductivity is derived from a Bose-Einstein distribution of phonons. The Bose-Einstein distribution considers phonons indistinguishable and allows repeated phonons per quantum state. The calculation must be considered over different polarizations (P), with phonon phase (v_p) and group velocities (v_g), and with the limits of integration range from a frequency of zero to the maximum frequency of each polarization branch.

$$k_l = \frac{k_b}{6\pi^2} \left(\frac{2\pi k_b T}{h} \right)^3 \sum_P \int_0^{x_m} \tau \frac{v_g}{v_p^2} \frac{x^4 e^x}{(e^x - 1)^2} dx \quad (3.67)$$

Figure 3.4 shows the general dependence of Seebeck coefficient, electrical conductivity, and thermal conductivity as a function of carrier density. Since the main design goal of thermoelectrics is to find materials with a large figure of merit materials must be selected to have a nominal carrier density to optimize the numerator of the figure of merit, known as the power factor ($S^2\sigma$). The range of this optimal carrier density falls typically in the range of heavily doped semiconductor materials. To maximize figure of merit the lattice component of thermal conductivity must be decreased to ensure that heat is predominantly transferred by charge carriers. The challenge in thermoelectrics lies in the difficulty of reducing the thermal conductivity without also reducing the electrical conductivity. It has been proposed

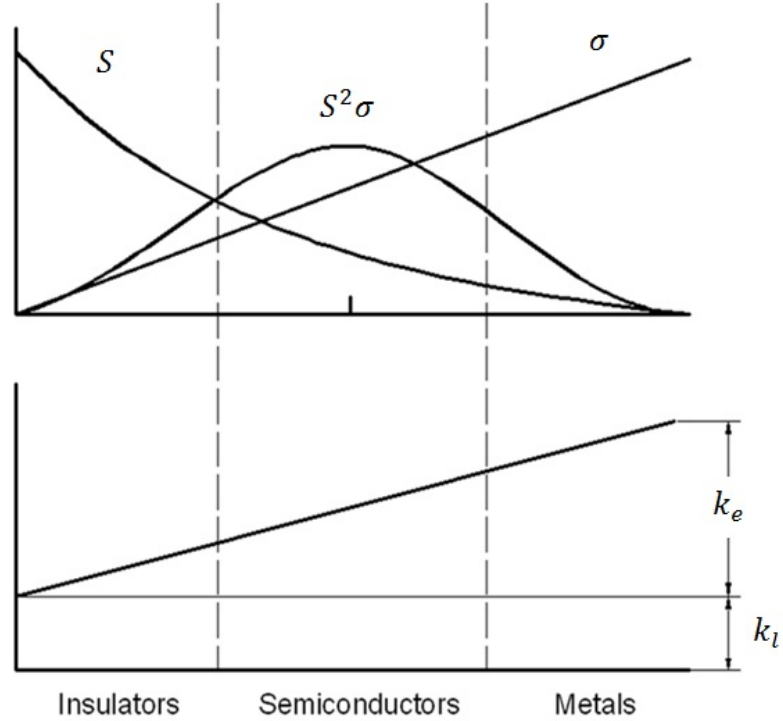


Figure 3.4: Trends in Seebeck coefficient, electrical conductivity, and thermal conductivity as a function of carrier density. Adapted from reference [148]

and demonstrated that materials benefit from improvements in figure of merit by nano-structuring [60, 121–127].

In practice the measured thermal conductivity is the total conductivity, from which the electronic and lattice components must be estimated. In order to estimate the electronic conductivity the Weidman-Franz law must be used, along with an estimation of the Lorentz number. The classic Lorentz number can be estimated from combining equations 3.63 and 3.66 as shown in Equation 3.68. Additionally, a more detailed Lorentz number can be derived involving Fermi integrals for a heavily doped semiconductor (Eqn. 3.69) [146].

$$L = \frac{k_e}{\sigma T} = \frac{1}{3} \left(\frac{\pi k_b}{e} \right)^2, \quad (3.68)$$

$$L = \frac{k_b^2 (1 + \lambda)(3 + \lambda) F_\lambda F_{\lambda+2} - (2 + \lambda)^2 F_{\lambda+1}^2}{e^2 (1 + \lambda)^2 F_\lambda^2}. \quad (3.69)$$

3.4 Summary

This chapter introduced the classic thermoelectric figure of merit as a parameter in couple conversion efficiency. The couple conversion efficiency was demonstrated to be related to both the thermodynamic Carnot efficiency and the thermoelectric figure of merit. The material properties found in figure of merit (Seebeck coefficient, electrical resistivity, and thermal conductivity) were each studied independently from a solid-state transport perspective. The dependence of the material properties on carrier density was discussed in an effort to understand some of the techniques used to optimize figure of merit.

The analysis provided in this chapter is an overly simplified view of thermoelectric transport. Design of devices based on the work of this chapter ignores many complicating factors which can lead to poor device performance. Some of these complicating factors are addressed in Chapter 4.

CHAPTER IV

ADVANCED THERMOELECTRIC ANALYSIS

4.1 Introduction

This chapter introduces an analysis of a thermoelectric couple which accounts for factors that are neglected in the ideal analysis presented in Chapter 3. This advanced analysis allows for (i) variable couple boundary conditions, (ii) lateral heat transfer, (iii) variable material properties, and (iv) transient operation. In addition to developing a new set of design factors, similar to the thermoelectric figure of merit, a set of design guidelines are also developed. The analysis is performed analytically to obtain simple but generally applicable solutions, rather than focusing on detailed numerical studies of very specific cases. An application of the design guidelines introduced in this chapter can be found in Chapter 5 where the two material systems investigated in this work are used as demonstration couples.

4.2 Motivation for Advanced Analysis

The classic analytic analysis of a thermoelectric couple assumes (i) steady-state operation, (ii) a one dimensional rectangular domain, (iii) constant isotropic material properties, (iv) insulated TE leg sides, and (v) fixed hot and cold shoe temperatures.

The model with the simplifying assumptions result in the straight-forward solution outlined in Chapter 3. The success of the model is the definition of the thermoelectric figure of merit (ZT), and the expression of conversion efficiency in terms of ZT . In practice conditions in a thermoelectric device may violate some or all of these simplifications. By analytically investigating less restrictive models additional design factors, similar to figure of merit, can be found. The following sections investigate a set of less restrictive thermoelectric problems including (i) a thermoelectric couple in cylindrical coordinates, (ii) a couple with finite thermal resistance on the hot and cold shoes, (iii) a couple subject to lateral heat transfer, (iv) a couple with variable material properties, and (v) a couple subject to transient operation. To investigate these five cases a dimensionless form of the governing equations is introduced.

TE devices are being increasingly considered for applications like automotive and aerospace where transient timescales become important. Additionally, many applications of TE devices require legs to be coupled to a convective fluid, which can introduce a significant thermal resistance to the system. It is desired to understand the magnitude of effect these and other simplifications on factors like conversion efficiency and power density. More importantly it is critical that design rules can be established to minimize the effect of these factors.

4.3 Problem Statement

The general model is outlined in the sketch of Figure 4.1. The model consists of four coupled ordinary differential equations and a fifth coupled algebraic equation

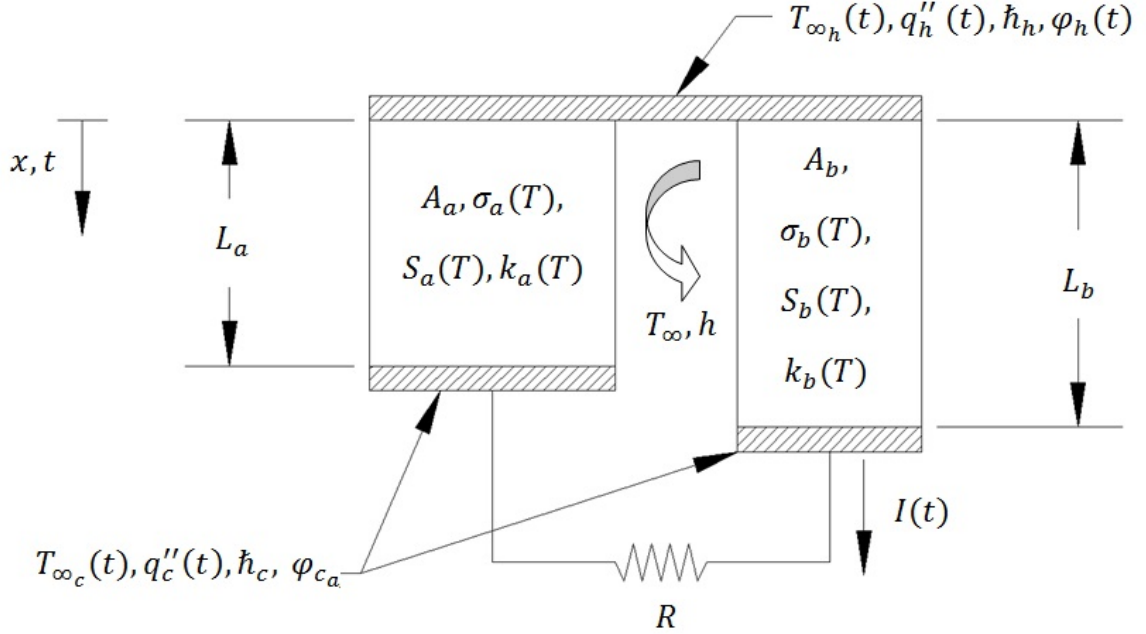


Figure 4.1: A thermoelectric couple configured for electrical power generation. Two legs (a and b) are connected thermally in parallel between thermal reservoirs T_{∞_h} and T_{∞_c} and electrically in series with load resistance R . Heat transfer coefficients in the hot and cold shoes are denoted \hbar_h and \hbar_c and the leg side convection coefficient h corresponds to side ambient temperature T_{∞} . Geometric parameters of legs include A cross-sectional area and L leg length. Material properties include σ electrical conductivity, S Seebeck coefficient, and k thermal conductivity. Electrical dependant parameters include ϕ voltage and I electrical current. The spatial x coordinate originates at the hot shoe of the legs.

(4.1-4.3). Equation 4.1 gives the thermal governing equations for two legs, a and b , while equation 4.2 gives the electrical governing equations for the same legs. The last equation (Eqn. 4.3) represents Ohm's Law.

$$-\frac{d^2\hat{T}_{a,b}}{d\hat{x}^2} + \beta_{a,b}\hat{I}_{a,b}\frac{d\hat{T}_{a,b}}{d\hat{x}} - \gamma_{a,b}\hat{I}_{a,b}^2 = 0, \quad (4.1)$$

$$\frac{d\hat{\phi}_{a,b}}{d\hat{x}} = -\xi_{a,b}\frac{d\hat{T}_{a,b}}{d\hat{x}} - \lambda_{a,b}\hat{I}_{a,b}, \quad (4.2)$$

$$\hat{\phi}_b(\hat{x} = 1) - \hat{\phi}_a(\hat{x} = 1) = \hat{I}_b. \quad (4.3)$$

The complete model for a rectangular couple with insulated leg sides and two legs electrically in series, a and b , is described in terms of dimensionless parameters. The assumed dimensionless variables of the model include a space coordinate $\hat{x} = x/L$ normalized with leg length, temperature $\hat{T} = T/\Delta T$ normalized with the temperature difference driving the Seebeck effect, voltage $\hat{\phi} = \phi/(\Delta S \cdot \Delta T)$ normalized with a characteristic couple open circuit voltage due to couple Seebeck coefficient $\Delta S = S_b - S_a$ and electrical current $\hat{I} = IR/(\Delta S \cdot \Delta T)$ normalized with characteristic load resistance R and open circuit voltage. Substitution of the dimensionless parameters into the governing equation results in a set of characteristic parameters which govern the behavior of all couples and provide validation for assumptions. The effect of Thomson heat is captured in the dimensionless parameter $\beta = \tau\Delta S\Delta TL/(ARk)$, which serves as a measure of the accuracy of neglecting Thomson heat τ , in terms of couple Seebeck ΔS , operating temperature difference ΔT , length L , cross sectional area A , load resistance R , and thermal conductivity k . This heat is classically neglected as part of the assumption of constant material properties by the second Kelvin relation $\tau = T\frac{dS}{dT}$ [144, 145]. Work in accounting for this heat has been performed by Sherman et al. [29], Yamashita [31], Min and Rowe [32], and Huang et al. [40]. For β values

much smaller than unity the assumption of neglecting Thomson heat is valid, but in the case of a couple with β on the order of unity this assumption is no longer justified. Notice the term involves not only material properties but also a geometric slenderness ratio L/A as well as operational parameters ΔT and R . The effect of Joule heating is captured by the dimensionless parameter $\gamma = \Delta S^2 \Delta T L^2 / (A^2 R^2 k \sigma)$, with the introduction of electrical conductivity σ . The dimensionless voltage due to Seebeck effect is captured by $\xi = S / \Delta S$, and the voltage due to electrical losses is found in $\lambda = L / (AR\sigma)$. Included in the model are the six boundary conditions required for complete specification of the problem statement. These governing equations and boundary conditions have been modified to investigate less restrictive couples.

4.4 Cylindrical Coordinates

The introduced method was applied to a cylindrical couple configured with radial heat transfer. *Legs in a cylindrical couple are configured as a solid washer or ring shape with the temperature gradient ranging from the inside to outside radius.* Sets of p- and n-type washers can be electrically connected in series to complete a circuit (Fig. 4.2), similar to their rectangular counterparts. Cylindrical couples may prove to be well suited for the design of compact heat exchangers which require a radial conduction path. For instance, the cylindrical couple would serve well in an energy harvesting application of a coolant line passing through a hot exhaust chamber. The outside radius of the legs would be in communication with the hot ambient thermal reservoir, and the cold junction would be in direct thermal contact with a coolant

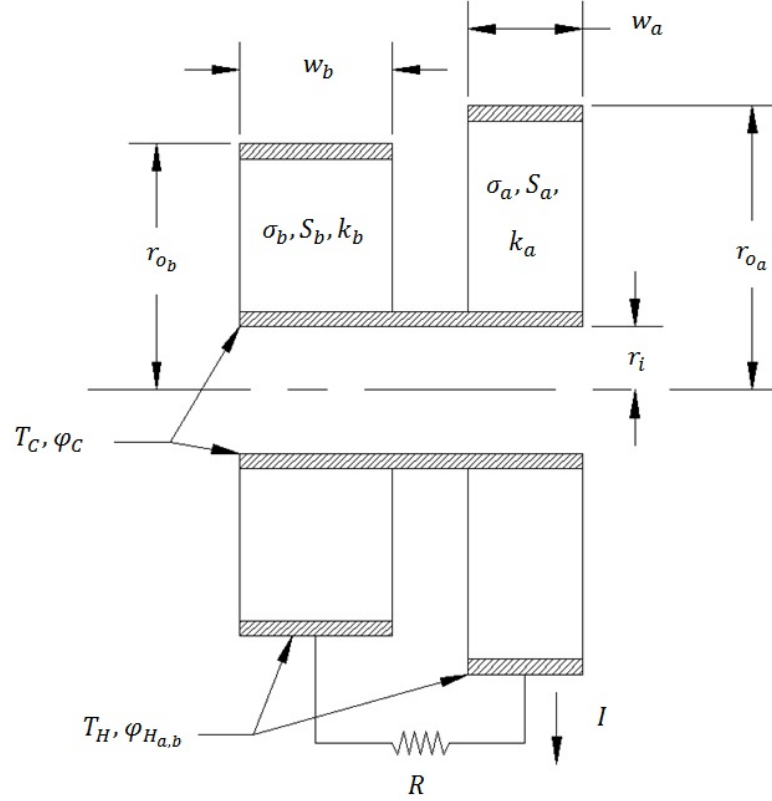


Figure 4.2: Schematic of a cylindrical couple, highlighting the geometric parameters of interest: leg width w , and inner/ outer radius r_i and r_o .

fluid. Cylindrical couples have been theoretically and experimentally investigated by Min and Rowe [33, 34], Landecker [35], Lund [36], and Liu [37]. The temperature and voltage profiles, now functions of radius r and leg width w , can be used to calculate the couple's thermodynamic conversion efficiency.

The cylindrical thermal equation must be expressed in terms of radius r rather than the spacial rectangular coordinate x . The dimensional form of the governing equation is

$$\frac{d}{dr} \left(-k_{a,b} r \frac{dT_{a,b}}{dr} \right) + \frac{I_{a,b} \tau_{a,b}}{2\pi w_{a,b}} \frac{dT_{a,b}}{dr} - \frac{I_{a,b}^2}{4\pi^2 w_{a,b}^2 r \sigma_{a,b}} = 0. \quad (4.4)$$

The solution of the cylindrical thermal gradient under the classic assumptions outlined in the previous section is

$$\frac{dT_{a,b}}{dr} = -\frac{I_{a,b}^2}{4\pi^2 w_{a,b}^2 r \sigma_{a,b} k_{a,b}} \ln r + \frac{I_{a,b}^2}{8\pi^2 w_{a,b}^2 r \sigma_{a,b} k_{a,b}} \left[\frac{(\ln r_i)^2 - (\ln r_o)^2}{\ln r_i - \ln r_o} \right] - \frac{\Delta T}{r (\ln r_i - \ln r_o)}. \quad (4.5)$$

The cylindrical electrical current solution is

$$I = \frac{(S_b - S_a) \Delta T}{\frac{\ln r_i / r_{o_b}}{2\pi w_b \sigma_b} + \frac{\ln r_i / r_{o_a}}{2\pi w_a \sigma_a} + R}. \quad (4.6)$$

Again, two design parameters, with similar physical meaning to their rectangular counterparts, can be extracted. The appropriate geometric factor as derived by this work becomes

$$X = \frac{w_b \ln \frac{r_{o,a}}{r_i}}{w_a \ln \frac{r_{o,b}}{r_i}}, \quad (4.7)$$

with subscript o indicating outside radius and i inside radius. Likewise the new cylindrical load factor derived in this work becomes

$$Y = \frac{R}{\frac{\ln \frac{r_{o,a}}{r_i}}{2\pi \sigma_a w_a} + \frac{\ln \frac{r_{o,b}}{r_i}}{2\pi \sigma_b w_b}}. \quad (4.8)$$

Optimization of the efficiency in terms of the cylindrical X and Y design factors is identical to the rectangular case and results in the same final optimized values, as suggested by Min and Rowe [33]. The similarity of the rectangular and cylindrical solutions is expected and reported in literature, but the new cylindrical X and Y design factors of this work are required to optimize a cylindrical couple. For instance, the new geometric factor and load factor allow one to realize the maximum theoretical conversion efficiency or power density in terms of couple radius and leg width. The classic rectangular design factors do not capture geometries useful to a cylindrical couple.

4.5 Variable Boundary Conditions

In real life application the temperatures of the hot and cold reservoirs are known; the difference of which can be different than the temperature drop across the legs, due to factors such as conductive resistance of the shoes t/k , interface resistances $h_{interface}$, and convection $h_{h,c}$ or radiation resistance between thermal reservoirs and the shoes. Therefore in device design it is important to leave the thermal boundary conditions of the legs free. This can be achieved by introduction of a heat transfer coefficient

$$\bar{h}_{h,c}^{-1} = h_{h,c}^{-1} + h_{interface}^{-1} + \sum_i \frac{t_i}{k_i}. \quad (4.9)$$

This heat transfer coefficient boundary condition can be used to represent an equivalent thermal resistance of a lumped combination of the aforementioned factors. The appropriate thermal boundary conditions to apply to the model are

$$-k_{a,b} \frac{dT_{a,b}(0)}{dx} + \frac{I_{a,b} S_{a,b}}{A_{a,b}} T_{a,b}(0) = \hbar_h [T_{\infty_h} - T_{a,b}(0)], \quad (4.10)$$

$$-k_{a,b} \frac{dT_{a,b}(L_{a,b})}{dx} + \frac{I_{a,b} S_{a,b}}{A_{a,b}} T_{a,b}(L_{a,b}) = \hbar_c [T_{a,b}(L_{a,b}) - T_{\infty_c}], \quad (4.11)$$

where \hbar_h and \hbar_c are the heat transfer coefficients of the hot ($x = 0$) and cold ($x = L$) shoes respectively and $T_{\infty_{h,c}}$ are the ambient reservoir temperatures. The dimensional forms of the boundary conditions are presented for convenience. The first term which accounts for the conductive heat, and the last term which accounts for convective heat are the classic boundary condition used for a non-thermoelectric conductor, see Arpaci [149]. The Peltier heat is introduced by the second term on the left hand side of the boundary condition. Constant material properties and a negligible Thomson heat term are used with the model. As discussed previously the Thomson heat term is negligible for constant material properties through the second Kelvin relation [144]. Solution using the full boundary condition proceeds with a straightforward uncoupling of the differential equations, resulting in a nonlinear expression to solve for the electrical current. The solution with the actual boundary conditions as described is solvable but makes obtaining a closed form efficiency equation difficult; optimization can still be performed numerically and will stand to justify the simplifying assump-

tion of neglecting the Peltier heat term from the boundary. The simplified boundary condition leads to a useful solution of the couple, which allows shoe temperature the freedom to float with the solution as desired. The solution introduces a Device Design Factor, a dimensionless parameter of range zero to one, with the ideal device having a value of unity

$$\text{Device Design Factor: } D_{a,b} = \frac{1}{1 + \frac{k_{a,b}(\hbar_h + \hbar_c)}{L_{a,b}\hbar_h\hbar_c}}. \quad (4.12)$$

In the limit of heat transfer coefficients approaching infinity this Device Design Factor approaches unity and the entire model reduces to the classic solution with the ambient temperatures replacing the shoe operating temperatures. *For a real couple the Design Factor serves as an approximation of the operating temperature in terms of the ambient temperature.* The couple's realized temperature difference can be estimated by an effective temperature, $\Delta T_{Effective} = (D_a + D_b)\Delta T_\infty/2$, an estimation of the actual temperature difference in terms of the Design Factor and ambient temperatures. This effective temperature can be used both to assist in couple design as well as thermoelectric module integration in a system. Thermodynamic conversion efficiency η for the variable boundary condition can be derived in terms of the Design Factor D with the simplifying assumption of $\hbar_h = \hbar_c$ and by assuming that the hot shoe temperature can be approximated with the aforementioned effective couple temperature (ΔT_{Eff}). The $\hbar_h = \hbar_c$ assumption is only required to obtain clean and meaningful solutions for presentation; this assumption is not required to hold for the general application of the model.

$$\eta = \frac{\eta_{c_\infty} Y}{\frac{(1+Y)^2}{T_{\infty_h} Z_D(X, D_a, D_b)} + \frac{(1+Y)(S_b - S_a)}{D_b S_b - D_a S_a} \left[1 - \frac{\eta_{c_\infty}}{2} \left(1 - \frac{D_a + D_b}{2} \right) \right] - \frac{\eta_{c_\infty}}{2}}, \quad (4.13)$$

$$Z_D(X, D_a, D_b) = \frac{(D_b S_b - D_a S_a)^2}{\left(\frac{1}{\sigma_a} + \frac{1}{\sigma_b X} \right) (D_a k_a + D_b k_b)}, \quad (4.14)$$

where Z_D is analogous to the classic dimensionless couple parameter Z used in figure of merit ZT and η_{c_∞} is the thermodynamic Carnot efficiency based on the ambient temperatures. The efficiency can be optimized in terms of the four design parameters X , Y , and $D_{a,b}$ as

$$X_{\eta_{opt}} = \sqrt{\frac{k_a \sigma_a D_a}{k_b \sigma_b D_b}}, \quad (4.15)$$

$$Y_{\eta_{opt}} = \sqrt{1 + Z_D(X_{\eta_{opt}}, D_a, D_b) \left[T_{\infty_h} \frac{S_b - S_a}{D_b S_b - D_a S_a} \left(1 - \frac{D_a + D_b}{2} \right) - \frac{\Delta T_\infty}{2} \right]}, \quad (4.16)$$

$$Z_D(X_{\eta_{opt}}, D_a, D_b) = \frac{(D_b S_b - D_a S_a)^2}{\left(\sqrt{\frac{k_a D_a}{\sigma_a}} + \sqrt{\frac{k_b D_b}{\sigma_b}} \right)^2}. \quad (4.17)$$

The efficiency increases with increasing D . The optimal value for D is unity -in the range zero to unity- which causes the conversion efficiency to reduce to the conversion efficiency of the classic case, equation 4.13. For a D of unity no losses exist through the shoes and the temperature drop between the hot and cold reservoirs are the same as the temperature drop across the legs.

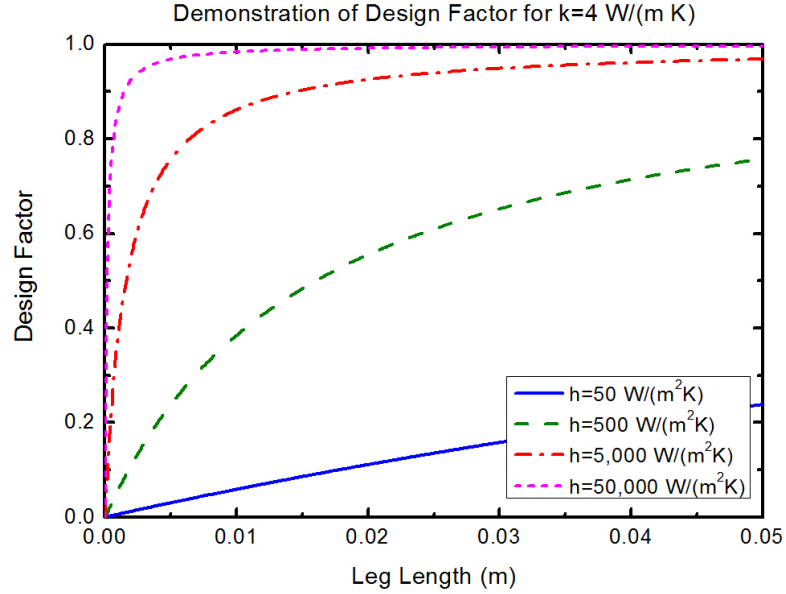


Figure 4.3: Device Design Factor as a function of leg length for a range of heat transfer coefficients.

As a guideline, the efficiency optimized couple should be designed with optimal X and Y values in addition to using long legs, having a high boundary heat transfer coefficient, and as small a leg thermal conductivity as possible. To exemplify this, the dependence of Device Design Factor is illustrated in Figure 4.3 as a function of leg length, for a wide range of heat transfer coefficients. For the clarity of this demonstration only shoe conduction resistance was taken into account, neglecting additional terms such as the interface resistance and shoe convection. A shoe heat transfer coefficient can be approximated as the thermal conductivity of shoe material divided by the shoe thickness using equation 4.9; for instance a 1.9 mm thick SiMo shoe would have roughly $13,000 \text{ W}/(\text{m}^2\text{K})$. The typical shoe used

in the GPHS-RTG is 1.9 mm thick SiMo [1, 106]. *The practical design rule stands to design a short couple, in order to produce the largest power, without reducing the Design Factor significantly.* For example, for legs shorter than 10 mm and a shoe heat transfer coefficient of $50,000 \text{ W}/(\text{m}^2\text{K})$, the Design Factor starts diverging from unity (Fig. 4.3). In the case of 1.9 mm thick SiMo shoe, with the conduction resistance of $13,000 \text{ W}/(\text{m}^2\text{K})$, legs shorter than 10 mm will start exhibiting non-trivial divergence from unity, typical GPHS-RTG legs are sufficiently designed to be 20.3 mm [1]. Furthermore, this divergence will occur at longer leg lengths as the (i) shoe thickness increases, (ii) the conductivity of the shoe material decreases, and (iii) other factors such as convection and interface resistance are included. In an application such as NASA's GPHS-RTG where the heat source is in direct contact with the shoe, the conduction resistance will dominate, however in other possible industrial applications (i.e., exhaust of automobiles) the convection will become the dominant factor with practical convection coefficients in the range of $5\text{-}50 \text{ W}/(\text{m}^2\text{K})$ [150]. In such applications, the importance of this design parameter becomes even more significant due to large divergence from unity. *While the classic solution predicts the same conversion efficiency of a couple of any length this model analytically demonstrates the effect of length with the introduction of Design Factor.* A couple with Design Factor near unity approaches the maximum conversion efficiency as predicted by classic theory, while a reduced factor will have significant reductions on efficiency. As a result of the model a couple's length can be devised in order to bring the Design Factor satisfactorily

Table 4.1: Comparison of simplified boundary condition to numerical solution of actual condition.

B.C.	Design	X_{opt}	Y_{opt}	η_{opt}	X_{opt}	Y_{opt}	η_{opt}
Coefficient	Factor (Eqn. 4.15)	(Eqn. 4.16)	(Eqn. 4.13)	Exact	Exact	Exact	
$[W/(m^2K)]$	[-]	[-]	[-]	[%]	[-]	[-]	[%]
∞	1.00	1.09	1.22	6.15	1.09	1.22	6.15
500,000	0.99	1.09	1.22	6.14	1.09	1.22	6.14
50,000	0.98	1.09	1.22	6.05	1.09	1.22	6.05
5,000	0.85	1.10	1.22	5.30	1.09	1.23	5.26
500	0.37	1.11	1.22	2.37	1.09	1.27	2.28

close to unity, a reasonable value for Design Factor may be selected to have a value such as 0.99 so we can then calculate the length required to reach this level as $L_{99\%}$.

$$L_D = \frac{D(\bar{h}_h + \bar{h}_c)k}{(1 - D)\bar{h}_h\bar{h}_c} \quad \text{for instance } L_{99\%} = \frac{99k(\bar{h}_h + \bar{h}_c)}{\bar{h}_h\bar{h}_c} \quad (4.18)$$

Equations 4.13 to 4.18 provide a complete description of the thermoelectric conversion efficiency of a couple, taking into account total thermal resistance of shoes. The solution is consistent with the classic case of fixed hot and cold temperatures in which heat transfer coefficients can be thought of as being infinite resulting in Design Factors of unity.

To this point the formulation has neglected the Peltier term in the boundary condition, in order to obtain the desired analytic efficiency equation (Eqn. 4.13). A

solution including the Peltier term has been optimized numerically and provides a contrast for the simplified analytic model. A comparison of the approximate boundary condition with the exact boundary condition is presented in Table 4.1. The table displays the X_{opt} and Y_{opt} values required to obtain the optimal conversion efficiency η_{opt} . The X_{opt} , Y_{opt} , and η_{opt} values are calculated for both the analytic and the exact solutions over a range of boundary heat transfer coefficients. For an infinite heat transfer coefficient, Design Factor 1.0, the analytic solution is identically equal to the exact solution. For very large coefficients, greater than $50,000 \text{ W}/(\text{m}^2\text{K})$, the difference between the analytic model and the exact solution are negligible. For coefficients below $5,000 \text{ W}/(\text{m}^2\text{K})$, Design Factor 0.85, the difference between the analytic model and the exact solution becomes apparent. At a coefficient of $5,000 \text{ W}/(\text{m}^2\text{K})$ the difference in the analytically calculated conversion efficiency (5.30%) and the exact solution (5.26%) contains less than a 1% difference. Similarly the differences between the analytic and exact models are less than 1% for the X_{opt} and Y_{opt} values. Lower heat transfer coefficients lead to larger differences between the analytic model and the exact solution. For a coefficient of $500 \text{ W}/(\text{m}^2\text{K})$, Design factor 0.37, the difference between the analytic conversion efficiency (2.37%) and the exact solution (2.28%) is 3.9%. The analytic model, using the simplified boundary condition, was reasonably close to the exact solutions. The simplification is valid in the case $S\Delta S\Delta TL/(ARk) \ll 1$.

4.6 Lateral Heat Transfer

The primary heat transfer in a thermoelectric couple is down the leg length, although some heat will travel in the lateral direction into the region between legs or from the region between legs into the couple. Insulating the volume between the legs, or operating in a vacuum will reduce this effect. However, it is of interest to investigate the magnitude of such lateral heat transfer on the thermoelectric couple's operation in order to determine critical design parameters.

The lateral heat transfer can be considered using a one dimensional thermoelectric conduction equation, derived for a control volume which extends across the width of a leg so as to include heat transfer at the boundary as part of the governing equation. In this fashion the formulation resembles the classic heat transfer in a fin [149, 151, 152]. The modified thermal governing equations now include a Fin Factor, a dimensionless parameter with the ideal device having a value of zero.

$$\text{Fin Factor: } F = L\sqrt{\frac{Ph}{kA}}, \quad (4.19)$$

where the leg perimeter P , and side convection coefficient h have now been introduced. Similar to the convection boundary condition solution, the leg side convection coefficient may be an effective coefficient to account for any mode of heat transfer.

The thermal governing equations now become

$$-\frac{d^2\hat{\theta}_{a,b}}{d\hat{x}^2} + \beta_{a,b}\hat{I}_{a,b}\frac{d\hat{\theta}_{a,b}}{d\hat{x}} + F_{a,b}^2\hat{\theta}_{a,b} - \gamma_{a,b}\hat{I}_{a,b}^2 = 0 \quad (4.20)$$

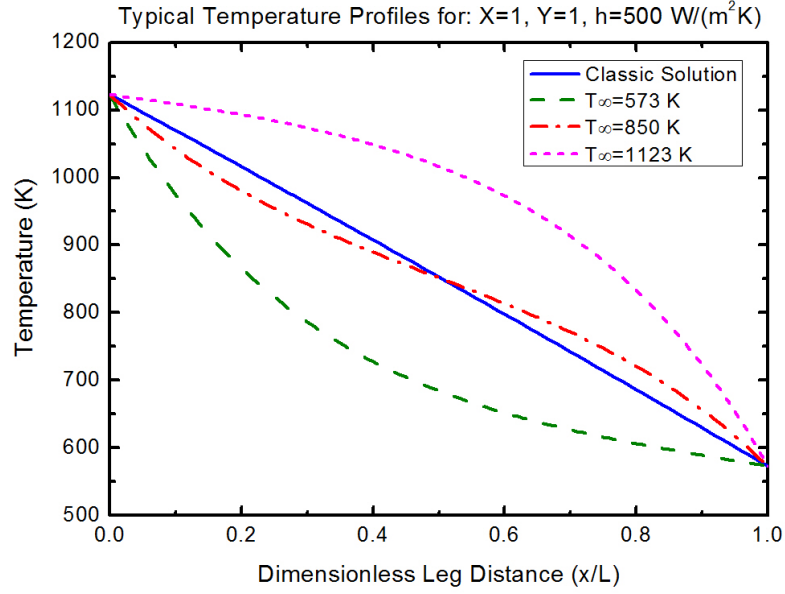


Figure 4.4: Typical temperature profiles for a range of ambient temperatures, with $X=1$ and $Y=1$ for convenience.

A change of variables has been performed as $\theta(x) = T(x) - T_\infty$ with T_∞ the ambient leg side temperature, assumed to be fixed along the leg length for simplicity. In fact the ambient temperature, which the leg communicates with, may be a function of space, but the fixed ambient temperature approximation allows for insightful investigation without unneeded complexity. The dimensionless temperature is now defined as $\hat{\theta}(x) = \theta(x)/\Delta T$. The remainder of the model consists of equations 4.2 and 4.3 in their presented form as the leg sides are still assumed to be electrically insulated. Following the previous case the Thomson heat term will be neglected and constant material properties will be assumed. Solution of the temperature profile is hyperbolic in the space coordinate, in accordance with a fin type formulation. The electrical current reduces to the same result as the classic case, as expected.

The inclusion of an ambient temperature introduces an inflection point, near the ambient temperature, into the thermal solution, shown exaggerated in Figure 4.4 by employing a large convection coefficient $h = 500 \text{ W}/(\text{m}^2\text{K})$. A practical convection coefficient may be in the range of 5-50 $\text{W}/(\text{m}^2\text{K})$ [150]. The electrical current is fixed to that calculated in the classic solution; therefore the power output of the fin couple is limited to the classic solution, thus for a system that is constructed to have Design Factor of unity. *Any couple which produces the same power output but draws a larger heat input or rejects a larger heat output will be a less efficient device.*

The four cases in Figure 4.4 have hot and cold end temperatures of 1123 and 573 K, respectively. The profiles are generated with $X = 1$ and $Y = 1$ for convenience, as these are typical values used in practice. Since the electrical solution is the same in all four cases both the power output and the Peltier heat terms are identical. Therefore the difference in conversion efficiency is determined from the lateral heat transfer and the conductive heat transfer through the ends of the legs. The heat transferred through the ends of the legs is proportional to the temperature gradient at the ends. For the extreme case of an ambient temperature equal to that of the cold shoe, lateral heat can transfer only out of the device and a larger heat input is drawn for the same power output; thus the couple will be less efficient than the classic case. From Figure 4.4 this case can be seen to have a steeper temperature gradient at the hot shoe, compared to the classic solution, confirming the larger heat input. In the other extreme, the case of ambient temperature equal to that of the hot shoe, the couple will again produce the same power output and Peltier heat.

In this case lateral heat is transferred only into the couple, so the output thermal energy is directly proportional to the thermal gradient at the cold shoe. Compared to the classic solution this case will have a larger heat output for the same power generation, so the couple will be less efficient. Thus any intermediate temperature can follow similar reasoning to be less efficient than the classic case. However, for intermediate temperatures the lateral heat will pass into the leg along some portion of the length, and out of the leg along the remainder. Therefore, the evaluation of conversion efficiency becomes more involved. Figure 4.4 shows exaggerated profiles by employing a large convection coefficient.

The efficiency equation is given below for the case of ambient temperature equal to the cold shoe temperature. Two new geometric factors, a thermal fin geometric factor (G), and an electrical fin geometric factor (H) are defined. In the limit of fin factor (F) approaching zero -the ideal couple- both G and H approach the traditional geometric factor X. Although only F_a is found in the efficiency equation, the influence of both leg's fin factors (F_a and F_b) impact the efficiency through the introduction of the geometric factors G and H.

$$\eta = \frac{\eta_c Y}{\frac{F_a(1+Y)^2}{\tanh(F_a)T_h Z_F(X,G)} + (1+Y) - \eta_c \frac{\tanh(\frac{F_a}{2})(\frac{1}{\sigma_a} + \frac{1}{H\sigma_b})}{F_a(\frac{1}{\sigma_a} + \frac{1}{X\sigma_b})}}, \quad (4.21)$$

$$Z_F(X, G) = \frac{(S_b - S_a)^2}{\left(\frac{1}{\sigma_a} + \frac{1}{X\sigma_b}\right)(k_a + Gk_b)}, \quad (4.22)$$

$$G(F) = \sqrt{\frac{P_b A_b h_b k_a \tanh(F_a)}{P_a A_a h_a k_b \tanh(F_b)}}, \quad (4.23)$$

$$H(F) = \sqrt{\frac{P_b A_b h_b k_a \tanh(\frac{F_a}{2})}{P_a A_a h_a k_b \tanh(\frac{F_b}{2})}}, \quad (4.24)$$

where Z_F is analogous to the classic dimensionless couple parameter Z used in figure of merit ZT and η_c is the thermodynamic Carnot efficiency. The conversion efficiency of the fin couple simplifies to the classic solution when F approaches zero as $F/\tanh(F)$ approaches unity and $\tanh(F/2)/F$ approaches $1/2$. The design rule stands to design a couple with a P/A ratio small enough to force the Fin Factor satisfactorily near zero. This small P/A ratio requires the use of large cross-sectional area legs; for instance a square cross-section leg will have the P/A ratio inversely proportional to the side length. Therefore, to obtain a small P/A ratio the use of a large side length is required. Using values typical for the NASA GPHS-RTG (legs of 2.74x6.50x20.3 mm) [1] the fin factor as developed in this work could be as large as 0.84 under a He atmosphere testing condition assuming an h of $5 \text{ W}/(\text{m}^2\text{K})$. The He atmosphere testing condition is common for pre-mission tests before venting to the vacuum of space [1]. For non-space applications of thermoelectrics, where a vacuum is not available, lateral losses will always be present. *While the classic solution predicts the same conversion efficiency of a couple of any P/A ratio this model analytically demonstrates the effect of P/A with the introduction of Fin Factor.* Similar to the couple length selection of the previous section, to keep Device Design Factor near

unity, a P/A ratio can be selected to keep the Fin Factor near zero. A suitably small Fin Factor may be 0.1 so we can then calculate the P/A ratio required to reach this level as $(P/A)_{10\%}$.

$$\left(\frac{P}{A}\right)_F = \frac{F^2 k}{L^2 h} \quad \text{for instance} \quad \left(\frac{P}{A}\right)_{10\%} = \frac{0.1^2 k}{L_{99\%}^2 h} \quad (4.25)$$

4.7 Comparison of Variable Boundary Conditions and Lateral Heat

Table 4.2 summarizes a set of couple parameters and illustrates how it can reduce conversion efficiency, a hazard of a poorly designed couple. The table is calculated from typical values for couples found in the GPHS-RTG, all cases use matching couple material properties and leg sizes. The parameters of study in the table are the end heat transfer coefficient and side convection coefficient, the calculated Device Design Factor and Fin Factor are also shown. The effect of a range of Design and Fin Factors can be clearly observed on maximum conversion efficiency and power density. The ideal couple, case 1 with Design Factor of unity and Fin Factor of zero, gives the greatest maximum conversion efficiency and power density. In the realistic cases of Design Factor deviating from unity, cases 2-5, significant reductions in both maximum conversion efficiency and power density are observed. Fin Factor is kept zero for the study of cases 2-5. Case 2 represents a case with very low leg end thermal resistance, such as direct conduction contact, while case 5 represents a condition with significant leg end thermal resistance typical of a convection coupled fluid. Between cases 2 and 5 the conversion efficiency drops from 6.14 to 2.28% and power density drops

Table 4.2: Comparison of couple parameters demonstrating the importance of considering several factors.

Case #	B.C. Coefficient [$W/(m^2K)$]	Leg Side Convection [$W/(m^2K)$]	Design Factor [-]	Fin Factor [-]	Max Efficiency [%]	Efficiency Optimized X_{opt}	Max Power Density Y_{opt}	Max Power Density [W/m^2]
1	∞	0	1.00	0.00	6.15	1.09	1.22	17,733
2	500,000	0	0.99	0.00	6.14	1.09	1.22	17,670
3	50,000	0	0.98	0.00	6.05	1.09	1.22	17,118
4	5,000	0	0.86	0.00	5.26	1.09	1.23	12,780
5	500	0	0.38	0.00	2.28	1.09	1.27	2,300
6	∞	0.5	1.00	0.09	6.14	1.09	1.22	17,733
7	∞	5	1.00	0.32	6.05	1.10	1.21	17,733
8	∞	50	1.00	1.00	5.33	1.20	1.19	17,733
9	∞	500	1.00	3.16	2.70	1.59	1.09	17,733

from 17,670 to 2,300 W/m^2 . Additionally, the optimal geometric factor X remains unchanged, while the optimal load factor Y shifts with decreasing Design Factor.

The remaining cases 6-9 show reduced maximum conversion efficiency as a function of an increasing Fin Factor. Device Design Factor is kept to a value of one for cases 6-9. As a result the maximum power density remains constant. The cases 6-9 show the behavior of the leg side convection coefficient, with four orders of magnitude, a range which covers the full span of realistic devices. Between case 6 and 9 convection coefficient varies from 0.5 to 500 $W/(m^2K)$ with a resulting change in conversion efficiency from 6.14 to 2.70%. The location of both the optimal X and Y parameters shift as a function of the Fin Factor.

The reductions in conversion efficiency and power density suggest a strong need to consider additional design parameters than simply the material figure of merit. The design factors introduced, along with equations 4.13 and 4.21, provide a simple means of evaluating couple design without requiring lengthy work with numerical simulations. Additionally, the parameters of study introduced in this work serve to help map out efficient testing matrices for experimental work. For instance the Device Design Factor and Fin Factor incorporates the influence of several couple properties and can save the experimentalist the time of studying the influence of each property individually.

4.8 Variable Material Properties

Some of the effects of variable material properties may be accounted for by incorporating the standard integral-averaged approach for the calculation of the thermoelectric properties, see Sandoz-Rosado [42]. As an alternate approach the temperature dependant properties can be accounted for with numerical techniques, such as the finite element method. These techniques serve well for design purposes but often do not provide insight into the role of the temperature dependence. Analytic techniques, while only approximating the problem, provide insight into the role of the temperature dependence.

The method of asymptotic expansions provides a means of accounting for slight temperature variations in material properties. While it is only an approximate solution to the problem it provides useful insight and guidelines for temperature dependence. The method allows for the solution of a set of non-linear differential equations by expanding the solution into a leading order solution followed by higher order corrections. The dependant variables can be expanded into a series of corrections involving a small parameter ϵ as

$$\hat{T} = \hat{T}_0 + \epsilon\hat{T}_1 + \epsilon^2\hat{T}_2, \quad (4.26)$$

$$\hat{\Phi} = \hat{\Phi}_0 + \epsilon\hat{\Phi}_1 + \epsilon^2\hat{\Phi}_2. \quad (4.27)$$

Likewise the temperature dependant thermoelectric transport properties can be expanded using the same set of small parameters. The expansion is performed by non-dimensionalizing the transport properties with their temperature averaged values (average values for property p denoted as \tilde{p})

$$S = \tilde{S} \frac{S(T)}{\tilde{S}} = \tilde{S}(S_0 + \epsilon S_1 \hat{T} + \epsilon^2 S_2 \hat{T}^2), \quad (4.28)$$

$$\sigma = \tilde{\sigma} \frac{\sigma(T)}{\tilde{\sigma}} = \tilde{\sigma}(\sigma_0 + \epsilon \sigma_1 \hat{T} + \epsilon^2 \sigma_2 \hat{T}^2), \quad (4.29)$$

$$k = \tilde{k} \frac{k(T)}{\tilde{k}} = \tilde{k}(k_0 + \epsilon k_1 \hat{T} + \epsilon^2 k_2 \hat{T}^2). \quad (4.30)$$

Solutions of the governing equations (Eqns. 4.1-4.3) follow from inserting the above expansions and separating by order of the small parameter ϵ . The result is a system of linear differential equations to solve the leading order solution, first correction, and additional corrections. By the nature of the method the leading order solution is the classic solution of a thermoelectric couple with constant material properties. The additional corrections introduce the shape of the property versus temperature curves.

Figure 4.5 displays a set of contour plots of maximum conversion efficiency as a function of property slope (dimensionless slope of property p is denoted p_1) for both n- and p-type legs of a couple. Each contour plot is created such that the temperature averaged material properties are uniform over the entire space. Figure 4.5 a), b), and

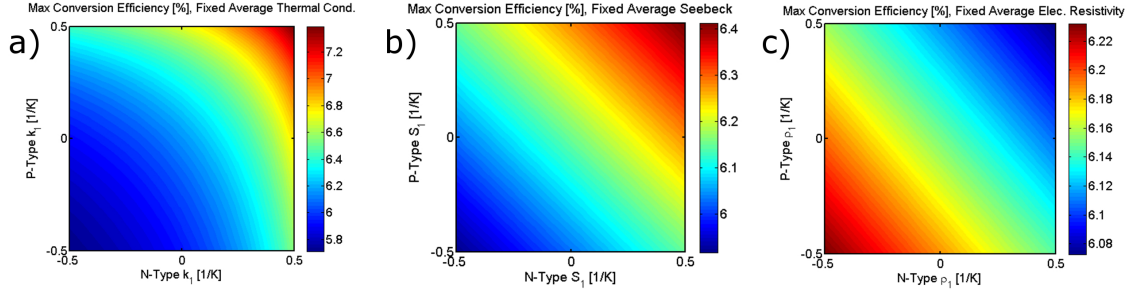


Figure 4.5: Max conversion efficiency for a range of property slopes, for fixed average properties. a) Thermal conductivity, b) Seebeck coefficient, c) Electrical resistivity.

c) show the dependence of the slope of thermal conductivity, Seebeck coefficient, and electrical resistivity, respectively. In each case only one material property is studied and the remaining properties are held fixed with temperature. The center of each contour map represents a couple fabricated from a theoretical n- and p-type material with temperature independent properties, equal to the average values. The resulting conversion efficiency of the (0,0) couple is 6.15% across all three maps. For regions of the map to the right of center the n-type leg has the same average properties but an increasingly steeper slope with a higher absolute value at higher temperature. For regions of the map to the left of the center the n-type leg has the same average properties with a lower absolute value at higher temperature. Vertical regions of the map follow similarly for the p-type leg. Such that the upper-right corner of the map represents a couple composed of n- and p-type materials which increase in property values with temperature.

The contour plots of Figure 4.5 provide an understanding of the sensitivity of conversion efficiency to slope change in the three material properties thermal conductivity, Seebeck coefficient, and electrical resistivity. The conversion efficiency is most sensitive to thermal conductivity as the range of the map conversion efficiency is 5.71 to 7.39%. Seebeck coefficient range is 5.91 to 6.41% and electrical resistivity range is 6.07 to 6.23% over the same span of property slopes. The shapes of the contour maps indicate that the conversion efficiency increases smoothly and monotonically as a function of changes in property slope. For thermal conductivity the conversion efficiency increases for couples composed of materials with positive thermal conductivity slope. The same trend follows for the absolute value of the Seebeck coefficient, and the trend is the opposite for electrical resistivity. These guidelines can assist in material selection. For instance, two couples with the same ZT can have up to a 2% difference in conversion efficiency as a result of the temperature dependence of the properties. In practice the temperature dependence of properties will be more complicated than the simple linear relations investigated here, but this solution provides a good scale of the importance of considering variable material properties.

4.9 Transient Operation

Investigation into transient behavior has been performed by Meng [43], Alata [38], and Montecucco [39] among others, but they have not investigated the problem from the general format provided by Green's functions. Green's functions allow for the general solution of a problem so that arbitrary boundary or initial conditions can be

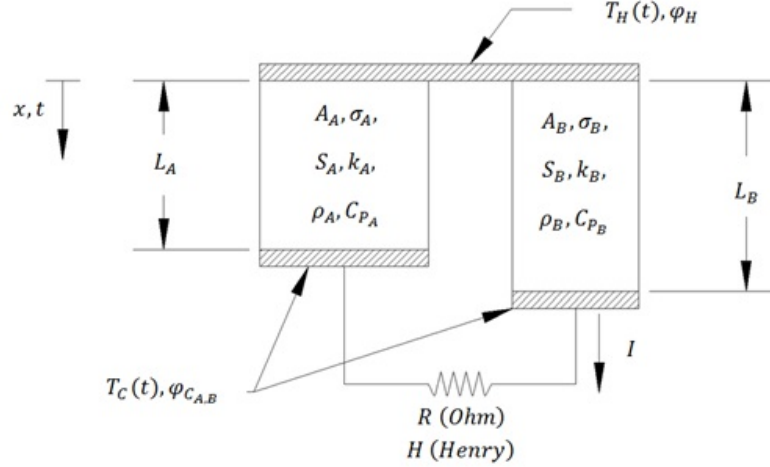


Figure 4.6: Transient thermoelectric couple introducing the density ρ , specific heat c_p , and electrical inductance H .

easily applied later. The general transient couple is presented in Figure 4.6, which introduces the material's density ρ and specific heat c_p . The boundary conditions of a transient couple may be either i) time varying fixed temperatures, ii) time varying fixed temperature gradients (a time varying heat flux), or iii) a mixture of the two (as in a convection coefficient condition). An additional source of transient behavior is the electrical load, which may vary with time and can involve an inductive load H in addition to a purely resistive load R . Finally, the initial temperature and electrical profiles of the couple become significant factors which will result in a component of the transient solution. The governing equations for a transient couple become a set of partial differential equations

$$\frac{\partial}{\partial x} \left(-k_{a,b} \frac{\partial T_{a,b}}{\partial x} \right) + \frac{I_{a,b} \tau_{a,b}}{A_{a,b}} \frac{\partial T_{a,b}}{\partial x} - \frac{I_{a,b}^2}{A_{a,b}^2 \sigma_{a,b}} = \rho_{a,b} c_{p_{a,b}} \frac{\partial T_{a,b}}{\partial t}, \quad (4.31)$$

$$\frac{\partial \phi_{a,b}}{\partial x} = -S_{a,b} \frac{\partial T_{a,b}}{\partial x} - \frac{I_{a,b}}{A_{a,b} \sigma_{a,b}}, \quad (4.32)$$

$$\phi_b(L_b) - \phi_a(L_a) = IR + H \frac{dI}{dt}. \quad (4.33)$$

The system can be simplified by assuming constant material properties, as a result the Thomson coefficient vanishes along with the second term in the thermal equation 4.31. The initial and boundary conditions can be defined

$$T_{a,b}(x, 0) = T_i, \quad (4.34)$$

$$T_{a,b}(L_{a,b}, t) = T_c, \quad (4.35)$$

$$\frac{\partial T_{a,b}(0, t)}{\partial x} = -(A \sin \omega t + B), \quad (4.36)$$

$$\phi_{a,b}(x, 0) = 0, \quad (4.37)$$

$$\phi_a(0, t) = \phi_b(0, t), \quad (4.38)$$

$$\phi_a(L_a, t) = 0, \quad (4.39)$$

$$I(0) = 0, \quad (4.40)$$

where T_i is the uniform initial temperature, T_c is a fixed cold shoe temperature, and $(A \sin(\omega t) + B)$ is a time varying heat flux or other generic function of time. The appropriate dimensionless Green's function can be found by solving the corresponding adjoint operator of the dimensionless thermal equation subject to an impulse response

$$\Gamma_{a,b} \frac{\partial G_{a,b}}{\partial t} = \frac{\partial^2 G_{a,b}}{\partial x^2} + \delta(\xi - x, \tau - t), \quad (4.41)$$

$$\frac{\partial G_{a,b}(0, t)}{\partial x} = 0, \quad (4.42)$$

$$G_{a,b}(1, t) = 0, \quad (4.43)$$

$$G_{a,b}(x, 0) = 0, \quad (4.44)$$

$$\Gamma_{a,b} = \frac{\alpha_{avg} L_{a,b}^2}{\alpha_{a,b} L_{avg}^2}, \quad (4.45)$$

where α is the thermal diffusivity, $G_{a,b}$ is the Green's function, ξ is an alternative spacial coordinate, and τ is an alternative time. The solution of the Green's function is

$$G_{a,b}(\xi, \tau; x, t) = \frac{-2}{\Gamma_{a,b}} H(t - \tau) \sum_{n=0}^{\infty} e^{\frac{\lambda_n^2}{\Gamma_{a,b}}(\tau - t)} \cos(\lambda_n x) \cos(\lambda_n \xi), \quad (4.46)$$

$$\lambda_n = \frac{(2n + 1)\pi}{2}, \quad (4.47)$$

where $H(t-\tau)$ is the Heaviside step function. The dimensionless temperature solution can then be expressed in terms of the Green's function as

$$\begin{aligned} \hat{T}_{a,b}(x, t) = & -\Gamma_{a,b} \int_0^1 G_{a,b}(\xi, 0; x, t) T_i d\xi + \int_0^t G_{\xi_{a,b}}(1, \tau; x, t) T_c d\tau \\ & - \int_0^t G_{a,b}(0, \tau; x, t) (A \sin(\omega\tau) + B) d\tau - \int_0^t \int_0^1 G_{a,b}(\xi, \tau; x, t) \gamma I^2(\tau) d\xi d\tau. \end{aligned} \quad (4.48)$$

The first term in the temperature solution accounts for the initial temperature profile, the second term accounts for the fixed temperature of the cold shoe, the third term accounts for the heat flux at the hot shoe, the final term includes the effect of Joule heating. The dimensionless voltage profile follows directly from the temperature solution and equation 4.32. For the case $\gamma \ll 1$ the fourth term of the temperature solution can be neglected, which leads to a straightforward solution for the electrical current. The electrical current is solved by a Green's function solution of equation 4.33 involving the voltage profile solution. The electrical current solution simplifies to a Volterra integral equation of the second kind, for which a closed form solution exists. Once the electrical current solution is obtained it can be used in the temperature and voltage profiles to complete the problem.

Several cases have been investigated, two will be discussed. i) An On/Off cyclic operation of a couple and ii) a couple subject to a sinusoidal heat flux. The first case applies to a couple which will be subject to start-up and cool-down transients, this is a common case for terrestrial applications of thermoelectrics where things are often started and stopped. The solution follows from the above derivation with the

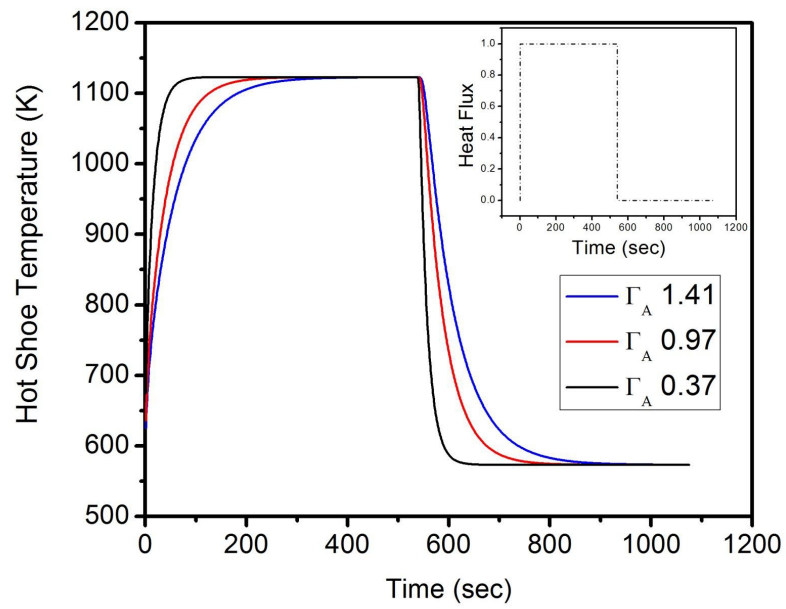


Figure 4.7: A study on hot shoe temperature of three different geometrically and electrically similar couples under On/Off heat flux cycles; parameter of study is the Thermal Diffusivity Factor Γ . Inset is the applied hot shoe heat flux.

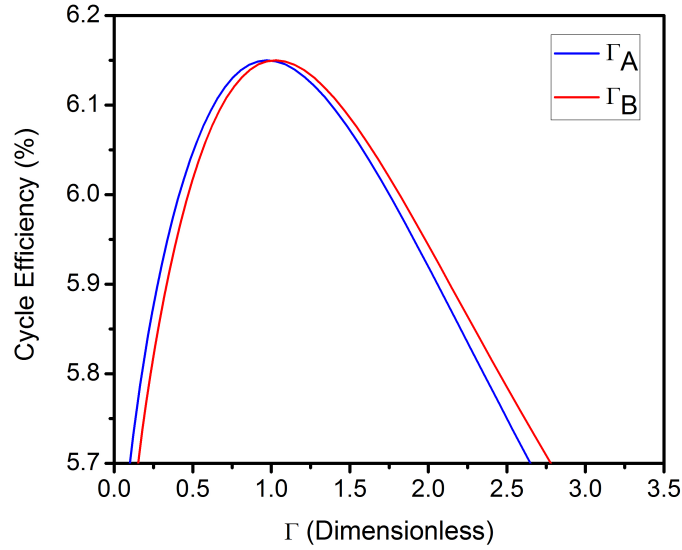


Figure 4.8: Cycle efficiency of a transient couple as a function of the thermal diffusivity parameter Γ .

general heat flux ($A \sin(\omega t) + B$), where A is zero and B varies between zero and one. A solution of the hot shoe temperature, Figure 4.7, shows the time profile for three different Γ values. The full cycle efficiency has been calculated for a range of Γ values, Figure 4.8. A maximum cycle efficiency exists for a Γ value of unity, this fact leads to a design guideline on length ratio as

$$\frac{L_a}{L_b} = \frac{\sqrt{2a} + 1}{2a - 1}, \quad (4.49)$$

$$a = 1 + \frac{\alpha_b}{\alpha_a}. \quad (4.50)$$

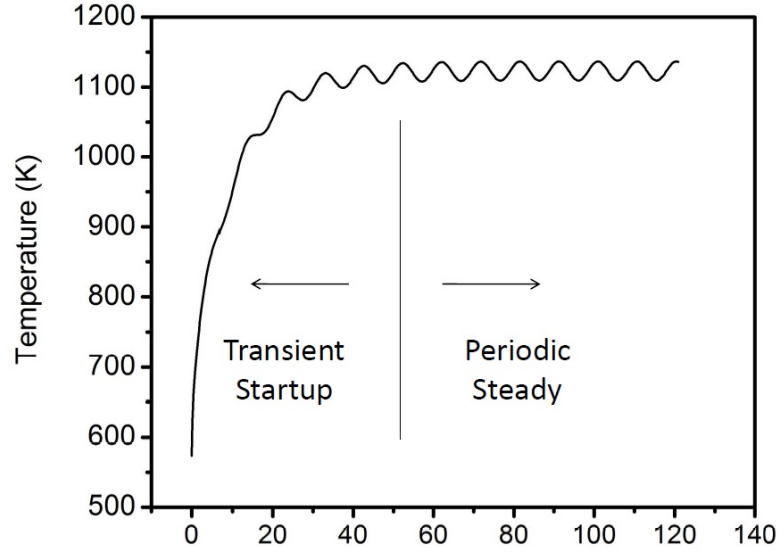


Figure 4.9: Hot shoe temperature due to a sinusoidal heat flux, displaying a transient startup and a periodic steady state.

This length ratio constraint compliments the couple design by adding another constraint to the geometric factor $X_{\eta_{opt}}$.

The second transient case, a sinusoidal heat flux ($A \sin(\omega t) + B$), can approximate any number of more complicated profiles. For instance the standard driving cycle, in the case of thermoelectrics in an automotive exhaust system, can be approximated as a fourier series expansion of sinusoidal solutions. Furthermore, a thermoelectric mounted in a pulse detonation engine will be subject to a sinusoidal heat flux. A solution of the hot shoe temperature, Figure 4.9, shows a transient start-up period followed by a periodic steady state where the hot shoe temperature varies sinusoidally about some nonzero average value. The solution introduces a di-

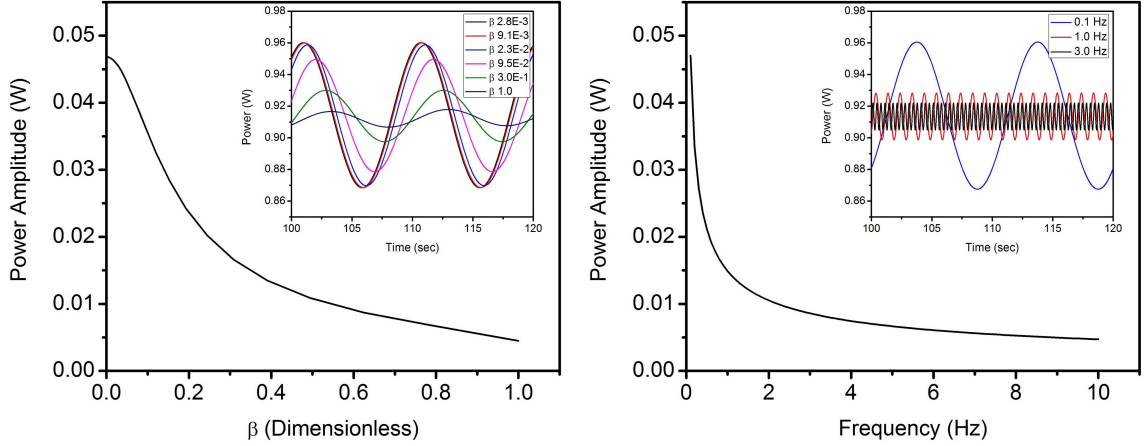


Figure 4.10: Left) Power amplitude versus Inductance Factor β with power versus time curves inset. Right) Power amplitude versus frequency with power versus time curves inset.

dimensionless parameter β which captures the influence of the electrical and thermal inductance as

$$\beta = \frac{H\alpha_{avg}}{RL_{avg}^2}. \quad (4.51)$$

The influence of this Inductance Factor β is shown in Figure 4.10 along with a study on the frequency of the heat flux ω . The average power level in the periodic steady state region is not a function of either Inductance Factor β or heat flux frequency ω . The amplitude of the periodic power decreases with increasing β as electrical inductance begins to dominate thermal inductance, see Figure 4.10 left. The left inset of Figure 4.10 shows six power vs. time curves, in addition to a decrease in power amplitude the Inductance Factor alters the phase angle between the applied heat flux and the electrical power. The amplitude of the periodic power also decreases

with increasing frequency, see Figure 4.10 right, as faster frequencies provide less time for the heat flux to penetrate the domain.

4.10 Conclusion

By assuming less restrictive conditions on the classic thermoelectric couple a set of new design parameters have been derived. These include the (i) Device Design Factor, (ii) Fin Factor, (iii) Thermal Diffusivity Factor, and the (iv) Inductance Factor. The Device Design Factor allows for an estimation of the effect of thermal resistance between the heat/cold source/sink and the thermoelectric material. The factor provides a simple estimation of the conversion efficiency of a device as a result of poorly designed couples. In addition the solution introduces a design guideline on couple leg length to minimize the effect of thermal resistance of the shoes. The Fin Factor allows for estimation of the effect of lateral heat transfer on the conversion efficiency. Additionally, the factor provides a design guideline on the cross-sectional area to perimeter ratio to minimize the effects of heat transfer. The Thermal Diffusivity Factor investigates the transient operation of a couple and provides a guideline on the length ratio of legs in a couple. The two material systems developed in this work (Si/Ge-WSi₂ Chapter 8 and Co_xNi_{4-x}Sb_{12-y}Sn_y Chapter 9) have been applied to the couple design theory introduced within this chapter (see sections 5.2 and 5.3).

CHAPTER V

COUPLE DESIGN EMPLOYING ADVANCED ANALYSIS

5.1 Introduction

This chapter outlines the application of the advanced analysis techniques introduced in the previous chapter. The new parameters Device Design Factor, Fin Factor, and Thermal Diffusivity Factor are demonstrated. The material properties used in this chapter are from the high temperature $\text{WSi}_2\text{-Si}_{1-x}\text{Ge}_x$ system designed in Chapter 8 and the medium temperature Skutterudite system designed in Chapter 9. The design of the optimal couple for each system is outlined using the guidelines developed in Chapter 4.

5.2 $\text{WSi}_2\text{-Si}_{1-x}\text{Ge}_x$ Couple Design

The design work of Chapter 4 was applied to the $\text{WSi}_2\text{-Si}_{1-x}\text{Ge}_x$ system by designing and building proof-of-concept couples, details of the couple fabrication and testing can be found in Appendix A. The best figure of merit materials obtained in this work are summarized in Table 5.1. The properties are temperature averaged between 300 and 950 °C, the temperatures were selected to match RTG operating temper-

Table 5.1: Temperature averaged material properties (300 – 950 °C)

Material Property	N-Type Leg	P-Type Leg
Thermal Diffusivity (m ² /s)	1.56 * 10 ⁻⁶	1.58 * 10 ⁻⁶
Thermal Conductivity (W/m-K)	3.03	2.99
Seebeck Coefficient (μV/K)	-215	+193
Electrical Conductivity (S/m)	5.62 * 10 ⁴	6.90 * 10 ⁴

atures [1]. In addition to the traditional thermoelectric transport coefficients the theory as introduced in Chapter 4 requires the material’s thermal diffusivity.

Table 5.2 outlines the design steps of a couple. The design incorporates end effects with variable temperature boundary conditions, lateral heat transfer with a leg side convection coefficient, and optimal transient operation with balanced thermal diffusivity. To match the fabricated couples of this work the boundary heat transfer coefficient was calculated from the thickness and thermal conductivity of an alumina nitride shoe material (thermal conductivity 285 W/m²-K) of thickness 1.55 mm. The heat transfer coefficient can be calculated

$$\bar{h} = \frac{285 \frac{W}{mK}}{1.55mm} = 183871 \frac{W}{m^2K} \approx 180,000 \frac{W}{m^2K}, \quad (5.1)$$

and used in equations 4.13 to 4.18. The side leg convection coefficient was assumed to be 5 W/m-K, to account for natural convection within the device. The assumed side convection coefficient should be a conservative estimate as the confined nature

of a thermoelectric couple will impede natural convection. Constraints 1 and 2 in Table 5.2 specify the minimum required length of the n- and p-type legs to reduce effects of the thermal boundary resistance, per the Device Design Factor. Constraint 3 applies a transient balance to the couple based on thermal diffusivity, this leg length ratio constraint ensured the most efficient start-up and cool-down operation, per the Thermal Diffusivity Factor. Constraints 4 and 5 incorporate constraints 1-3 to design the highest power couple (ie. shortest couple) which will not be hindered by thermal boundary resistance or transient operation. Constraints 6 and 7 check to ensure that the Device Design Factors of the selected leg lengths are satisfactorily near unity. Constraint 8 optimizes the geometric X factor for maximum conversion efficiency, and then limits the cross-sectional area ratio in constraint 9. Constraints 10 and 11 place an upper limit on the perimeter to cross-sectional area of legs to reduce the effects of lateral heat transfer, per the Fin Factor. The leg side length s (assuming a square shaped cross-section) was selected to satisfy constraints 9, 10, and 11. Constraint 14 calculates the Device Design Factor Z_D to be used in optimizing the load resistance design factor in constraint 15. The balanced load resistance including end effects is then calculated for a single couple in constraint 16. The design steps can be summarized simply as: satisfying the guiding factors Device Design (Constraints 1 and 2), Thermal Diffusivity (Constraint 3), and Fin (Constraints 10 and 11), then optimizing geometrically (Constraint 8), and electrically (Constraint 15).

The final couple design is stated as the n- and p-type leg lengths (Constraints 4 and 5) along with the square cross-section leg side lengths (Constraints 12 and 13)

Table 5.2: W/Si/Ge couple design

Constraint #	Parameter	Value	Equation
1	N-leg $L_{99\%}$ (mm)	3.33	4.18
2	P-leg $L_{99\%}$ (mm)	3.29	4.18
3	L_n/L_p	0.99	4.49
4	L_n (mm)	3.33	Set by 1
5	L_p (mm)	3.35	Set by 3 & 4, Check 2
6	D_n	0.99	4.12
7	D_p	0.99	4.12
8	$X_{\eta_{opt}}$	0.91	4.15
9	A_n/A_p	1.09	Set by 8,4,5
10	N-Leg $P/A_{10\%}$ (mm^{-1})	0.54	4.25
11	P-Leg $P/A_{10\%}$ (mm^{-1})	0.55	4.25
12	s_n (mm)	7.33	Set by 10
13	s_p (mm)	7.01	Set by 9 & 12, Check 11
14	Z_D	8.49E-4	4.17
15	$Y_{\eta_{opt}}$	0.86	4.16
16	R (Ohm)	1.79E-3	Set by 4,5,12,13,15

Table 5.3: W/Si/Ge couple design summary

Parameter	Value
N-Leg Length (mm)	3.33
P-Leg Length (mm)	3.35
N-Leg Side Length (mm)	7.33
P-Leg Side Length (mm)	7.01
Load Resistance (Ohm)	$1.79 * 10^{-3}$
Maximum Conversion Efficiency	8.4%
Power Density at Maximum Conversion Efficiency	$57 \frac{kW}{m^2}$

and the balanced electrical load (Constraint 16). A summary of the critical design parameters is highlighted in Table 5.3. In addition to the geometric parameters of the n- and p-type legs the balanced electrical load was also reported for a single couple. The predicted maximum conversion efficiency including effects from boundary thermal resistance, lateral heat transfer, and transient operation was 8.4%. The power density corresponding to this maximum conversion efficiency design point was $57 \frac{kW}{m^2}$. This conversion efficiency represents roughly a 2% improvement in figure of merit as a result of the new composite system introduced in this work, compared to traditional RTG values.

Table 5.4: Temperature averaged material properties (20 – 250 °C)

Material Property	N-Type Leg	P-Type Leg
Thermal Diffusivity (m ² /s)	3.28 * 10 ⁻⁶	1.41 * 10 ⁻⁶
Thermal Conductivity (W/m-K)	5.65	2.53
Seebeck Coefficient (μV/K)	-37.0	+17.0
Electrical Conductivity (S/m)	3.84 * 10 ⁵	2.07 * 10 ⁵

5.3 Skutterudite Couple Design

Due to the low figure of merit of the system a couple was not fabricated, but the critical design parameters were still calculated. The drastically different values of the transport properties make the skutterudite system a nice contrast to the previous W/Si/Ge based system. The designed couple was selected from n-type Ni₄Sb₇Sn₅ and p-type Co₂Ni₂Sb₇Sn₅, the temperature averaged values (20-250 °C selected due to material stability) are in Table 5.4.

Table 5.5 outlines the design steps of a skutterudite couple, which follows the steps outlined for the W/Si/Ge system. The design incorporates end effects with variable temperature boundary conditions, lateral heat transfer with a leg side convection coefficient, and optimal transient operation with balanced thermal diffusivity. A shoe of alumina nitride was assumed (thermal conductivity 285 W/m-K) with thickness 1.55 mm. The effective heat transfer coefficient can be calculated

Table 5.5: $\text{Co}_x\text{Ni}_{4-x}\text{Sb}_{12-y}\text{Sn}_y$ couple design

Constraint #	Parameter	Value	Equation
1	N-leg $L_{99\%}$ (mm)	6.21	4.18
2	P-leg $L_{99\%}$ (mm)	2.78	4.18
3	L_n/L_p	0.18	4.49
4	L_n (mm)	6.21	Set by 1
5	L_p (mm)	34.7	Set by 3 & 4, Check 2
6	D_n	0.99	4.12
7	D_p	0.99	4.12
8	$X_{\eta_{opt}}$	2.03	4.15
9	A_n/A_p	0.09	Set by 8,4,5
10	N-Leg $P/A_{10\%}$ (mm^{-1})	0.29	4.25
11	P-Leg $P/A_{10\%}$ (mm^{-1})	0.65	4.25
12	s_n (mm)	13.6	Set by 10
13	s_p (mm)	45.8	Set by 9 & 12, Check 11
14	Z_D	5.37E-5	4.17
15	$Y_{\eta_{opt}}$	0.99	4.16
16	R (Ohm)	1.67E-3	Set by 4,5,12,13,15

$$\bar{h} = \frac{285 \frac{W}{mK}}{1.55mm} = 183871 \frac{W}{m^2K} \approx 180,000 \frac{W}{m^2K}, \quad (5.2)$$

and used in equations 4.13 to 4.18. The side leg convection coefficient was assumed to be $5 \text{ W/m}^2\text{-K}$, to account for natural convection within the device. The assumed side convection coefficient should be a conservative estimate as the confined nature of a thermoelectric couple will impede natural convection. Constraints 1 and 2 in Table 5.5 specify the minimum required length of the n- and p-type legs to reduce effects of the thermal boundary resistance. Constraint 3 applies a transient balance to the couple based on thermal diffusivity, this leg length ratio constraint ensured the most efficient start-up and cool-down operation. Constraints 4 and 5 incorporate constraints 1-3 to design the highest power couple (ie shortest couple) which will not be hindered by thermal boundary resistance or transient operation. Constraints 6 and 7 check to ensure that the Device Design Factors of the selected leg lengths are satisfactorily near unity, these values are also used in the work to follow. Constraint 8 optimizes the geometric X factor for maximum conversion efficiency, and then limits the cross-sectional area ratio in constraint 9. Constraints 10 and 11 place an upper limit on the perimeter to cross-sectional area of legs to reduce the effects of lateral heat transfer. The leg side length s (assuming a square shaped cross-section) was selected to satisfy constraints 9, 10, and 11. Constraint 14 calculates the Device Design Factor Z_D to be used in optimizing the load resistance design factor in constraint 15. The balanced load resistance including end effects is then calculated for a single couple in constraint 16. The final couple design is stated as the n- and p-type leg lengths

Table 5.6: $\text{Co}_x\text{Ni}_{4-x}\text{Sb}_{12-y}\text{Sn}_y$ couple design summary

Parameter	Value
N-Leg Length (mm)	6.21
P-Leg Length (mm)	34.7
N-Leg Side Length (mm)	13.6
P-Leg Side Length (mm)	45.8
Load Resistance (Ohm)	$1.67 * 10^{-3}$
Maximum Conversion Efficiency	0.7%
Power Density at Maximum Conversion Efficiency	$2 \frac{kW}{m^2}$

(Constraints 4 and 5) along with the square cross-section leg side lengths (Constraints 12 and 13) and the balanced electrical load (Constraint 16). The design steps can be summarized simply as: satisfying the guiding factors Device Design (Constraints 1 and 2), Thermal Diffusivity (Constraint 3), and Fin (Constraints 10 and 11), then optimizing geometrically (Constraint 8), and electrically (Constraint 15).

The final couple design is stated as the n- and p-type leg lengths (Constraints 4 and 5) along with the square cross-section leg side lengths (Constraints 12 and 13) and the balanced electrical load (Constraint 16). A summary of the critical design parameters is highlighted in Table 5.6. In addition to the geometric parameters of the n- and p-type legs the balanced electrical load was also reported for a single couple. The predicted maximum conversion efficiency including effects from boundary

thermal resistance, lateral heat transfer, and transient operation was 0.7%. The power density corresponding to this maximum conversion efficiency design point was $2 \frac{kW}{m^2}$. The low conversion efficiency and power density are a direct result of the low figure of merit of the system, highlighting the importance of suitable material design.

5.4 Conclusion

This chapter employed the theory introduced in Chapter 4 to design two couples from the material systems designed later in Chapters 8 and 9. Beyond the traditional couple design the couples designed here account for (i) end effects by incorporating the Device Design Factor, (ii) lateral heat transfer by incorporating the Fin Factor, and (iii) optimal transient performance by incorporating the Thermal Diffusivity Factor. Using only the traditional thermoelectric figure of merit would not have constrained the couple design enough to ensure ideal operation. As demonstrated in Chapter 4 the penalty of a poorly designed couple can cause even a high figure of merit material to have significantly reduced performance.

CHAPTER VI

EXPERIMENTAL PROCEDURE

6.1 Introduction

The experimental details summarized in this chapter apply to the work in the silicon germanium and skutterudite material systems to follow in Chapters 8 and 9. System specific details are discussed in their respective chapters, a general overview of the methods is presented in this chapter. Companies are cited only to provide a detailed account of the work, and are not intended to endorse any commercial entity. The chapter is broken into three main sections i) Materials Synthesis, ii) Chemical and Structure Analysis, and iii) Transport Property Characterization. Each section is divided into subsections that introduce the individual experimental details.

6.2 Materials Synthesis

The materials synthesis techniques used in this work included solidification work and powder processing. Solidification work was done in a vertical Bridgman type furnace. Powder processing work included planetary milling of powders followed by densification by either spark plasma sintering, hot pressing, or microwave sintering.

6.2.1 Solidification

Directional solidification was accomplished using the vertical Bridgman method. Alloys were melted in a helium atmosphere in a graphite resistance heated furnace (Thermal Technology LLC, Santa Rosa, CA). Temperature was controlled by an optical pyrometer. Boron nitride (BN) (Momentive Performance Materials, Albany, NY) and fused silica (SiO_2) (Momentive Performance Materials, Albany, NY) crucibles were used. For silicon germanium samples calcium chloride (CaCl_2) was added to the SiO_2 crucible as an interfacial material between the crucible and the melt to eliminate mechanical failure of the crucible during cooling [153]. Skutterudite samples were prepared directly in fused silica crucibles without CaCl_2 . Skutterudite containing crucibles were placed in threaded graphite containers (Graphite Sales Inc, Chagrin Falls, Ohio) sealed with a grafoil gasket. Encapsulating the fused silica crucibles helped to reduce antimony loss.

Solidification Theory

Bridgman furnace provides the means to control the pull rate of the sample from a hot zone to a cold zone to better control the solidification of a melt. Depending on the temperature profile and the pull velocity the solid-liquid interface thermal gradient G_i and velocity V can be controlled. The furnace used in this work has had the temperature profile mapped for a range of set point temperatures. A typical temperature profile is shown in Figure 6.1 with the x-axis as the pull distance of the ingot and the red line marking a temperature at which the ingot will solidify, the

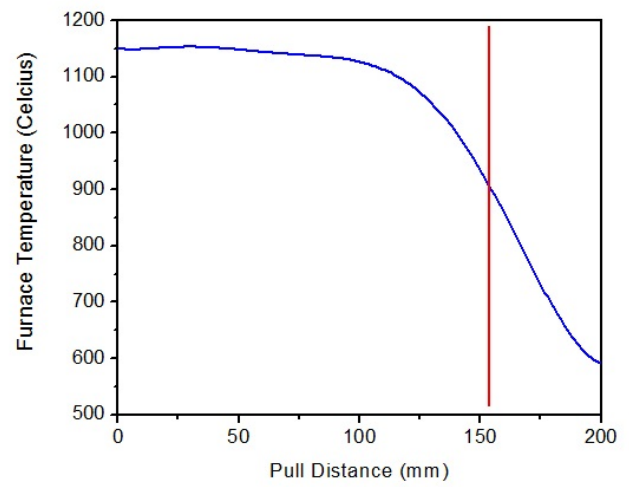


Figure 6.1: Temperature profile along the pull direction of the vertical Bridgman furnace used for this study. Red line indicates a solidifying temperature of 900°C at which a thermal gradient can be calculated. The white arrow in the picture indicates the pull direction.



Figure 6.2: Picture of the MBRAUN glovebox (Left) and PM100 planetary mill (Right) used for this study.

solidus temperature depends on composition and material system shown is a typical value for Si/Ge. The profiles can be generated for any set-point of the furnace and the thermal gradient at the location of solidification can be calculated (the slope of the profile at the location of the red line). Simple solidification theory of a binary solute in solvent solidification provides the maximum stable pulling velocity as

$$V_{stable} < \frac{G_i D_l}{(T_l - T_s)}, \quad (6.1)$$

where D_l is the solute diffusivity, T_l the composition liquidus temperature, and T_s the composition solidus temperature. This stable pull velocity can be calculated for simple compositions and can guide the experimental specifications.

6.2.2 Milling

Powder processing was performed with a Retsch PM100 planetary mill (Retsch, Haan, Germany) mounted inside an Ar glovebox (MBRAUN) (see Fig. 6.2). The mill has a

planet and sun gear set to rotate the milling jar at a fixed ratio of the jar's revolution. As a result of the revolution speed the milling acceleration can be controlled, which would otherwise be fixed to that of earth gravity for a standard roller mill. The mill can be operated at speeds up to 600 rpm, although due to a resonance frequency of the glovebox the mill cannot be safely operated within the limits of 500-550 rpm. The mill was generally operated at 300 rpm and 580 rpm given the fixed revolution radius the acceleration was 100 m/s^2 and 370 m/s^2 , respectively. Milling was performed inside a 150 ml tungsten carbide lined jar. Tungsten carbide milling media was used; spherical 30 count 10 mm media was used for aggressive milling and spherical 100 count 5 mm media was used for gentle milling. A rubber gasket was used to seal the milling jar, and a new gasket was used for different material systems. The jar was cleaned by bead blasting followed by an Ethanol wash. Milling media was cleaned by running the media in a roller mill with Ethanol for over two hours. Between material system changes the milling jar and media were further cleaned by running a batch of sacrificial powder of the new system. For the Si/Ge system 70 g of granular elemental Si was used as the sacrificial powder while Sb shot was used for the skutterudite system. The Ar glovebox was kept at an atmosphere generally containing <5 ppm moisture and <15 ppm oxygen. The mill was mounted in the glovebox to reduce the risk of exposing powder to air in the event of a failure of the jar's seal. Catastrophic failure of the mill can result from extremely fine powders being exposed to air as the increased surface area of fine powder can become explosive.



Figure 6.3: Powder being pressed in graphite dies: cold pressed die (Left) and die mounted with insulation for SPS run (Right).

6.2.3 Sintering

Sintering routes investigated in this work include: spark plasma sintering (SPS also known as field-assisted sintering, FAST), hot pressing, and microwave sintering (MW). SPS was performed on a FCT Systeme GmbH using optical pyrometer control and an Ar atmosphere. Powder in 12 g batches was loaded into 1” graphite dies (Graphite Sales, Chagrin Falls, OH) coated with BN as a release agent (Boron Nitride Spray II Momentive Performance Materials, Waterford, NY). The die and push rod axial faces were lined with graphite foil to encapsulate the powder. Powder was initially cold pressed in a lab Carver hand press at 2 ksi for 2 mins to provide the initial consolidation of powders before SPS, see Figure 6.3 left. The green die was wrapped in thermal insulation before insertion into the SPS, see Figure 6.3 right.

Details of the SPS profile are discussed in the Si/Ge chapter to follow. Temperature, chamber pressure, ram pressure, and ram travel were recorded and monitored during sintering. Hot pressing was performed on $\frac{1}{2}$ " graphite dies with powder in 20-22 g batches. Similar to the SPS sample preparation, the hot press dies were lined with BN and graphite foil to both encapsulate the powder and act as a release agent. A lab built hot press was used for the work. Temperature was monitored with a thermocouple placed in a hole in the outside wall of the graphite die. Temperature, chamber pressure, ram pressure, and ram travel were recorded and monitored during sintering. MW sintering was performed on a 2 kW 2.45 GHz HY-Tech Microwave System (Gerling Applied Engineering Inc., GAE, Modesto, CA). The sample chamber was configured for a standing wave and the chamber was tuned with a Homer Automatic Impedance Analyzer and Matching System (S-TEAM, Bratislava, Slovak Republic). Temperature was measured with an optical pyrometer but feed-back control was not setup, instead microwave power was manually tuned by opening a gate in the waveguide. MW sintered samples were processed either in air or under a nitrogen atmosphere. MW sintering was performed on green pellets cold pressed on a lab Carver hand press at 2 ksi for 2 mins.

6.3 Chemical and Structure Analysis

The chemical content and structure analysis of the samples in this work were characterized using a range of microscopy techniques, X-ray diffraction, inductively coupled

plasma mass spectroscopy, oxygen/nitrogen determination, Brunauer-Emmett-Teller surface area analysis, and dynamic light scattering particle size analysis.

6.3.1 Microscopy

Microscopy of sectioned and polished samples included: optical microscopy, scanning electron microscopy (SEM), transmission electron microscopy (TEM), and electron probe micro-analysis (EPMA). Optical microscopy was performed using an Olympus DP71 (Olympus Corporation, Shinjuku, Japan), and was generally only used to obtain preliminary information prior to using other types of microscopy. SEM was performed on a field emission scanning electron microscope Hitachi S4700-II (Hitachi High Technologies, Gaithersburg, MD) operating between 10 and 20 kV with beam currents between 5 and 15 μA . The SEM was equipped with energy dispersive X-ray spectroscopy (EDS) (EDAX, Mahwah, NJ), a secondary electron detector (SE), and a backscatter electron detector (BSE). TEM was performed by a collaborating group, lead by Beth Guiton from The University of Kentucky operating equipment at Oak Ridge National Laboratory. The TEM employed a high resolution high-angle annular darkfield detector (HAADF). EPMA was performed on a JEOL JXA-8200 WD/ED (Jeol USA, Peabody, MA) operated at 15 kV with 30 nA beam current. Standards used included Co, Ni, Sn, and Sb obtained from a Taylor 203 standard. Crystals for analysis included LIF for Ni, PETJ for Sb/Sn, and LIFH for Co. Most samples were prepared by mounting in a 1" epoxy puck and grinding with silicon carbide paper to obtain a cross-section of the sample. Polishing was performed on a Metprep4 (Allied

High Tech Products, Los Angeles, California) using up to 800 grit silicon carbide paper followed by polishing with 0.05 μm alumina suspension on a polishing magnetic disk.

6.3.2 X-ray Diffraction

X-ray diffraction (XRD) was performed on a Bruker D-8 Advance (Bruker, Billerica, MA) with Cu $K\alpha$ radiation. The Bragg-Brentano configuration was used with 4° Soller and a 300 mm radius. A scan rate from 1.0 to 3.5° per minute was used over the range of $10 - 80^\circ$ for simple phase identification or $10 - 120^\circ$ for detailed Rietveld refinement. Samples were powder prepared by hand grinding in an alumina mortar and pestle and loading into a zero background powder holder made of single crystal Si cut to a non-diffracting plane. For air sensitive samples, powder holders were loaded in a glovebox then sealed with an X-ray transparent enclosure. Phase identification was performed with PANalytical's Highscore (Almelo, Netherlands) software using the ICDD PDF database. Rietveld refinement was performed using Bruker's TOPAS software.

6.3.3 Chemical Analysis and Particle Size

Global chemical analysis on samples included oxygen/nitrogen determination and inductively coupled plasma mass spectroscopy (ICP). All chemical analysis was performed at NASA Glenn Research Center by Dereck Johnson. Oxygen nitrogen determination was performed on a Leco TC-436 (Leco, St. Joseph, MI). Inductively coupled plasma mass spectroscopy (ICP) was performed with a Varian Vista-PRO

(Varian, Palo Alto, CA). ICP was used to measure trace amounts of impurities in samples as well as to check the intended elemental stoichiometry.

Particle size was measured by three techniques i) SEM microscopy, ii) surface area analysis, and iii) dynamic light scattering. Each method is prone to its own set of challenges such as small sample size in SEM. Brunauer-Emmett-Teller surface area analysis (BET, Micromeritics Instrument Corporation, Atlanta, GA) measures the surface area of a powder sample. Then average particle size can be estimated from an assumption of spherical shape. The BET method is, therefore, only capable of producing an average particle size and can prove nothing about the distribution of sizes. Dynamic light scattering (DLS) was performed on a Malvern Zetasizer Nano (Worcestershire, UK) and the method uses a suspension of powder in a known fluid combined with a series of laser flashes. That allows determination of velocities of particles which then can be related to particle size with knowledge of fluid's viscosity. The method is capable of providing a size distribution and is not limited to small sample size, but is dependant on the ability to find a suitable fluid to disperse the powder in.

6.4 Transport Property Characterization

Thermoelectric transport properties of interest include Seebeck coefficient, electrical conductivity, thermal conductivity, thermal diffusivity, charge carrier hall density, and charge carrier hall mobility. Furthermore the temperature and composition dependence of these properties was critical to this investigation.

6.4.1 Seebeck Coefficient and Electrical Conductivity

Measurement of Seebeck coefficient (S) and electrical conductivity (σ) were made simultaneously using a modified ZEM-3 System (Ulvac Technologies, Methuen, MA). The system performs a four-point electrical conductivity measurement using two type-K thermocouples while simultaneously measuring temperature differential and calculating Seebeck coefficient. Thermocouple Seebeck voltage was automatically compensated for by the software. The ZEM-3 system has been modified from its original configuration with a higher power current source and creation of an in house software package. The developed software allows for improved control, enables pulsed V-I plot generation at temperature, and includes a comprehensive uncertainty analysis of data. The uncertainty analysis includes statistical, geometric, instrument, and thermal contact resistance sources; details of the uncertainty analysis are in Chapter 7 with further details covered in Appendix B. Specimens were subjected to a thermal gradient up to $0.5^{\circ}\text{C}/\text{mm}$ by a Pt wire heater mounted in the lower support arm. Specimen dimensions were nominally $4\times 4\times 18$ mm, testing was performed in a He environment at 85 Torr between $100-1000^{\circ}\text{C}$. Detailed discussion on the measurement of Seebeck coefficient and electrical conductivity can be found in the works of Martin et al. [154–156].

6.4.2 Thermal Conductivity and Specific Heat

The laser flash method (Flashline 5000, Anter Corporation, Pittsburg, PA) was used to measure thermal diffusivity of disc shaped samples with nominal dimensions of 2.5

mm thickness and 12.5 mm diameter. Samples were measured in accordance with ASTM E1461 for the laser flash method. Samples were coated with 1 μm Pt film by physical vapor deposition (PVD-75, Kurt J. Lesker, Jefferson Hills, PA) to ensure an opaque surface to laser irradiation. Pt thickness is negligible when compared to specimen thickness, therefore is not believed to alter thermal measurements significantly. Specimens were also coated with carbon paint in accordance with standard flash method to ensure a consistent emissivity. Thermal diffusivity was calculated from the average of three time-temperature curves, using the method of Clark and Taylor [157]. Thermal conductivity (k) was calculated from laser flash diffusivity (α), Archimedes immersion density (ρ), and specific heat (c_P) following the relationship

$$k = \alpha \rho c_P. \quad (6.2)$$

Specific heat was both measured using the laser flash method and calculated using the Debye model or Dulong-Petit model. Thermographite and Pyroceram were used as standards for the calculation of specific heat from the laser flash method [158]. Samples were prepared with the same physical dimensions to the standards and the carbon coating was performed simultaneously on the samples and standards. The work of Parker et al. provides a good introduction to the measurement of thermal diffusivity, specific heat, and thermal conductivity by the laser flash method [159]. A more recent discussion on the topic can be found in the work of M.A. Thermitus [160].

6.4.3 Hall Carrier Density and Carrier Mobility

Hall carrier density and carrier mobility were measured on a Lakeshore Cryotronics (Westerville, OH) Hall System. Samples were measured in the Van der Pauw configuration with an applied field of 2 T and an applied electrical current of 50 mA. Samples were discs of 12.5 mm diameter with <0.5 mm thickness. No sample to probe interface was required as contacts were determined to be ohmic through a set of V-I plots. The Van der Pauw method can be found discussed in the work of Van der Pauw [161] and Chwang et al. [162].

6.5 Conclusion

In support of the work presented in this dissertation, Table 6.1 provides a general summary of the number of samples and testing performed. The table is broken into a processing section for silicon-germanium based samples, a processing section for skutterudite samples, and a testing section summarizing the number of X-ray diffraction (XRD) scans, scanning electron micrographs (SEM), and transport property measurement runs performed. The transport property measurement category includes measurement of Seebeck coefficient, electrical resistivity, thermal conductivity, carrier density, and carrier mobility. The chapters to follow highlight only a sub-section of the total project completed. The samples presented and discussed were selected in support of the dissertation.

Table 6.1: Summary of samples and testing supporting the dissertation.

Category	Count
# Sintered Si/Ge Samples	> 60
# Solidified Si/Ge Samples	> 30
# Sintered Skutterudite Samples	> 20
# Solidified Skutterudite Samples	> 20
# XRD Scans	> 700
# SEM Micrographs	> 3,000
# EDS Scans	> 500
# Transport Property Measurement Runs	> 550

CHAPTER VII

MEASUREMENT UNCERTAINTY ANALYSIS

7.1 Introduction

Along with increased research in thermoelectric materials, a number of characterization systems have been developed for the measurement of Seebeck coefficient and electrical resistivity. [155, 163–180] This chapter introduces an uncertainty analysis on the electrical resistivity and Seebeck measurements performed in the chapters to follow. No high temperature standards exist for thermoelectric measurement making comparison between laboratories difficult or impossible. The uncertainty analysis provided in this chapter introduces a method to help standardize sample measurement.

7.2 Measurement Definition

A generic potentiometric (four probe) measurement configuration can be described by Figure 7.1. Electrodes mechanically clamp the sample, while two thermocouple probes make contact with the side of the sample with probe spacing (L). As will be discussed, the thermocouples exhibit positional tolerance which can introduce measurement error. Common sample shapes include rectangular prisms and cylindrical



Figure 7.1: Potentiometric configuration for Seebeck coefficient or electrical resistivity measurement. Samples cut to the shape of a rectangular prism or cylinder are held in place by electrodes, top and bottom, while two probe thermocouples make contact on a single face of the sample.

bars. The differential Seebeck method is used by means of a heater mounted below or above the sample, average sample temperature is controlled separately by a high temperature furnace.

The sample Seebeck coefficient (S) is calculated by subtracting the thermocouple Seebeck coefficient from the measured Seebeck coefficient. Equation 7.1 is used to calculate the sample Seebeck coefficient using a linear regression on measured voltage and temperature difference as

$$S = -\frac{\Delta V}{\Delta T} + S_{Wire}(T) = -\frac{\sum x_i \sum y_i - N \sum x_i y_i}{(\sum x_i)^2 - N \sum x_i^2} + S_{Wire}(T), \quad (7.1)$$

where x_i is the probe to probe temperature difference, y_i is the probe to probe voltage along similar wires (Chromel or Alumel wires for type-k thermocouples), N is the sampling size, and S_{Wire} is the temperature dependent Seebeck coefficient of the appropriate wires used for the y_i variable. The temperature dependent Seebeck coefficient used for this work has been extracted from the work of Heikes and Ure [181] and fit to the following equations

$$S_{Chromel} = 21.035 + 2.3955 \times 10^{-2}T - 6.4380 \times 10^{-5}T^2 + 2.8792 \times 10^{-8}T^3, \quad (7.2)$$

$$S_{Alumel} = 18.123 + 1.6420 \times 10^{-2}T - 2.6611 \times 10^{-4}T^2 + 1.1925 \times 10^{-6}T^3 \\ - 2.1104 \times 10^{-9}T^4 + 1.6948 \times 10^{-12}T^5 - 5.1597 \times 10^{-16}T^6, \quad (7.3)$$

where temperature (T) is in Celsius, and Seebeck coefficient is in $\mu\text{V}/\text{K}$.

Electrical resistivity is measured using the potentiometric method. A current is pulsed through the electrodes and sample. Voltage response is measured on the same thermocouple probes used for the Seebeck measurement. It is critical for a thermoelectric sample to be isothermal during a resistivity measurement as a thermal gradient will lead to thermoelectric voltages. This coupled behavior is used as the basis for the Harman method, and can be used for direct figure of merit measurement. [182–185] For measurement of electrical resistivity, the test current must be pulsed sufficiently fast in order to extract only the voltage due to the electrical

conduction, rather than a Seebeck voltage generated from Peltier heating. For this work it was experimentally determined that a pulse time less than 300 ms is suitably fast for many thermoelectric samples. The acceptable pulse time is a function of the thermal parameters of the sample, instrument configuration, and sample size. Equation 7.4 is used to calculate the electrical resistivity of a sample

$$\rho = \frac{\sum z_i \sum y_i - N \sum z_i y_i}{(\sum z_i)^2 - N \sum z_i^2} \frac{wD}{L}, \quad (7.4)$$

where y_i is the probe to probe voltage along similar wires, z_i is the current through the test sample, N is the sampling size, w is the sample width, D is the sample depth, and L is the probe spacing. The wD term defines the cross-sectional area and can be modified according to the geometry. For example, for cylindrical samples the wD term is replaced by πr^2 , where r is the cylinder radius. A natural thermal gradient will often exist in the sample during the resistivity measurement; presence of this gradient during the resistivity measurement does not affect the validity of the result as long as the gradient remains constant. A main source of this thermal gradient is uneven sample heating, which can be reduced with proper shielding. Experience on typical measurement systems has shown an acceptable range for this thermal gradient to be less than $1^\circ C$ per 20 mm.

The sections to follow discuss the uncertainty associated with these electrical measurements, taken on a potentiometric configuration as described. The work to follow is intended to provide an interval of measurement certainty, for example to compare measurements obtained between different laboratories and different test

equipment. The analysis was specifically completed for the ZEM-3 measurement system (ULVAC Technologies), but the methodology is applicable to any potentiometric system.

7.3 Uncertainty Sources

Uncertainty in the Seebeck and resistivity measurements can arise from a number of sources, discussed in detail by Martin [156] and Martin et al. [154] In this work a number of sources are addressed to quantify the uncertainty for common potentiometric systems. Listed in table 7.1 are the sources of uncertainty for resistivity measurements.

Potentiometric resistivity measurements assume dimensionless point contacts with infinitesimal area so as to avoid any area averaging effect. However in reality there is finite contact area quantified by the tip radius (Source #1 in table 7.1). A typical value for such a thermocouple tip, 0.25 mm radius, is also listed in the third column. This measurement area, though very small, adds some uncertainty to the length used for the resistivity measurement (L variable in equation 7.4). In order to reduce the magnitude of this source finer gauge thermocouple wires or carefully prepared thermocouple beads must be employed to obtain a spot size smaller than 0.25 mm. However, the probes are generally spring loaded to provide good contact. Accommodating this load can limit how small the bead can be.

The measurement of the probe separation itself, measured between the centerlines of probes, is a challenging measurement with inherent uncertainty. This

Table 7.1: Sources of resistivity uncertainty

#	Source	Typical values
1	Thermocouple tip radius	0.25mm
2	Thermocouple separation length	± 0.1 mm
3	Sample uniformity	± 0.1 mm/cm
4	Caliper resolution	± 0.01 mm
5	Statistical variation	Calculated
6	Wire discrepancy	Calculated
7	DAQ voltage uncertainty	50 ppm + $1.2\mu\text{V}$
8	DAQ current uncertainty	0.2%+0.3 mA

separation length measurement is listed as source #2 in table 7.1, uncertainty on this measurement is assumed to be ± 0.1 mm if measurement is done with a caliper. Depending on the method used to make this measurement, the uncertainty interval may vary from the assumed value. This uncertainty can be decreased below ± 0.01 mm if the measurement is performed using a calibrated optical microscope or a similar more accurate system. However, such systems bring additional complexity to the instrumentation.

Source #3 accounts for the possibility of non-uniform cross sectional area along the leg length. Figure 7.2 displays three possible (highly exaggerated for clarity) geometrical shape non-uniformities. The center sample in Figure 7.2 is shown to have

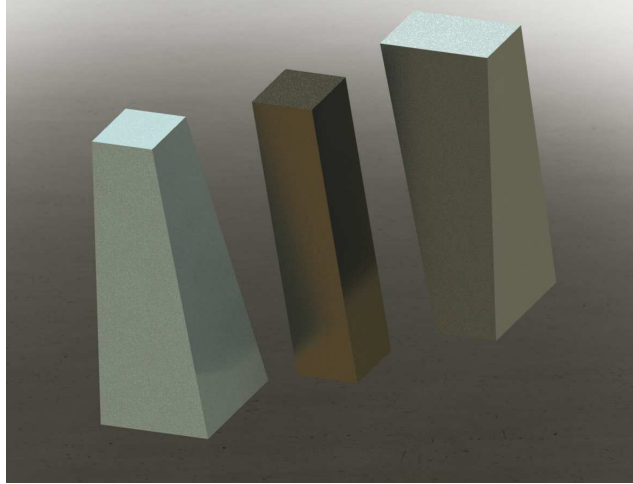


Figure 7.2: Examples of possible sample uniformity challenges. (Center) an ideal sample, (Left and Right) practical samples shown with exaggerated draft angles.

perfectly parallel faces while the outer two samples display draft angles which lead to a variation of cross-sectional area along the sample length. In practical sample machining some level of sample non-uniformity is permitted and common. Source #3 assumes less than 0.1 mm variation in the width or depth over a sample length of 1 cm. The error associated with this sample non-uniformity can be reduced with careful sample preparation. Source #4 accounts for caliper resolution of the sample size and probe spacing measurements, ± 0.01 mm is a reasonable resolution for most calipers.

Source #5 accounts for statistical variation in the slope statistic calculated for the resistivity measurement. Equation 7.5 is used to calculate the uncertainty in the slope statistic

$$U_{Stat} = t_{\nu,95\%} \sqrt{\frac{N \sum (y_i - y_c(z_i))^2}{\nu(N \sum z_i^2 - (\sum z_i)^2)}}, \quad (7.5)$$

where t is the 95% t-distribution for $\nu = N - 2$ degrees of freedom, z_i is the test current, y_i the test voltage, y_c the linear curve fit voltage, and N the sampling size. While this uncertainty is random in nature and cannot be directly controlled, the selection of test profile can have a large effect on its magnitude. Thus, increasing the sampling size used for each resistivity measurement can enhance the certainty of the results. In general, it is advisable to use a large sample size to force this uncertainty to a negligible level.

Source #6 includes the discrepancy between the resistivity calculated from voltages taken on the Chromel and Alumel wires (assuming type-K thermocouple probes). Ideally both wires will return identical resistivity values. The wire discrepancy uncertainty is more prone to lead to uncertainty in the Seebeck measurement as standard data is used for each wire to subtract the effect of the wires. Proper maintenance of the thermocouple probes should mitigate the magnitude of this source of uncertainty.

Source #7 accounts for the data acquisition (DAQ) uncertainty for voltage measurements. A Keithley datasheet (Keithley, Cleveland Ohio) specifies 2 year accuracy of 50 ppm(reading)+1.2 μ V for the range typically used in resistivity measurement [186]. Source #8 accounts for the uncertainty for current measurements, estimated to be 0.2%+0.3 mA for common current sources employed in resistivity systems [187]. The reported accuracies are the best cases for stable equipment, oper-

ating within the recommended temperature and ambient condition ranges. Regular device calibration on the individual meters could be performed to ensure operation within the specification.

Several of the listed sources of error can be considered in selecting sample dimensions and measurement parameters. For instance, assuming a ± 0.1 mm uncertainty on the probe separation distance, the selection of 4, 6, or 8 mm probe spacing contributes 2.5, 1.6 or 1.2% to uncertainty, respectively. Likewise, thinner samples introduce greater error as a result of sources #3 and #4. Additionally, factors not addressed in table 7.1 must be considered in sample selection. For instance, probe placement must be suitably far from the sample end to ensure a uniform conduction profile within the sample. This criterion can be met with proper selection of the probe spacing. This work does not consider, or attempt to quantify, issues of this nature.

Table 7.2 lists the sources of uncertainty in the Seebeck measurement. Source #1 includes a problem common to all surface thermocouple thermometry, known as the cold-finger effect. The effect is the result of measuring a hot surface with a relatively cooler thermocouple. Heat is transferred into the thermocouple, altering the temperature profile in the sample and establishing a thermal gradient in the thermocouple. Due to heat flow in the thermocouple, any thermal resistance results in a temperature drop and slight under-estimation of the actual surface temperature. A thermal finite element analysis (FEA) model was developed to quantify this error in the Seebeck measurement. The thermal contact resistance is accounted for

Table 7.2: Sources of Seebeck uncertainty

#	Source	Typical values
1	Cold-finger effect	10,000W/(m ² K)
2	Wire Seebeck variation	±5%
3	Absolute temperature	±2 K
4	Statistical variation	Calculated
5	Wire discrepancy	Calculated
6	DAQ voltage uncertainty	50 ppm + 1.2μV
7	DAQ temperature uncertainty	50 ppm + 1.2μV

with a contact conductance parameter, ranging from 100,000 to 10,000 $W/(m^2K)$, with larger numbers representing good contact and smaller numbers representing poor contact. Given the potentiometric configuration, this source of error cannot be completely removed.

Source #2 highlights the uncertainty introduced by error from using a curve fit (Eqns. 7.2 and 7.3) for the thermocouple wire Seebeck coefficient. Additionally, the 5% error on Seebeck coefficient for the thermocouple wire can account for alloying or other changes which can happen to the thermocouple wires during measurement. The use of a high grade calibrated thermocouple wire, combined with frequent replacement, can help reduce the magnitude of this source. Source #3 also deals with

the wire Seebeck coefficient, the absolute value of the temperature used in Eqns. 7.2 and 7.3 can be within a range of ± 2 K.

Source #4 is the same statistical variation uncertainty estimate used for the resistivity measurement; calculation is based on the Seebeck voltage and temperature difference between probes. Reduction of this factor occurs through the control of testing profile. In the case of steady-state measurement, large sampling size can become time consuming. In contrast, using a quasi-equilibrium method can provide large sampling sizes. The statistical uncertainty is generally reduced for larger sample sizes, meaning the quasi-equilibrium method has the potential to improve upon the steady-state method.

Source #5 is the difference in sample Seebeck coefficients calculated by the Chromel and Alumel wires (assuming type-K probes). For probes which match the standard Seebeck curves (Eqns. 7.2 and 7.3) this source will be negligibly small. For probes which deviate from the standard data, possibly due to contamination, this source highlights the need to consider replacing the probes.

Source #6 is the same data acquisition accuracy error used for the resistivity measurement, applied to the Seebeck voltage measurement [186]. Source #7 is similar to #6 but emphasizes the temperature measurements, which are particularly sensitive to measurement error.

7.4 Cold-Finger Modeling using FEA

The challenge of measuring surface temperatures with a thermocouple in contact with a hotter surface, known as the cold-finger effect, are discussed by several sources. [154, 156, 163, 188] Some characterization systems take advantage of the effect as a means to generate the necessary temperature gradient within a thin film sample. [164] In the case of a potentiometric arrangement, this parasitic heat transfer results in an over estimation of the Seebeck coefficient. The manifestation of this error is displayed in Figure 7.3, illustrating the geometrical model for analysis. T1 is the actual sample temperature and T2 is the average temperature of the thermocouple bead. Due to the small heat flux (Q) transfer to the thermocouple and thermal resistance of the interface and thermocouple bead, a temperature difference exists between points T1 and T2. The measurement error arises when both the upper and lower measurement probes are considered. The cold finger effect is predominant at the lower probe than the upper probe due to increased heat flux as a result of the delta temperature heater being located at the bottom of the sample in the model. To highlight this effect, the modeling results are shown in Figure 7.3; details of the modeling work are presented in the following paragraphs. The actual temperature of the upper (blue color) and lower probes (red color) are shown for points T1 and T2. The probe to probe temperature difference (PPTD) on point T2 of the upper and lower probes represents the experimentally measured temperature difference (1.04 K). The PPTD at point T1 is the actual sample temperature difference (1.33 K). Thus, ΔT at point

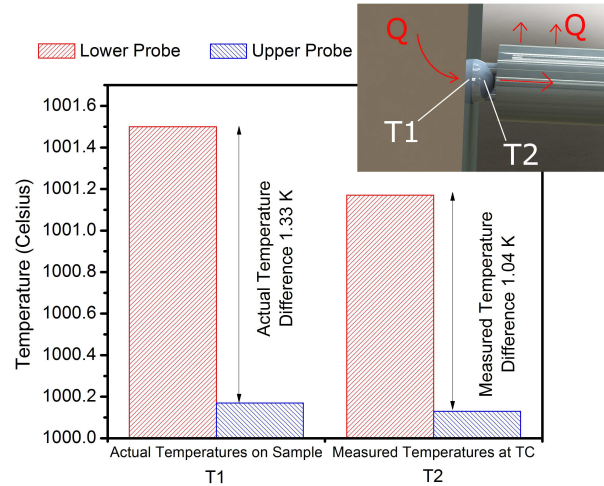


Figure 7.3: Demonstration of the cold-finger effect leading to an under-estimated temperature difference.

T1 is 0.29 K larger than ΔT at point T2. Although this value is rather small, it results in a 22% over-estimation of the Seebeck coefficient.

The cold finger effect has been quantified with a steady-state thermal FEA study, using Autodesk Simulation (Autodesk, San Rafael, CA) multiphysics FEA software. No thermoelectric modeling was required as Seebeck coefficient is measured in an open circuit condition, only Fourier heat transfer is considered. The FEA model is intended to capture the thermal gradient of a sample as a result of the applied thermal boundary conditions. The case selected is for a measurement at a furnace ambient temperature of $1000^{\circ}C$ with a hot end temperature of $1006^{\circ}C$, probe separation of 8 mm, sample length of 18 mm, and sample to probe thermal contact conductance of $33,000 W/(m^2K)$.

The model shown in Figure 7.1 was discretized into 55,476 primarily brick elements. The sample was selected to have a thermal conductivity of $4 W/(mK)$, and dimensions $4 \times 4 \times 18$ mm; both are reasonable numbers encountered in thermoelectric material development. The sample ends in contact with the outer electrodes were constrained to fixed temperatures. The remaining faces of the sample couple with the furnace temperature only through radiation. A non-linear iterative solver was employed to account for the radiation treatment. A radiation emissivity of 0.7 is assumed for the sample faces. [167, 184] The probes were simplified to be cylindrical with thermal conductivity of $30 W/(mK)$, radius of 0.5 mm, and length of 150 mm. The simplified cylindrical probes avoid unnecessary complexities of modeling a thermocouple bead with two individual thermocouple wires. The selected thermal conductivity and radius of the probes are intended to serve as a reasonable average of the complicated true geometry of a thermocouple. The cold ends of the probes were fixed to $20^\circ C$. A similar assumption about radiation emissivity with a factor of 0.7 was made for the cylindrical faces of the probes. [167, 184] Points T1 and T2 were selected to include the thermal interface resistance between sample and probes as well as temperature averaging in the thermocouple bead. The selection of location for T2 was based on an assumed thermal contact conductance parameter. The point T1, shown in Figure 7.3 and used in all subsequent calculations, was on the sample at the centerline of the probe. The point T2 was also selected to be at the centerline of the probe, but 0.3, 1, or 3 mm away from the point of contact to estimate 100,000, 33,000, or 10,000 $W/(m^2K)$ respectively. Except where noted otherwise, results to

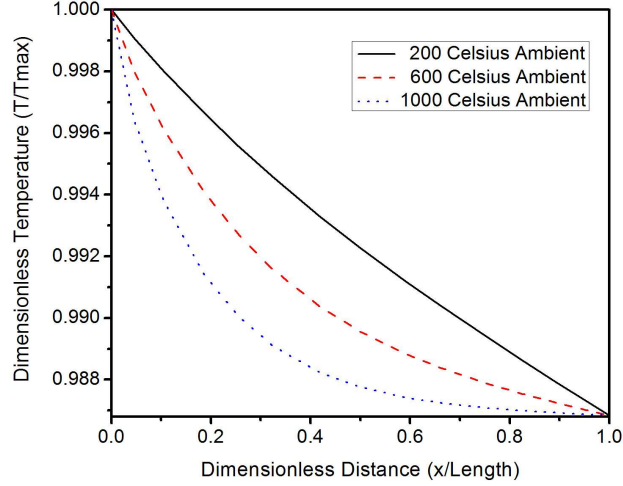


Figure 7.4: Sample temperature profiles for three ambient temperatures.

follow assume a contact conductance of $33,000 \text{ W}/(\text{m}^2\text{K})$ by employing a T2 location of 1 mm.

The main parameters in the study include furnace temperature, temperature drop between the outside electrodes, and the thermal contact conductance. The measurement uncertainty is defined as

$$U_{\text{Cold-finger}} = (T1_{\text{Lower}} - T1_{\text{Upper}}) - (T2_{\text{Lower}} - T2_{\text{Upper}}). \quad (7.6)$$

Figure 7.4 shows the calculated leg temperature profile for three ambient furnace temperatures. The temperatures were normalized to the maximum temperatures for each case; 203.62 , 602.91 , and $1002.53 \text{ }^\circ\text{C}$ on the hot end, with a cold end of 200 , 600 , and $1000 \text{ }^\circ\text{C}$ respectively. The dimensionless end temperatures (temperature/maximum temperature) were selected to generate profiles with matching boundary dimension-

less temperatures. The matching dimensionless temperatures at the ends of the samples allow for comparison between the three profiles. The profile varies with changes in ambient temperature; moves from nearly linear behavior at 200°C , to a highly non-linear behavior at 1000°C due to a significant increase in radiation losses.

The cold-finger effect is demonstrated in Figure 7.5 as a temperature contour plot on a plane taken through the sample and probes, at the probe centerlines. The bottom of the sample is constrained to 1006°C , while the top is constrained to 1000°C . This case represents a realistic measurement configuration, which clearly demonstrates the importance of the cold-finger effect. The faces of the sample and cylindrical faces of the probes are subject to radiation with the environment at 1000°C . The temperature gradient observed in the lower probe indicates a heat flux from sample to probe and cause a disturbance in the temperature profile of the sample, in the vicinity of the probe. The temperature profiles of the two probes are different due to the difference in the temperatures of the contact points. In the upper probe both T1 and T2 are at practically the same temperature, but in the lower probe a significant temperature difference exists. This discrepancy defines the uncertainty due to the cold-finger effect. Due to the direction of heat transfer this effect can only lead to an underestimation of temperature difference, thus an overestimation of the Seebeck coefficient. As a result of the steep gradient near the hot end of the sample (observed in both figures 7.4 and 7.5) a wider probe separation will lead to a bigger temperature difference between the upper and lower probes. The uncertainty will correspondingly increase for a wider probe separation distance.

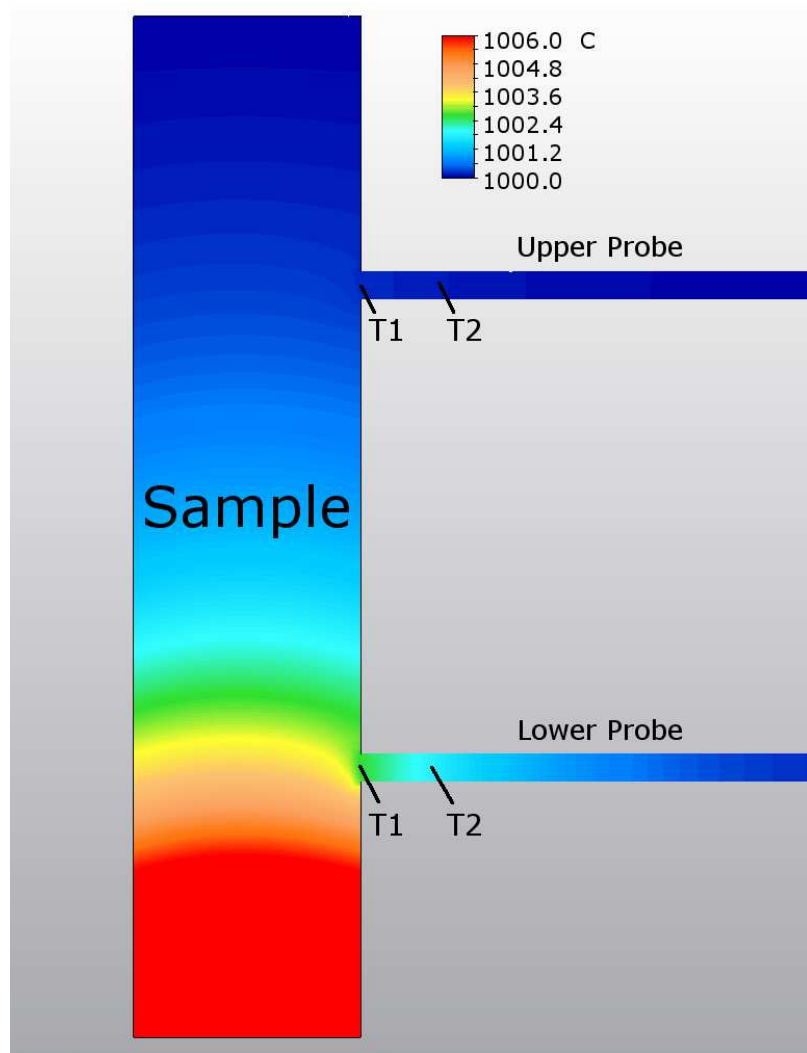


Figure 7.5: Temperature contour of sample and probes, demonstrating the cold-finger effect.

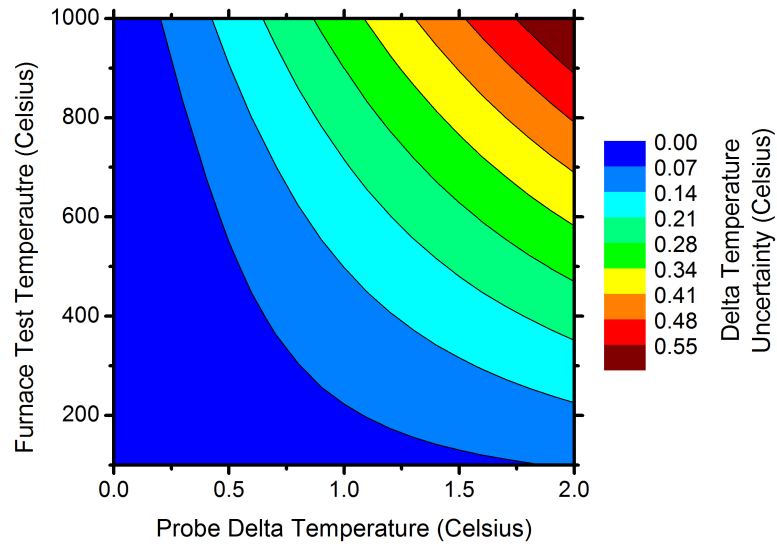


Figure 7.6: Sample temperature profiles for three ambient temperatures.

The uncertainty as a function of both furnace temperature and PPTD is presented in Figure 7.6 for a contact conductance of $33,000 \text{ W}/(\text{m}^2\text{K})$. The uncertainty increases with increasing furnace temperature and PPTD. Higher furnace temperatures allow greater lateral heat transfer due to radiation out of the thermocouple probes, thus leading to a larger heat flux and amplified cold-finger effect. At higher delta temperatures the upper and lower probe temperature contours are dissimilar, leading again to a more exaggerated cold-finger effect. Varying the contact conductance produces a similar profile in the furnace temperature and PPTD space. For lower contact conductance the uncertainty at a given furnace temperature and PPTD is higher. The curve fit form of the data is used for calculating the propagation of error onto the Seebeck coefficient.

$$\begin{aligned}
U_{\text{Cold-finger}_i} = & 7.188 \times 10^{-3} - 4.590 \times 10^{-5}T + 4.584 \times 10^{-8}T^2 + 5.068 \times 10^{-3}x_i \\
& - 4.833 \times 10^{-4}x_i^2 + 8.409 \times 10^{-5}Tx_i, \quad (7.7)
\end{aligned}$$

$$\begin{aligned}
U_{\text{Cold-finger}_i} = & 3.606 \times 10^{-2} - 1.682 \times 10^{-4}T + 1.385 \times 10^{-7}T^2 - 9.511 \times 10^{-3}x_i \\
& + 1.894 \times 10^{-3}x_i^2 + 3.178 \times 10^{-4}Tx_i, \quad (7.8)
\end{aligned}$$

$$\begin{aligned}
U_{\text{Cold-finger}_i} = & 2.010 \times 10^{-1} - 1.144 \times 10^{-3}T + 9.820 \times 10^{-7}T^2 - 5.855 \times 10^{-2}x_i \\
& - 1.215 \times 10^{-2}x_i^2 + 1.447 \times 10^{-3}Tx_i, \quad (7.9)
\end{aligned}$$

where both the furnace temperature T and the PPTD x_i are in Celsius. Equation 7.7 is calculated for convection coefficient of 100,000 $W/(m^2K)$, while equation 7.8 is calculated for 33,000 $W/(m^2K)$, and equation 7.9 is for 10,000 $W/(m^2K)$. Uncertainties for intermediate contact conductance can be calculated from a power law regression of eqns. 7.7-7.9. Equation 7.9 represents the most conservative estimation of the cold-finger effect, while equation 7.7 represents a case in which the effect is nearly negligible.

This modeling can be compared against the experimental work of Joshua Martin. [156] In Martin's work an apparatus was built to directly compare the potentiometric and two point Seebeck measurement configurations. As described in

the article, a single sample can be measured with both configurations to compare the calculations. The experimental trend was the same as the calculated trend of our FEA model, the cold-finger effect in a potentiometric configuration leads to an overestimation of Seebeck coefficient and this effect monotonically increases with increasing furnace temperature. The experimentally measured magnitude of the difference between the two configurations is 12% at 626 °C. When compared to the uncertainty calculated using the FEA model (8% at 622 °C employing contact conductance 10,000W/(m²K)), the experimental data is in fair agreement. Sources of the discrepancy on magnitude include i) the fact that a two point measurement will be subject to a hot-finger effect and ii) the FEA model is strongly dependent on additional factors such as surface emissivity and the thermal resistance of probe/sample interface, which are difficult to quantify directly. The hot-finger effect of the two probe measurement results when the thermocouples are in direct contact with the sample heater on the ends of the sample and heat is transferred into the sample through the thermocouples, rather than out for the cold-finger effect. The hot-finger effect is such that the probes have a tendency to overestimate the temperature difference, which will calculate a lower than actual Seebeck coefficient. As a result the actual Seebeck coefficient is likely to lie somewhere between the two measurements which would lower the uncertainty towards values calculated by FEA. The FEA model was designed with emissivity of 0.7, a value close to emissivity of Silicon. When the emissivity in the FEA model was varied from 0.5 to 0.9 at 600 °C, the uncertainty was increased by 12%. The larger emissivity results in a larger uncertainty, due to

the increased lateral heat transfer. For a typical ceramic material a more appropriate emissivity may be 0.2. Varying the model emissivity from 0.5 to 0.1 at 600 °C resulted in a 40% decrease in the calculated uncertainty.

7.5 Uncertainty Analysis Example

A set of high temperature data has been measured for a Si/Ge alloy (80/20 at%) to provide an experimental example of quantitative uncertainty analysis. The uncertainty analysis is presented only to serve as an outline of trends and is not intended to demonstrate the uncertainty of any particular system. Samples were p- and n-type doped with 2 at% B and P, respectively. All samples were prepared by milling elemental powders in a planetary mill under Ar atmosphere until alloying of the Si and Ge powders was achieved, as confirmed by X-ray diffraction. Powders were densified with spark plasma sintering to obtain 1 inch diameter pucks that were machined to 4x4x18 mm bars. Details of the material system used in this section will be covered in Chapter 8. The Si/Ge system is well-studied [16, 105, 106, 118] and serves as an established benchmark for new material systems, thus is a suitable system for demonstration. There is no universally established high temperature standard. The purpose of the verification reported here is to understand the influence of measurement factors on the uncertainty of the resistivity and Seebeck coefficients and it does not stand as a verification of any particular measurement system.

Electrical resistivity and Seebeck coefficient were measured during a single run as furnace temperatures stepped from room temperature to 900 °C by intervals of

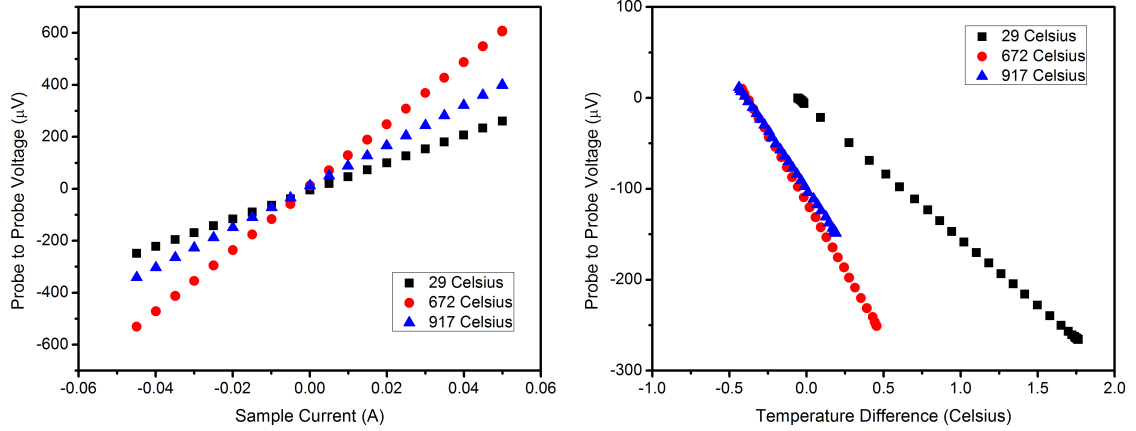


Figure 7.7: (Left) voltage versus current plots used to measure electrical resistivity. (Right) voltage versus temperature difference plots used to measure Seebeck coefficient. Data measured on a 2 at% P doped 80/20 Si/Ge sample.

50 °C. The measurement profile at each set point temperature consisted of 1) a check on the furnace stability 2) a check on sample isothermal conditions 3) measurement of the resistivity 4) measurement of the Seebeck coefficient. Thermal stability was verified following the definition of less than 5% furnace temperature deviation in 120 seconds. The steady isothermal condition was defined as less than 0.1 °C change in PPTD for a time of 120 seconds. The electrical resistivity was measured with test currents varying from -50 mA to 50 mA with 5 mA intervals. The current was pulsed for 300 ms, at the end of which voltage was measured between Chromel and Alumel wires. After a period of 700 ms, current was pulsed again. The heater driving the temperature drop across the material was heated at a rate of 1 °C/min up to 10 °C. Probe to probe Seebeck voltages were measured along Chromel and Alumel wires at a rate of one data point per second.

Data used to calculate electrical resistivity and Seebeck coefficient are shown in Figure 7.7. The electrical resistivity was calculated from the slope of the voltage versus current data, Figure 7.7 left. Seebeck coefficient was calculated from the slope of the voltage versus PPTD, Figure 7.7 right. The data has not been normalized in any way other than to show every 7th data point, highlighting the large sample size obtained with the quasi-equilibrium method. Even though the maximum temperature difference (10°C) was kept constant at each furnace temperature, the resulting maximum PPTD varies. At low furnace temperatures a larger range of PPTD ($\Delta T = 1.7^\circ\text{C}$ at 29°C) can be achieved, while high furnace temperature results in a smaller PPTD range ($\Delta T = 0.8^\circ\text{C}$ at 672°C and $\Delta T = 0.6^\circ\text{C}$ at 917°C). Despite the fact that the temperature dependent thermal conductivity of the material will have a contribution to this observation, the primary cause is the lateral radiation. The FEA model, which does not account for temperature varying material properties, displays the same trend. As shown in Figure 7.4 the temperature drop occurs rapidly near the hot end when the ambient temperature is high, thus results in flatter profiles over the majority of the sample. Such flat profiles lead to narrower PPTD.

The quantified influence of sources discussed in tables 7.1 and 7.2 on measurement uncertainty for this case study is summarized in Figure 7.8. Uncertainty due to each source is displayed at three ambient temperatures 29, 672, and 917°C to elucidate their temperature dependence. The largest sources of uncertainty on resistivity measurement are the thermocouple tip radius 6.4%, sample uniformity 2.5%, and thermocouple separation distance 1.3%. Since these measurements are

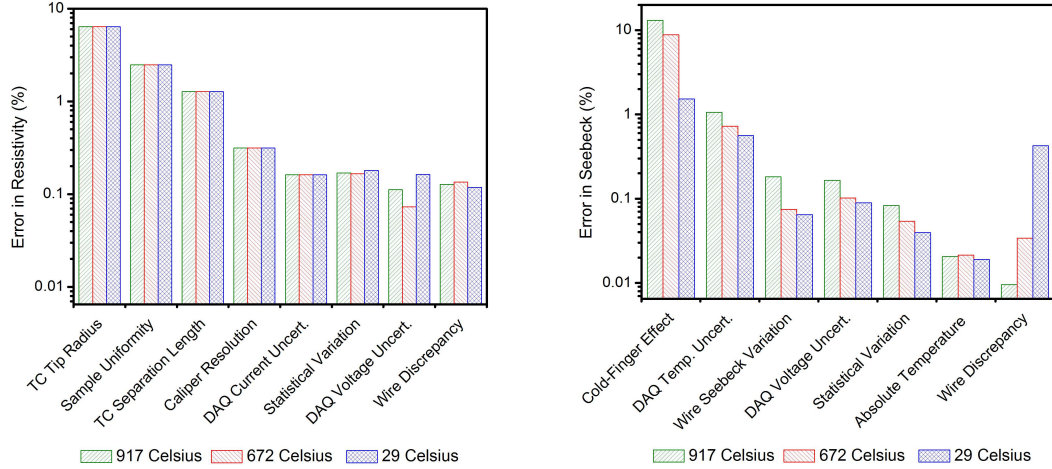


Figure 7.8: Uncertainty in electrical resistivity (Left) and Seebeck coefficient (Right) due to several sources. Data measured on a 2 at% P doped 80/20 Si/Ge sample.

all geometric they are temperature independent. Note that thermal expansion could lead to temperature dependence of geometric factors. However, due to small thermal expansion coefficients of typical thermoelectric materials (less than $5.5K^{-1} \times 10^{-6}$ at $1000^{\circ}C$ [106] for Si/Ge alloys), such variations are much smaller than the range of values assumed in table 7.1. The remaining sources considered contributed to less than a combined 1% uncertainty and can therefore be safely neglected. A significantly larger statistical uncertainty or wire discrepancy for any single data point would flag the measurement as questionable and would suggest the need to further investigate the data, or repeat the measurement at the temperature in question. Since the non-negligible uncertainty sources for resistivity measurement are geometric, careful sample preparation and measurement practices can be employed to obtain reliable data. For the case of values assumed in table 7.1, a combined uncertainty of $\pm 7.0\%$

can be safely assumed for all resistivity measurements obtained on similar samples under a comparable measurement configuration.

The uncertainties of the Seebeck measurement are inherently temperature dependent. The uncertainty is dominated by the cold-finger effect with 13% at 917°C, 8.8% at 672°C, and 1.5% at 29°C. The temperature dependence of the cold-finger uncertainty is calculated from FEA modeling (Fig. 7.6) and the greater cold-finger effect at high temperature is due to increased radiation transfer. As shown in Figure 7.7, the PPTD that can be obtained is a function of ambient temperature ($\Delta T = 1.7^\circ C$ at room temperature, $\Delta T = 0.6^\circ C$ at 917°C). Thus the DAQ uncertainty contributes to a larger percentage of the lower probe to probe temperature differences which are obtained at high ambient temperatures. The temperature dependence of the wire Seebeck variation uncertainty is a result of the fixed 5% uncertainty on the curve fit data. The remaining sources contributed to less than a 0.2% combined uncertainty and can safely be neglected. At high temperatures, the uncertainty on absolute Seebeck measurement can be calculated to be +1.0%/-13.1%, while at low temperatures Seebeck measurement uncertainty is $\pm 1.0\%$.

The full uncertainty analysis is found in Figure 7.9, calculated at every temperature for resistivity, Seebeck coefficient, and thermoelectric power factor. As a result of the asymmetry of the cold-finger effect, the final uncertainty on the power factor is also asymmetric, and will likely result in overestimated power factors. In this example, near room temperature, the final power factor calculated should be reported with an uncertainty of $\pm 7.5\%$. At high temperature the power factor should

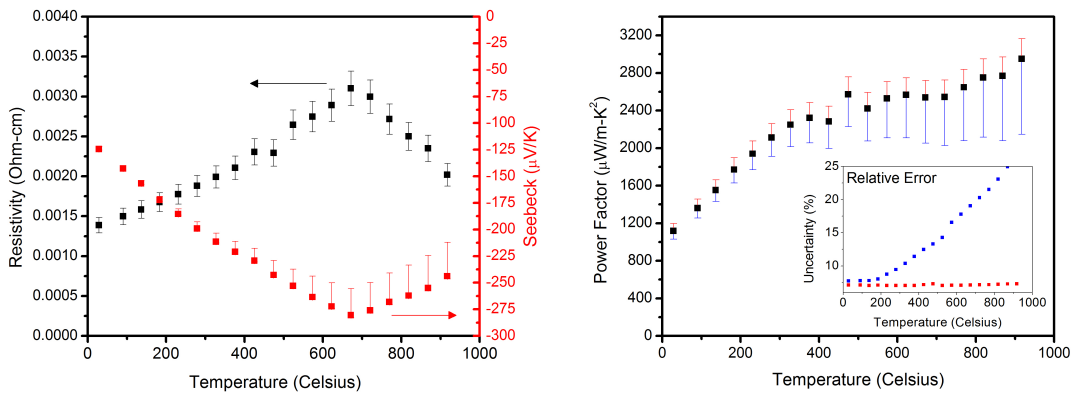


Figure 7.9: Electrical resistivity and Seebeck coefficient data (Left) and power factor (Right) with uncertainty. Data measured on a 2 at% P doped 80/20 Si/Ge sample.

be reported with an uncertainty of $+7.3\%/-27.0\%$. Thus, any figure of merit calculation will have at a minimum the same uncertainty as the power factor. In fact, due to the difficulty of measuring thermal conductivity the final uncertainty on the figure of merit will likely be noticeably larger than the values reported here. It should be pointed out that these uncertainty values are strongly dependant on the assumed values in tables 7.1 and 7.2. With careful measurement practice, many of the assumed values will be reduced or neglected, resulting in a lower final uncertainty.

7.6 Conclusion

An uncertainty analysis has been performed on a common Seebeck and electrical resistivity measurement configuration used for thermoelectric characterization. This analysis highlights the largest contributing sources of uncertainty in the configuration, and offers insight into obtaining reliable data. The results indicate that the

largest factors on electrical resistivity include the thermocouple tip radius, sample uniformity, and probe separation length. Using reasonable estimates on these sources of uncertainty it has been calculated that typical samples measured with the described configuration contain uncertainty of $\pm 7.0\%$ across any measurement temperature. The uncertainty on Seebeck coefficient has been demonstrated to be temperature dependent, and asymmetric. At high temperature the largest contribution is the cold-finger effect with DAQ temperature uncertainty and wire Seebeck variation significant at lower temperatures. The Seebeck coefficient of the configuration is $+1.0\%/-13.1\%$ at high temperature and $\pm 1.0\%$ near room temperature. The power factor has a combined uncertainty of $+7.3\%/-27.0\%$ at high temperature and $\pm 7.5\%$ near room temperature. Any figure of merit calculations performed using this type of measurement system should include at a minimum these ranges on all data.

CHAPTER VIII

WSi₂-Si_{1-x}Ge_x COMPOSITES: PROCESSING AND THERMOELECTRIC PROPERTIES

8.1 Introduction

This chapter discusses the design of a new high temperature thermoelectric material system based on the classic silicon germanium system. The chapter investigates different composites of WSi₂ in a matrix of doped silicon and germanium. The system was investigated using both i) melt/solidification techniques and ii) powder metallurgy techniques. A better understanding of the system was possible by investigating both fabrication techniques. Using the materials synthesized by powder metallurgy a proof-of-concept two-couple device was built, see Appendix A. The modeling work of Chapter 4 has been applied to the materials of this chapter as a demonstration of typical values, see Chapter 5 for design calculations.

8.2 System Background

The traditional high temperature thermoelectric material has been silicon germanium since the work by NASA on RTGs in the 1960s and 1970s. The system is stable to temperatures of 1000 °C, does not have sublimation challenges like other

thermoelectrics, and is mechanically robust. The classic silicon germanium system is a zone-leveled $\text{Si}_{80}\text{Ge}_{20}$ composition doped to less than 2 at% with B for p-type and P or As for n-type, the system exhibits peak ZTs of 0.5 for p-type and 1.0 for n-type [103, 106]. Recent work in nano-structuring has improved the figure of merit by introduction of nano-sized grains in a spark plasma sintered Si/Ge sample [128, 129]. Several groups have identified the possibility for improvement to Si/Ge through the introduction of a nano-precipitate silicide phase, most notably Mingo et al. [130–135]. The introduction of a thermally stable silicide nano-precipitate into a Si/Ge matrix provides the opportunity to scatter phonons preferentially over electronic charge carriers. As a result the thermal conductivity may be reduced through a reduction in the lattice component, while leaving the electrical conductivity unaffected. Experimental work on the nano-precipitate in Si/Ge approach has been reported for the $\text{Si}_{80}\text{Ge}_{20}\text{B}_6\text{-Er}$ [136], $\text{Si}_{80}\text{Ge}_{20}\text{-CrSi}_2$ [137], and $\text{Si}_{92}\text{Ge}_8\text{-MoSi}_2$ [138] systems. This chapter will introduce a study on the introduction of tungsten silicide (WSi_2) into a $\text{Si}_{1-x}\text{Ge}_x$ matrix.

8.3 Solidification Processing

Directional solidification of off-eutectic and eutectic-compositions is well-known to yield self-assembled microstructures that are non-achievable by solid state sintering. The self-assembled structure can be controlled or engineered by process variables and material volume fraction. Additionally, formation of low energy coherent interfaces and textured/oriented microstructures often occur by directional solidification.

Unfortunately directional solidification is not well suited to obtain the desirable nano-structured materials, as grain growth is promoted by the long solidification time.

Due to their abundance, low cost and low toxicity, metal silicides have been investigated as potential high temperature TE materials [189]. A recent work that has focused on Mg-Si alloys achieved $ZT > 1$ [95]. We have investigated directional solidification of a number of M/Si and M/Si/Ge (where M = Ti, Mo, W, Cr, Zr, Ta, V) systems [190]. Directional solidification in these systems does not yield an alloy containing nanoparticles. However, the W/Si/Ge system exhibits good TE properties.

Investigation centered on minor addition of W (≥ 3 at%) to $\text{Si}_x\text{Ge}_{1-x}$ alloys. The W addition forms metallic WSi_2 inclusions with a melting point of 2437 K. Metallic inclusions in thermoelectric materials are an untraditional approach for TE composites. The work shows that the addition of WSi_2 can reduce Ge content by 50% for optimal thermoelectric performance.

Directional solidification was accomplished using the vertical Bridgman method. Starting materials for ingot preparation were 5 mm silicon granules (Cerac, Milwaukee, WI, $\geq 99.9\%$), 100 mesh germanium powder (Alfa Aesar, Ward Hill, MA, $\geq 99.9\%$) and 100 mesh tungsten powder (Alfa Aesar, $\geq 99.9\%$). Alloys were melted in a helium atmosphere in a graphite resistance heated furnace (Thermal Technology LLC, Santa Rosa, CA). Boron nitride (BN) (Momentive Performance Materials, Albany, NY) and fused silica (SiO_2) (Momentive Performance Materials, Albany, NY) crucibles were used. Calcium chloride (CaCl_2) was added to the SiO_2 crucible as an

interfacial material between crucible and melt; eliminating mechanical failure of the crucible during sample cooling [153]. Ingots were prepared through two solidification runs. The first solidification served to consolidate the raw material into an ingot. Processing temperatures ranged from 1798 K to 1973 K with soak times of 1-3 hours. After the first solidification, additional raw material was added to achieve a 30-40 g sample with approximate dimensions of 20 mm in length and 22 mm in diameter. The second solidification included directional solidification with a pull rate of 200 mm/hr over the temperature gradient that naturally exists in the furnace. The measured temperature gradient was 8.5 K/mm. The high pull rate is greater than the pull rates recommended (<10 mm/hr) to avoid constitutional undercooling [115]. It should be noted that zone leveling was not performed on the specimens presented in this work; rather the specimens were investigated as obtained at the completion of the second solidification run. Table 8.1 summarizes the nominal compositions of ingots solidified in this work.

8.3.1 Microstructure

All specimens showed similar microstructures, an example of which is shown in the back-scattered SEM micrograph in Figure 8.1 (taken at 15 kV) for an alloy containing 0.9 at% W and 9.3 at% Ge (Sample 3 in Table 8.1). Chemical mapping by EDS is also added to show the Si, Ge and W distribution in the microstructure. Large 10 to 100 μm faceted precipitates were observed in the matrix. Chemical map shows that the entire W content is contained within the precipitates. Precipitates were identified as

Table 8.1: Nominal compositions of the specimens studied

Sample	Si	Ge	W	Si	Ge	W
#	(at%)	(at%)	(at%)	(wt%)	(wt%)	(wt%)
1	99.2	0.0	0.8	95	0	5
2	94.8	4.3	0.9	85	10	5
3	89.8	9.3	0.9	75	20	5
4	84.3	14.9	0.8	66	30	4
5	82.4	14.6	3.0	59	27	14
6	77.6	19.4	3.0	53	34	13
7	72.7	24.3	3.0	47	40	13

WSi₂ via XRD (Fig. 8.2). Determination of crystal growth habits was not integral to this investigation. Solidified microstructures are irregular with very little indication for preferred ordering of the WSi₂ phase. The solidification parameters inevitably lead to a considerable amount of Ge segregation resulting in a non-uniform matrix as shown in Figure 8.1. Although Si and Ge exhibit complete solid state solubility, it is well known that solidification is non-congruent with the melt [13]. Local Ge concentration content was determined through standard less EDAX ZAF quantification. For sample 3, with a nominal 9.3 at% Ge content, the Ge segregation ranged from 6.4 to 15.6 at% Ge. Although Ge segregation is intrinsic from the solidification process, The Ge rich areas of the samples tend to coincide near or surrounding the

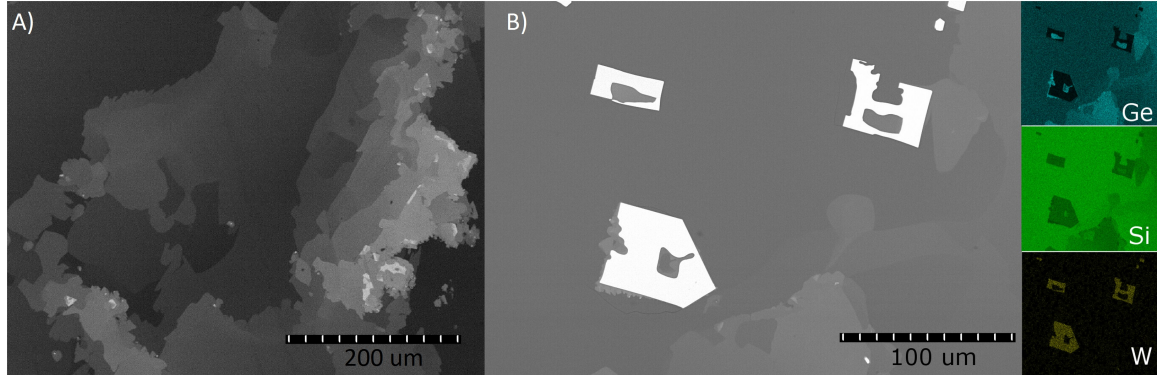


Figure 8.1: Back-scattered SEM images (A and B) with EDS chemical maps (Right) of Ge, Si, and W. Large WSi_2 precipitates (white faceted precipitates) are in an inhomogeneous Si/Ge matrix.

WSi_2 precipitates. In the micrograph shown (Fig. 8.1) the areas with the highest Ge concentration are either adjacent to, or enclosed by the WSi_2 precipitates. This is likely due to a Ge rich boundary layer that forms as Ge was rejected from the WSi_2 precipitates during crystallization. Thus, this silicide precipitation aids in Ge driven micro-segregation which may help explain some of the composite properties introduced later in section 8.4. Thermoelectric properties. Figure 8.2 shows powder XRD pattern for $\text{Si}_{89.8}\text{Ge}_{9.3}\text{W}_{0.9}$ (Sample 3). XRD of a melt derived $\text{Si}_{90}\text{Ge}_{10}$ is included for comparison. Both samples have the same Si/Ge ratio and were solidified under identical conditions. Additional peaks present in the W containing sample correspond to tetragonal WSi_2 precipitates. The XRD patterns shown in Figure 8.2 are typical for all the W/Si/Ge compositions investigated.

Rietveld refinement was performed using Topas (Bruker) software. The WSi_2 phase was analyzed over a 2θ range of 30° to 45° to exclude reflections from the

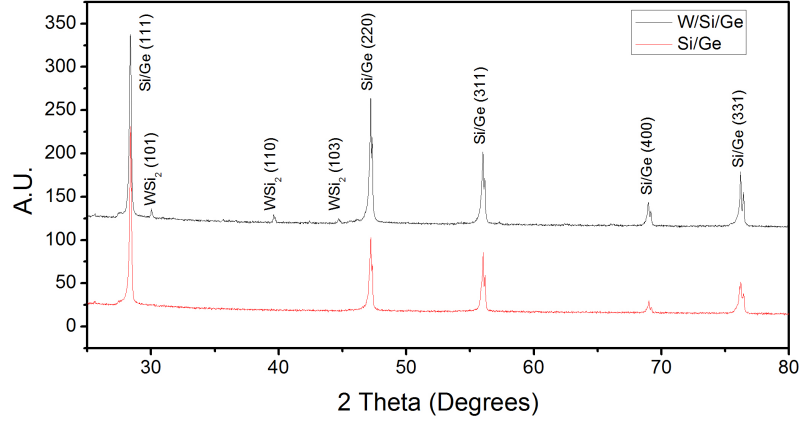


Figure 8.2: Pattern for Sample 3, $\text{Si}_{89.8}\text{Ge}_{9.3}\text{W}_{0.9}$ (top), and $\text{Si}_{90}\text{Ge}_{10}$ (bottom), addition of W component forms WSi_2 second phase with no shift in Si/Ge reflections [191, 192].

$\text{Si}_x\text{Ge}_{1-x}$ phase. Data was acquired in a Bragg-Brentano configuration with 300 mm radius, 4° sollers, at a rate of 3.5° per min. The model had a R_{exp} value of 4.51 and GOF value of 1.27, lattice parameters and Lorentzian crystallite domain size were the parameters of study in the model. The data analysis shows crystallite domain size of 238 nm with tetragonal lattice parameters of $a = b = 0.321$ nm and $c = 0.783$ nm. The measured lattice parameters match the reported values for WSi_2 , $a = b = 0.32138$ nm and $c = 0.78299$ nm [191]. XRD results indicate that the large WSi_2 precipitates are polycrystalline. The $\text{Si}_x\text{Ge}_{1-x}$ matrix could not be accurately represented by the model, making quantitative phase analysis impractical [192]. Model failure arises from compositional peak broadening due to Ge segregation. The compositional fluctuations cause fluctuations in lattice constant which creates strain and dislocations. Thus, crystallite size and lattice strain could not be de-convoluted from the XRD data for the Si/Ge matrix. A more advanced fitting technique must be employed in order to

account for the peak broadening due to the range of alloying present, such a model has been presented in the work of Leineweber and Mittemeijer [193]. The average matrix lattice parameter from the $\text{Si}_x\text{Ge}_{1-x}$ peak positions revealed predominate cubic lattice parameter of 0.544 nm for both compositions. This $\text{Si}_x\text{Ge}_{1-x}$ lattice parameter is in good agreement with the work of Dismukes et al. [103], reporting a lattice parameter for $\text{Si}_{90}\text{Ge}_{10}$ composition as 0.545 nm. The introduction of W into the system had no observable effect on the lattice spacing of the bulk matrix, suggesting that little to no W is soluble into the $\text{Si}_x\text{Ge}_{1-x}$ matrix.

Jackson and Hunt [194] developed a method to predict eutectic microstructures based upon entropy of fusion. Theory states that phases with high entropy of formation (ΔS_f) form faceted interfaces when $\Delta S_f/R > 2$ (where R=gas constant). The entropies of formation of interest in this system are roughly ΔS_{Si} 30 J/K-mol, ΔS_{Ge} 30 J/K-mol [195], and ΔS_{WSi_2} 18 J/K-mol [196]. The dimensionless $\Delta S_f/R$ values are >2 , Si and Ge exhibiting $\Delta S_f/R$ of 3.6 and 2.1 for WSi_2 , crystal growth favors faceted precipitates. Growth direction of the faceted phase is determined by the specific crystallographic orientations. Thus, directional growth is not necessarily controlled by the thermal gradient of solidification. We have observed a large number of Si systems that exhibit faceted growth: Si-MoSi₂, Si-Ge-MoSi₂, Si-ZrSi₂, Si-VSi₂ and Si-TaSi₂. Contradictory to Jackson and Hunt model, rod growth has been reported for Si-TiSi₂ [190] and Si-CrSi₂ [197].

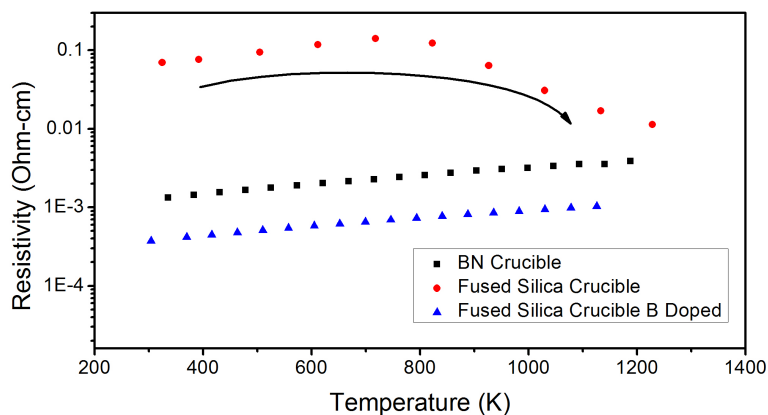


Figure 8.3: Electrical resistivity of three comparable samples prepared using BN or SiO₂ crucibles. Trend indicates un-intentional doping resulting from the BN crucible.

8.3.2 Crucible Selection

The crucible selection was a critical process parameter. All specimens were solidified under identical parameters using BN and SiO₂ crucibles. In order to prevent reaction between SiO₂ crucible and W/Si/Ge melts, 1.5 g of CaCl₂ powder was added to the charge. Liquid CaCl₂ forms a barrier between the melt and SiO₂ crucible, which eliminated fracturing of the ingot during cooling. Residual CaCl₂ on the ingot surface was removed by rinsing with water [153].

Figure 8.3 shows the temperature dependent resistivity data for sample 3 (Si_{89.8}Ge_{9.3}W_{0.9}) solidified in BN and SiO₂ crucibles. The Si_{89.8}Ge_{9.3}W_{0.9} alloy processed in SiO₂ crucible exhibits a high electrical resistivity and extrinsic to intrinsic semiconductor behavior around 773 K. In conjunction with extrinsic to intrinsic electrical transport behavior, the alloy transitioned from p-type to n-type Seebeck behavior. However, the same alloy processed in BN crucible exhibited a lower electrical

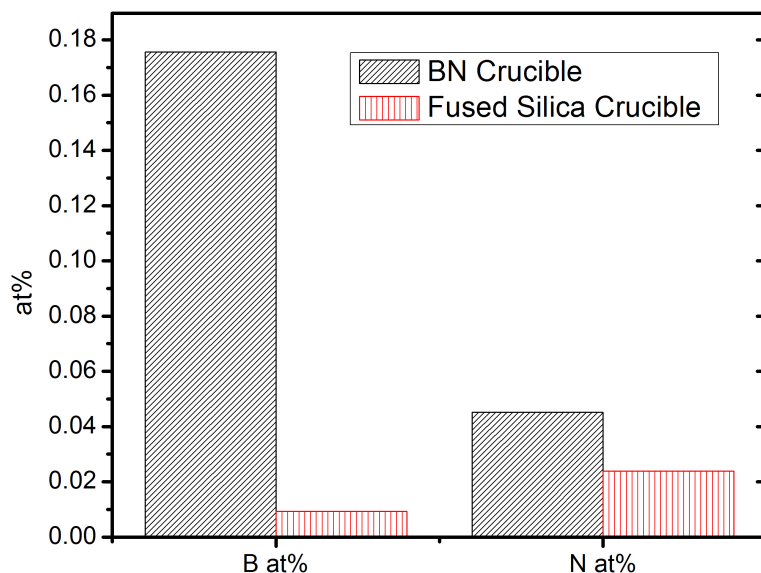


Figure 8.4: Composition for ingots prepared in BN and SiO₂ crucibles as determined by ICP and Nitrogen determination. Samples are not intentionally doped.

resistivity and p-type extrinsic semiconductor behavior over the measured temperature range. Thus, electrical behavior is consistent with B doping.

Chemical analysis of the specimens was performed to provide B and N concentrations. Figure 8.4 shows that sample 3 (Si_{89.8}Ge_{9.3}W_{0.9}) processed in a BN crucible had significantly higher B content (0.17 at%) than the specimen derived from the SiO₂ crucible (0.009 at%). The N content was low (≤ 0.04 at%) but it was twice as high for the sample derived from BN crucible. The B concentration from the sample derived from the fused silica crucible was unexpected. The most probable cause was the CaCl₂, purity level was 99%. Chemical analysis of the W raw powder showed 0.0003 at% B impurity. The B level in the Si and Ge starting materials was below the instrument detection limit. B was not observed in the microstructure as either

B precipitate or within the matrix, especially near the BN-melt interface. XRD also displayed no evidence of second phases formed due to B contamination or lattice parameter shift. Optimizing the B content can be beneficial in optimizing the TE properties in the W/Si/Ge system. To emphasize this point a third specimen was prepared by intentional doping of $\text{Si}_{89.8}\text{Ge}_{9.3}\text{W}_{0.9}$ with 1.9 at% B and processed in SiO_2 crucible; the electrical resistivity is also shown as a function of temperature in Figure 8.3. The temperature dependent electrical resistivity behavior is similar to the ingot processed in BN crucible, exhibiting extrinsic semiconductor behavior for the whole temperature range. The absolute values of the electrical resistivity were lower due to the larger B-doping.

The rest of this section focuses on specimens processed in BN crucibles. For consistency, all BN crucibles were filled to the same levels and subjected to similar solidification profiles. This ensured the contact area, and dopant diffusion kinetics were comparable between samples. Additionally, the thermodynamic solubility limit of B in Si serves to provide a consistent upper limit. Typical RTG samples are doped to the solubility limit, as dopant segregation is a commonly reported phenomenon [112, 198]. Since the electrical properties of these samples are similar to RTG properties, the doping levels provided by the crucibles are also likely to be near the solubility limit. As a result the sample set is believed to have comparable doping levels, although a controlled doping scheme using SiO_2 crucibles may be preferable for future work.

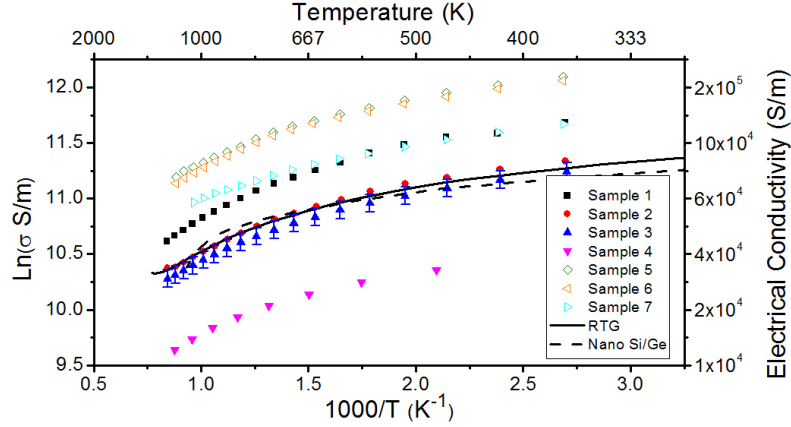


Figure 8.5: Arrhenius plot of electrical conductivity of several W/Si/Ge samples. Closed symbols represent 0.8 at% W, open symbols 3 at% W. Included are published values for RTG [106] and nano-structured [128] $\text{Si}_{80}\text{Ge}_{20}$ alloys.

8.4 Solidification Thermoelectric Properties

Figure 8.5 shows an Arrhenius plot of electrical conductivity as a function of temperature and composition for all samples processed in BN crucibles. Reported results for p-type $\text{Si}_{80}\text{Ge}_{20}$ are also included in Figure 8.5 for melt derived RTG (zone leveled) [106] and sintered nano-structured materials [128]. The temperature dependent behavior of electrical conductivity was very similar to published results for p-type B doped $\text{Si}_{80}\text{Ge}_{20}$. With increasing temperature the electrical conductivity decreased over the temperature range of 373-1273 K. Composition did not have any effect on the temperature dependent behavior. All the samples exhibited the characteristics of a degenerate semiconductor, metal like σ -T relationship. None of the samples exhibit intrinsic conduction behavior up to 1273 K, the instrumentation limit. For clarity, data uncertainty was calculated for sample 3 and represents typical measurement

uncertainty for all samples. Typical uncertainties are on average $\pm 7.9\%$, with details covered in Chapter 6 and Appendix B. The observed trend in electrical conductivity for the investigated compositions is a uniform reduction in conductivity with increasing Ge concentration (Specimens 1-4 shown with solid symbols, Figure 8.5) at a given W concentration (0.8 at%). This trend can be understood from the disorder introduced in the matrix as Ge occupies Si lattice sites. Ge on Si sites introduce fluctuations in lattice potential, strain and crystalline defects that result in an extra electron scattering term, which is proportional to the fraction of Ge in the alloy [119]. Alloy scattering is non-existent for sample 1 containing no Ge, exhibiting a higher electrical conductivity than Ge containing samples. Samples 2-4 have increasing levels of Ge content where alloy scattering caused a uniform reduction in electrical conductivity. On average electrical conductivity decreased 68.2% with an increase of Ge content from 0 to 14.9 at% Ge. The samples containing 4.4 and 9.3 at% Ge (samples 2 and 3) exhibit similar electrical conductivity to the published data for both zone-refined and nano-structured p-type $\text{Si}_{80}\text{Ge}_{20}$ [106, 128].

Increasing the W content increased the electrical conductivity (Samples 4 and 5) at similar Ge concentrations. Increasing the W at% content from 0.8% to 3% (shown with open symbols, Figure 8.5) resulted in an enhancement of 79% in the electrical conductivity on average. Er additions to Si have been reported by Zhao et al. to enhanced electrical conductivity [136]. The work of Nonomura et al. has reported WSi_2 to be a narrow gap p-type semiconductor with an activation energy of 0.005 eV and electrical conductivity of 2.5×10^4 S/m near room temperature [199].

The reported electrical conductivity of WSi_2 is lower than all the samples measured in this work. Therefore, the increase in electrical conductivity observed between samples 4 and 5 cannot be explained directly by the presence of the WSi_2 phase. The trend is instead believed to be due to the change in carrier density as a result of the two W levels. Samples 1-3 with 0.8 at% W have carrier densities ranging from $1.2 \times 10^{20} \text{ cm}^{-3}$ to $2.9 \times 10^{20} \text{ cm}^{-3}$ while sample 5 with 3 at% W has $8.5 \times 10^{20} \text{ cm}^{-3}$. As discussed in the previous microstructure section the W is only observed in the precipitates and is not detected in the matrix. Therefore, the carrier density difference may be a result of the silicide phase influencing the solubility limit and kinetics of B in the $\text{Si}_x\text{Ge}_{1-x}$ matrix. Further work is needed to elucidate the enhanced transport mechanism.

The effect of Ge content on the electrical conductivity shows some dependence on W content. In both W cases, there is an optimal Ge concentration and higher Ge concentrations lead to reduction in electrical conductivity. The higher W concentration allows higher Ge addition. Thus, the data shows that a combination of WSi_2 and Ge additions can control electrical conductivity. Reduction in Ge content helps in reducing material cost.

The temperature dependence of Seebeck coefficient for the same set of samples is shown in Figure 8.6. All samples exhibited p-type behavior over the temperature range investigated. The measured values fell in the range of 70 to 300 $\mu\text{V}/\text{K}$. Seebeck coefficient increased with temperature; typical behavior for a degenerate extrinsic semiconductor. For clarity, uncertainty in the data is reported for sample 3 and represents typical uncertainties of all samples. The uncertainty accounts for the

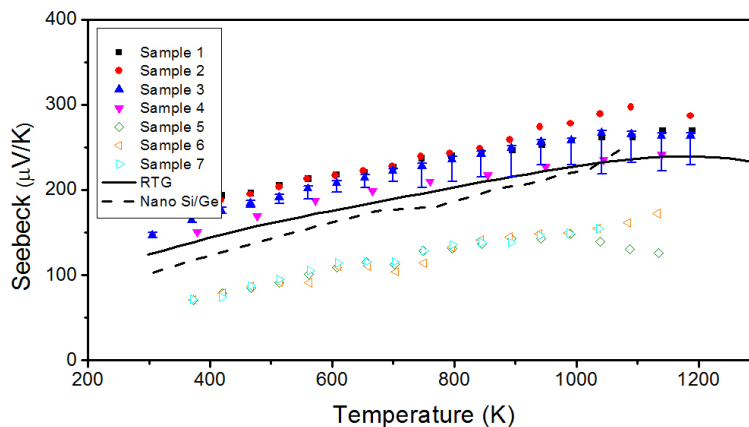


Figure 8.6: Seebeck coefficient of several W/Si/Ge samples. Closed symbols represent 0.8 at% W, open symbols 3 at% W. Included are published values for RTG [106] and nano-structured [128] $\text{Si}_{80}\text{Ge}_{20}$ alloys.

probe wire Seebeck uncertainty, statistical variation, multimeter uncertainty, and the cold finger effect. The cold finger effect is an artifact of the four point measurement configuration, in which heat is parasitically transferred down the probe length. The effect leads to an over-estimation of the Seebeck coefficient. The total uncertainty was estimated with a thermal FEA along with standard measurement error propagation. The uncertainty ranges from $\pm 2\%$ near room temperature to $+2\% - 17\%$ at high temperature. The asymmetry of the uncertainty at high temperature is due to the cold finger effect. The 0.8 at% W samples (shown with solid symbols, Figure 8.6) all exhibit Seebeck coefficients higher than published values for p-type $\text{Si}_{80}\text{Ge}_{20}$ [106, 128]. At low temperature the Seebeck coefficients decrease slightly with increasing Ge content (samples 1-4). The high Seebeck coefficient combined with comparable electrical conductivity leads to power factor improvements as large as 50% over RTG. Seebeck enhancement of PbTe has been discussed by Faleev and Leonard [200] by introducing

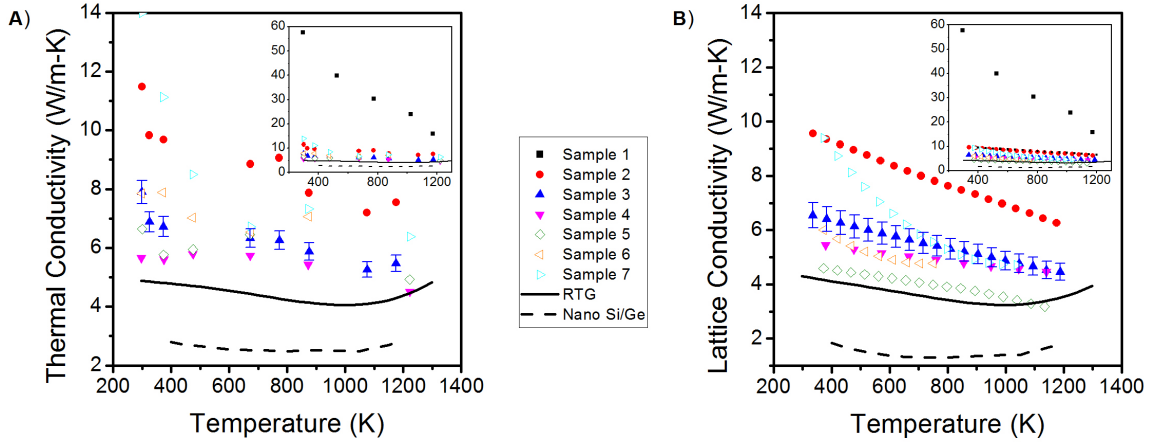


Figure 8.7: A) Total thermal conductivity of several W/Si/Ge samples. B) Calculated lattice thermal conductivity component. Closed symbols represent 0.8 at% W, open symbols 3 at% W. Included are published values for RTG [106] and nano-structured [128] $\text{Si}_{80}\text{Ge}_{20}$ alloys.

metallic precipitates into a PbTe matrix. Band bending at the interface can filter low energy electrons and leave high energy electrons undisturbed, leading to enhanced Seebeck coefficient and power factor for the composite. This observed trend due to electron filtering phenomenon was dependent on precipitate size and can therefore not explain the trend observed in this micron-scale system. Further work is required to understand the dependence of carrier concentration and mobility with temperature. At this time the enhancement of power factor is not clearly understood. The 3 at% W samples (shown with open symbols, Figure 8.6) have lower Seebeck coefficients than the 0.8 at% samples. The decrease is consistent with carrier concentration data, which is higher for the 3 at% W samples.

Figure 8.7 shows the total thermal conductivity of the compositions investigated and the lattice thermal contribution calculated by the Wiedemann-Franz law. Uncertainty on total thermal conductivity is estimated to be $\pm 5\%$ [159]. The uncertainty in lattice thermal conductivity is calculated based on both the electrical conductivity and the thermal conductivity. The data shows that WSi_2 is not effective in reducing thermal conductivity; Sample 1 exhibit thermal conductivity 57.7 to 15.5 W/m-K in the temperature range of 295-1173 K (Figure 8.7). The addition of Ge is effective in reducing the thermal conductivity significantly over the entire temperature range of interest; the inset shows that Ge; reduced the thermal conductivity to <12 W/m-K. After the initial large reduction in thermal conductivity, smaller reductions were obtained with by increasing Ge concentration, samples 2-4. However, there was no observable trend in thermal conductivity with higher Ge concentrations.

A least squares regression was used to interpolate thermal conductivity data in order to calculate the lattice thermal contribution and ZT . The correlation coefficient of the thermal data ranges from 0.76 to 0.98, the statistical uncertainty of the measurement data is understood to provide low correlation, but the regression is still thought to provide accurate averages for the purpose of calculating figure of merit and lattice contribution. A more complicated fitting method would model the statistical variation of the measurement rather than focusing on capturing the representative values. The Wiedemann-Franz law estimates the lattice contribution of thermal conductivity as

$$k_l = k - L\sigma T, \quad (8.1)$$

$$L = \frac{\pi^2 k_b^2}{3e^2}, \quad (8.2)$$

where k_l is the lattice thermal contribution, k the total thermal conductivity, T the temperature, σ the electrical conductivity, and L Lorenz number. The Lorenz number is classically approximated from k_b the Boltzmann constant and the charge of an electron e , $L = 2.44 * 10^{-8} W\Omega K^{-2}$.

Lattice thermal conductivity decreased significantly with the initial increase in Ge content. As the Ge content increased further, samples 2 to 4, smaller reductions in the lattice thermal conductivity was observed, with values almost unchanged between specimens 3 and 4 for the whole temperature range. The trend is understood as a result of phonon scattering by the mass difference of Si and Ge [101–103, 114]. Increasing the W content, sample 4 to 5, resulted in a minor decrease in lattice thermal conductivity; as the total thermal conductivity remained similar despite increasing electrical conductivity. The alloy composition with the lowest lattice thermal conductivity was specimen 5 with values similar to the lattice thermal conductivity of published data for p-type RTG Si₈₀Ge₂₀ [106]. The higher lattice thermal conductivities of the samples, as compared to RTG, were due to a combination of the lower Ge content and the observed micro-segregation in the samples (Figure 8.1). The work of Lee and Hwang [134] theoretically demonstrated the importance of homogeneous

Table 8.2: Calculated thermal conductivity of WSi₂-Si/Ge samples

Sample #	Si in Matrix at%	Silicide vf%	Thermal Conductivity (W/m-K) at 300 K			
			Matrix	Precipitate	Composite	Measured
1	100.0	1.7	59.6	46.6	59.3	60
2	95.6	1.8	14	46.6	14.2	12
3	90.5	1.9	8.8	46.6	8.96	8
4	84.8	1.7	6.8	46.6	6.91	6
5	84.0	6.5	6.8	46.6	7.26	7
6	78.7	6.4	4.8	46.6	5.15	8
7	73.4	6.4	4.4	46.6	4.72	14

segregation of the Si/Ge matrix. In the simulations of Lee and Hwang, clusters of Ge atoms were found to significantly increase the thermal conductivity, as clusters of Ge atoms reduced the number of Si-Ge bonds which provided the desired phonon scattering. Increases as large as $3\times$ were calculated for Ge precipitates of 2 nm [134]. The trend in samples 5-7 was counter intuitive as conductivity increases with increasing Ge content. The behavior may be a result of increased micro-segregation of the Ge as a result of the higher 3 at% W phase. In the previous section (Microstructure) Ge segregation was observed to be correlated with the silicide precipitates. The higher W content may be driving more Ge micro-segregation, leading to increased conductivity.

The 10-100 μm scale of precipitates and low volume fraction of the composites allows for a straight-forward estimation of the thermal conductivity. The precipitate/matrix interface surface area, normalized with bulk volume, was estimated to be $10\text{ cm}^2/\text{cm}^3$ for the samples in this study. To provide a contrast, the surface area per volume of a nano-structured composite containing 10 nm precipitates has on the order of $1 \times 10^5\text{ cm}^2/\text{cm}^3$. The surface area is calculated employing the range of volume fractions for the samples in this work. The influence of phonon scattering at the interface of the silicide precipitates should be negligible for the samples of this work. Therefore a straight-forward estimation of thermal conductivity can be based on considering the samples as composite bodies of two phases, the $\text{Si}_x\text{Ge}_{1-x}$ matrix and WSi_2 precipitates. As previously discussed, the thermal conductivity of the matrix will be strongly dependant on the alloying level of $\text{Si}_x\text{Ge}_{1-x}$ [101–103, 114]. Additionally, the dopant level will have a large influence on thermal conductivity as point scattering inhibits phonon transport. To gain a deeper understanding, without unneeded complexity, the matrix of the samples is assumed to be homogeneous, i.e. no micro-segregation of $\text{Si}_x\text{Ge}_{1-x}$, with doping levels comparable between samples. The precipitates are modeled as a periodic arrangement of tungsten silicide cubes with side length (d) of $50\text{ }\mu\text{m}$. Figure 8.8 shows the simplified model of the composite, with the repeating unit highlighted. The geometry of the repeating unit (captured by x and the precipitate size d) is a function of the area fraction (γ) of the precipitate phase, which can be estimated from the nominal volume fraction of the silicide phase.

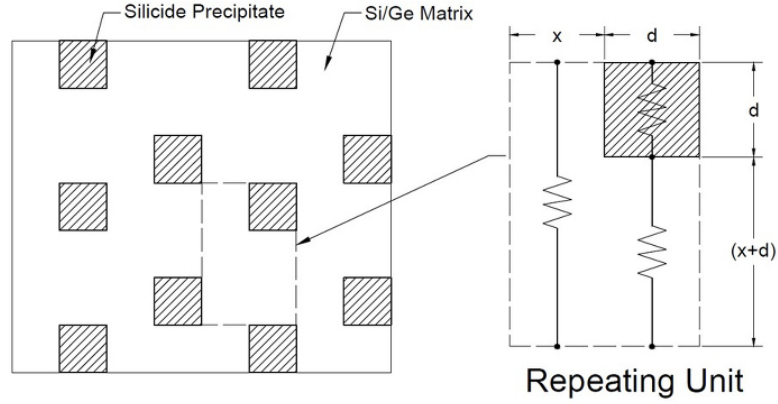


Figure 8.8: Schematic diagram of Si/Ge matrix with silicide precipitate. Repeating unit highlighted to the right to outline the geometric parameters x and d .

$$x = \frac{d(\sqrt{4 + \gamma} - 3\sqrt{\gamma})}{2\sqrt{\gamma}}, \quad (8.3)$$

$$k_{Composite} = \frac{2d + x}{d + x} \left(\frac{xk_{Matrix}}{2d + x} + \frac{1}{\frac{d+x}{dk_{Matrix}} + \frac{1}{k_{Precipitate}}} \right). \quad (8.4)$$

The composite thermal conductivity can be estimated by considering the series/parallel nature of the components of the repeating unit. The method employed is classically used for the analysis of composite bodies under steady thermal conduction [149]. Table 8.2 shows the predicted influence of the silicide phase on the samples. The silicon at% used for the calculations are the nominal level of silicon minus the silicon consumed by the silicide phase. These levels compare well to average values measured with EDS. The matrix thermal conductivity is calculated based on the experimental work of Maycock [114]. The silicide volume fraction is used to establish the geometry of the model. For sample 1 the matrix is 100% Si and the

nominal silicide volume fraction is 1.7%, Table 8.2. As a result of the volume fraction the model x parameter is calculated to be $307 \mu\text{m}$. The calculated composite conductivity 59.3 W/m-K is lower than the matrix conductivity 59.6 W/m-K , as a result of the relatively lower conductivity of the precipitate phase 46.6 W/m-K . The calculated conductivity for sample 1 matches reasonably well with the measured value 60 W/m-K . For the remaining samples 2-7 the calculated composite conductivity are higher than the matrix conductivity as a result of the precipitates. The precipitate driven increase in thermal conductivity is undesirable for these samples, but the calculation shows an average increase of 1.6% for the 0.8 at% W samples and 7.1% for the 3 at% W samples. Compared to the 50% improvement of electrical properties the WSi_2 precipitates are found to be desirable. For samples 1-4 the calculated composite conductivities compare well with the measured data, while samples 5-7, with 3 at% W, show poor comparison between the model and the actual data. The deviation could be explained by the Ge micro-segregation driven by the WSi_2 phase. Ge micro-segregation is well known to drastically alter thermal conductivity [134] and is unaccounted for in the matrix conductivity of the model.

The figure of merit is shown in Figure 8.9. Similar to $\text{Si}_{80}\text{Ge}_{20}$ alloy, the ZT increases in value over the measured temperature range. Trends in Seebeck coefficient as a function of composition dominated the trends in the calculated ZT values for a given W content. ZT maximized for the specimen 3 for the whole temperature range. At higher Ge contents (samples 5-7) the ZT did not change in any significant amount similar to the observations in Seebeck coefficient. However, electrical conductivity

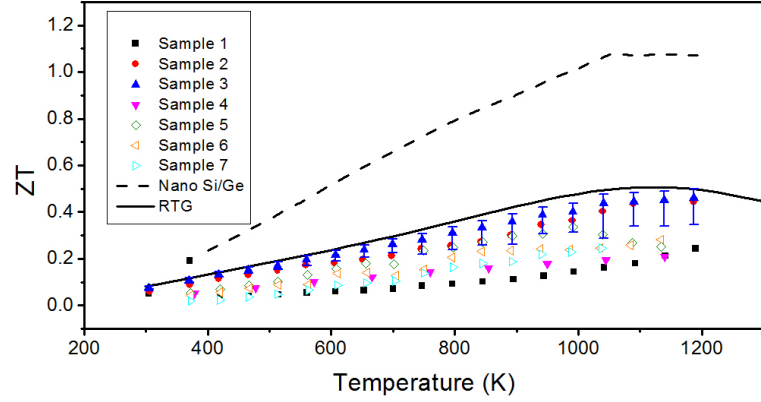


Figure 8.9: Figure of merit (ZT) of several W/Si/Ge samples. Closed symbols represent 0.8 at% W, open symbols 3 at% W. Included are published values for RTG [106] and nano-structured [128] $\text{Si}_{80}\text{Ge}_{20}$ alloys.

was the dominant factor in deciding the trends in ZT as a function of W content; thus the ZT increased slightly with increasing W content, samples 4 to 5, despite a decrease in Seebeck coefficient. This was due to the greater increase in electrical conductivity even though the ZT changes with square of Seebeck coefficient. The optimal composition from this investigation with a ZT near RTG was 0.8 at% W/9.3 at% Ge (Sample 3). This sample was created without the need for lengthy, thus costly, zone leveling. The results suggest that W addition can reduce the use of expensive Ge component of the alloy.

8.5 Powder Processing

Increased figure of merit can be achieved by enhancing the power factor ($S^2\sigma$) or by reducing the thermal conductivity k , specifically the lattice portion of thermal conductivity. Nano-structuring has been proposed and demonstrated to be an effec-

tive means of enhancing figure of merit, both with increasing power factor resulting from quantum confinement and reducing lattice thermal conductivity from phonon scattering [125]. Both theoretical and experimental work has been completed on a number of thermoelectric systems by introducing nano-structuring. Proof of principal work has been performed on several systems such as PbTe [201], InGaAs [202], and Bi₂Te₃/Sb₂Te₃ superlattice [60]. Theoretical work of Mingo et al. demonstrates the possibility of obtaining significant reductions in thermal conductivity of an alloyed Si/Ge matrix by phonon scattering from nano-silicide inclusions [130]. The silicide inclusions in the alloyed matrix serve to scatter phonons preferentially over electrical charge carriers, causing a significant reduction in thermal conductivity which increases ZT. Such nano-structuring or introduction of scatterers can specially be designed to tune phonon dispersion to scatter the dominant phonon wavelength. Inclusion size and size-dispersion become design parameters and material processing challenges. Modeling predicts an optimum range of 2-10 nm, but significant reduction is still predicted for inclusion sizes as large as 30 nm [130, 135].

Reported here is the investigation of these critical thermoelectric transport properties in the W/Si/Ge system. Our previous work on solidification in the W/Si/Ge system produced large micron-sized WSi₂ inclusions that improved electrical performance but did not improve ZT. Motivated from our previous work and theoretical work, powder processing techniques were pursued to achieve nano-sized WSi₂ inclusions in a Si/Ge matrix. The results show that nano-sized WSi₂ inclusions can improve the thermoelectric performance of both n- and p-type Si/Ge by as much as

30%. The improvements are the result of reductions in lattice thermal conductivity as large as 40% (compared to a benchmark silicide free sample).

WSi₂-Si/Ge alloys were synthesized by mechanical alloying (MA) and consolidated by spark plasma sintering (SPS). Starting materials included: i) 3-5 mm Si granules ($\geq 99.96\%$, Cerac, Milwaukee, WI), ii) 100 mesh Ge powder ($\geq 99.999\%$, Alfa Aesar, Ward Hill, MA), iii) 1 μm W powder ($\geq 99.95\%$, Alfa Aesar), iv) >70 nm nano-W powder ($\geq 99.95\%$, US Research Nanomaterials, Houston, TX), v) 100 mesh P powder ($\geq 99\%$, Alfa Aesar), and vi) 325 mesh B powder ($\geq 99\%$, Alfa Aesar). MA was performed under an argon atmosphere in a Retsch planetary mill using 150 ml tungsten carbide vials (Retsch, Haan, Germany) and 30 count 10 mm tungsten carbide milling media (Retsch). Alloy compositions were synthesized in 70 g batches using a three step MA procedure, which is discussed in detail in a section below.

A compositional map was established by controlling composition factors such as Si/Ge ratio, dopant level, and W level. Alloy compositions investigated are summarized in Table 8.3. Except for sample 8, all samples were doped with 2 at% P or B to achieve n-type or p-type behavior, respectively. The Si/Ge ratios were varied at 70/30, 80/20 and 90/10. The WSi₂ volume fraction was varied from 0-5 vf%, with the majority being at 2 vf%. It should be noted that Sample 8 contains no W or B/P dopant. In addition to the composition, the particle size of the raw W powder has been varied between a nano- and micron-source.

After milling, powders consisted of alloyed Si/Ge with unreacted W; WSi₂ formation occurred in the densification step. Alloys were consolidated by SPS (FCT

Table 8.3: Nominal compositions and processing details of powder processed W/Si/Ge

Sample #	Si/Ge at%	WSi ₂ vf%	Dopant 2 at%	Sintering Temperature (Celsius)	W Source
1	70/30	2	P	800	Nano Powder
2	80/20	0	P	800	N/A
3	80/20	0	B	1100	N/A
4	80/20	1	P	800	Nano Powder
5	80/20	2	P	800	Nano Powder
6	80/20	2	B	1100	Nano Powder
7	80/20	5	P	800	Nano Powder
8	90/10	0	N/A	1100	N/A
9	90/10	2	P	800	Nano Powder
10	90/10	2	B	1100	Nano Powder
11	90/10	2	P	800	Micron Powder
12	90/10	2	B	1100	Micron Powder

Table 8.4: Sintering schedule

Profile Segment	Temperature	Load
1 Ramp	+200 C/min	+20 KN/min
2 Ramp	+100 C/min	Hold at Max Load
3 Dwell	Dwell at Max Temperature	Dwell at Max Load
4 Ramp	-200 C/min	-20 KN/min

Systeme GmbH, Germany). MA powder, 12 g, was loaded into 1" graphite dies (Graphite Sales, Chagrin Falls, OH). Graphite dies were coated with BN as a release agent on radial faces (Boron Nitride Spray II Momentive Performance Materials, Waterford, NY). The die and push rod axial face was lined with graphite foil to encapsulate the MA powder. The assembled die was cold pressed and wrapped in thermal insulation before insertion into the SPS. Samples were processed using the schedule in Table 8.4. A load of 35 kN and 10 min hold time, at the maximum temperature and pressure, was used for all samples. B doped samples were sintered at 1100°C while P samples were sintered at 800°C. Heating was achieved with a constant DC electric current passed through the push rods. Pulsed DC current heating was not found to provide any advantage over constant DC current. Additional samples were prepared at hold times of 4 minutes and 0 minutes to observe the effect of sintering profile on densification and microstructure. A set of typical sintered pellets is shown in Figure 8.10.

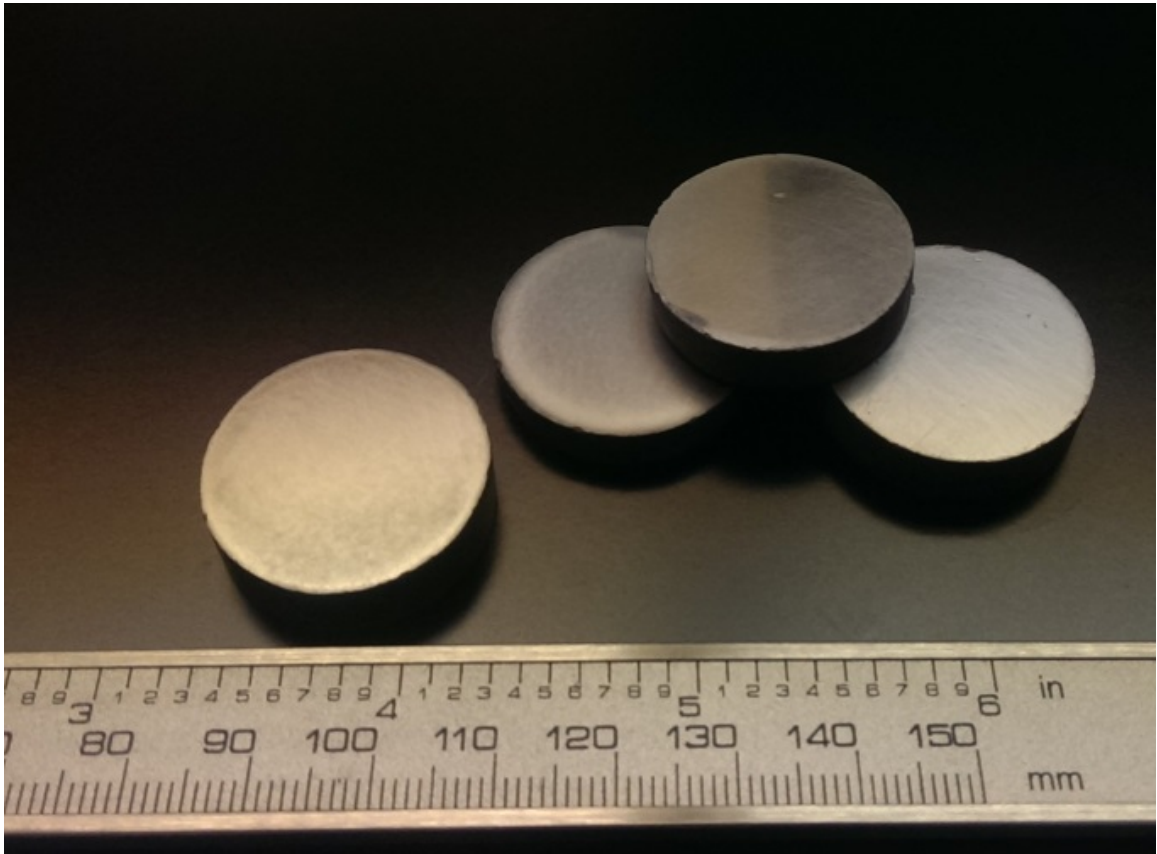


Figure 8.10: A set of typical powder processed W/Si/Ge samples. Pellets have 1" diameter.

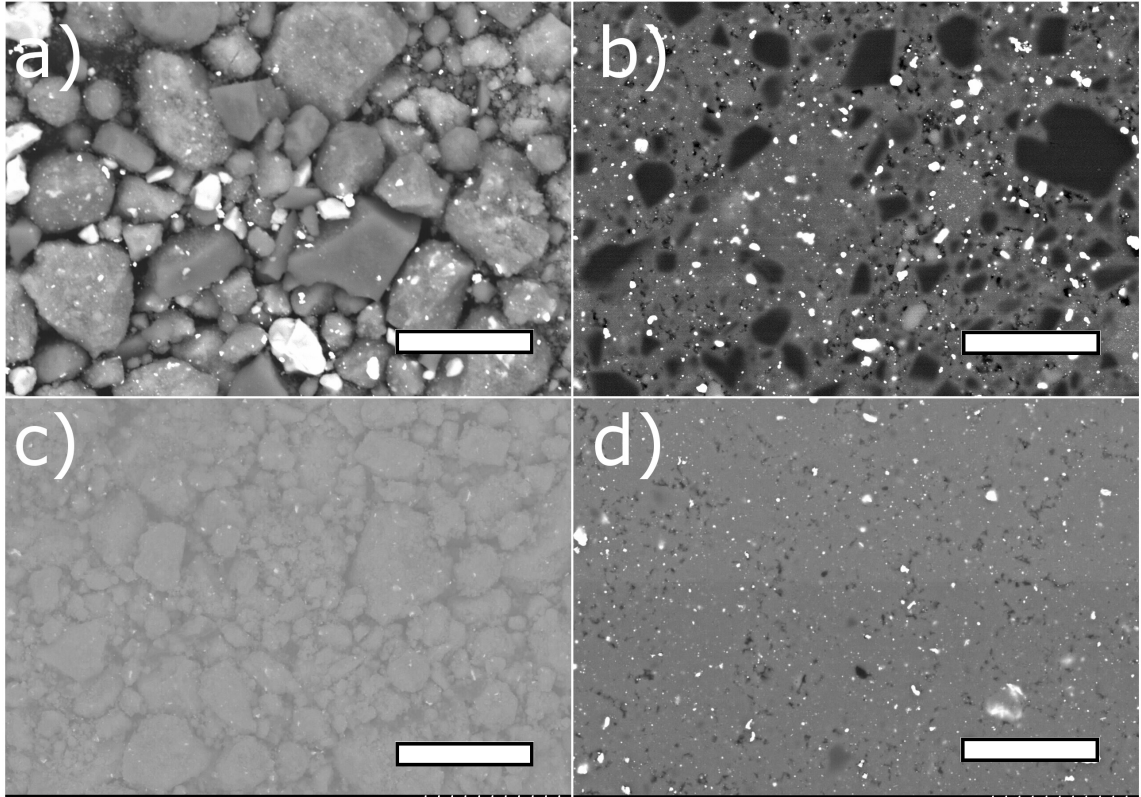


Figure 8.11: a) Milled powder after the first MA procedure, b) BSE image of sintered pellet of powder shown in 1a, c) Milled powder after the second three-step MA procedure, d) BSE image of sintered pellet of powder shown in 1c. All micrographs are shown for sample 9 (Si/Ge at% 90/10, WSi₂ 2 vf%, P Doped); scale bars 15 μm .

8.5.1 Mechanical Alloying

A direct relationship between milling procedure and final sintered microstructure was observed for samples processed under identical sintering conditions. Figure 8.11 shows sintered microstructures for samples derived from two different MA processes; nominal composition for the sample shown is listed in table 8.3 as sample 9, all micrographs were taken at 15 kV. Backscattered electron (BSE) micrograph in Figure 8.11a represents a typical W/Si/Ge sample milled at 300 rpm for 48 hours using 100 count

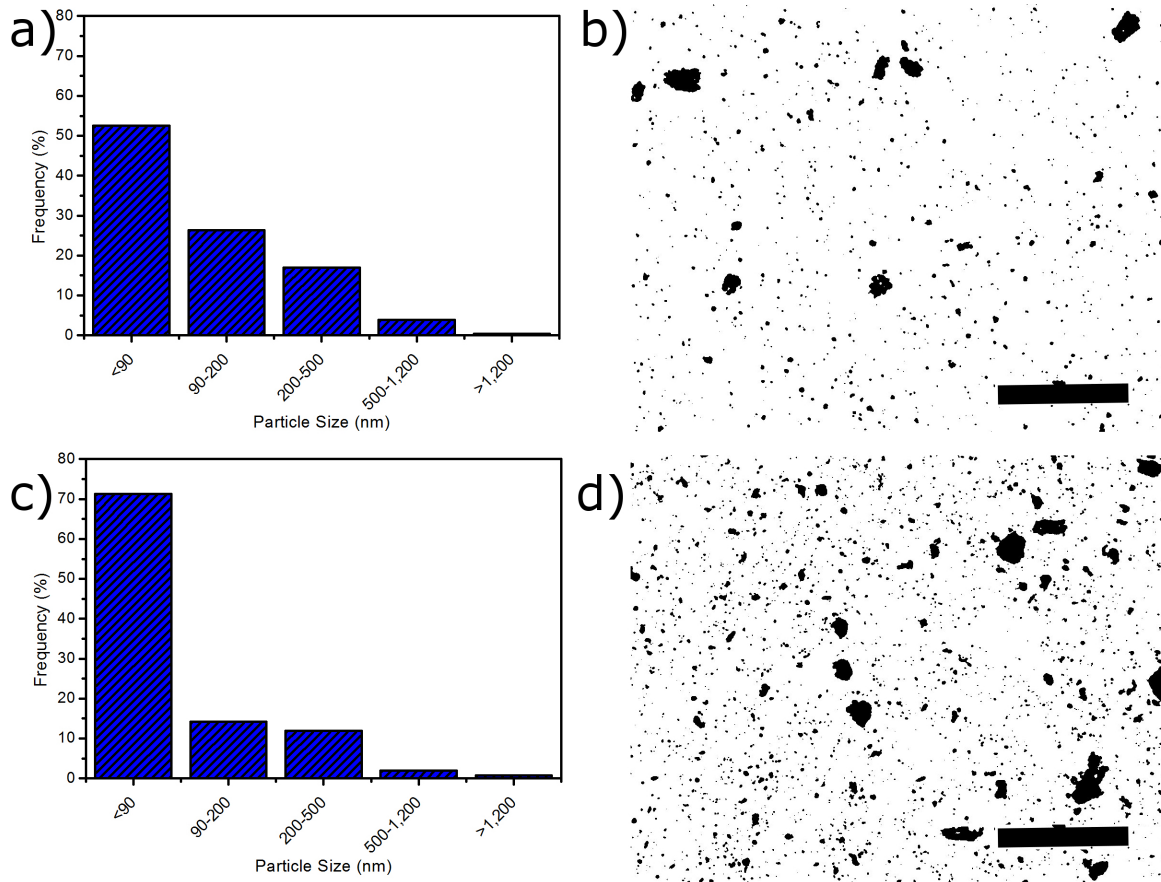


Figure 8.12: WSi₂ precipitate size distribution histogram and precipitate count mask for sample 1 (a and b, 2 vf% WSi₂) and sample 7 (c and d, 5 vf% WSi₂). Count mask scale bars are 10 μm.

5 mm WC media. Starting materials consisted of 3 mm granular Si (to decrease the oxygen content due to the native oxide layer on the surface), -100 mesh Ge, 1 μm W, and -100 mesh P. Large micron sized unreacted Si (dark phase), Ge (light gray phase), and W (white phase) are found. The final sintered microstructure, Figure 8.11b, resulted in a Si/Ge matrix characterized by WSi₂ precipitates and large unreacted Si and Ge particles. The resulting microstructure of this first MA process is undesirable for thermoelectric materials, as both elemental Si and Ge have significantly higher

thermal conductivity than an alloyed Si/Ge phase. An improved MA process was designed for the remainder of samples in this study. A multi-step procedure was developed to successfully MA Si/Ge. Figure 8.11c represents alloyed powder after a multi-step processing procedure which consisted of three parts: i) milling granular Si for 6 hours at 300 rpm, ii) milling Si powder with the remaining constituents at 300 rpm for 2 hours to ensure a mixed batch, and iii) milling the mixed powders at 580 rpm for 6 hours for alloying. The multi-step milling was performed with 10 mm WC media, and the milling proceeded in one hour intervals to clean powder from the jar wall. As a result of the first MA step, Si and Ge with similar particle sizes were achieved which lead to a uniformly mixed and alloyed Si/Ge matrix as a product of the second and third steps, respectively. The final alloyed powder contained small unreacted W particles. The final sintered microstructure, Figure 8.11d, was composed of the desired uniform Si/Ge matrix with WSi_2 precipitates generally $<1 \mu\text{m}$. Some porosity could be observed as the dark regions in the micrograph; density of the sample was greater than 97% of theoretical density. Phases were identified using XRD analysis of crushed pellets combined with qualitative EDS. A large range of precipitate sizes is undesirable and difficult to control by powder processing techniques. Image processing of SEM micrographs with ImageJ (software developed by the National Institute of Health) was performed at $\times 2\text{k}$ and $\times 10\text{k}$. The precipitate sizes were corrected to account for random precipitates in a cross-section. Micrographs oriented in both the radial and axial directions were analyzed. The image processing revealed a great number of small precipitates ($<90 \text{ nm}$) in addition to a

broad range of precipitates up to several microns. Figure 8.12 shows particle distribution histograms and count masks of micrographs for two samples. Figure 8.12a and 8.12b show the particle distribution of sample 1, which has 2 vf% WSi₂. The majority of precipitates are less than 90 nm, with some large precipitates (>5 μm). Figure 8.12c and 8.12d show the particle distribution of sample 7, which has a noticeably higher precipitate fraction of 5 vf% WSi₂. The majority of particles are in the smallest category (<90 nm) observed while precipitates as large as >5 μm also exist. Figure 8.12 clearly demonstrates the difficulty of controlling precipitate size by powder processing techniques.

To develop the second rigorous multi-step milling procedure, a milling study on Si was performed. Pure Si was milled at 300 rpm in a planetary mill under an Ar environment using 10 mm media with ball-to-powder mass ratio of 3.5. Given the geometric configuration of the planetary mill, 300 rpm coincides with a milling acceleration of 100 m/s². Milling proceeded with 1 hour intervals; interruption in milling was needed to clean vial walls and reset the powder above the milling media. A summary of average particle size and particle size distribution as a function of milling time is shown in Figure 8.13. Average particle size was determined from BET surface area analysis and particle size distribution was measured by dynamic light scattering (DLS) in a de-ionized water solution. There was clear correlation between the particle size distribution and average particle size for three different milling times (2 hours, 8 hours, and 14 hours). Both the particle size and distribution width decreased monotonically over longer milling time. The size distributions for the three

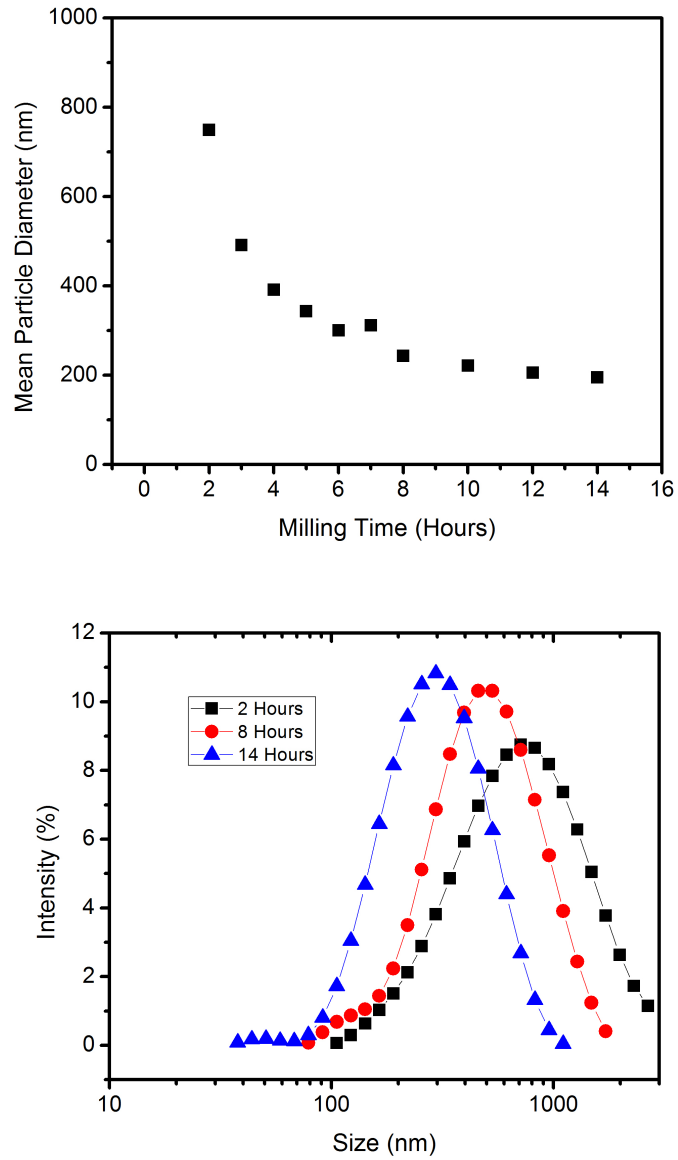


Figure 8.13: BET average particle size versus milling time (Top). DLS particle size distributions for three different milling times (Bottom).

selected times shown were predominantly single modal. The rate of size decrease asymptotically approached a lower limit around 200 nm after 14 hours of milling. A time of 6 hours was selected for the first step of milling to provide a balance between fine particle size (approx. 300 nm) and milling time which can increase contamination.

Work in MA Si/Ge has been thoroughly demonstrated and documented by Davis and Koch [203] among others. Davis and Koch observed MA of Si/Ge using a Spex 8,000 Mixer Mill after 4-8 hours depending on atmosphere and composition. For this study, alloying was observed to occur between 1 and 6 hours with 10 mm media at 580 rpm. This speed introduces a milling acceleration of 370 m/s^2 . Alloying of Si and Ge was confirmed by XRD. Figure 8.14 shows typical XRD profiles comparing the initial mixed powders after the second step (bottom) to MA powders after the third step (top) of the milling procedure. The Si and Ge reflections coalesced into a single broad reflection. WSi_2 reflections were not observed in the MA profile, however elemental W reflections broadened. Similar behavior was reported by Bokhonov et al. [204].

Attempts to synthesize the WSi_2 phase by MA of pre-milled Si powder (prepared by milling at 6 hours at 300 rpm achieving average particle size of 300 nm) with W-nano powder was unsuccessful. The starting W nano-powder had a bi-modal distribution of particle sizes centered on 70 nm and 400 nm as determined by DLS. By volume, 24% of the W particles had a size range of 43 to 141 nm, and 76% ranged between 141 and 1,106 nm. Broadening of W XRD reflections and relative reduction of Si reflections was observed in accordance with Bokhonov's et al., where the

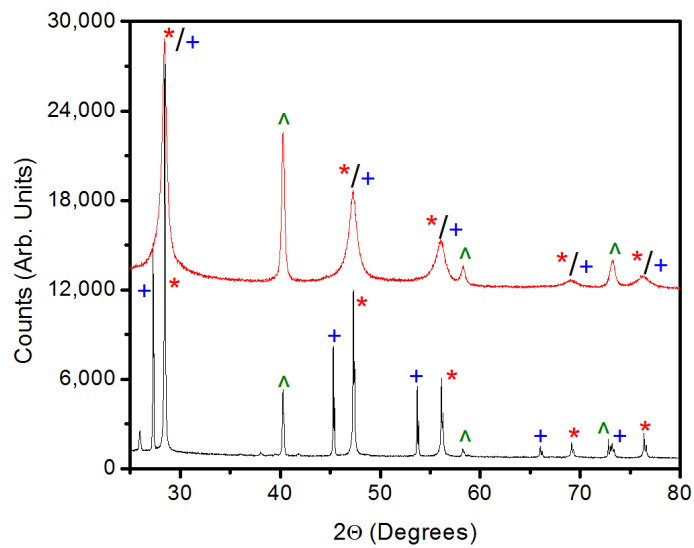


Figure 8.14: XRD for sample 9 (Si/Ge at% 90/10, WSi₂ 1.9 vf%, P Doped). Mixed powder after the second step of milling (Bottom), MA powder after the third step of milling and before sintering (Top). Si (*) and Ge (+) reflections coalesce into a single broad reflection, while W (^) reflections broaden.

Table 8.5: Strain rate of six samples demonstrating the influence of W

Sample #	W Source	Dopant	Strain Rate* (%/min)	Density (%)	95% Time** (min)
11	Micron Powder	P	2.9	97.0	3.1
9	Nano Powder	P	5.1	97.1	2.5
2	None	P	6.6	95.8	2.6
12	Micron Powder	B	5.9	95.8	2.3
10	Nano Powder	B	8.5	95.8	2.2
3	None	B	9.1	95.5	1.9

*Strain rate calculated at the beginning of the dwell step during the SPS run.

**Time to 95% of maximum ram travel

reduction in Si reflections was attributed to drastic plastic deformation disordering the crystal lattice [204].

8.5.2 Sintering

The sintering profile was studied by varying the dwell time at temperature and pressure, with the goal of using the shortest hold time possible to prevent grain growth. Based on the ram travel, the strain rate at the beginning of the SPS dwell was lower for W containing samples than samples without W. Si/Ge ratio did not show any effect on the sintering characteristics. Table 8.5 summarizes the trend in strain rate for six samples which were grouped according to the dopant type. Within each group the

WSi₂ content and the source powder for W was varied. In general, P doped samples, sintered at 800 °C, exhibited lower strain rates than the comparable (i.e., same WSi₂ content and W raw-powder source) B doped samples sintered at 1100 °C. A trend in the data was observed, strain rate showed dependency on W particle size regardless of the dopant type. For P doped specimens, strain rates were 2.9 %/min and 5.1 %/min for W particles sizes of 1 μm and 70 nm, respectively. B doped samples required higher sintering temperature, higher strain rates were observed at 5.9 %/min and 8.5 %/min for W particles sizes at 1 μm and 70 nm, respectively. In both cases, in the absence of W, greater strain rates were observed; 6.6 %/min and 9.1%/min for P and B doped specimens, respectively. Thus, both the presence and particle size of W have a noticeable influence on the sintering kinetics of the samples, as demonstrated by the strain rate data. Further dilatometer work would be required to fully understand the mechanisms by which W influences the sintering behavior, but the data presented herein highlights the importance of the effect. The final sintered density across all samples was comparable.

The dwell time for the ram to reach to 95% of the maximum travel was between 2.5 and 3.1 minutes for P doped samples and 1.9 and 2.3 minutes for B doped samples. The shorter dwell time of B doped samples is consistent with the higher sintering temperature. To investigate the influence of hold time, three batches of B doped powder, sample 2, were sintered with dwell times of 0, 4, and 10 minutes. Sintered densities were compared to theoretical density. Sintered density was 94% ± 0.5% for dwell time of 0 minute while it was 96% ± 0.5% for 4 and 10 minutes. The

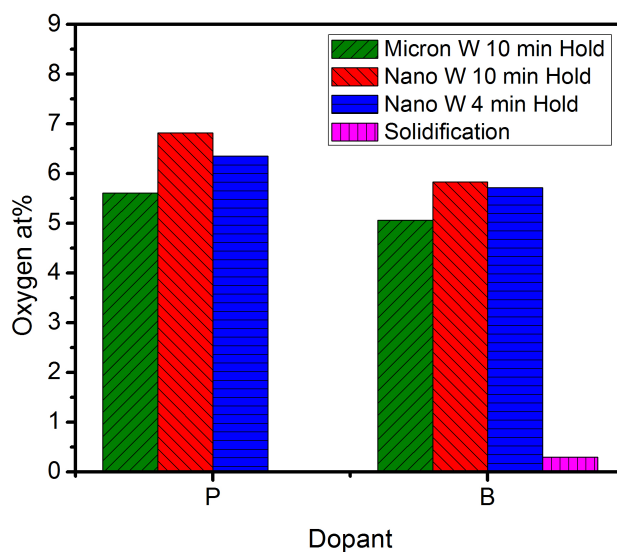


Figure 8.15: Oxygen content of six samples compared against a sample prepared by solidification techniques.

calculated density measurement uncertainty included both statistical repeatability and scale resolution. Thus any hold time between 4 and 10 minutes is equivalent. All samples in this study were sintered under a profile with a 10 minute dwell and were concluded to be at the highest density achievable at the given processing conditions.

SPS was performed in Ar atmosphere and the dwell time at high temperature did not have any effect on the oxygen content with similar values obtained for both 4 min and 10 min dwell times (Fig. 8.15). The source of the oxygen was mainly the content in the raw powders, with smaller W particle sizes (greater surface area per volume) resulting in higher oxygen content. Dopant raw materials were additional sources of oxygen with B showing up to 2.1 wt% oxygen. P cannot be characterized in the oxygen determination system, however, in general, P containing systems lead

to higher oxygen content than comparable (same WSi_2 content, and W-source) B doped systems. Overall the oxygen levels of these samples were higher than desirable and better control of the oxygen contamination must be considered. To provide a contrast an ingot with composition of sample 12 (Si/Ge at% 90/10, WSi_2 1.9 vf%, B Doped) was prepared by solidification in a He atmosphere using the Bridgman method. Starting materials were not MA before solidification, rather starting Ge and W powders and granular Si was loaded into a BN crucible directly. The oxygen contamination of the final melt sample was 0.3 at%, which was significantly lower than the comparable SPS prepared samples (Fig. 8.15). However, such techniques as directional solidification does not yield a desirable WSi_2 precipitate size and size distribution.

8.6 Powder Processed Thermoelectric Properties

The carrier density, carrier mobility, Seebeck coefficient, electrical resistivity, and thermal conductivity of the samples were studied as a function of temperature and composition. Additionally, the thermal stability of the dopant was investigated to understand the influence of the silicide precipitate.

8.6.1 Carrier Density and Mobility

The carrier density and mobility data were collected over the temperature range 25 – 400 °C determined by instrument capabilities. Figure 8.16 shows the temperature dependent hall carrier density and mobility of samples 5 and 6, which are typical

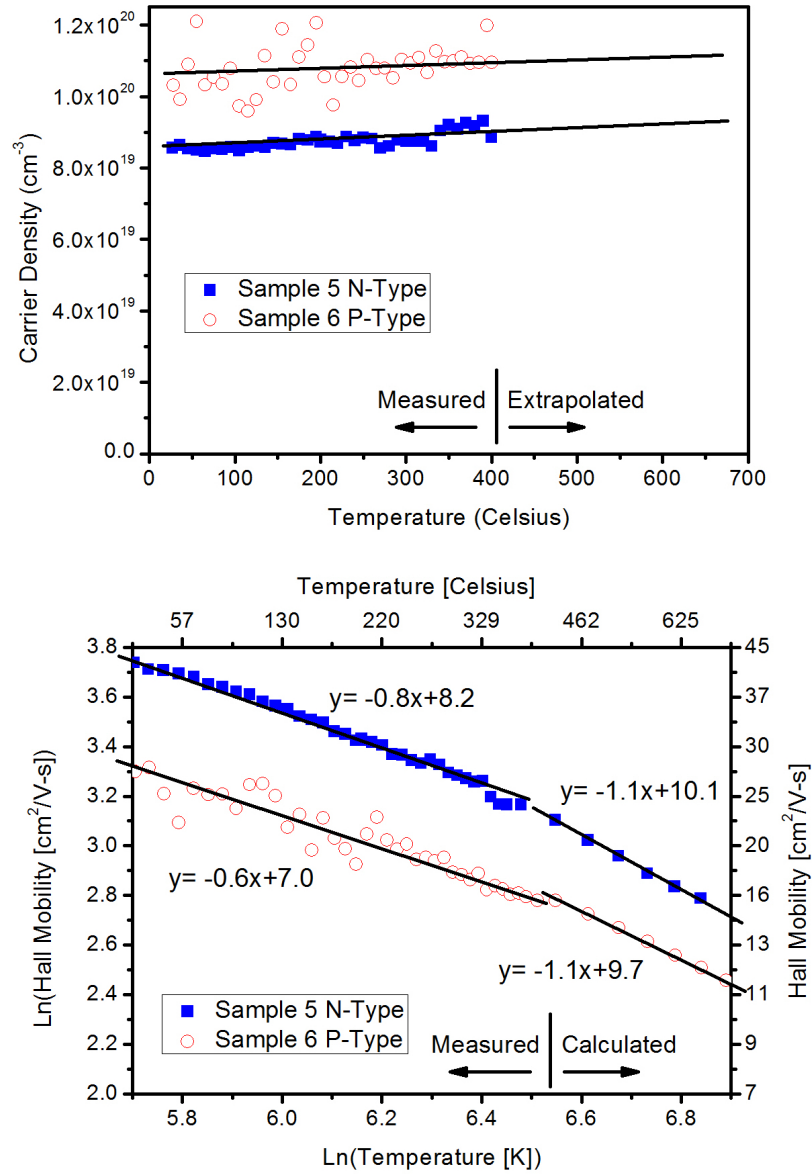


Figure 8.16: Hall carrier density (Top) and Hall mobility (Bottom) of samples 5 and 6 versus temperature.

of the sample set. Sample 5 exhibited n-type conduction, consistent with P doping. Carrier density was $9 \times 10^{19} \text{ cm}^{-3}$ and hall mobility was $42 \text{ cm}^2/\text{Vs}$ at room temperature, which was a 35% decrease in mobility compared to similarly doped values, reported in literature for P doped Si/Ge processed through solidification with no silicide precipitates [103]. Sample 6 exhibited p-type conduction, consistent with B doping. Carrier density was $1.1 \times 10^{20} \text{ cm}^{-3}$ and mobility $27 \text{ cm}^2/\text{Vs}$ at room temperature, which was a 32% decrease in mobility compared to similarly doped values, reported in literature for B doped Si/Ge again processed through solidification with no silicide precipitates [103]. Both samples had a nearly constant carrier density over the measured temperature range, consistent with a highly doped extrinsic semiconductor. The higher carrier density of the B doped sample compared to the P doped sample was consistent with the B and P solubility in Si/Ge. The solubility of P in 70/30 at% Si/Ge at 750°C is $1 \times 10^{19} \text{ cm}^{-3}$ while the solubility of B is over $1 \times 10^{21} \text{ cm}^{-3}$ [106].

$$\mu_H = \frac{e}{m} \frac{\int_0^\infty \epsilon^{3/2} \tau^2 \frac{\partial f}{\partial \epsilon} d\epsilon}{\int_0^\infty \epsilon^{3/2} \tau \frac{\partial f}{\partial \epsilon} d\epsilon} \quad (8.5)$$

The temperature dependence of the Hall mobility provides insight into the transport and scattering mechanisms in a semiconductor. Equation 8.5 is an expression of Hall mobility using a single parabolic band model (SPB). The mobility is dependent on e/m , the charge to mass ratio of a carrier, τ the temperature dependent carrier relaxation time, ϵ the reduced carrier energy ($\epsilon = \frac{E}{k_b T}$) normalized with Boltzmann's constant k_b and absolute temperature T , and f the Fermi distribution.

The influences of different scattering mechanisms enter into the mobility through the carrier relaxation time, with different temperature dependence for each scattering mechanism. The overall mobility temperature dependence is a result of both the relaxation time and the temperature involved in the evaluation of the Fermi integrals. To simplify the complicated temperature dependence, the Hall mobility is presented in the power law form $\mu \propto T^{-\rho}$. A ρ -value between 0.5 and 1.0 indicates alloy scattering of carriers while a ρ -value between 1.0 and 1.5 suggests phonon scattering [146]. For sample 5, the ρ value over the measured temperature range ($< 400^\circ\text{C}$) was 0.8, whereas sample 6 exhibited a ρ value of 0.6. In the low temperature range the samples were dominated by alloy scattering. To investigate mobility at higher temperatures the carrier density data was extrapolated and measured electrical resistivity was used. The mobility was calculated up to 700°C , above which the n-type systems began to exhibit intrinsic conduction, thus invalidating the extrapolated carrier density. The calculated ρ values between $400 - 700^\circ\text{C}$ for samples 5 and 6 were both 1.1. This ρ value indicated that the phonon scattering was dominant at high temperatures. The combined extrinsic semiconductor behavior with phonon scattering makes the SPB model a reasonable tool to investigate the system. The SPB model will be used later to calculate the lattice contribution to thermal conductivity.

8.6.2 Dopant Segregation

Dopant segregation is a well-known phenomenon in the Si/Ge system, as dopant solubility is thermodynamically limited and temperature dependent [112, 113, 198].

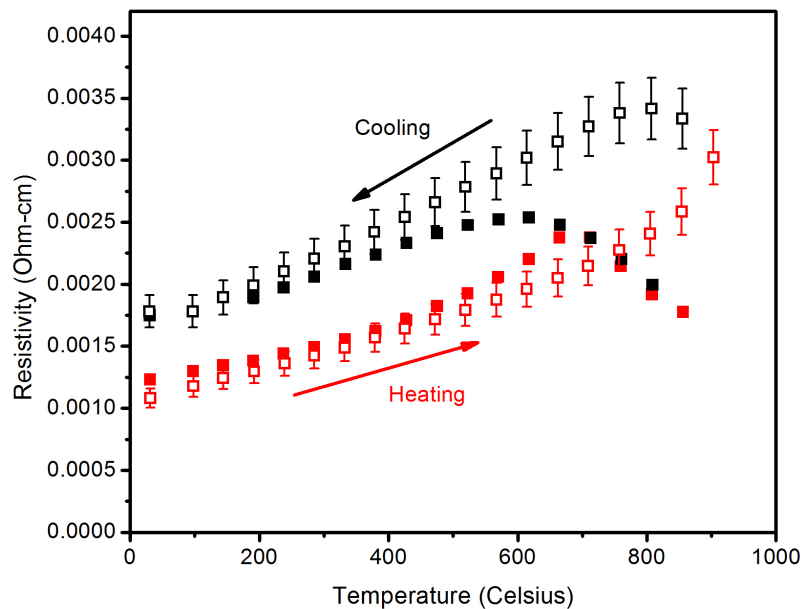


Figure 8.17: Electrical resistivity of n-type sample 9 (filled squares) and p-type sample 10 (open squares) upon the first heating and cooling cycle after densification.

Figure 8.17 shows the hysteresis of the electrical resistivity upon heating and cooling during the first measurement of two as-sintered samples as an example. The filled squares are for the n-type sample 9 and the open squares are for the p-type sample 10, both of which are Si/Ge 90/10 with 2 vf% WSi₂. After heating, the dopants segregated out of the matrix and were no longer electrically active. Thus higher electrical resistivity was measured upon cooling. The measured decrease in charge carrier density after the first heating further confirmed this segregation. After the initial segregation, subsequent heating and cooling followed the same curve; the cooling curve shown in Figure 8.17. These stable curves, obtained from repeated testing, are the data presented throughout this work. The segregation phenomenon was reversible; heating the samples to 1100 °C for $\frac{1}{2}$ hour then quickly air quenching

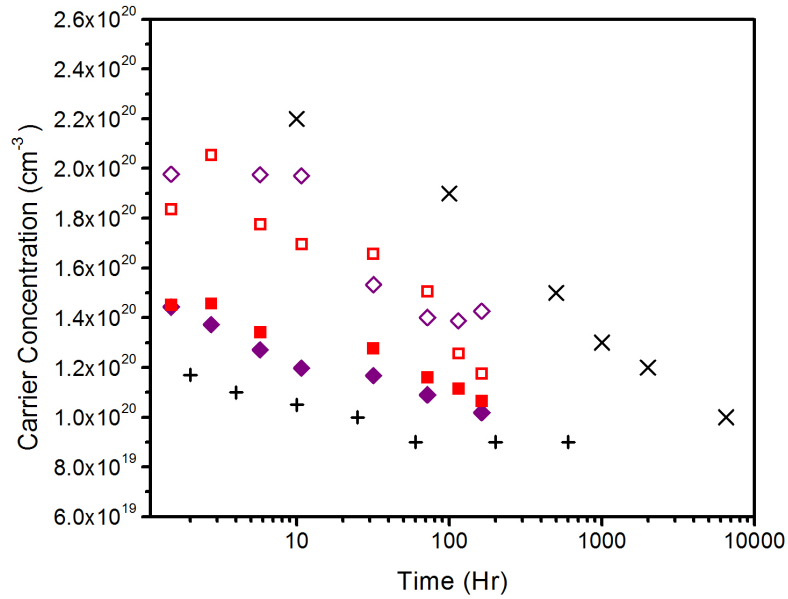


Figure 8.18: Dopant stability of samples 2, 3, 5, and 6 (n-type filled shapes, p-type open shapes). Samples annealed at 700°C with room temperature carrier density measured after quenching. N-type Si/Ge + symbols reference [113], P-type Si/Ge x symbols reference [112].

returned the samples to the as-sintered state. During this high temperature heat treatment, due to their higher solubility in the matrix, dopants dissolved back into the matrix and became electrically active; thus decreased the resistivity to the same values that were obtained during the first heating of the specimens. Note that the lack of hysteresis in the high temperature data of the n-type material during the first heating and cooling further confirmed that the change in slope of resistivity was due to an extrinsic-intrinsic transition.

An endurance test has been performed to compare the dopant stability of the samples in this work to previously studied Si/Ge alloys. Room temperature carrier density was measured on four samples including both p-type and n-type samples

with both 0 and 2 wt% WSi_2 . Samples were annealed in air at 700°C then air quenched by quickly removing the sample from the furnace at temperature. The quenched samples were then polished and measured for room temperature carrier density. Testing was repeated for varying heat treatment times from $\frac{1}{2}$ to 200 hours. The rate of decrease in carrier density with time is the principal parameter of interest for the study. Included in Figure 8.18 are four samples of this work as well as data from the works of Rowe and Savvides who performed similar measurements on silicide free Si/Ge melt samples [112, 113]. Literature values are shown as + for the n-type samples and x for the p-type samples. The slope of the data reveals the rate of decrease in carrier density. The samples in this work showed comparable quantitative behavior to the published work on classic Si/Ge, indicating that the additional WSi_2 phase did not adversely affect the thermal stability of the samples. Similar to the literature the B doped p-type samples had a faster rate of decrease than the P doped n-type samples. The smaller atomic radius of the B atom compared to the P atom may explain the faster segregation rate. Thermodynamically the higher solubility of B in Si/Ge should cause the equilibrium value to be higher than the P value. In general the P levels are always lower than the B levels for a given heat treatment time. While dopant segregation can adversely affect the performance of the Si/Ge system, the common use of Si/Ge thermoelectrics in the RTGs displays the system's reliability. It is well known that the segregation effects of the Si/Ge system have an influence on NASA's RTG powered spacecraft but by studying the phenomenon the couple behavior can be suitably designed with segregation in mind. Since the silicide

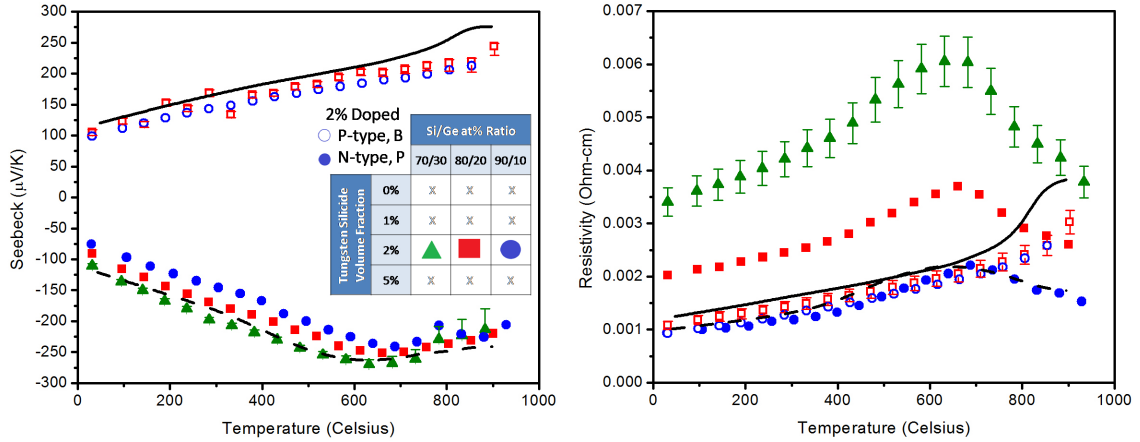


Figure 8.19: Seebeck coefficient (Left) and electrical resistivity (Right) of samples with constant WSi_2 volume fraction. Including: sample 1 (filled triangle), sample 5 (filled square), sample 6 (open square), sample 9 (filled circle), and sample 10 (open circle). Included are two published nano Si/Ge data sets (with no silicide precipitates) from Joshi et al. (solid line) [128], and Wang et al. (dashed line) [129].

composite samples displayed a similar behavior to the classic Si/Ge system, it should be reasonable to assume that the silicide system will behave in a comparable fashion.

8.6.3 Seebeck Coefficient, Electrical Conductivity, Thermal Conductivity

Figure 8.19 shows Seebeck coefficient and electrical resistivity as a function of temperature for three different Si/Ge ratios, with constant WSi_2 volume fraction. Both B (open symbols) and P doped (filled symbols) samples are included. To provide a contrast previously published nano Si/Ge is included with the black lines. The table inset in the Seebeck graph serves as a key for both graphs. The error bars shown on the plots represent typical uncertainty for all samples and are only shown on selected curves to retain readability. The uncertainty calculation was discussed Chapter 6. The bars include a range of measurement uncertainty sources rather than simply sta-

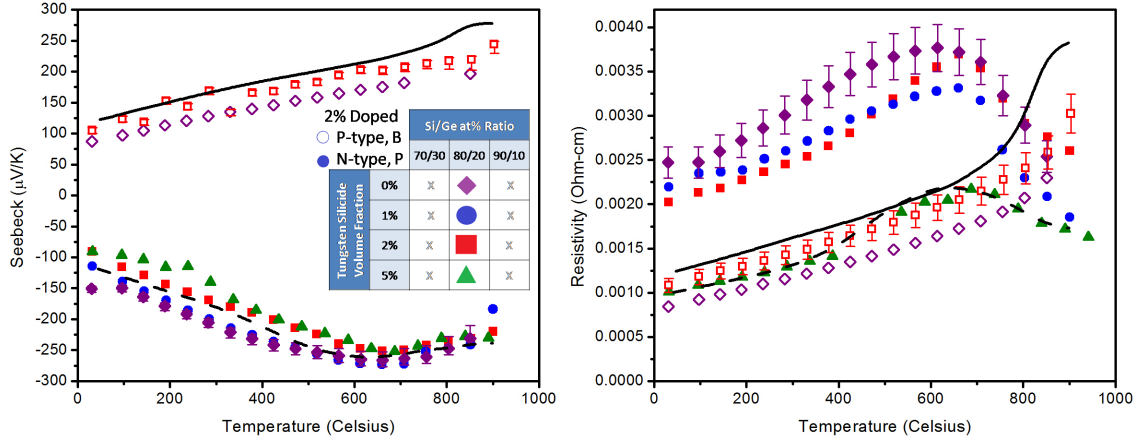


Figure 8.20: Seebeck coefficient (Left) and electrical resistivity (Right) of samples with constant Si/Ge ratio. Including: sample 2 (filled diamond), sample 3 (open diamond), sample 4 (filled circle), sample 5 (filled square), sample 6 (open square), sample 7 (filled triangle). Included are two published nano Si/Ge data sets from Joshi et al. (solid line) [128], and Wang et al. (dashed line) [129].

tistical error and the asymmetry in the Seebeck error bars at high temperatures are due to the cold-finger effect.

Samples with higher Si content had both a lower electrical resistivity and lower absolute Seebeck coefficient over the 25 – 950 °C temperature range, especially for the P doped systems. The increase in resistivity for samples containing more Ge was due to increased alloy scattering. Resistivity and absolute Seebeck coefficient increased with increasing temperature for all samples up to around 700 °C, exhibiting metallic like conduction. Above 700 °C the n-type samples all exhibited intrinsic conduction due to thermal excitation of minority carriers. The extrinsic to intrinsic change was above the measured temperature range for p-type alloys, which is consistent with the higher carrier concentration of the p-type samples (Fig. 8.16).

Figure 8.20 shows Seebeck coefficient and electrical resistivity for four different WSi_2 volume fractions at a fixed Si/Ge ratio. Included in the test matrix are both p-type and n-type samples without the WSi_2 component (purple diamonds) and published nano Si/Ge (black lines), these samples serve as the control for the experiment. The following should be noted in comparison of the previously published 80/20 nano Si/Ge data sets (with no silicide precipitates, black lines) with the SPS processed 80/20 Si/Ge materials (with no silicide precipitates, purple diamonds): (i) The resistivity of the published nano Si/Ge (black lines) was higher when B doped but was lower when P doped compared to this work (purple diamonds) and (ii) consistently the Seebeck coefficient of published nano Si/Ge was higher when B doped and lower when P doped. At high temperatures, in the intrinsic section ($> 700^\circ\text{C}$), the difference in Seebeck coefficient for P-doped systems, regardless of the processing technique, disappeared.

WSi_2 addition on p-type samples increased both electrical resistivity and absolute Seebeck coefficient. In contrast, on the n-type samples both resistivity and absolute Seebeck coefficient decreased. The magnitude of change was greater for n-type materials. These trends are related to the sample carrier densities. For the n-type samples, an increase in WSi_2 content from 0 to 5% volume fraction increased the room temperature carrier density from 1.3×10^{20} to $2.1 \times 10^{20} \text{ cm}^{-3}$. For the p-type samples an increase in WSi_2 content from 0 to 2% volume fraction decreased the room temperature carrier density from 2.6×10^{20} to $1.6 \times 10^{20} \text{ cm}^{-3}$. The data shown

in Figures 8.19 and 8.20 are measured in a relatively stable state after the initial dopant segregation.

The specific heat, used to calculate thermal conductivity, was calculated using Debye's model for the Si/Ge matrix and temperature dependent data reported on WSi₂ [205]. The calculated specific heat values were also compared to measured values taken with a Pyroceram standard in the laser flash method. The Debye calculated values are used for this work, as the measured values often displayed a large range of measurement uncertainty in repeated testing. The varying Si/Ge ratios were accounted for with Lindemann's rule [101, 206] and the WSi₂ contribution was taken into account by the rule of mixtures. Lattice conductivity was calculated by the Wiedemann-Franz law

$$k_l = k - L\sigma T, \quad (8.6)$$

where k_l is the lattice thermal contribution, k the total thermal conductivity, T the absolute temperature, σ the electrical conductivity, and L Lorenz number. The Lorenz number was approximated from a SPB model. The justification for applying the SPB model was discussed previously. Using a band model rather than the classic Lorenz number allows the inclusion of the effects of both temperature and the WSi₂ phase. The Lorenz number was calculated as

$$L = \frac{k_b^2}{e^2} \frac{3F_0F_2 - 4F_1^2}{F_0^2}, \quad (8.7)$$

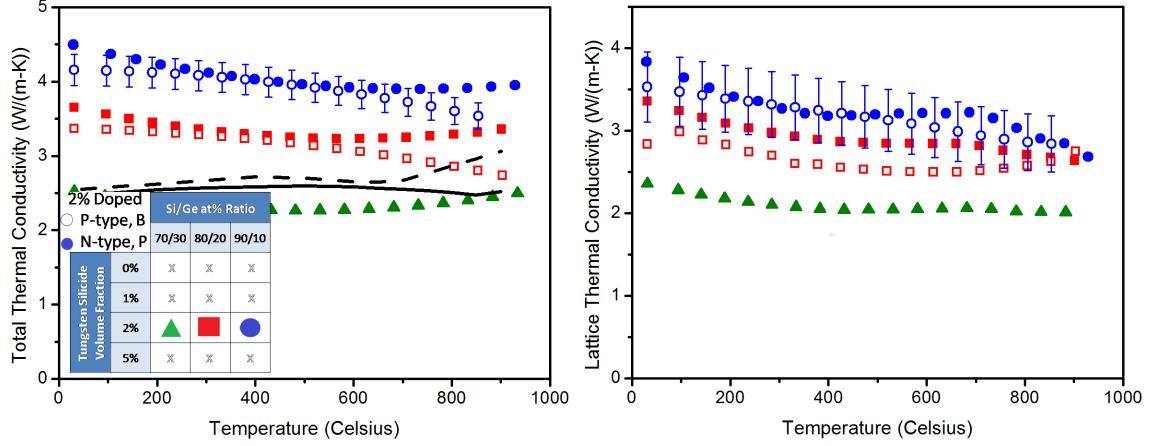


Figure 8.21: Total thermal conductivity (Left) and lattice thermal conductivity (Right) of samples with constant WSi_2 volume fraction. Including: sample 1 (filled triangle), sample 5 (filled square), sample 6 (open square), sample 9 (filled circle), and sample 10 (open circle). Included are two published nano Si/Ge data sets from Joshi et al. (solid line) [128], and Wang et al. (dashed line) [129].

where k_b is the Boltzmann's constant, e the charge on an electron, and F_i the i^{th} Fermi integral, which is dependent on the reduced electrochemical potential η . The electrochemical potential was calculated iteratively from the temperature dependent Seebeck coefficient data as

$$S = \frac{k_b}{e} \left(\frac{2F_1}{F_0} - \eta \right). \quad (8.8)$$

The total thermal conductivity of samples with varying Si/Ge ratios is shown in Figure 8.21-left. The values are compared to published work on nano-structured Si/Ge systems (with no silicides, black lines) [128, 129]. N-type Si/Ge ratio of 70/30 exhibits a total thermal conductivity comparable to published nano systems with Si/Ge ratio of 80/20 of Joshi et al. and Wang et al.; conductivity range of 2.5 W/m-K

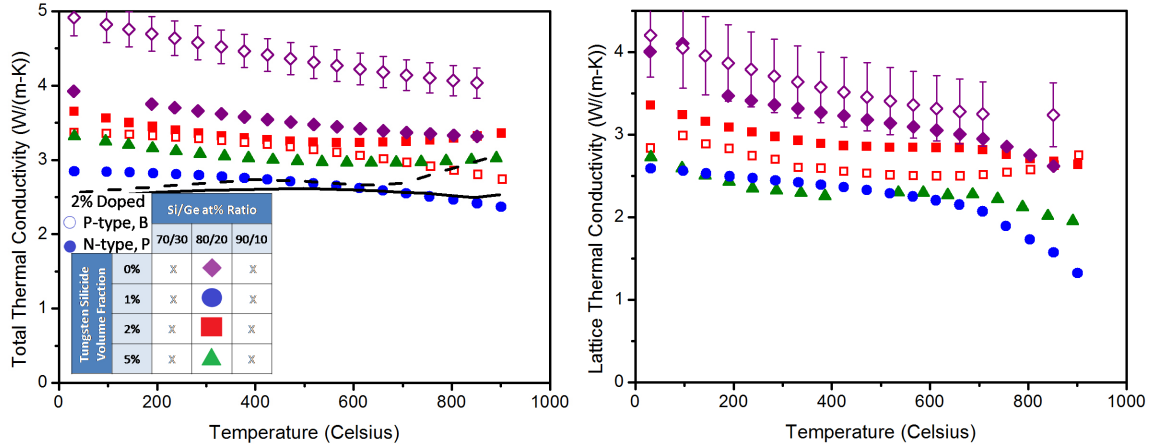


Figure 8.22: Total thermal conductivity (Left) and lattice thermal conductivity (Right) of samples with constant Si/Ge ratio. Including: sample 2 (filled diamond), sample 3 (open diamond), sample 4 (filled circle), sample 5 (filled square), sample 6 (open square), sample 7 (filled triangle). Included are two published nano Si/Ge data sets from Joshi et al. (solid line) [128], and Wang et al. (dashed line) [129].

was achieved. The calculated lattice thermal conductivity is shown in Figure 8.21-right for three different Si/Ge ratios. Increasing the Ge content decreased the lattice conductivity over the entire temperature range due to Si/Ge alloy scattering, a well-known mechanism for optimizing Si/Ge based thermoelectrics. However, it must be balanced by the corresponding changes in electrical properties for optimized figure of merit. The lowest lattice conductivity measured was around 2 W/m-K for the sample containing 30 at% Ge. A large portion of the total thermal conductivity, nearly 90%, was due to lattice conductivity.

Total thermal conductivity of samples with constant Si/Ge ratios are shown in Figure 8.22-left. The addition of the WSi_2 phase reduced the baseline conductivity to a level comparable with values for published nano Si/Ge [128, 129] in the range

of 2.5 W/m-K. Lattice thermal conductivity of the WSi₂ containing samples can be directly compared to an identically prepared silicide free sample in Figure 8.22-right (purple diamonds). The desired reduction in lattice component with the addition of the WSi₂ phase was observed over the measured temperature range. All three shown levels of WSi₂ displayed reductions in lattice component in comparison with the silicide free sample, although some scatter in the calculated data obscures a clear trend. The measurement uncertainty bars included are typical of all samples, and include sources from both resistivity and thermal conductivity. The uncertainty bars highlight that while all silicide containing samples have reduced nominal lattice conductivities, these differences may not all be statistically significant. In the best case, the reduction in lattice conductivity was 40%, with less of an effect at high temperatures. The lowest lattice thermal conductivity was around 2 W/m-K. The lattice conductivity contributed to nearly 90% of the total thermal conductivity.

The final temperature dependent figure of merit as a function of Si/Ge content and WSi₂ content is summarized in Figure 8.23, left and right, respectively. In addition to the samples of this work, curves for the state-of-the art Si/Ge systems are included. The brown lines represent the p-type (brown dotted line) and n-type (brown dot-dash line) curves for the radioisotope thermoelectric generators (RTG). The black lines represent published nano Si/Ge work by Joshi et al. and Wang et al. For the samples shown in Figure 8.23-left only the p-type sample with Si/Ge 80/20 and 2% WSi₂ (sample 6) offered any improvement over the comparable RTG data, but the sample was not as strong as published p-type nano Si/Ge. At 900 °C the

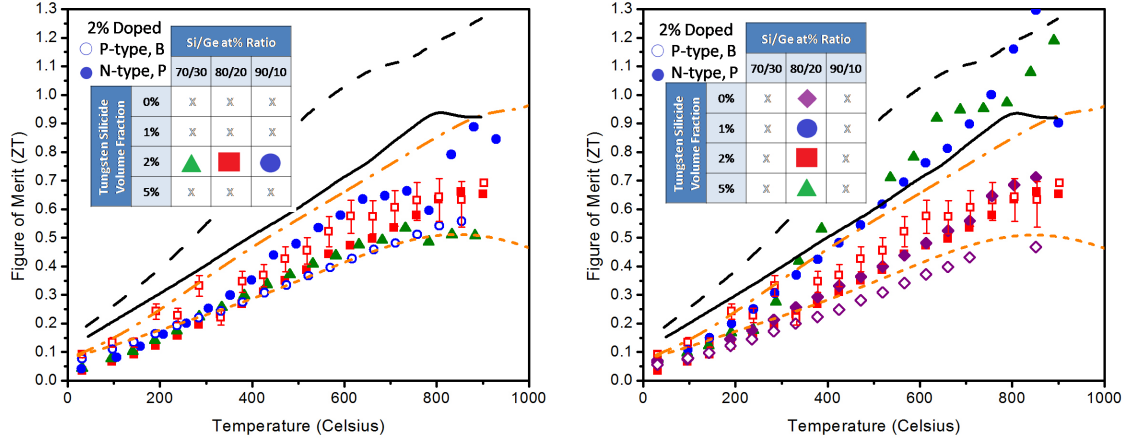


Figure 8.23: Figure of merit of samples with constant WSi_2 volume fraction (Left) and constant Si/Ge ratio (Right). Included are two published nano Si/Ge data sets (with no silicide precipitates) from Joshi et al. (solid black line) [128], and Wang et al. (dashed black line) [129], and Si/Ge RTG data (dot-dash brown line and dotted brown line) [106].

calculated ZT of 0.65 was a 30% improvement over the comparable silicide free p-type RTG data. The n-type samples, regardless of the Si/Ge content, all displayed figure of merit lower than RTG as shown in Figure 8.23-left. Possible sources of the low figure of merit include oxygen contamination and sample porosity. Calculated figure of merit as a function of WSi_2 content is shown in Figure 8.23-right. Included again are the RTG samples and published nano Si/Ge data, although direct comparison is best made against the silicide free samples of this work (purple diamonds). The 1% and 5% WSi_2 samples displayed the largest increase in figure of merit over both the silicide free samples of this work as well as the RTG data. The increase in figure of merit for both n-type and p-type systems was mainly due to the lower lattice component of thermal conductivity. At 900 °C the calculated ZT of 1.19 was

a 30% improvement over the comparable silicide free n-type RTG data. Given the observed trends improvements in both n-type and p-type Si/Ge are possible with the introduction of a nano-structured WSi₂ phase. The improvement in p-type samples were not as strong as the improvement seen in the n-type samples.

8.7 Influence of Oxygen Contamination

The level of oxygen contamination has been studied on the samples in this system. Samples processed with solidification have the lowest oxygen contamination because during loading of the furnace the exposed starting materials are shot sized chunks rather than fine powder. In contrast the powder processed samples have higher levels of oxygen contamination due to the increased surface area of the fine powders, which are inevitably exposed to some amount of air. The oxygen level of samples prepared by solidification and powder processing are summarized in Table 8.6. The data in the table is averaged over samples with different levels of W and Si/Ge, the level of oxygen is most correlated to the processing conditions. To better understand oxygen contamination the powder processed samples were either (i) loaded into SPS dies in air or (ii) in an argon glovebox. The dies loaded under argon had a significantly lower level of oxygen contamination than samples loaded in air (see Table 8.6).

Two identical samples were prepared with one SPS die loaded in air and the other loaded in argon, the resulting microstructures are shown in Figure 8.24. The black phase in the micrographs is the oxygen containing SiO₂ silica phase, the white phase is the WSi₂ silicide precipitate, and the gray phase is the Si_{1-x}Ge_x matrix.

Table 8.6: Oxygen level of $\text{WSi}_2\text{-Si}_{1-x}\text{Ge}_x$ composites using different processing conditions.

Processing Condition	Average Oxygen at%	Std. Dev. Oxygen at%
Solidified	0.49	0.07
Powder- Argon Loaded	1.54	0.35
Powder- Air Loaded	5.85	0.92

The air loaded sample (Figure 8.24a) shows a higher level of the silica phase than the argon loaded sample (Figure 8.24b). Figure 8.24c shows an overlay of oxygen (green) and tungsten (red) EDS chemical maps on an EBSD grain boundary map of a sample loaded in air. It is clear that the silica phase preferentially forms at the grain boundaries of the silicon germanium matrix and is on the order of 50 nm.

The effect of the silica phase on the thermoelectric properties is shown in Figure 8.25. The electronic properties (Figure 8.25a) of the samples are unchanged by loading the samples in air compared to argon. Interestingly the same is not true of the thermal properties. The lattice component of thermal conductivity of the air loaded samples is significantly lower than the argon loaded samples (Figure 8.25). The scale of the silica phase may be causing a preferential scattering of phonons over electronic charge carriers, leading to the reduction in lattice component of thermal conductivity. As a result the samples loaded in air have a lower total thermal conductivity and improved figure of merit. The samples presented in section 8.6 were all loaded under air, so the calculated figure of merits are as good as can be expected for the system.

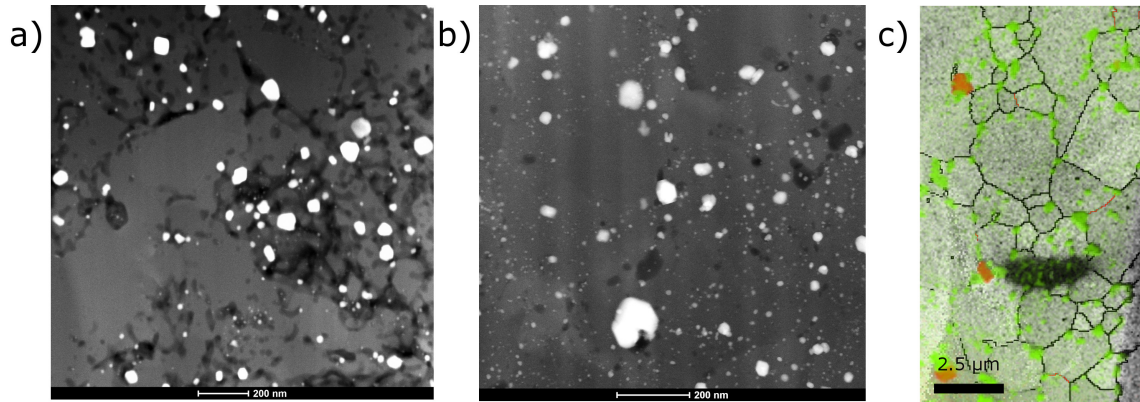


Figure 8.24: Micrographs of a) air loaded and b) argon loaded samples. White phase is WSi_2 , black phase is SiO_2 , gray phase is $\text{Si}_{1-x}\text{Ge}_x$. c) oxygen (green) and tungsten (red) EDS chemical maps on an EBSD grain boundary map of a sample loaded in air.

8.8 Conclusion

The work presented has demonstrated the feasibility of a W/Si/Ge system for high temperature thermoelectric applications. Directional solidification in the W/Si/Ge system resulted in formation of randomly ordered WSi_2 precipitates in the micron-size range, exhibiting faceted growth. The large separation of the solidus and liquidus lines during solidification leads to micro-segregation of Ge. Processing in BN crucibles resulted in B dissolution in the melt on the order of 0.17 at%. The results show that a combination of WSi_2 and B can affect electrical transport, reduction in Ge concentration can lead to potential cost savings. The ability to control the dopant level through the use of more readily available fused silica crucibles provides a potential pathway for optimizing the system.

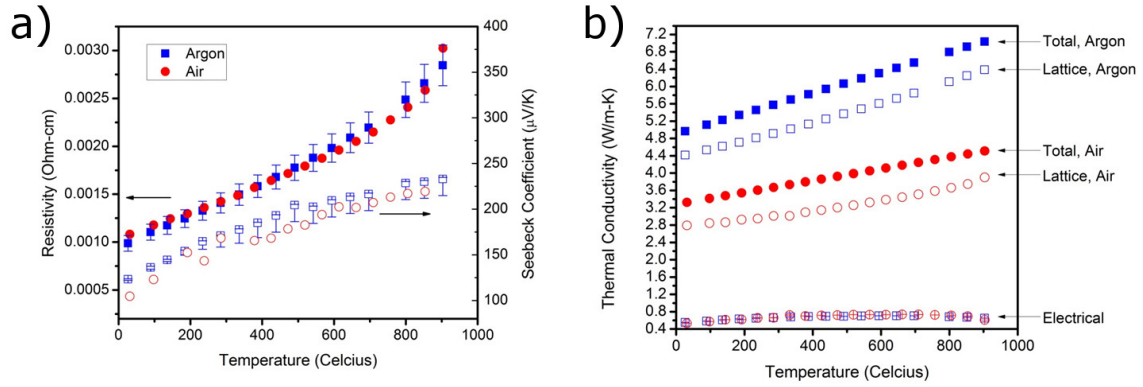


Figure 8.25: Study on loading powders in 'Air' compared to 'Argon'. a) Electrical resistivity and Seebeck coefficient b) Thermal conductivity including electrical and lattice components.

With addition of B doping, electrical properties are enhanced. Seebeck coefficients are on the order of $+300 \mu\text{V/K}$ along with electrical conductivities around $2.8 \times 10^4 \text{ S/m}$ and high power factors up to $3,000 \mu\text{W/m-K}^2$ in the temperature range of 373–1173 K were observed. The highest power factor was achieved at a composition of $\text{Si}_{89.8}\text{Ge}_{9.3}\text{W}_{0.9}$; a 50% higher power factor is observed compared to published results for sintered and zone-leveled $\text{Si}_{80}\text{Ge}_{20}$. Strong electrical properties combined with good thermal conductivity resulted in a figure of merit comparable to the traditional high-temperature $\text{Si}_x\text{Ge}_{1-x}$ materials developed by NASA for use in RTGs ($ZT=0.5$).

The effect of nano-structuring through powder processing of Si/Ge and WSi_2 nano-inclusions has also been studied and demonstrated. Effects of processing, including milling and sintering parameters, have been carefully identified to control the final structure, composition, and phase distribution of the composite. The effects of the W component on milling and sintering were investigated and found to reduce the sinter-

ing strain rate and increase the required sintering time of the samples. The effects of the WSi_2 phase have been investigated on the thermoelectric transport properties and was found to play a role in the carrier density, electrical resistivity, Seebeck coefficient and thermal conductivity. Nano-structuring of the composite achieved substantial reductions, up to 40%, in lattice component of thermal conductivity for the samples investigated. The final result on material figure of merit was an increase above that of traditional RTG Si/Ge. Enhancements as large as 30% were obtained for both p-type and n-type samples. The WSi_2 containing samples have been investigated for electrical stability at a temperature of 700°C and have been shown to be as stable as classically obtained Si/Ge samples. Oxygen contamination on samples was found to produce a silica phase which reduces the thermal conductivity without significantly altering the electronic properties. The largest source of oxygen contamination was found to be during the loading of the SPS dies.

Optimal couples have been designed from the materials developed in this chapter, with actual couple fabrication covered in Appendix A. The couples designed from the powder processed Si/Ge with WSi_2 composites are a higher efficiency couple than the high temperature couples currently used in spacecraft RTG. Further work must be done to effectively bond the couple together and ensure that metallization of the legs does not impede the thermoelectric properties of the system. Additionally long term endurance testing of the couples would be required to verify that the thermal stability of the composites is comparable to the traditional zone-leveled Si/Ge system.

CHAPTER IX

$\text{Co}_x\text{Ni}_{4-x}\text{Sb}_{12-y}\text{Sn}_y$ QUATERNARY SKUTTERUDITE SYSTEM: PROCESSING AND THERMOELECTRIC PROPERTIES

9.1 Introduction

This chapter discusses the design of a new medium temperature thermoelectric material based on the skutterudite crystal structure. The system of interest is a quaternary $\text{Co}_x\text{Ni}_{4-x}\text{Sb}_{12-y}\text{Sn}_y$ with $0 \leq x \leq 2$ and $3 \leq y \leq 5$. Lanthanide series fillers Ce, Dy, and Yb have been investigated in the system. The samples were primarily synthesized from a melt, mill, hot press technique but other fabrication methods were also investigated. The modeling work of Chapter 4 has been applied to the materials of this chapter as a demonstration of typical couple design, see Chapter 5 for design calculations.

9.2 System Background

Skutterudites have proven to be a suitable system with potential for high ZT, thermal stability, and favorable mechanical properties. Skutterudite structure is represented by a chemical formula of BX_3 and body-centered cubic space group Im-3, where B is Co, Rh, or Ir and X is a pnictogen atom P, As, or Sb. A prominent feature of

the skutterudite structure is the existence of two relatively large voids per unit cell and four member planar pnictogen rings (see Figure 2.6). The cubic unit cell can then be written in a general formula as $A_2B_8X_{24}$ where A is an electropositive filler element [82]. Most binary skutterudite compounds exhibit large Seebeck coefficients and good electrical conductivity, resulting in large power factor values. Filler cations can be inserted in the voids to reduce thermal conductivity and improve ZT over unfilled. Numerous skutterudite compositions have been investigated and characterized over a wide range of temperatures. Common binary skutterudites studied include $CoSb_3$ [62, 64, 67, 70, 85, 86], $CoAs_3$ [62, 86], and $FeSb_3$ [73, 207] among others. Binary skutterudites have been studied with a number of different filler elements. A variety of fillers are added in an effort to cover large frequency spectra for phonon scattering, thereby reducing lattice thermal conductivity.

Ternary skutterudites may be formed from a binary variant through isovalent replacement on either the B or X site. Some investigated ternary skutterudites include $CoGe_{1.5}S_{1.5}$ [74], $CoGe_{1.5}Se_{1.5}$ [74], $IrGe_{1.5}S_{1.5}$ [63], $IrGe_{1.5}Se_{1.5}$ [63], $IrSn_{1.5}S_{1.5}$ [63], $RhGe_{1.5}S_{1.5}$ [63], $Co_4Ge_6Se_6$ [75] and $Ni_4Sb_8Sn_4$ [77, 78]. Lists of potential ternary skutterudites can be found summarized in the works of Bauer et al. [76] and Fleurial et al. [65]. In this work, three potential skutterudite systems were investigated: $Ni_4Bi_8Ge_4$, $Ni_4Sb_8Ge_4$, and $Ni_4Sb_8Sn_4$. These systems were predicted to be stable skutterudite structures but little experimental verification has been performed until now.

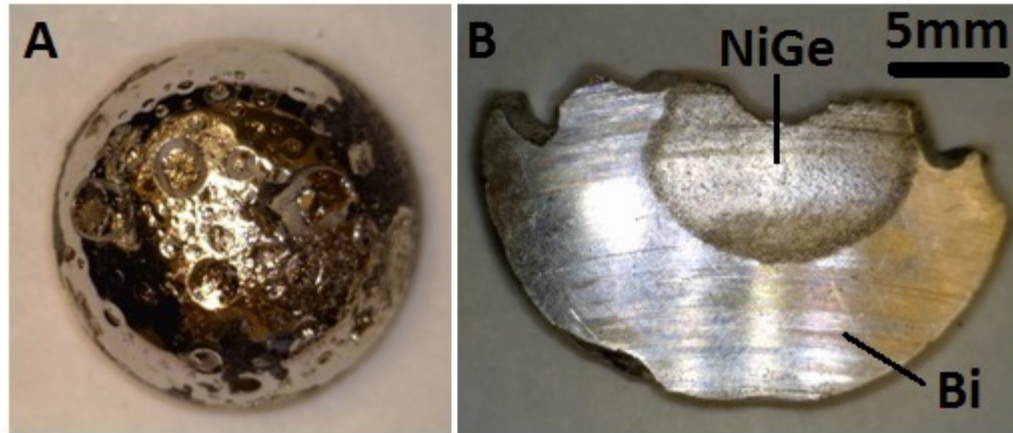


Figure 9.1: A) Ingot of Ni/Bi/Ge melt (25 mm diameter). B) Cross-section view of ingot showing phase segregation of Bi and Ni_xGe phases.

9.2.1 Ni/Bi/Ge System

Elemental constituents of the Ni/Bi/Ge system were melted for 2 hours at 1100 °C at heating and cooling rates of +20 °C/min and -10 °C/min, respectively. Due to the lack of a ternary phase diagram for this system, processing temperatures were based on binary phase diagrams. Crucibles were weighed before and after solidification and material loss was less than 1%. Phase segregation was observed in the ingot (Fig. 9.1). It consisted of a Bi phase (melting temperature 271 °C) surrounding a region of NiGe (peritectic temperature 850 °C) and Ni_{2.74}Ge₂ phases. Skutterudite phase was not achieved; furthermore Bi did not react with the Ni/Ge components.

In an attempt to react Bi with Ni, a sample was prepared by melting stoichiometric amounts of Ni and Bi for 1 hour at 1150 °C (+20 °C/min, -10 °C/min). The phases in the ingot were identified as Bi, NiBi₃ (peritectic temperature 469 °C), and NiBi (peritectic temperature 654 °C). The ingot was crushed and combined

with stoichiometric amount of Ge and re-melted for 1 hour at 1150°C ($+20^{\circ}\text{C}/\text{min}$, $-10^{\circ}\text{C}/\text{min}$). The final ingot was similar to that shown in Figure 9.1, consisting of a large region of segregated Bi surrounding a region of Ni_xGe phases. The ingot was annealed at 600°C for 67 hours in N_2 atmosphere. Annealing did not change the sample phase content. It was evident from the microstructural analysis that Bi melted and solidified during annealing, while the Ni_xGe phase appeared to remain intact. Thus, Ni_xGe is not highly soluble in liquid Bi.

Powder processing was pursued for the Ni/Bi/Ge system. The elemental powders were milled for 7 hours at 580 rpm. Milling consisted of 1 hour intervals; the powder was scraped from the wall of the milling jar between each interval. Densification of powders was performed by microwave (MW) sintering. Samples were processed at both low power (200 W -4 min) and higher power (400 W -34 min). Low MW power was chosen to avoid possible melting and segregation of the Bi phase. However, Bi still melted regardless and formed a Bi rich outer layer on portions of the sample. Both the low and high power MW sintered samples exhibited porosity and heterogeneous microstructure of Bi and Ni_xGe phases. Higher density was achieved at the higher MW power, 5.7 g/cc versus 4.6 g/cc at low power. The microstructure of the specimen sintered at low power MW is shown in Figure 9.2; light phase is Bi whereas the darker phases are Ni_xGe . Additionally, not shown in Figure 9.2, some outer regions consisted exclusively of segregated Bi.

In addition, milled powders were hot pressed, in an attempt to reactively hot press the desired phase. Pellets were densified at 180°C for 30 minutes under an ap-

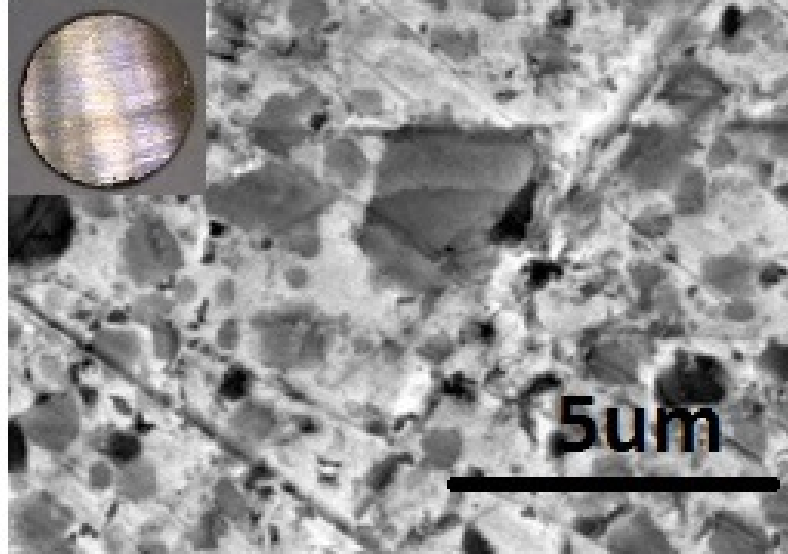


Figure 9.2: Secondary electron SEM micrograph of microwave sintered sample showing heterogeneous phases and porosity. Inset) cross-section view of sample.

plied pressure of 62 MPa in Ar atmosphere. Higher temperatures caused formation of liquid phase and catastrophic die failure. Similar to the specimens obtained through solidification, the final pellets were composed of a heterogeneous mixture of Bi and Ni_xGe phases. The electrical resistivity of the Bi and Ni_xGe composites averaged 0.50 mOhm*cm at room temperature and 0.55 mOhm*cm at 250 °C. The Seebeck coefficient of the composites averaged -52 $\mu\text{V}/\text{K}$ at room temperature and -41 $\mu\text{V}/\text{K}$ at 250 °C. Thermal conductivity was not measured on the samples. An approximate figure of merit was calculated by using estimated thermal data for the primarily Bi composites. The maximum figure of merit on these Bi/ Ni_xGe composites is likely less than 0.06 at a peak temperature of 150 °C. More detailed thermoelectric character-

ization was not performed, as a ternary skutterudite could not be achieved for this system.

9.2.2 Ni/Sb/Ge System

The powder processing route was utilized by milling the elemental constituents Ni, Sb, and Ge. Milling proceeded at 1 hour intervals at 300 rpm for the first 12 hours and 550 rpm for the remaining time (19 hours maximum). Powder was scrapped off the milling jar wall at each interval. Figure 9.3 shows selected XRD profiles of the mechanically alloyed powder at selected times. After 2 hours of milling, the identified phases were Ni, Sb, and Ge. After 13 hours, NiSb phase formed, and this phase continued to grow in quantity as the milling time increased. The final powder consisted of Sb, Ge, and NiSb phases. Broadening of the reflections throughout the milling study suggested reduction of crystallite size.

When pressed discs were pressure-less sintered at 600°C for 35 hours in N_2 , liquid phase rich in Sb (melting temperature 630°C) formed and segregated during densification. Decreasing the sintering temperature to 550°C (for 20 hours) resulted in elimination of the liquid phase. Skutterudite phase did not form at either sintering conditions. Phases observed were Sb, $\text{Ni}_{2.74}\text{Ge}_2$, Ni, and Ge. Figure 9.4 shows the microstructure; it consisted of a large amount of porosity (black regions) and a heterogeneous mixture of Ni_xGe (dark gray) and Sb (light) phases. A similar microstructure was observed for the Ni/Bi/Ge system. No skutterudite phase could be obtained for this system.

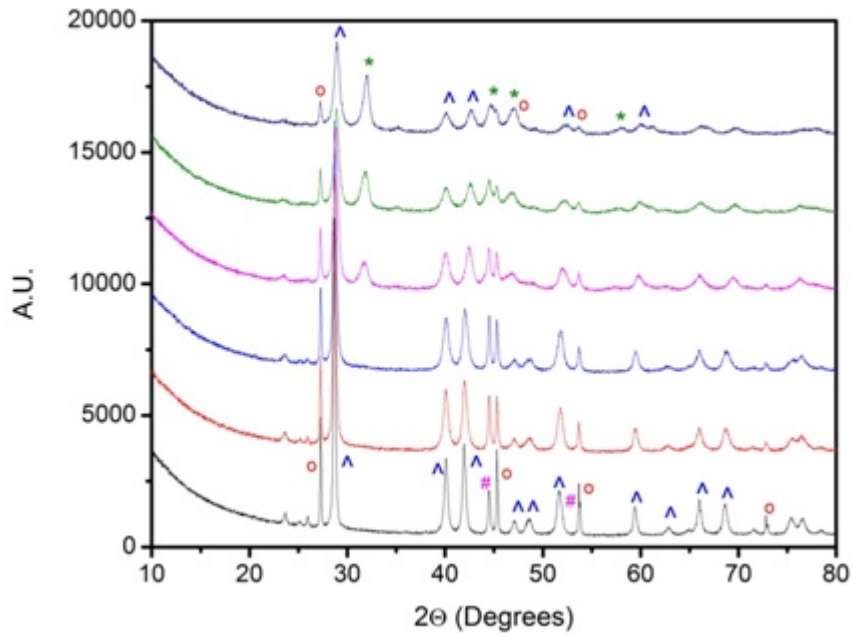


Figure 9.3: XRD of milling study on Ni/Sb/Ge system, milling interval between selected profiles was 1-3 hours. Bottom profile (milling time 2 hours) contains Sb (\wedge), Ge (o), and Ni ($\#$) phases. Top profile (milling time 19 hours) contains Sb (\wedge), NiSb ($*$), and Ge (o) phases.

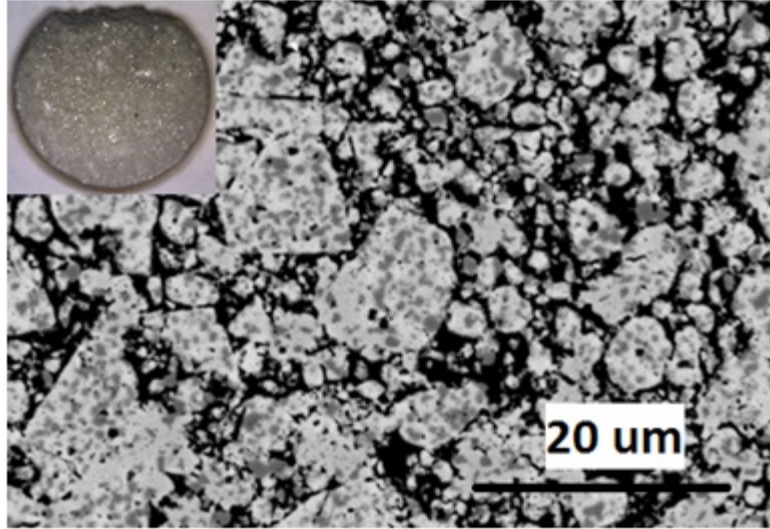


Figure 9.4: Backscattered SEM micrograph of cold pressed and sintered sample showing heterogeneous phases and porosity. Inset) cross-section view of sample.

9.2.3 Ni/Sb/Sn System

It was found that the Ni/Sb/Sn system successfully forms a skutterudite phase. This phase has been reported in the previous work of Grytsiv et al. [77] as an n-type skutterudite. The remainder of this chapter will focus on the work done with this system, including work on a related p-type skutterudite $\text{Co}_x\text{Ni}_{4-x}\text{Sb}_{12-y}\text{Sn}_y$.

9.3 $\text{Co}_x\text{Ni}_{4-x}\text{Sb}_{12-y}\text{Sn}_y$ Processing

Samples were prepared from elemental Co powder (99.8%, Alfa Aesar), Ni powder (99.9%, Cerac), Sb shot (99.999%, Alfa Aesar), and Sn shot (99.99%, Alfa Aesar). Samples were made by melting and solidifying stoichiometric amounts of the metallic elements in quartz crucibles placed in threaded graphite containers (Graphite Sales Inc, Chagrin Falls, Ohio) sealed with a grafoil gasket. Samples were melted under

a He atmosphere in a graphite resistance heated furnace (Thermal Technology LLC, Santa Rosa, CA) at 1100°C for 2 hours, then samples were solidified at a rate of $-10^{\circ}\text{C}/\text{min}$. Ingots were crushed in a mortar and pestle and mechanically alloyed in a planetary mill to obtain the desired skutterudite phase. Milling was performed in a PM100 planetary ball mill (Retsch, Haan, Germany) using 125 ml WC milling jar and 10 mm WC media. Powder was consolidated on a hot press at a temperature between 200 and 250°C with an applied pressure of 62 MPa. The pressed samples were held at the densifying temperature and pressure for $> \frac{1}{2}$ hour, then were allowed to cool to room temperature at a rate of $-1.5^{\circ}\text{C}/\text{min}$. Temperature, pressure, and ram travel were monitored on the hot press during consolidation. Samples were handled in an Ar glovebox (MBRAUN, Garching, Germany) to minimize moisture and oxygen exposure. Details of sample processing will be addressed in the following section. Tables 9.1 and 9.2 summarize the samples investigated in this work, listed with their nominal stoichiometries. Samples 1 and 2 contained no Co (indicated with x parameter) and varied in Sn (indicated with y) level from 4.0 to 5.0. Samples 2-6 had the same level of Sn (5.0) but varied in Co level from 0.0 to 2.0. Samples 6-8 had the same Co level (2.0) but varied in Sn from 5.0 to 3.0. Samples 9-13 in Table 9.2 are identical to sample 7, but with various lanthanide series fillers including Ce, Dy, and Yb. Tables 9.1 and 9.2 also summarize the measured skutterudite lattice parameters, skutterudite phase quantity, and the room temperature transport properties. Discussion on the thermoelectric transport properties will be found in section 9.4.

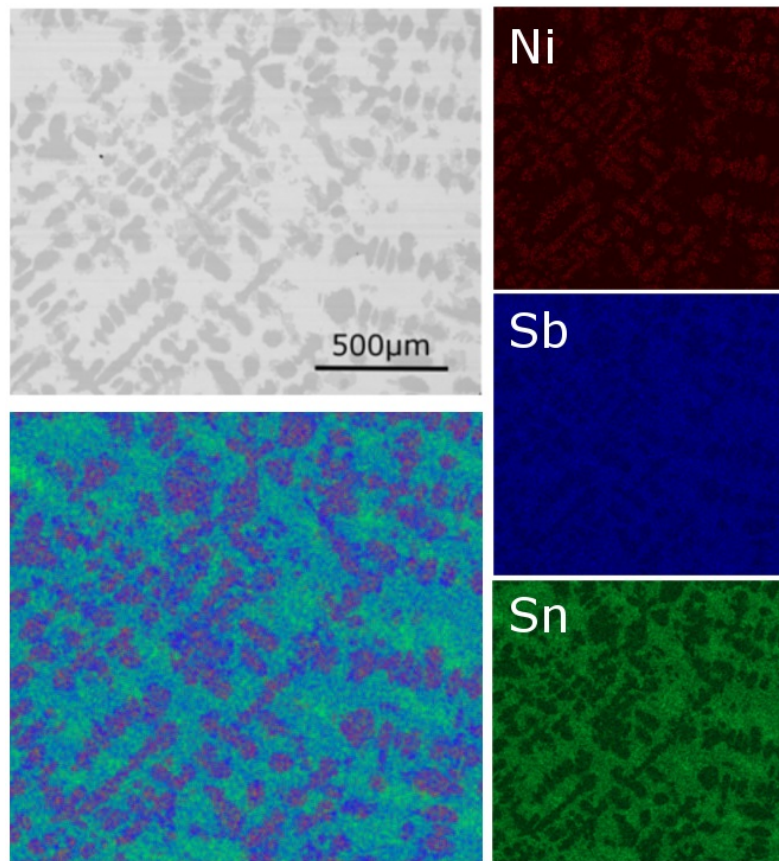


Figure 9.5: Backscattered electron and EDS chemical map of the solidified ingot of sample 1 ($\text{Ni}_4\text{Sb}_8\text{Sn}_4$).

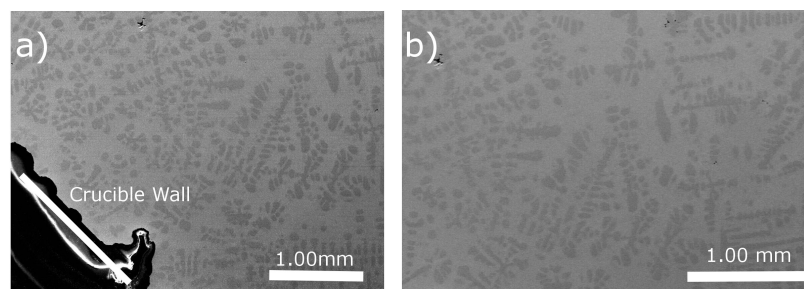


Figure 9.6: Backscattered electron micrographs a) near the crucible wall and b) toward the center of the ingot of sample 3 ($\text{Co}_{0.5}\text{Ni}_{3.5}\text{Sb}_7\text{Sn}_5$).

Table 9.1: Summary of $\text{Co}_x\text{Ni}_{4-x}\text{Sb}_{12-y}\text{Sn}_y$ skutterudite samples and room temperature properties.

Sample #	Co (x)	Sn (y)	Lattice Parameter (\AA)	SKD (wt%)	Seebeck Coefficient ($\mu\text{V/K}$)	Electrical Resistivity ($\mu\text{Ohm-cm}$)	Thermal Conductivity (W/m-K)
1	0.0	4.0	9.113	96.8	-40.7	233	4.7
2	0.0	5.0	9.128	86.9	-33.4	255	4.1
3	0.5	5.0	9.126	95.1	-8.7	560	2.2
4	1.0	5.0	9.118	89.0	32.9	784	1.6
5	1.5	5.0	9.123	91.5	13.7	449	1.4
6	2.0	5.0	9.104	79.2	7.1	233	3.9
7	2.0	4.0	9.109	93.4	17.7	540	2.5
8	2.0	3.0	9.087	98.8	37.9	2282	1.5

Initial melting and solidification step was necessary to obtain mechanical properties of powders suitable for mechano-chemical alloying. If starting constituents without melting were milled directly agglomeration occurred limiting the milling and alloying. The intermediate set of phases processed through melting and solidifying the elements were brittle and allowed the powders to mechanically alloy. Figure 9.5 shows a backscattered electron (BSE) micrograph and EDS chemical maps of the sample 1 ($\text{Ni}_4\text{Sb}_8\text{Sn}_4$) ingot (dimensions of approximately 1" diameter by 2" tall). The ingot consisted of a dendritic network of large NiSb (1147 °C melting temperature)

Table 9.2: Summary of $A_z\text{Co}_2\text{Ni}_2\text{Sb}_8\text{Sn}_4$ skutterudite samples and room temperature properties.

Sample #	Filler A	Level (z)	Lattice Parameter (\AA)	SKD (wt%)	Seebeck Coefficient ($\mu\text{V/K}$)	Electrical Resistivity ($\mu\text{Ohm-cm}$)	Thermal Conductivity (W/m-K)
7	N/A	0.0	9.109	93.4	25.3	659	2.5
9	Ce	0.1	9.108	94.8	35.1	1036	2.1
10	Dy	0.1	9.114	93.7	27.4	681	2.9
11	Yb	0.05	9.019	94.5	23.3	618	2.6
12	Yb	0.1	9.111	94.6	25.6	592	2.9
13	Yb	0.2	9.114	94.5	-	-	-

dendrites surrounded by a boundary layer $< 40\mu\text{m}$ of NiSb_2 (630°C melting) in a matrix of SbSn (425°C melting). Primary arm spacing of NiSb dendrites is on average $54\mu\text{m}$. No skutterudite phase was found in the solidified ingot for sample 1. Figure 9.6 shows two BSE micrographs of the sample 3 ($\text{Co}_{0.5}\text{Ni}_{3.5}\text{Sb}_7\text{Sn}_5$) ingot taken in the center and near the edge of the ingot, where the melt made contact with the crucible wall. EDS and powder XRD confirmed that the presence of Co promotes the formation of the skutterudite phase in the ingots. The microstructure of Figure 9.6 consists of large dendrites of the desired skutterudite phase surrounded by a phase of $\text{Ni}_x\text{Co}_{1-x}\text{Sb}_2$ in a matrix of SbSn . The average primary dendrite arm spacing of the

skutterudite phase is $75\ \mu\text{m}$, no strong dendrite orientation was observed near the crucible wall indicating equiaxed growth.

The ingots were investigated for trace impurities, spatial compositional homogeneity, and phase with ICP, powder XRD, and EDS all sampled from different regions of the ingots. The ingots were found to contain <300 ppm of Ca, Mg, and Na impurities. Impurities were found primarily near the ingot's top surface and the side, where the ingot made contact with the quartz crucible. Composition of the bulk of the ingot was within $\pm 1\%$ of the target nominal composition, indicating Sb loss is not significant during the melting process. As indicated by the micrographs, Figures 9.5 and 9.6, the bulk of the ingots were fully dense but the top 3 mm of the ingots displayed a high level of porosity. ICP and XRD did not reveal a significant difference in composition and phase between the bulk of the ingot and the porous top 3 mm, other than the higher levels of impurity.

The ingots were crushed by hand in a mortar and pestle and were milled; powder was sampled intermittently for XRD. Rietveld refinement was performed on the XRD data using Bruker's TOPAS software. The refinement results, shown for two samples in Figure 9.7, calculated the quantitative wt% of phases as a function of milling time. Additionally, the change in lattice parameters and crystallite size of the phases was refined. The XRD data was collected twice, once with the powder under an inert Ar atmosphere and a second time in air. The difference between the two datasets was negligible, so further XRD was collected in air to avoid an undesirable artifact of the inert atmosphere sample holders, which superimpose a

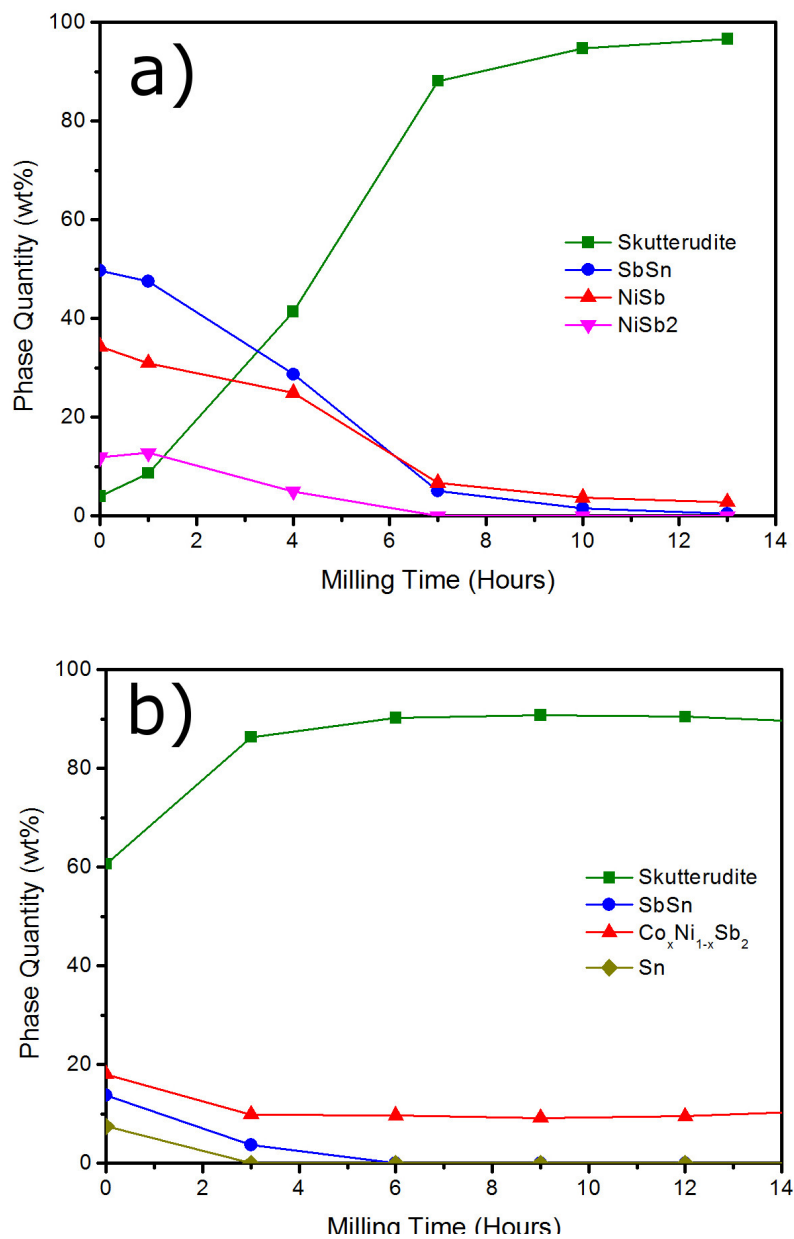


Figure 9.7: Milling study of phase change calculated from XRD taken at intervals during milling: a) sample 1 $\text{Ni}_4\text{Sb}_8\text{Sn}_4$ nominal, b) sample 4 $\text{Co}_1\text{Ni}_3\text{Sb}_7\text{Sn}_5$ nominal.

large amorphous hump near 30° . The goodness-of-fit (GOF) of the refinements were all less than 2.5. As shown in Figure 9.7a the initial ingot sample 1 ($\text{Ni}_4\text{Sb}_8\text{Sn}_4$) contained only 4 wt% of the desired skutterudite phase and was primarily SbSn, NiSb, and NiSb_2 . After 7 hours of milling the powder began to approach 88 wt% of the desired skutterudite phase with all other phases decreasing uniformly. By 12 hours the undesired phases were nearly consumed into the main skutterudite phase (97 wt%). The final milled skutterudite lattice parameter was 9.106 \AA and the crystallite size was 52 nm. Introduction of Co into the system stabilized the structure as shown in the milling study on sample 4 ($\text{Co}_1\text{Ni}_3\text{Sb}_7\text{Sn}_5$) in Figure 9.7b. The 0 hour ingot contained nearly 60 wt% skutterudite with the secondary phases NiSb, SbSn, and Sn. After only 6 hours of milling, under the same conditions of the previous sample, the skutterudite phase approached 90 wt%. In addition to stabilizing the skutterudite phase the Co addition also resulted in a $\text{Co}_x\text{Ni}_{1-x}\text{Sb}_2$ phase (refined lattice parameters $a\text{-}3.913$ $c\text{-}5.136 \text{ \AA}$ as compared to NiSb $a\text{-}3.915$ $c\text{-}5.144 \text{ \AA}$ [208]) which could not be reduced below 10 wt% with milling. The milling study was continued up to 18 hours but the phase concentration remained stable after 6 hours of milling. The skutterudite lattice parameter was 9.132 \AA and the crystallite size was 24 nm.

The powder was consolidated in a hot press to form $\frac{1}{2}$ " diameter by 1" tall pellets (Fig. 9.8). Pellets were cut for transport property characterization and sectioned for SEM/microprobe; remaining pieces were crushed for powder XRD. The microstructure of the pellets is highlighted for three samples in Figure 9.9, showing two scales of BSE micrographs and an XRD Rietveld summary. Sample 1, Figure 9.9a



Figure 9.8: Typical hot pressed skutterudite ingots, 1/2" diameter by 1" tall. Shown cut for electrical measurement (rectangular prism) and thermal measurement (disk).

and 9.9b, is composed of a matrix of skutterudite (96.6 wt%, space group Im-3), NiSb precipitates with mean diameter 1.0 μm (2.3 wt%, space group P63/mmc, dark phase in BSE micrographs), and larger SbSn precipitates 30 μm (1.1 wt%, space group R-3m). The matrix skutterudite was found to be $\text{Ni}_4\text{Sb}_{8.5}\text{Sn}_{4.6}$ per electron probe microanalysis (EPMA). The EPMA results are presented for all samples in Table 9.3. The XRD calculated crystallite size of the skutterudite was 155 nm with lattice parameter 9.113 Å (before pressing the powders had 52 nm crystallite size and 9.106 Å lattice parameter). The 1 μm NiSb phase has a crystallite size of 93 nm and the 30 μm SbSn phase has a crystallite size of 59 nm, indicating polycrystalline precipitates.

Sample 2, shown in Figure 9.9c and 9.9d, was identified as $\text{Ni}_{4.0}\text{Sb}_{7.9}\text{Sn}_{5.4}$ (87.4 wt%) per EPMA. Showing that the desired change in Sn content was achieved despite the presence of a new Ni_3Sn_4 precipitate that did not exist for samples with lower Sn content. In addition to the skutterudite phase the sample also contained 1

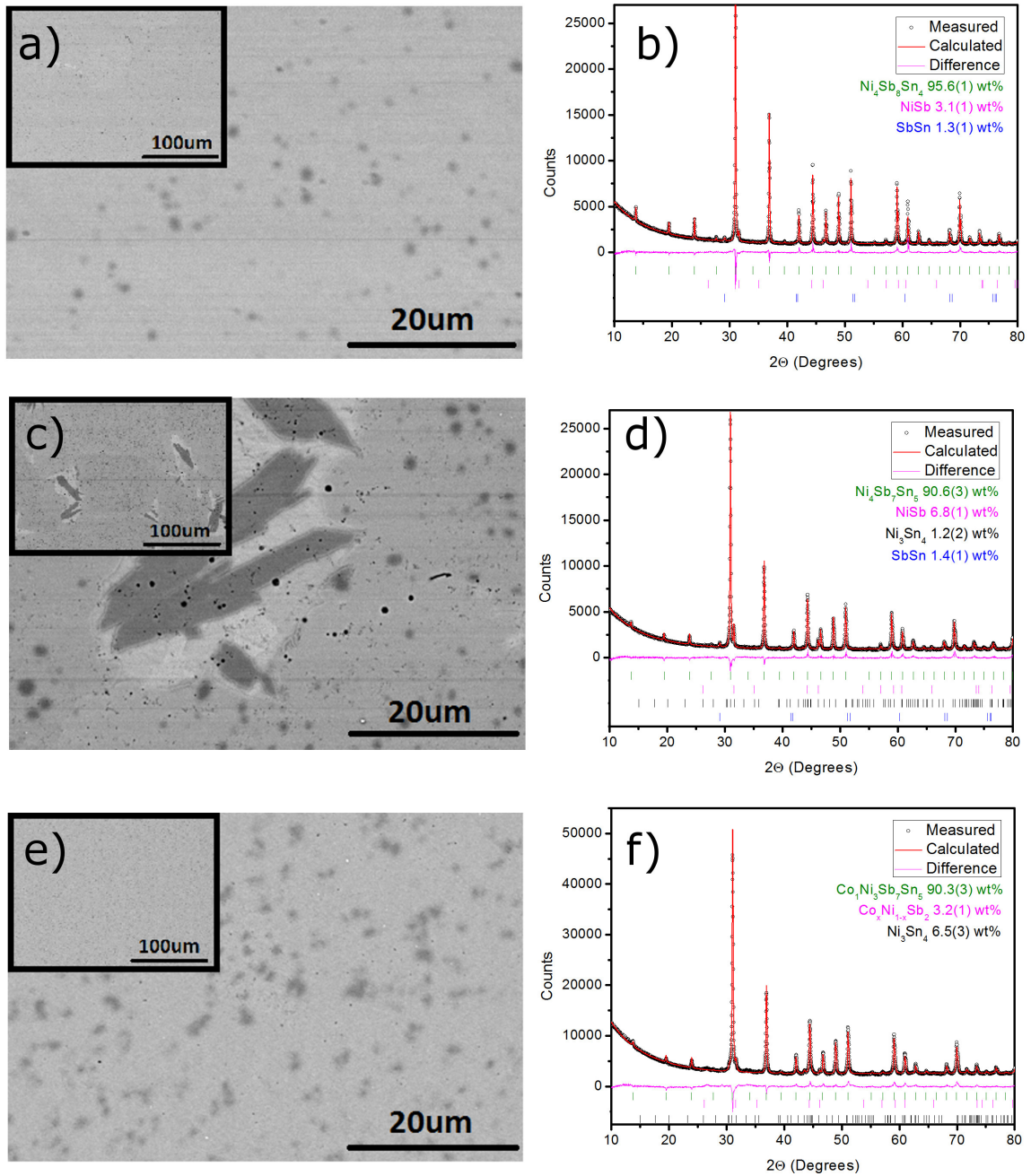


Figure 9.9: Microstructure and XRD Rietveld refinement on three hot pressed samples. a) and b) sample 1 c) and d) sample 2 e) and f) sample 4.

Table 9.3: Electron probe microanalysis (EPMA) of skutterudite samples

Sample	Co	Co	Ni	Ni	Sb	Sb	Sn	Sn
#	Nom.	EPMA	Nom.	EPMA	Nom.	EPMA	Nom.	EMPA
1	0.0	0.0	25.0	23.5	50.0	49.7	25.0	26.8
2	0.0	0.0	25.0	23.2	43.8	45.7	31.3	31.2
3	3.1	3.3	21.9	21.0	43.8	44.8	31.3	30.9
4	6.3	6.6	18.8	15.7	43.8	46.0	31.3	31.8
5	9.4	-	15.6	-	43.8	-	31.3	-
6	12.5	11.9	12.5	8.2	43.8	48.6	31.3	31.3
7	12.5	12.7	12.5	11.1	50	53.1	25	23.1
8	12.5	13.1	12.5	12.2	56.3	57.1	18.8	17.5

μm NiSb (8.5 wt%, small dark phase in BSE micrograph) with 30 μm Ni_3Sn_4 (1.7 wt%, space group C12/m1, large dark phase in BSE micrograph) surrounded by SbSn (2.5 wt%, light phase in BSE micrograph). Sample 4, shown in Figure 9.9e and 9.9f, was identified as $\text{Co}_{1.2}\text{Ni}_{2.8}\text{Sb}_{8.3}\text{Sn}_{5.7}$ (89.3 wt%) selected to demonstrate the influence of Co addition. The sample also contained precipitates of $\text{Co}_x\text{Ni}_{1-x}\text{Sb}_2$ (3.5 wt%) and Ni_3Sn_4 (7.2 wt%) although the two phases could not be discerned from one another in the BSE micrographs. The Ni_3Sn_4 phase was found in all samples with the higher Sn level (samples 2-6, $y = 5$). The SbSn phase was suppressed in Co containing samples (samples 3-8).

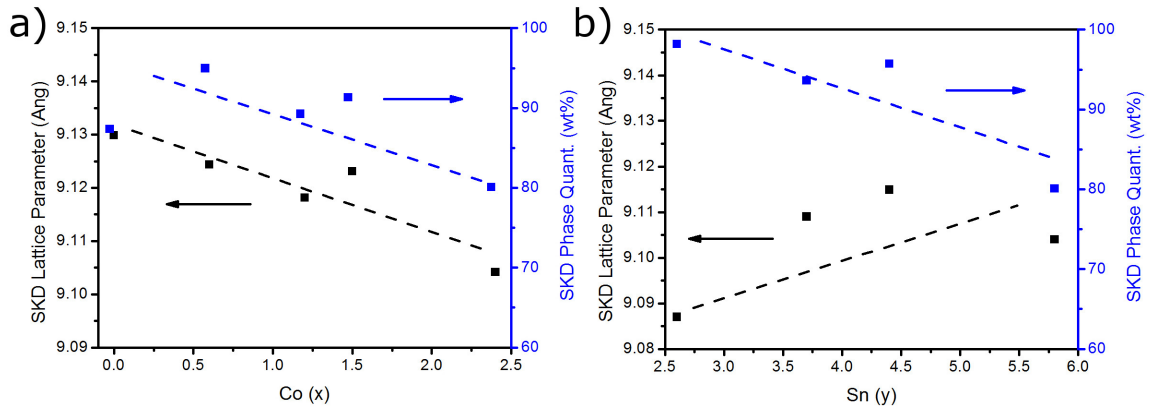


Figure 9.10: Summary of data presented in Table 9.1 with skutterudite lattice parameter and phase quantity (wt%) for a) Co (x) study and b) Sn (y) study. Dashed lines are added to guide the eye.

Figure 9.10 summarizes the lattice parameter and skutterudite phase quantity data shown in Table 9.1 for the composition $\text{Co}_x\text{Ni}_{4-x}\text{Sb}_7\text{Sn}_5$ with x from 0 to 2.4. The skutterudite lattice parameter decreases with increasing Co level from 9.128 Å at a Co (x) level of 0 to 9.104 Å at an Co (x) level of 2.4. Likewise from a Co (x) level of 0.6 the skutterudite phase purity decreases from 94.97 wt% to 80.08 wt% at a Co (x) level of 2.4. The skutterudite lattice parameter generally increases with increasing Sn (y) level from 9.087 Å at a Sn (y) level of 2.6 to 9.104 Å at a Sn (y) level of 5.8. The skutterudite phase purity decreases with increasing Sn (y) level from 98.20 wt% for Sn (y) level of 2.6 to 80.08 wt% at a Sn(y) level of 5.8. These trends (Fig. 9.10b) are for the compositions $\text{Co}_2\text{Ni}_2\text{Sb}_{12-y}\text{Sn}_y$ with y from 2.6 to 5.8 as evaluated from EPMA data of Table 9.3. Thus the stability of the skutterudite phases is highly dependant on both Co and Sn level with high levels of both resulting in undesired secondary

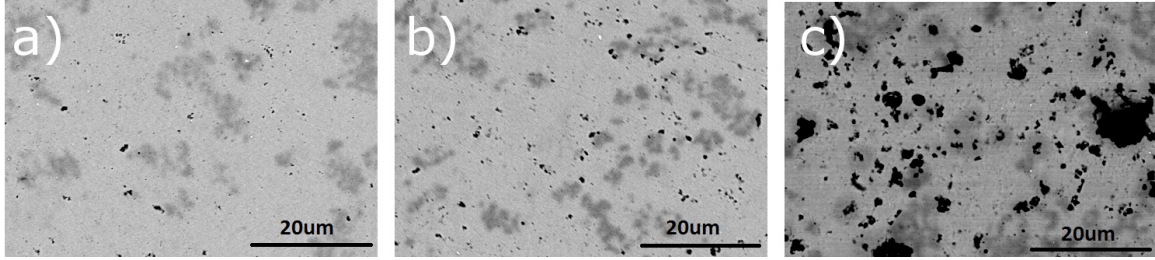


Figure 9.11: Annealing of sample 6 displaying increased porosity and decomposition to the Ni_3Sn_4 phase. a) As sintered sample, b) after 200°C anneal for 72 hours, c) after 400°C anneal for 72 hours

phases. The presence of secondary phases in the system make characterization of the intended skutterudite phase more difficult.

An annealing study was performed on the hot pressed sample 6 ($\text{Co}_2\text{Ni}_2\text{Sb}_7\text{Sn}_5$) to improve the phase purity of the samples. Pieces of the sample were annealed for 72 hours in an inert N_2 atmosphere at 200°C and 400°C . Figure 9.11 displays the microstructure of a) as sintered b) 200°C anneal and c) 400°C anneal samples. The dark regions of the micrographs are porosity, which increases with higher temperature anneal. The gray precipitates are a combination of Ni_3Sn_4 and $\text{Co}_x\text{Ni}_{1-x}\text{Sb}_2$ secondary phases. The as sintered sample density decreased from 99% (7.64 g/cm^3) after annealing at 200°C to 95% (7.25 g/cm^3) and to 88% (6.75 g/cm^3) after annealing at 400°C . Along with increased porosity, samples decomposed into Ni_3Sn_4 and Sn phases. The increased porosity is a result of the phase change from the skutterudite phase with a nominal density of 7.2 g/cm^3 to the Ni_3Sn_4 phase with a density of 8.6 g/cm^3 . The $\text{Co}_2\text{Ni}_2\text{Sb}_7\text{Sn}_5$ skutterudite is not thermally stable above 200°C .

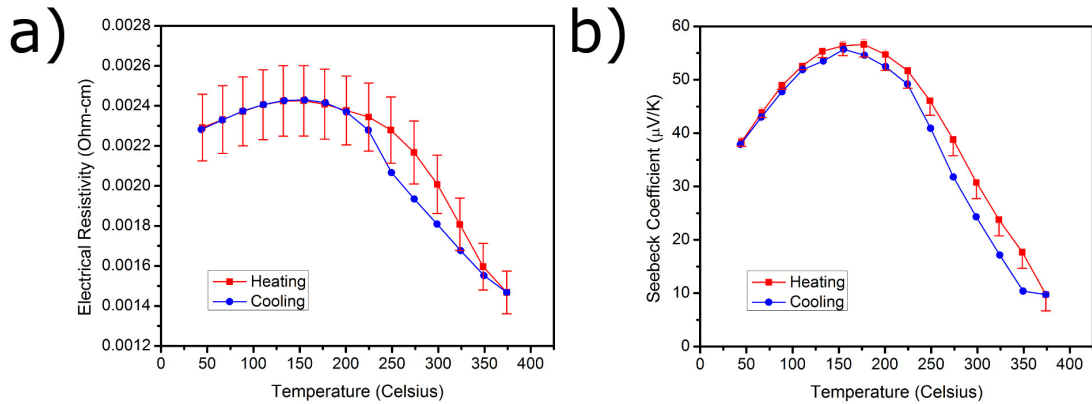


Figure 9.12: a) Resistivity versus temperature and b) Seebeck coefficient versus temperature for sample 8 displaying repeatable hysteresis loops on heating and cooling curves.

Thus, this phase transition has also been observed in the thermoelectric transport properties.

Figure 9.12 shows the electrical conductivity and Seebeck coefficient of sample 8 ($\text{Co}_2\text{Ni}_2\text{Sb}_9\text{Sn}_3$) as a function of temperature. Sample 8 has the greatest amount of skutterudite phase among the compositions in the set (see Table 9.1). The heating and cooling curves of the measurement are plotted separate to highlight the hysteresis of the measurement. The heating measurement was obtained over 8 hours as the temperature increased from 40°C to 460°C with a $\frac{1}{2}$ hour hold at each measurement for thermal stability. Likewise the cooling measurement was obtained over 8 hours as the temperature decreased from 460°C to 40°C with the same $\frac{1}{2}$ hour steps. The path plotted for sample 8 was repeated with a high level of repeatability over four heating/cooling cycles thus the hysteresis was repeatable indicating reversible changes. The change in properties on heating and cooling around 250°C are indicative of a

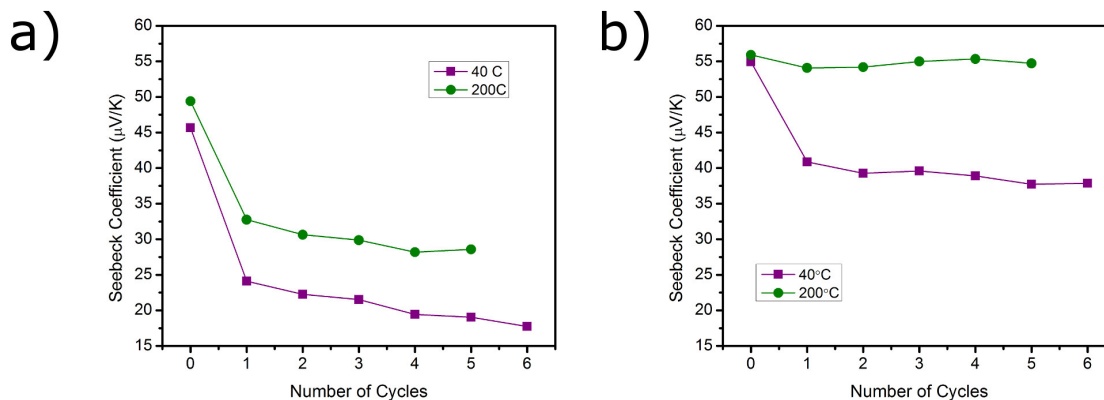


Figure 9.13: Seebeck coefficient at 40°C and 200°C as a function of testing cycle count. Shown for a) sample 7 and b) sample 8, sample 7 trend is typical of samples 1-7.

phase transformation. Below 250°C the properties of sample 8 are stable, repeatable, and hysteresis free. This section of repeatable results defines the usable range for the thermoelectric transport data. Similar discontinuities around 250°C were observed for all samples in this study, but the properties of the other samples degraded with repeated testing. The discontinuity at 250°C coincides with a peak at 237°C in DSC data, which is near the reported eutectic temperature of $(\text{Sn})+\text{Ni}_3\text{Sn}_4$ (231°C).

The thermal stability of the electrical properties of samples is displayed in Figure 9.13. The plots show Seebeck coefficient at 40°C and 200°C as a function of testing cycle count. The data is shown for sample 7 (Fig. 9.13a) and sample 8 (Fig. 9.13b). Sample 7 displays electronic properties which continuously degrade with repeat testing cycles. The largest reduction in properties is in the first measurement cycle, with smaller reductions for further cycles. The trend is found in both the resistivity and Seebeck data for sample 7. Similar trends were found for the other

samples with the exception of sample 8, which has a large initial reduction after the first measurement cycle followed by stable and repeatable properties.

9.4 $\text{Co}_x\text{Ni}_{4-x}\text{Sb}_{12-y}\text{Sn}_y$ Thermoelectric Properties

The electrical resistivity and Seebeck coefficient of the samples in this set were measured between 40°C and 250°C (Fig. 9.14) to avoid the complexities of the phase change described in the previous section. Samples 3 ($\text{Co}_{0.5}\text{Ni}_{3.5}\text{Sb}_7\text{Sn}_5$) and 4 ($\text{Co}_1\text{Ni}_3\text{Sb}_7\text{Sn}_5$) exhibited intrinsic semiconductor behavior, characterized by decreasing electrical resistivity with increasing temperature. The remainder of the samples in the set displayed properties of a heavily doped extrinsic semiconductor, increasing electrical resistivity with increasing temperature. The uncertainty bars included in the plots are typical of all samples, but only one set per plot is presented to avoid crowding of the data. The variation of Co (x) content (Fig. 9.14a and b) resulted in electrical resistivity ranging from 250 to 800 $\mu\text{Ohm-cm}$ and showed both p- and n-type behavior with Seebeck coefficients ranging from -40 to $+40$ $\mu\text{V/K}$. The variation of Sn (y) content (Fig. 9.14c and d) resulted in a larger range of electrical resistivity from 250 to 2500 $\mu\text{Ohm-cm}$ and only p-type behavior was observed with Seebeck Coefficients of 10 to 58 $\mu\text{V/K}$. For the entire set the Seebeck coefficients were too low to be used as a valuable thermoelectric material and further improvements must be made.

The electrical resistivity and Seebeck coefficient data is summarized in Figure 9.15. The plots show the 40°C and 200°C measurements as a function of Co (x)

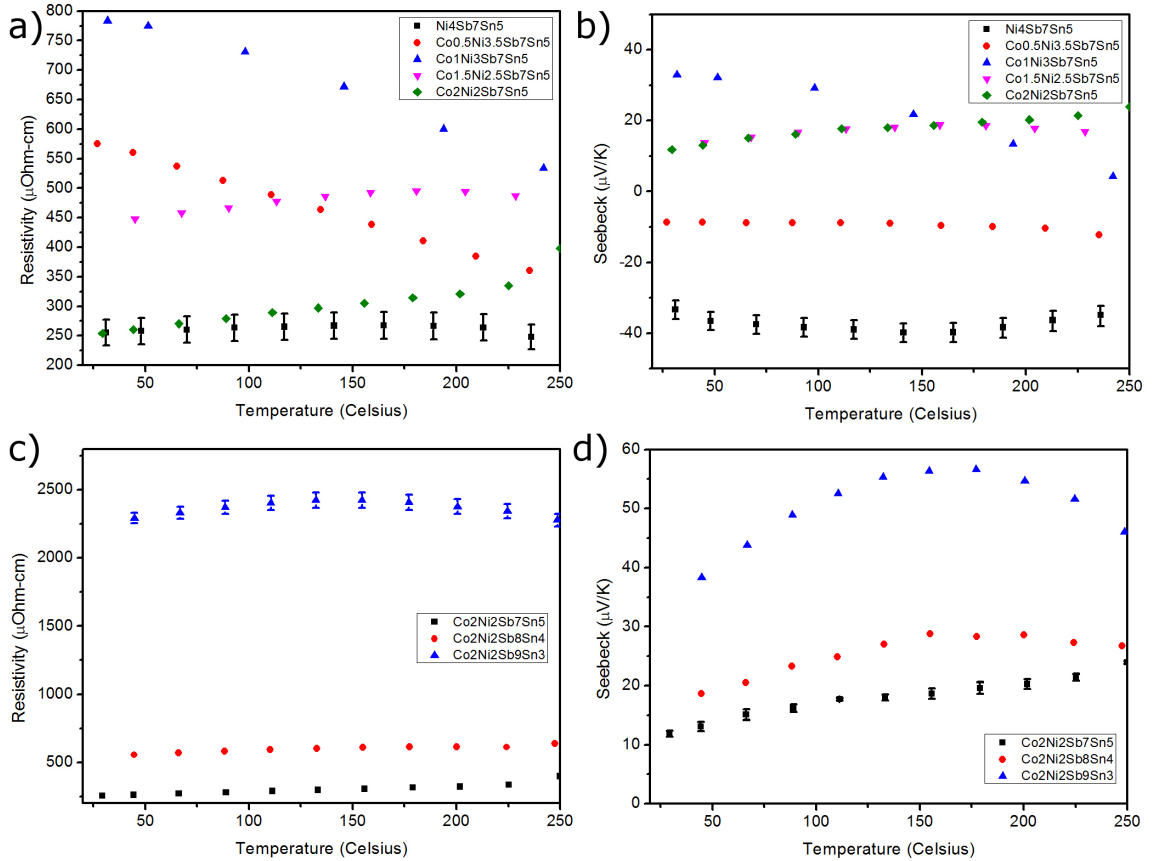


Figure 9.14: (a and c) Resistivity versus temperature and (b and d) Seebeck coefficient versus temperature for samples 2-6 (a and b) and samples 6-8 (c and d).

and Sn (y). The Co and Sn content was measured using EPMA data, not the nominal values. The results presented are taken from repeat testing of the samples to avoid the misleading data measured on the first run, as shown previously in Figure 9.13. The electrical resistivity initially increased with Co (x) content from 0 to 1.2, then decreased with higher levels of Co (Fig. 9.15a). The n-type behavior crossed over to p-type at and above $x = 0.8$ based on Seebeck coefficient measurements (Fig. 9.15b). The ability to tune for both n-type and p-type behavior allows couple fabrication with

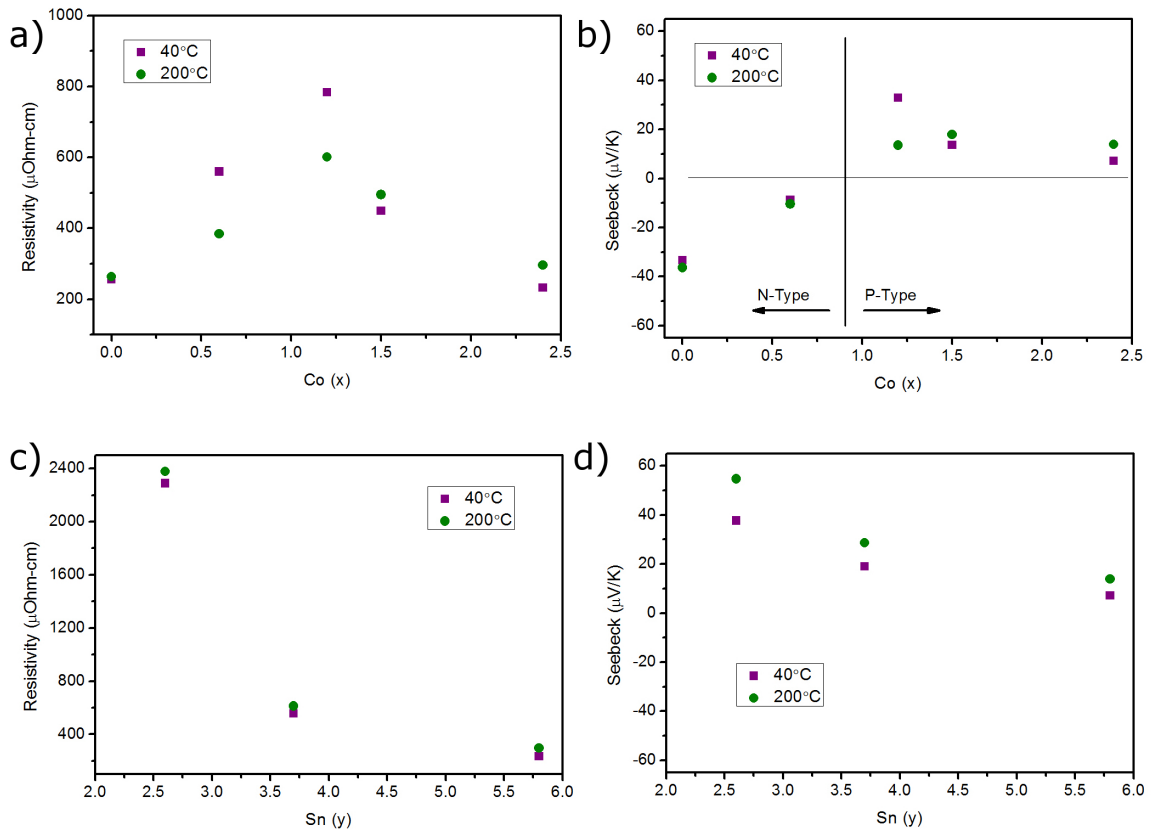


Figure 9.15: Room temperature and 200°C resistivity and Seebeck coefficient for Co (x) level (a and b) and Sn (y) level (c and d) in $\text{Co}_x\text{Ni}_{4-x}\text{Sb}_{12-y}\text{Sn}_y$ system.

compatible n- and p-type legs. Sn (y) content continuously decreased both the electrical resistivity and the absolute value of the p-type Seebeck coefficient (Fig. 9.15c and d). The electrical resistivity was more sensitive to the Sn level than the Co level as nearly an order of magnitude difference in properties was achieved for a similar range of Sn content as Co content.

The thermal conductivity and material figure of merit of the samples in this set were measured between 40°C and 250°C (Fig. 9.16). Total thermal conductivity

is shown with the filled symbols while lattice thermal conductivity is shown with the open symbols. Lattice conductivity was calculated by the Wiedemann-Franz law

$$k_l = k - L\sigma T, \quad (9.1)$$

where k_l is the lattice thermal contribution, k the total thermal conductivity, T the absolute temperature, σ the electrical conductivity, and L Lorenz number. The Lorenz number was approximated from a SPB model. The justification for applying the SPB model was discussed previously in section 3.3. Using a band model rather than the classic Lorenz number allows the inclusion of the effects of temperature. The Lorenz number was calculated as

$$L = \frac{k_b^2}{e^2} \frac{3F_0F_2 - 4F_1^2}{F_0^2}, \quad (9.2)$$

where k_b is the Boltzmanns constant, e the charge on an electron, and F_i the i^{th} Fermi integral, which is dependent on the reduced electrochemical potential η . The electrochemical potential was calculated iteratively from the temperature dependent Seebeck coefficient data as

$$S = \frac{k_b}{e} \left(\frac{2F_1}{F_0} - \eta \right). \quad (9.3)$$

Total thermal conductivities ranged from 1.5 to 7.5 W/m-K as a function of Co content (Fig. 9.16a) and from 1.5 to 4.5 as a function of Sn content (Fig. 9.16c). Lattice conductivities ranged from accounting for 10% of total conductivity to 90% of

total conductivity for samples 6 ($\text{Co}_2\text{Ni}_2\text{Sb}_7\text{Sn}_5$) and 8 ($\text{Co}_2\text{Ni}_2\text{Sb}_9\text{Sn}_3$), respectively. In the case of sample 5 ($\text{Co}_{1.5}\text{Ni}_{2.5}\text{Sb}_7\text{Sn}_5$) the calculated lattice conductivity was negative below 125°C , a physical impossibility and indicator of a sample which may be too metallic to model using a single parabolic band model. As a result of the low Seebeck coefficients of the samples in the set, combined with their general metallic nature, the figure of merits were low. The peak figure of merit for the system with variable Co content was less than 0.05 (Fig. 9.16b) and the system with variable Sn content was less than 0.03 (Fig. 9.16d).

Figure 9.17 summarizes the total thermal conductivity and figure of merit trends for the Co (x) and Sn (y) systems. A key feature of the Co (x) system was the possibility to tune the thermal conductivity with Co level. A minimum thermal conductivity was achieved in the system for $x = 1.5$ with a room temperature thermal conductivity of 1.5 W/m-K (Fig. 9.17a). This low thermal conductivity can be understood by considering the disorder induced through Co-Ni bond phonon alloy scattering. For either pure Co or Ni the scattering on Co-Ni bonds would be minimized, but as the Co-Ni solid solution approaches 50% a maximum phonon scattering should be achieved resulting in a minimum thermal conductivity. The exact location of the minimum depends on the properties of the Co and Ni atoms, and is found at $x = 1.5$. The figure of merit for the Co (x) system was split between an n- and p-type material. The best room temperature figure of merit in the n-type region was 0.03 for $x = 0$ and was 0.05 for $x = 1.5$ in the p-type region (Fig. 9.17b). The room temperature thermal conductivity increased with increasing Sn content from

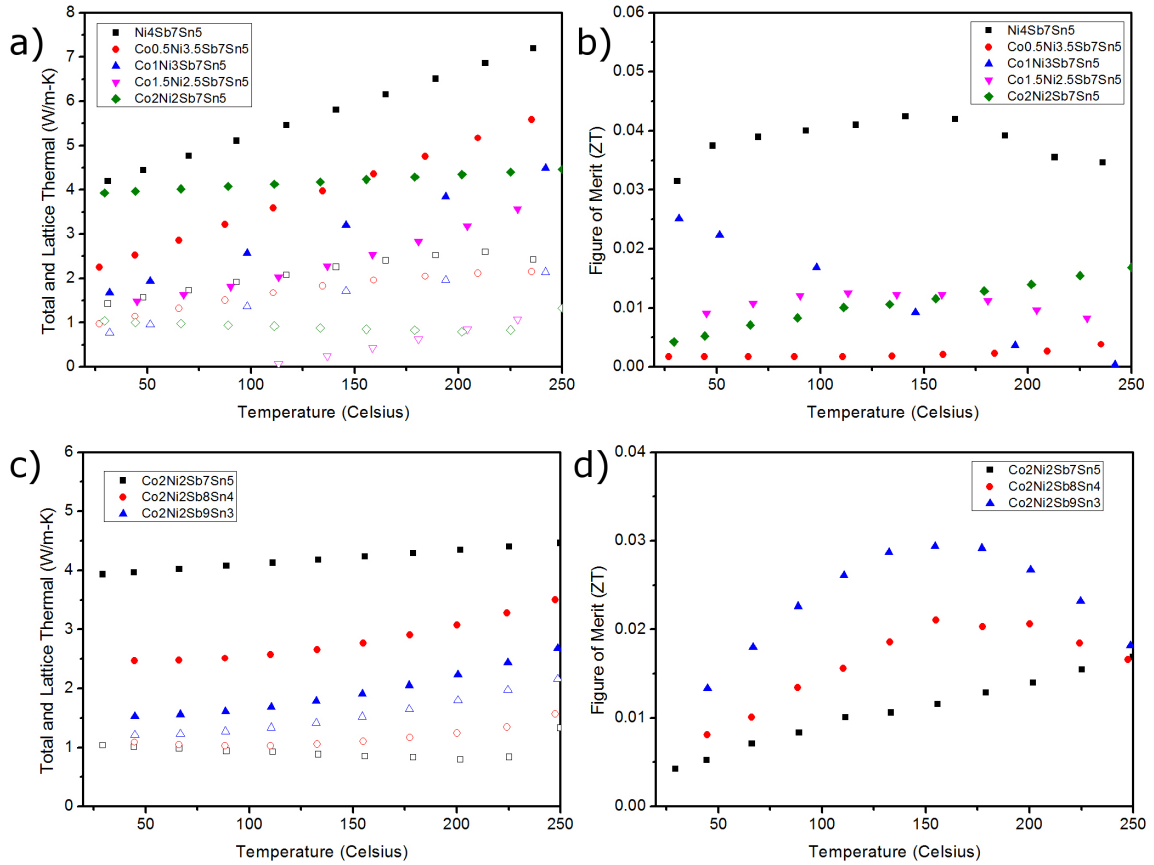


Figure 9.16: (a and c) Thermal conductivity versus temperature and (b and d) material figure of merit versus temperature for samples 2-6 (a and b) and samples 6-8 (c and d). Total thermal conductivity shown with solid symbols, calculated lattice thermal conductivity shown with open symbols.

1.5 to 4.0 W/m-K (Fig. 9.17c). Similar to the Co-Ni compositions a disorder induced reduction in thermal conductivity should be observed in the Sb-Sn pnictogen rings. Although, if a minimum thermal conductivity does exist it must have lie outside of the range of compositions tested here. The stability of the skutterudite phase may not permit the formation of the composition which would produce the minimum thermal conductivity. Samples with lower Sn levels should be investigated to confirm

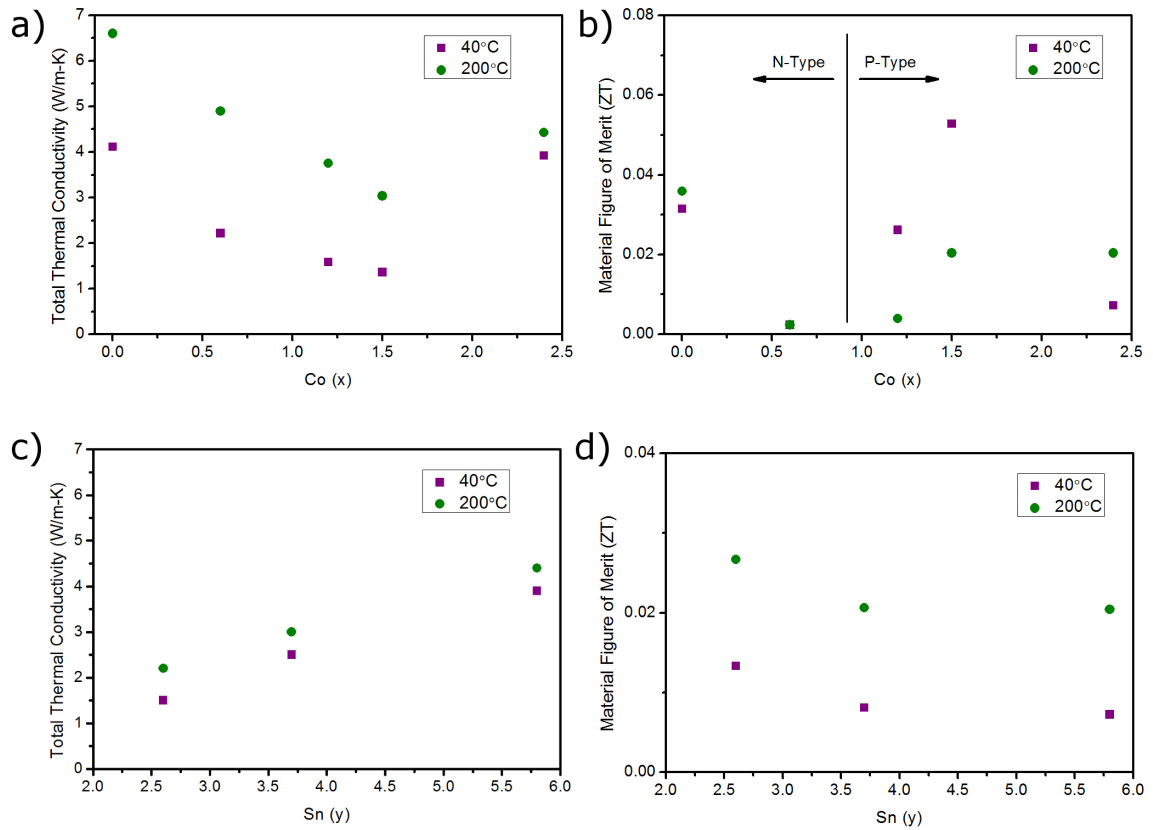


Figure 9.17: Room temperature and 200 °C total thermal conductivity and material figure of merit for Co (x) level (a and b) and Sn (y) level (c and d) in $\text{Co}_x\text{Ni}_{4-x}\text{Sb}_{12-y}\text{Sn}_y$ system

this. The figure of merit of the Sn (y) system uniformly decreased with increasing Sn content (Fig. 9.17d). The room temperature figure of merit of these samples is below 0.02.

The room temperature carrier density of skutterudites ranged from $1 * 10^{17}$ to $1 * 10^{21} \text{ cm}^{-3}$ with hall mobilities ranging from 3 to 9,000 $\text{cm}^2\text{V}^{-1}\text{s}^{-1}$ (Fig. 9.18) [64, 65, 87–90]. The samples created in this work are marked on the plot with red and blue stars, denoting n- and p-type respectively. In general the simple binary

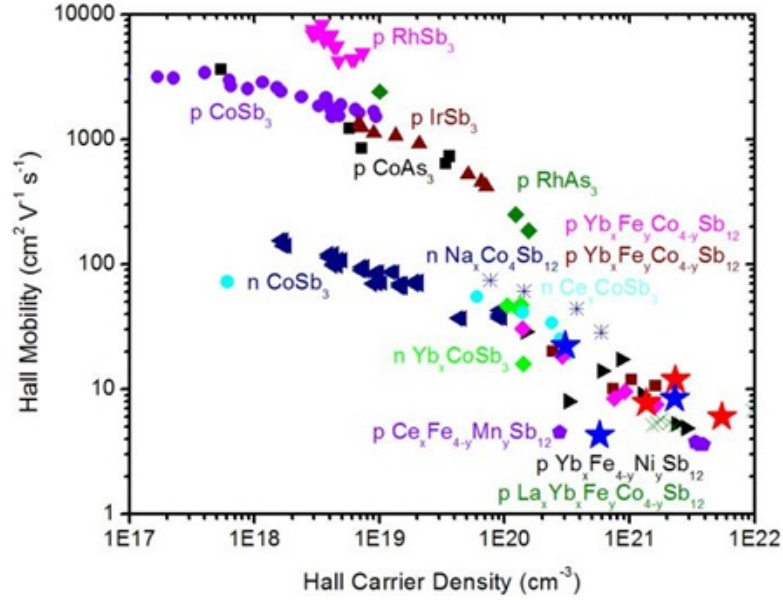


Figure 9.18: Room temperature hall mobilities and hall carrier densities of several skutterudites [64, 65, 87–90]. Samples in this work are shown with stars.

skutterudites (CoSb_3 , CoAs_3 , IrSb_3 , RhSb_3, \dots) have lower carrier densities and higher mobilities compared to the filled skutterudites ($\text{Ce}_x\text{CoSb}_3, \text{La}_x\text{Yb}_y\text{Fe}_z\text{Co}_{4-z}\text{Sb}$, $\text{Yb}_x\text{Fe}_{4-y}\text{Ni}_y\text{Sb}_{12}, \dots$). The samples of this work fell in-line with the filled skutterudites. Combining the carrier concentration, mobility, and thermoelectric transport data the system can be investigated further with a single parabolic band model (SPB). The model provides a simple means of predicting the optimal figure of merit which could be achieved in the system. The model was applied as discussed by May and Snyder [146] and followed the outline provided in Chapter 3. Figure 9.19 shows the optimal predicted figure of merit to be 0.5 for the n-type system and 0.25 for the p-type system at a temperature of 400K. The optimal carrier density for the n-type system was $2.1 \times 10^{19} \text{ cm}^{-3}$ and the p-type system was $2.7 \times 10^{19} \text{ cm}^{-3}$. The effective

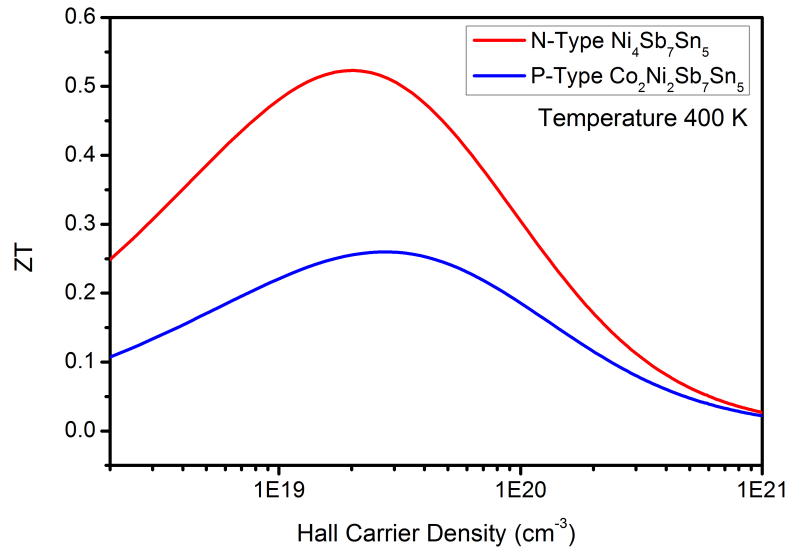


Figure 9.19: Predicted figure of merit as a function of carrier density, as calculated from a single parabolic band model. Sample 2 ($\text{Ni}_4\text{Sb}_7\text{Sn}_5$) and Sample 6 ($\text{Co}_2\text{Ni}_2\text{Sb}_7\text{Sn}_5$) calculated at 400K.

carrier mass of the system was calculated to be 5.5 for the n-type system and 1.5 for the p-type system. At this time the carrier densities of the system are much higher than the predicted optimal points, which explains the low measured figure of merit. The measured figure of merits of this system fit well with the predicted values from the SPB model.

The remaining samples of the set were duplicates of sample 7 with a range of lanthanide series fillers. The thermoelectric transport properties are shown in Figure 9.20. With the exception of the Ce filled sample the electrical resistivity of the filled samples were within measurement uncertainty of the baseline sample 7. The Ce filled sample's electrical resistivity followed the same trend as the rest of the

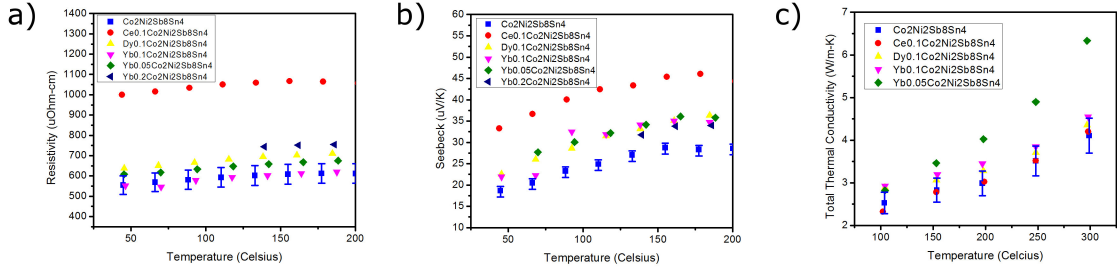


Figure 9.20: Thermoelectric properties of samples 7, 9-13. a) Electrical resistivity, b) Seebeck coefficient, and c) total thermal conductivity.

samples but is twice the magnitude. The Seebeck coefficient's of the filled samples were all higher than the baseline. The peak Seebeck coefficient of the baseline sample was 25 $\mu\text{V/K}$ compared to the Yb and Dy filled samples' 30 $\mu\text{V/K}$ while Ce had 45 $\mu\text{V/K}$. The thermal conductivity values of the entire set was within measurement uncertainty. The enhanced Seebeck coefficient of the filled samples was not significant enough to improve the figure of merit of the system drastically.

9.5 Conclusion

Ternary skutterudite systems were investigated with a number of processing routes. Formation of a skutterudite phase was not achieved for the $\text{Ni}_4\text{Bi}_8\text{Ge}_4$ and $\text{Ni}_4\text{Sb}_8\text{Ge}_4$ systems. Skutterudite phase occurred for the novel $\text{Co}_x\text{Ni}_{4-x}\text{Sb}_{12-y}\text{Sn}_y$ compositions for x value from 0 to 2.0 and y value from 3.0 to 5.0. The skutterudites were synthesized through a melt, mill, hot press procedure. Each step of the fabrication process was chemically and microstructurally characterized and it was found that high levels of Co and Sn lead to secondary phases. The thermal stability of the system

was studied through annealing studies, DSC, and by repeat testing of thermoelectric properties. It was found that samples with high Sn level decompose into a Ni_3Sn_4 phase above 231°C which increases sample porosity and degrades the thermoelectric properties.

Thermoelectric properties were measured from $25 - 400^\circ\text{C}$ and it was found that both p- and n-type conduction could be obtained, for x above and below 0.8, respectively. Electrical resistivity of samples ranged from 250 to 2500 $\mu\text{Ohm-cm}$ with Sn content (between $y=3.0$ and 5.0) providing the largest sensitivity. The Seebeck coefficient of the set was low, ranging from -40 to $58 \mu\text{V/K}$, which greatly hinders the usefulness of the system as a thermoelectric material. Thermal conductivity ranged from 1.5 to 7.0 W/m-K , with a minimum obtained for Co content of $x=1.5$. Due to the low Seebeck coefficients the resulting figure of merits were less than 0.05 for the samples measured. The system has carrier densities and mobilities comparable to filled skutterudites. Deliberately filled samples in this system were not found to have significantly improved thermoelectric properties compared to their unfilled counterparts.

CHAPTER X

CONCLUSIONS AND FUTURE WORK

10.1 Advanced Thermoelectric Design

In Chapter 4 the thermoelectric couple was discussed from several different perspectives, not classically accounted for by analytic means. Several cases were investigated including the classic assumptions from a cylindrical coordinate viewpoint. The case of variable temperature boundary conditions was investigated to account for thermal resistance between the thermoelectric elements and the heat source/sink. The investigation resulted in a Device Design Factor which incorporates the influence of end effects into the conversion efficiency equation. A guideline on required minimum leg length was established to reduce the adverse effects of the case. The case of lateral heat transfer was investigated to account for heat which travels into or out of the leg side. The investigation resulted in a Fin Factor which incorporates the influence of lateral heat into the conversion efficiency equation. A guideline on the required maximum perimeter to cross-sectional area ratio was established to reduce the adverse effects. The case of temperature dependant material properties was investigated using asymptotic expansions. The influence of variable material properties was investigated on conversion efficiency and found to cause as much as a 2% difference.

Finally, the case of a transient couple was investigated using Green's functions. The investigation resulted in an Inductance Factor and a Thermal Diffusivity Factor which capture different aspects of a transient couple. A design guideline on the required length ratio was established. The work of this chapter demonstrated the importance of considering factors other than figure of merit alone.

10.2 Measurement Uncertainty

In Chapter 6 an uncertainty analysis of the Seebeck coefficient and electrical resistivity measurements was discussed. The analysis included a number of sources such as geometric factors, statistical uncertainty, data acquisition uncertainty, and a difficult to quantify cold-finger uncertainty. The largest contributor to uncertainty at high temperature was the Seebeck uncertainty due to the cold-finger effect. The effect results in an asymmetry in the uncertainty of the measured value, likely causing over-estimation of the Seebeck coefficient. A thermal finite element analysis was performed to account for the phenomenon and the results were compared to experimental findings. As a result it was found that the uncertainty of the power factor near room temperature was $\pm 7.5\%$. At high temperature the power factor should be reported with an uncertainty of $+7.3\%/-27.0\%$. Meaningful uncertainty on thermoelectric transport data is important to the thermoelectric community because it allows for comparison of experiments between labs, and can explain discrepancies in literature.

10.3 WSi₂-Si/Ge System

In Chapter 8 a thermoelectric composite composed of a WSi₂ phase in a matrix of Si/Ge was studied. The system was investigated by both solidification and powder processing means. Studying the two processing routes helped to gain a deeper understanding of the system. In the solidified samples the microstructure was characterized by large micron sized WSi₂ precipitates in an inhomogeneous Si/Ge matrix. Thermoelectric transport properties revealed the silicide phase to cause a 50% enhancement in the electronic power factor, but the figure of merit was not increased due to a corresponding increase in thermal conductivity. It was also discovered that the selection of crucible used for the melt plays a significant role in controlling the doping of the system, as boron nitride crucibles significantly dope the samples to p-type. The powder processed samples were characterized by a broad spectrum of nano to micron sized WSi₂ precipitates in a comparatively homogeneous Si/Ge matrix. Additionally, oxygen contamination on powders lead to a silica phase distributed along grain boundaries. The milling and sintering kinetics of samples was studied in an effort to obtain the desired nano-sized precipitates. Thermoelectric transport properties revealed a significant 40% reduction in the lattice component of thermal conductivity which leads to a 30% improvement in both n- and p-type samples compared to RTG. The thermal stability of the nano-composites was studied as nano-structured bulk samples are prone to thermal instability. It was found that from a dopant stability perspective the composite samples were comparable to that of traditional zone-leveled Si/Ge.

To demonstrate the importance of studying factors other than only figure of merit, a couple design case was presented. The design incorporated several of the features of Chapter 4.

To better understand the system further work is required to better investigate the precipitate and matrix microstructure. TEM work is being performed on the samples of this work to understand the interface between precipitate and matrix. The interface serves as the phonon scattering center, so to better understand the performance of the materials the interface must be well characterized. High resolution TEM of the interface will provide a better understanding of the transport properties. In addition to studying the interface more work is being done to understand the influence of contaminants. Main sources of contamination include oxygen, which has been identified to influence thermal properties, and breakdown of the milling media. It is necessary to better understand where these contaminants are going within the microstructure to later understand their influence on transport properties.

10.4 $\text{Co}_x\text{Ni}_{4-x}\text{Sb}_{12-y}\text{Sn}_y$ Skutterudite System

In Chapter 9 work on a novel quaternary skutterudite system was introduced. While the figure of merit of this new skutterudite was low, less than 0.05, the system provides a new and interesting p-type skutterudite to consider. The system was interesting because it can be tuned for both n- and p-type conduction easily which could make couple fabrication easy. The system was synthesized from a melt, mill, hot press procedure. Each step of the fabrication was carefully characterized to provide the

study with the best chance of developing high quality materials. As a promising result it was shown that the thermal conductivity can be easily tuned with Co level, furthermore it was shown that a minimum exists in the thermal conductivity for a Co content of $x = 1.5$. Lanthanide series fillers were studied in the system and the effect on thermoelectric properties was investigated. It was found that the filled samples did not have significantly improved transport properties.

Further work is being done with the system to understand the structure and improve transport properties. TEM work is helping to understand the placement of filler atoms on the 2a Wyckoff site in the crystal structure. This information will lead to a better understanding of the transport properties and may help guide further lanthanide series filler work.

BIBLIOGRAPHY

- [1] G.L. Bennett, J.J. Lombardo, R.J. Hemler, G. Silverman, C.W. Whitmore, W.R. Amos, E.W. Johnson, R.W. Zocher, J.C. Hagan, and R.W. Englehart. The general purpose heat source radioisotope thermoelectric generator: A truly general purpose space RTG. *AIP Conference Proceedings*, 969:663–671, 2008.
- [2] W.P. Lange and R.G. Carroll. Review of recent advances of radioisotope power systems. *Energy Conversion and Management*, 49:393–401, 2008.
- [3] A.K. Misra. Overview of NASA program on development of radioisotope power systems with high specific power. *4th International Energy Conversion Engineering Conference and Exhibit*, pages 1–7, 2006.
- [4] W.R. Martini. Stirling engine design manual. Technical report, Martini Engineering, January 1983.
- [5] B. Kongtragool and S. Wongwises. A review of solar-powered stirling engines and low temperature differential stirling engines. *Renewable and Sustainable Energy Reviews*, 7(2):131–154, 2003.
- [6] D.L. Gardner and G.W. Swift. A cascade thermoacoustic engine. *The Journal of the Acoustical Society of America*, 114(4):1905–1919, 2003.
- [7] S. Backhaus and G.W. Swift. A thermoacoustic-stirling heat engine: Detailed study. *The Journal of the Acoustical Society of America*, 107(6):3148–3166, 2000.
- [8] B. Parida, S. Iniyar, and R. Goic. A review of solar photovoltaic technologies. *Renewable and sustainable energy reviews*, 15(3):1625–1636, 2011.
- [9] R. Evans. Goodyears geneva concepts, 2015.
- [10] J. Yang and F. Stabler. Automotive applications of thermoelectric materials. *Journal of Electronic Materials*, 38:1245–1251, 2009.
- [11] K. Saqr, M. Mansour, and M. Musa. Thermal design of automobile exhaust based thermoelectric generators: objectives and challenges. *International Journal of Automotive Technology*, 9:155–160, 2008.

- [12] G.W. Hunter, M.C. Scardelletti, G.E. Ponchak, G.M. Beheim, J.M. Mackey, D.J. Spry, R.D. Meredith, F.W. Dynys, R.G. Neudeck, J.L. Jordan, L.Y. Chen, K. Harsh, and C.A. Zorman. High temperature wireless smart sensor technology based on silicon carbide electronics. *ECS Transactions*, 61:127–138, 2014.
- [13] S.B. Riffat and X. Ma. Thermoelectrics: a review of present and potential applications. *Applied Thermal Engineering*, 23:913–935, 2003.
- [14] J. Mackey, A. Sehirlioglu, and F.W. Dynys. Analytic thermoelectric couple optimization introducing device design factor and fin factor. *Applied Energy*, 134:374–381, 2014.
- [15] J. Mackey, F.W. Dynys, and A. Sehirlioglu. Uncertainty analysis for common seebeck and electrical resistivity measurement systems. *Review of Scientific Instruments*, 85:085119, 2014.
- [16] F.W. Dynys, A. Sayir, J. Mackey, and A. Sehirlioglu. Thermoelectric properties of $\text{WSi}_2\text{Si}_x\text{Ge}_{1-x}$ composites. *Journal of Alloys and Compounds*, 604:196–203, 2014.
- [17] J. Mackey, F. Dynys, and A. Sehirlioglu. Thermoelectric properties of $\text{Co}_x\text{Ni}_{4-x}\text{Sb}_{12-y}\text{Sn}_y$ ternary skutterudites. *12th International Energy Conversion Engineering Conference*, 2014.
- [18] T.J. Seebeck. Magnetische polarisation der metalle und erze durch temperatur-differenz, abhandlungen der physikalischen klasse der kniglichen akademie der wissenschaften zu berlin, aus den jahren 1822 und 1823. Technical report, Academy of Sciences in Berlin, August 16, 1821, October 18, 25 1821, and February 11 1822 1825.
- [19] D.D. Allred. SCT-93 short course on thermoelectrics: An overview of thermoelectricity. Technical report, The International Thermoelectric Society, November 1993.
- [20] J.C.A. Pelier. Nouvelles experiences sur la caloricite des courants electrique. *Annales de Chimie et de Physique*, 56:371–386, 1834.
- [21] A. Polozine, S. Sirotinskaya, and L. Schaeffer. History of development of thermoelectric materials for electric power generation and criteria of their quality. *Materials Research*, 17(5):1260–1267, 2014.
- [22] A. Royne, C.J. Dey, and D.R. Mills. Cooling of photovoltaic cells under concentrated illumination: a critical review. *Solar energy materials and solar cells*, 86(4):451–483, 2005.

- [23] N. Wang, L. Han, H. He, N.H. Park, and K. Koumoto. A novel high-performance photovoltaic–thermoelectric hybrid device. *Energy & Environmental Science*, 4(9):3676–3679, 2011.
- [24] D. Kraemer, L. Hu, A. Muto, X. Chen, G. Chen, and M. Chiesa. Photovoltaic–thermoelectric hybrid systems: A general optimization methodology. *Applied Physics Letters*, 92(24):243503, 2008.
- [25] W.G.J.H.M. Van Sark. Feasibility of photovoltaic–thermoelectric hybrid modules. *Applied Energy*, 88(8):2785–2790, 2011.
- [26] E. Altenkirch. Elektrothermische Kltterzeugung und reversible elektrische heizung. *Physikalische Zeitschrift*, 12:920–924, 1911.
- [27] A.F. Ioffe and A Gelbtuch. Semiconductor thermoelements and thermoelectric cooling. 1957.
- [28] A. Bejan. *Advanced Engineering Thermodynamics*. Wiley, 1 edition, 2006.
- [29] B. Sherman, R.R. Heikes, and R.W. Ure Jr. Calculation of efficiency of thermoelectric devices. *Journal of Applied Physics*, 31:1–16, 1960.
- [30] F.E. Jaumot. Thermoelectric effects. *Proceedings of the IRE*, 46(3):538–554, 1958.
- [31] O. Yamashita. Effect of linear and non-linear components in the temperature dependences of thermoelectric properties on the cooling performance. *Appl. Energ.*, 86(9):1746–1756, September 2009.
- [32] G. Min, D.M. Rowe, and K. Kontostavlakis. Thermoelectric figure-of-merit under large temperature differences. *J. Phys. D: Appl. Phys.*, 37(8):1301–1304, April 2004.
- [33] G. Min and D.M. Rowe. *Thermoelectric Handbook*. CRC Press, Taylor and Francis Group, 1 edition, 2006.
- [34] G. Min and D.M. Rowe. Ring-structured thermoelectric module. *Semicond. Sci. Tech.*, 22(8):880–883, August 2007.
- [35] K. Landecker. Some aspects of the performance of refrigerating thermojunctions with radial flow of current. *J. Appl. Phys.*, 47:1846, 1976.
- [36] T. Lund. Refrigerating thermojunctions with radial flow of current. *J. Appl. Phys.*, 49(9):4942, 1978.
- [37] L. Liu. A continuum theory of thermoelectric bodies and effective properties of thermoelectric composites. *Int. J. Eng. Sci.*, 55:35, 2012.

- [38] M. Alata, M.A. Al-Nimr, and M. Naji. Transient behavior of a thermoelectric device under the hyperbolic heat conduction model. *Int. J. Thermophys.*, 24(6):1753–1768, November 2003.
- [39] A. Montecucco, J.R. Buckle, and A.R. Knox. Solution to the 1-D unsteady heat conduction equation with internal Joule heat generation for thermoelectric devices. *Appl. Therm. Eng.*, 35:177–184, March 2012.
- [40] M.J. Huang, R.H. Yen, and A.B. Wang. The influence of the thomson effect on the performance of a thermoelectric cooler. *International Journal of Heat and Mass Transfer*, 48(2):413–418, 2005.
- [41] K.S.M. Oliveira, R.P. Cardoso, and C.J.L. Hermes. Two-dimensional modeling of thermoelectric cells. *15th International Refrigeration and Air Conditioning Conference at Purdue*, 2014.
- [42] E. Sandoz-Rosado and R. Stevens. Robust finite element model for the design of thermoelectric modules. *J. Electron. Mater.*, 39(9):1848–1855, February 2010.
- [43] J.H. Meng, X.D. Wang, and X.X. Zhang. Transient modeling and dynamic characteristics of thermoelectric cooler. *Appl. Energ.*, 108:340–348, August 2013.
- [44] M. Chen, L.A. Rosendahl, and T. Condra. A three-dimensional numerical model of thermoelectric generators in fluid power systems. *International Journal of Heat and Mass Transfer*, 54(1):345–355, 2011.
- [45] X. Gou, H. Ping, Q. Ou, H. Xiao, and S. Qing. A novel thermoelectric generation system with thermal switch. *Applied Energy*, 2014.
- [46] D.T. Crane. An introduction to system-level, steady-state and transient modeling and optimization of high-power-density thermoelectric generator devices made of segmented thermoelectric elements. *Journal of electronic materials*, 40(5):561–569, 2011.
- [47] N.Q. Nguyen and K.V. Pochiraju. Behavior of thermoelectric generators exposed to transient heat sources. *Applied Thermal Engineering*, 51(1):1–9, 2013.
- [48] W. Thomson. Account of researches in thermo-electricity. *Proceedings of the Royal Society of London*, 7:49–58, 1854.
- [49] C.B. Vining. Short course on thermoelectrics: Thermoelectric fundamentals and physical phenomena. Technical report, International Thermoelectric Society, November 1993.
- [50] M.C. Clamond. On a new thermo-electric pile. *Telegraph Engineers, Journal of the Society of*, 4(11):253–257, 1875.

- [51] S.M. Kauzlarich, S.R. Brown, and G.J. Snyder. Zintl phases for thermoelectric devices. *Dalton Transactions*, 21:2099–2107, 2007.
- [52] A. Zevalkink, W.G. Zeier, G. Pomrehn, E. Schechtel, W. Tremel, and G.J. Snyder. Thermoelectric properties of Sr_3GaSb_3 - a chain forming Zintl compound. *Energy and Environmental Science*, 10:9121–9128, 2012.
- [53] A. Zevalkink, G. Pomrehn, S. Johnson, G.J. Gibbs, and G.J. Snyder. Influence of the trial elements (M=Al,Ga,In) on the transport properties of $\text{Ca}_5\text{M}_2\text{Sb}_6$ Zintl compounds. *Chemistry of Materials*, 24:2091–2098, 2012.
- [54] K. Star. *Synthesis and Characterization of 14-1-11 Ytterbium Manganese Antimonide Derivatives for Thermoelectric Applications*. PhD thesis, University of California Los Angeles, May 2013.
- [55] E.S. Toberer, A. Zevalkink, N. Crisosto, and G.J. Snyder. The Zintl compound $\text{Ca}_5\text{Al}_2\text{Sb}_6$ for low-cost thermoelectric power generation. *Advanced Functional Materials*, 24:4375–4380, 2010.
- [56] A. Zevalkink, E.S. Toberer, T. Bleith, E. Flage-Larsen, and G.J. Snyder. Improved carrier concentration control in Zn-doped $\text{Ca}_5\text{Al}_2\text{Sb}_6$. *Journal of Applied Physics*, 110:013721, 2011.
- [57] T.M. Tritt and M.A. Subramanian. Thermoelectric materials, phenomena, and applications: a birds eye view. *MRS Bulletin*, 31:188–198, 2006.
- [58] G.S. Nolas, J. Poon, and M. Kanatzidis. Recent developments in bulk thermoelectric materials. *MRS Bulletin*, 31:199–205, 2006.
- [59] C. Han, Z. Li, and S.X. Dou. Recent progress in thermoelectric materials. *Chinese Society Bulletin*, 59:2073–2091, 2014.
- [60] R. Venkatasubramanian, T. Colpitts, E. Watko, M. Lamvik, and N. El-Masry. MOCVD of Bi_2Te_3 , Sb_2Te_3 and their superlattice structures for thin-film thermoelectric applications. *Journal of Crystal Growth*, 170:817–821, 1997.
- [61] G. Nolas, D. Morelli, and T. Tritt. Skutterudites a phonon-glass-electron crystal approach to advanced thermoelectric energy conversion applications. *Annual Review of Materials Science*, 29:89–116, 1999.
- [62] J. Ackermann and A. Wold. The preparation and characterization of the cobalt skutterudites CoP_3 , CoSb_3 , CoAs_3 . *Journal of Physics and Chemistry of solids*, 38:1013–1016, 1977.
- [63] A. Lyons, R. Gruska, C. Case, S. Subbarao, and A. Wold. The preparation and characterization of some skutterudite related compounds. *Materials Research Bulletin*, 13:125–128, 1978.

- [64] D.T. Morelli, G.P. Meisner, B. Chen, S. Hu, and C. Uher. Cerium filling and doping of cobalt triantimonide. *Physical Review B*, 56:7376, 1997.
- [65] J.P. Fleurial, T. Caillat, and A. Borshchevsky. Skutterudites: an update. *Proceedings ICT'97 XVI International Conference on Thermoelectrics*, 1997.
- [66] H. Li, X. Tang, Q. Zhang, and C. Uher. High performance $\text{In}_x\text{Ce}_y\text{Co}_4\text{Sb}_{12}$ thermoelectric materials with in situ forming nanostructured InSb phase. *Applied Physics Letters*, 94:102114, 2009.
- [67] X. Shi, J. Yang, J.R. Salvador, M. Chi, J.Y. Cho, H. Wang, S. Bai, J. Yang, W. Zhang, and L. Chen. Multiple-filled skutterudites: high thermoelectric figure of merit through separately optimizing electrical and thermal transports. *Journal of the American Chemical Society*, 133:7837–7846, 2011.
- [68] H. Chi, H. Kim, J.C. Thomas, X. Su, S. Stackhouse, M. Kaviani, A.V. Ven, X. Tang, and C. Uher. Configuring pnictogen rings in skutterudites for low phonon conductivity. *Physical Review B*, 86:195209, 2012.
- [69] Y. Dong, P. Puneet, T.M. Tritt, J. Martin, and G.S. Nolas. High temperature thermoelectric properties of p-type skutterudites $\text{Ba}_x\text{Yb}_y\text{Co}_{4-z}\text{Fe}_z\text{Sb}_{12}$. *Journal of Applied Physics*, 112:083718, 2012.
- [70] J. Eilertsen, S. Rouvimov, and M.A. Subramanian. Rattler-seeded InSb nanoinclusions from metastable indium-filled $\text{In}_{0.1}\text{Co}_4\text{Sb}_{12}$ skutterudites for high-performance thermoelectrics. *Acta Materialia*, 60:2178–2185, 2012.
- [71] G.S. Nolas, G.A. Slack, D.T. Morelli, T.M. Tritt, and A.C. Ehrlich. The effect of rare-earth filling on the lattice thermal conductivity of skutterudites. *Journal of Applied Physics*, 79:4002–4008, 1996.
- [72] L. Chen, X. Tang, T. Goto, and T. Hirai. Synthesis of filled skutterudite compounds: $\text{Ba}_y\text{Fe}_x\text{Co}_{4-x}\text{Sb}_{12}$. *Journal of Materials Research*, 15:2276–2279, 2000.
- [73] P.F. Qiu, J. Yang, R.H. Liu, X. Shi, X.Y. Huang, G.J. Snyder, W. Zhang, and L.D. Chen. High-temperature electrical and thermal transport properties of fully filled skutterudites $\text{RFe}_4\text{Sb}_{12}$. *Journal of Applied Physics*, 109:063713, 2011.
- [74] R. Korenstein, S. Soled, A. Wold, and G. Collin. Preparation and characterization of the skutterudite-related phases $\text{CoGe}_{1.5}\text{S}_{1.5}$ and $\text{CoGe}_{1.5}\text{Se}_{1.5}$. *Inorganic Chemistry*, 16:2344–2346, 1977.
- [75] Y. Dong, K. Wei, and G.S. Nolas. Transport properties of partially filled skutterudite derivatives $\text{Ce}_{0.13}\text{Co}_4\text{Ge}_6\text{Se}_6$ and $\text{Yb}_{0.14}\text{Co}_4\text{Ge}_6\text{Se}_6$. *Physical Review B*,

87:195203, 2013.

- [76] E. Bauer, St. Berger, M. Della Mea, G. Hilscher, H. Michor, C. Paul, A. Grytsiv, P. Rogl, E.W. Scheidt, C. Godart, and M. Abd Elmeguid. Filled skutterudites: formation, ground state properties and thermoelectric features. *Acta Physica Polonica. Series B*, 34:595–608, 2003.
- [77] A. Grytsiv, P. Rogl, S. Berger, Ch. Paul, H. Michor, E. Bauer, G. Hilscher, C. Godart, P. Knoll, M. Musso, W. Lottermoser, A. Saccone, R. Ferro, T. Roisnel, and H. Noel. A novel skutterudite phase in the NiSbSn system: phase equilibria and physical properties. *Journal of Physics: Condensed Matter*, 14:7071, 2002.
- [78] S. Berger, C. Paul, H. Michor, E. Bauer, G. Hilscher, A. Grytsiv, and P. Rogl. Crystal structure and thermoelectric properties of novel skutterudite $\text{E}_y\text{Ni}_4\text{Sb}_{12-x}\text{Sn}_x$ with $\text{E}_p=\text{Sn}$, Eu, and Yb. *21st International Conference on Thermoelectrics*, 2:48–51, 2002.
- [79] R. Mishra, A. Kroupa, P. Terzieff, and H. Ipser. Thermochemistry of liquid NiSbSn alloys. *Thermochimica Acta*, 536:68–73, 2012.
- [80] R. Mishra, A. Kroupa, A. Zemanova, and H. Ipser. Phase Equilibria in the Sn-Rich Corner of the Ni-Sb-Sn System. *Journal of electronic materials*, 42:646–653, 2013.
- [81] C. Uher. *CRC Thermoelectrics Handbook Macro to Nano*. CRC Taylor and Francis, 1 edition, 2006.
- [82] K.S. Aleksandrov and B.V. Beznosikov. Crystal chemistry and prediction of compounds with a structure of skutterudite type. *Crystallography Reports*, 52:28–36, 2007.
- [83] G. Rogl, A. Grytsiv, P. Rogl, E. Bauer, and M. Zehetbauer. A new generation of p-type didymium skutterudites with high ZT. *Intermetallics*, 19:546–555, 2011.
- [84] X. Tang, Q. Zhang, L. Chen, T. Goto, and T. Hirai. Synthesis and thermoelectric properties of p-type-and n-type-filled skutterudite $\text{R}_y\text{M}_x\text{Co}_{4-x}\text{Sb}_{12}$ (R: Ce, Ba, Y; M: Fe, Ni). *Journal of Applied Physics*, 97:093712, 2005.
- [85] A. Grytsiv, P. Rogl, H. Michor, E. Bauer, and G. Giester. $\text{In}_y\text{Co}_4\text{Sb}_{12}$ Skutterudite: phase equilibria and crystal structure. *Journal of electronic materials*, 42:2940–2952, 2013.
- [86] G. Kliche and H.D. Lutz. Temperature dependence of the FIR reflection spectra of the Skutterudites CoAs_3 and CoSb_3 . *Infrared Physics*, 24:171–177, 1984.

- [87] J.Y. Cho, Z. Ye, M.M. Tessema, R.A. Waldo, J.R. Salvador, J. Yang, W. Cai, and H. Wang. Thermoelectric properties of p-type skutterudites $\text{Yb}_x\text{Fe}_{3.5}\text{Ni}_{0.5}\text{Sb}_{12}(0.8 \leq x \leq 1)$. *Acta Materialia*, 60(5):2104–2110, 2012.
- [88] P. Qiu, X. Shi, R. Liu, Y. Qiu, S. Wan, and L. Chen. Thermoelectric properties of manganese-doped p-type skutterudites $\text{Ce}_y\text{Fe}_{4-x}\text{Mn}_x\text{Sb}_{12}$. *Functional Materials Letters*, 6(05), 2013.
- [89] G.S. Joo, D.K. Shin, and I.H. Kim. Thermoelectric properties of double-filled p-type $\text{La}_{1-z}\text{Yb}_z\text{Fe}_{4-x}\text{Co}_x\text{Sb}_{12}$ Skutterudites. *Journal of Electronic Materials*, pages 1–5, 2014.
- [90] L. Fu, J. Yang, Y. Xiao, J. Peng, M. Liu, Y. Luo, and G. Li. AgSbTe₂ nanoinclusion in $\text{Yb}_{0.2}\text{Co}_4\text{Sb}_{12}$ for high performance thermoelectrics. *Intermetallics*, 43:79–84, 2013.
- [91] P. Rogl. *CRC Thermoelectrics Handbook Macro to Nano*. CRC Taylor and Francis, 1 edition, 2006.
- [92] W. Xie, A. Weidenkaff, X. Tang, Q. Zhang, J. Poon, and T.M. Tritt. Recent advances in nanostructured thermoelectric half-Heusler compounds. *Nanomaterials*, 2:379–412, 2012.
- [93] C. Xi, S.N. Girard, F. Meng, E. Lara-Curzio, S. Jin, J.B. Goodenough, J. Zhou, and L. Shi. Approaching the minimum thermal conductivity in rhenium-substituted higher manganese silicides. *Advanced Energy Materials*, 4, 2014.
- [94] S.W. Kim, Y. Mishima, and D.C. Choi. Effect of process conditions on the thermoelectric properties of CoSi. *Intermetallics*, 10:177–184, 2002.
- [95] S.K. Bux, M.T. Yeung, E.S. Toberer, G.J. Snyder, R.B. Kaner, and J.P. Fleurial. Mechanochemical synthesis and thermoelectric properties of high quality magnesium silicide. *Journal of Materials Chemistry*, 21:12259–12266, 2011.
- [96] M.I. Fedorov and V.K. Zaitsev. *CRC Thermoelectrics Handbook Macro to Nano*. CRC Taylor and Francis, 1 edition, 2006.
- [97] K. Koumoto, I. Terasaki, T. Kajitani, M. Ohtaki, and R. Funahashi. *CRC Thermoelectrics Handbook Macro to Nano*. CRC Taylor and Francis, 1 edition, 2006.
- [98] M. Backhaus-Ricoult, J. Rustad, L. Moore, C. Smith, and J. Brown. Semiconducting large bandgap oxides as potential thermoelectric materials for high-temperature power generation? *Applied Physics A*, 116:433–470, 2014.
- [99] M. Culebras, C.M. Gomez, and A. Cantarero. Review of polymers for thermoelectric applications. *Materials*, 7:6701–6732, 2014.

- [100] M.C. Steele and F.D. Rosi. Thermal conductivity and thermoelectric power of germanium-silicon alloys. *Journal of Applied Physics*, 29:1517–1520, 1958.
- [101] B. Abeles, D.S. Beers, G.D. Cody, and J.P. Dismukes. Thermal conductivity of Ge-Si alloys at high temperatures. *Physical Review*, 125:44, 1962.
- [102] B. Abeles. Lattice thermal conductivity of disordered semiconductor alloys at high temperatures. *Physical Review*, 131:1906, 1963.
- [103] J.P. Dismukes, L. Ekstrom, E.F. Steigmeier, I. Kudman, and D.S. Beers. Thermal and electrical properties of heavily doped Ge-Si alloys up to 1300 K. *Journal of Applied Physics*, 35:2899–2907, 1964.
- [104] C.J. Glassbrenner and G.A. Slack. Thermal conductivity of silicon and germanium from 3 k to the melting point. *Physical Review*, 134:A1058, 1964.
- [105] G. Stivers. Radioisotope thermoelectric space power supplies. *Aerospace, IEEE Transactions on*, 2:652–660, 1964.
- [106] RCA Corporation. Silicon germanium thermoelectric materials and module development program (u) 1st quarterly report. Technical Report Contract AT (292)-2510, RCA Corporation, 1969.
- [107] RCA Corporation. Silicon germanium thermoelectric materials and module development program (u) 2nd quarterly report. Technical Report Contract AT (292)-2510, RCA Corporation, 1969.
- [108] RCA Corporation. Silicon germanium thermoelectric materials and module development program (u) 3rd quarterly report. Technical Report Contract AT (292)-2510, RCA Corporation, 1969.
- [109] RCA Corporation. Silicon germanium thermoelectric materials and module development program (u) 4th quarterly report. Technical Report Contract AT (292)-2510, RCA Corporation, 1969.
- [110] RCA Corporation. Silicon germanium thermoelectric materials and module development program (u) 5th quarterly report. Technical Report Contract AT (292)-2510, RCA Corporation, 1969.
- [111] R.D. Nasby and E.L. Burgess. Precipitation of dopants in silicon-germanium thermoelectric alloys. *Journal of Applied Physics*, 43:2908–2909, 1972.
- [112] D.M. Rowe and N. Savvides. The reversal of precipitation in heavily doped silicon-germanium alloys. *Journal of Physics D: Applied Physics*, 12:1613, 1979.
- [113] N. Savvides and D.M. Rowe. Precipitation of phosphorous from solid solution in Si-Ge alloys and its effect on thermoelectric transport properties. *Journal of*

Physics D: Applied Physics, 14:723, 1981.

- [114] P.D. Maycock. Thermal conductivity of silicon, germanium, iiiv compounds and iiiv alloys. *Solid-state electronics*, 10:161–168, 1967.
- [115] J. Schilz and V.N. Romanenko. Review bulk growth of silicon-germanium solid solutions. *Journal of Materials Science: Materials in Electronics*, 6:265–279, 1995.
- [116] PDF 04-006-2527 (ICDD, 2005).
- [117] PDF 01-073-7012 (ICDD, 2004).
- [118] D.M. Rowe. Recent advances in silicon-germanium alloy technology and an assessment of the problems of building the modules for a radioisotope thermoelectric generator. *Journal of Power Sources*, 19:247–259, 1987.
- [119] G.A. Slack and M.A. Hussain. The maximum possible conversion efficiency of silicon-germanium thermoelectric generators. *Journal of Applied Physics*, 70:2694–2718, 1991.
- [120] D.M. Rowe, L.W. Fu, and S.G.K. Williams. Comments on the thermoelectric properties of pressure-sintered $\text{Si}_{0.8}\text{Ge}_{0.2}$ thermoelectric alloys. *Journal of Applied Physics*, 73:4683–4685, 1993.
- [121] L.D. Hicks and M.S. Dresselhaus. Effect of quantum-well structures on thermoelectric figure of merit. *Physical Review B*, 47:727–731, 1993.
- [122] L.D. Hicks and M.S. Dresselhaus. Thermoelectric figure of merit of a one-dimensional conductor. *Physical review B*, 47(24):16631, 1993.
- [123] L.D. Hicks, T.C. Harman, X. Sun, and M.S. Dresselhaus. Experimental study of the effect of quantum-well structures on the thermoelectric figure of merit. *Physical Review B*, 53:493–496, 1996.
- [124] G. Chen. Thermal conductivity and ballistic-phonon transport in the cross-plane direction of superlattices. *Physical Review B*, 57:14958–14973, 1998.
- [125] M.S. Dresselhaus, G. Chen, M.Y. Tang, R. Yang, H. Lee, D. Wang, Z. Ren, J.P. Fleurial, and P. Gogna. New directions for low-dimensional thermoelectric materials. *Advanced Materials*, 19:1043–1053, 2007.
- [126] G. Chen and A. Shakouri. Heat transfer in nano-structures for solid-state energy conversion. *Journal of Heat Transfer*, 124:242–252, 2002.
- [127] A.M. Rao, X. Ji, and T.M. Tritt. Properties of nano-structured one-dimensional and composite thermoelectric materials. *MRS Bulletin*, 31:218–223, 2006.

- [128] G. Joshi, H. Lee, Y. Lan, X. Wang, G. Zhu, D. Wang, R.W. Gould, D.C. Cuff, M.Y. Tang, M.S. Dresselhaus, G. Chen, and Z. Ren. Enhanced thermoelectric figure-of-merit in nanostructured p-type silicon germanium bulk alloys. *Nano Letters*, 8:4670–4674, 2008.
- [129] X.W. Wang, H. Lee, Y.C. Lan, G.H. Zhu, and G. Joshi. Enhanced thermoelectric figure of merit in nanostructured n-type silicon germanium bulk alloy. *Applied Physics Letters*, 93:193121, 2008.
- [130] N. Mingo, D. Hauser, N.P. Kobayashi, M. Plissonnier, and A. Shakouri. Nanoparticle-in-alloy approach to efficient thermoelectrics: silicides in SiGe. *Nano Letters*, 9:711–715, 2009.
- [131] Z. Aksamija. Lattice thermal transport in Si-based nanocomposites for thermoelectric applications. *Journal of Electronic Materials*, pages 1–7, 2014.
- [132] N. Kundu, A. Mingo, D.A. Broido, and D.A. Stewart. Role of light and heavy embedded nanoparticles on the thermal conductivity of SiGe alloys. *Physical Review B*, 84:125426, 2011.
- [133] J.N. Gillet and S. Voltz. Self-assembled germanium quantum-dot supercrystals in silicon with extremely low thermal conductivities for thermoelectrics. *Journal of Electronic Materials*, 39:2154–2161, 2010.
- [134] Y. Lee and G.S. Hwang. Microsegregation effects on the thermal conductivity of silicon-germanium alloys. *Journal of Applied Physics*, 114:174910, 2013.
- [135] Y. Ezzahri and K. Joulain. Effect of embedding nanoparticels on the lattice thermal conductivity of bulk semiconductor crystals. *Journal of Applied Physics*, 113:043510, 2013.
- [136] R. Zhao, L. Shen, and F. Guo. Enhanced electrical conductivity in $\text{Si}_{80}\text{Ge}_{20}\text{B}_{0.6}$ alloys with Er addition prepared by spark plasma sintering. *Journal of Materials Research*, 26:1879–1885, 2011.
- [137] Z. Zamanipour and D. Vashaee. Comparison of thermoelectric properties of p-type nanostructured bulk $\text{Si}_{0.8}\text{Ge}_{0.2}$ alloy with $\text{Si}_{0.8}\text{Ge}_{0.2}$ composites embedded with CrSi_2 nano-inclusions. *Journal of Applied Physics*, 112:093714, 2012.
- [138] K. Favier, G. Bernard-Granger, C. Navone, M. Soulier, M. Boidot, J. Leforestier, J. Simon, J.C. Tedenac, and D. Ravot. Influence of in situ formed MoSi_2 inclusions on the thermoelectrical properties of an n-type silicon germanium alloy. *Acta Materialia*, 64:429–442, 2014.
- [139] A.R.N.E. Kjekshus and T.R.O.N.D. Rakke. Compounds with the skutterudite type crystal structure. III. Structural data for arsenides and antimonides. *Acta*

- Chem. Scand. A*, 28:99–103, 1974.
- [140] N. Mandel and J. Donohue. The refinement of the crystal structure of skutterudite, CoAs_3 . *Acta Crystallographica Section B: Structural Crystallography and Crystal Chemistry*, 27:2288–2289, 1971.
- [141] G.J. Snyder and T.S. Ursell. Thermoelectric efficiency and compatability. *Physical Review Letters*, 91:148301, 2003.
- [142] T. Manyk and V. Bilynskyj-Slotylo. Modeling of sectional and multi-stage thermoelectric modules as waste heat recuperators. *Journal of Electrical Engineering*, 2:124–131, 2014.
- [143] T. Ming, Y. Wu, C. Peng, and Y. Tao. Thermal analysis on a segmented thermoelectric generator. *Energy*, 2015.
- [144] L. Onsager. Reciprocal relations in irreversible processes i. *Physical Review*, 37:405–426, 1931.
- [145] L. Onsager. Reciprocal relations in irreversible processes ii. *Physical Review*, 38:2265–2279, 1931.
- [146] A.F. May and G.J. Snyder. *Materials Preparation and Characterization in Thermoelectrics*. CRC Press, Taylor and Francis Group, 1 edition, 2012.
- [147] Z.M. Zhang. *Nano/Microscale Heat Transfer*. McGraw-Hill, New York, 1 edition, 2007.
- [148] C.M. Bhandari and D.M. Rowe. *CRC Handbook of Thermoelectrics*. CRC Taylor and Francis, 1 edition, 2006.
- [149] Arpaci. *Conduction Heat Transfer*. Addison-Wesley Pub. Co., 1966.
- [150] F.P. Incropera, D. Dewitt, T. Bergman, and A. Lavine. *Introduction to heat transfer*. Wiley, 6 edition, 2011.
- [151] Ozisik. *Heat Transfer: A Basic Approach*. McGraw-Hill, 1985.
- [152] H. Carslaw and J. Jaeger. *Conduction of Heat in Solids*. Clarendo Press, 1986.
- [153] P. Ravishankar. Liquid encapsulated Bridgman (LEB) method for directional solidification of silicon using calcium chloride. *Journal of Crystal Growth*, 94:62, 1989.
- [154] J. Martin, T. Tritt, and C. Uher. High temperature Seebeck coefficient metrology. *Journal of Applied Physics*, 108(12):121101, 2010.

- [155] J. Martin. Apparatus for the high temperature measurement of the Seebeck coefficient in thermoelectric materials. *Review of Scientific Instruments*, 83(6):065101, June 2012.
- [156] J. Martin. Protocols for the high temperature measurement of the Seebeck coefficient in thermoelectric materials. *Measurement Science and Technology*, 24(8):085601, August 2013.
- [157] L.M. Clark III and R.E. Taylor. Radiation loss in the flash method for thermal diffusivity. *Journal of Applied Physics*, 46(2):714–719, 1975.
- [158] D.E. Stroe, M.A. Thermitus, and R.A. Jacobs-Fedore. Thermophysical properties of Pyroceram 96061. In *Thermal Conductivity 27: Thermal Expansion 15: Joint Conferences, October 26-29, 2003, Knoxville, Tennessee, USA*, page 382. DEStech Publications, Inc, 2005.
- [159] W.J. Parker, R.J. Jenkins, C.P. Butler, and G.L. Abbott. Flash method of determining thermal diffusivity, heat capacity, and thermal conductivity. *Journal of applied physics*, 32:1679–1684, 1961.
- [160] M.A. Thermitus. Thermal diffusivity and the flash method. In *Thermal Conductivity 27: Thermal Expansion 15: Joint Conferences, October 26-29, 2003, Knoxville, Tennessee, USA*, page 3. DEStech Publications, Inc, 2005.
- [161] L.J. Van der Pauw. A method of measuring the resistivity and hall coefficient on lamellae of arbitrary shape. *Philips technical review*, 20(8):220–224, 1958.
- [162] R. Chwang, B.J. Smith, and C.R. Crowell. Contact size effects on the van der Pauw method for resistivity and hall coefficient measurement. *Solid-State Electronics*, 17(12):1217–1227, 1974.
- [163] S. Iwanaga, E.S. Toberer, A. LaLonde, and G.J. Snyder. A high temperature apparatus for measurement of the Seebeck coefficient. *Review of Scientific Instruments*, 82(6):063905, June 2011.
- [164] S. Iwanaga and G.J. Snyder. Scanning Seebeck coefficient measurement system for homogeneity characterization of bulk and thin-film thermoelectric materials. *Journal of Electronic Materials*, 41(6):1667–1674, April 2012.
- [165] J. De Boor, C. Stiewe, P. Ziolkowski, T. Dasgupta, G. Karpinski, E. Lenz, F. Edler, and E. Mueller. High-temperature measurement of Seebeck coefficient and electrical conductivity. *Journal of Electronic Materials*, 42(7):1711–1718, January 2013.
- [166] W.M.N. Wan Jaafar, J.E. Snyder, and G. Min. Apparatus for measuring Seebeck coefficient and electrical resistivity of small dimension samples using in-

- frared microscope as temperature sensor. *Review of Scientific Instruments*, 84(5):054903, May 2013.
- [167] A. Muto, D. Kraemer, Q. Hao, Z.F. Ren, and G. Chen. Thermoelectric properties and efficiency measurements under large temperature differences. *Review of Scientific Instruments*, 80(9):093901, September 2009.
- [168] H. Werheit, U. Kuhlmann, B. Herstell, and W. Winkelbauer. Reliable measurement of Seebeck coefficient in semiconductors. *Journal of Physics: Conference Series*, 176:012037, June 2009.
- [169] C. Wood, D. Zoltan, and G. Stapfer. Measurement of Seebeck coefficient using a light pulse. *Review of Scientific Instruments*, 56:719, 1985.
- [170] A.T. Burkov, A. Heinrich, P.P. Konstantinov, T. Nakama, and K. Yagasaki. Experimental set-up for thermopower and resistivity measurements at 100 - 1300 K. *Measurement Science and Technology*, 12:264–272, 2001.
- [171] Z. Zhou and C. Uher. Apparatus for Seebeck coefficient and electrical resistivity measurements of bulk thermoelectric materials at high temperature. *Review of Scientific Instruments*, 76(2):023901, 2005.
- [172] V. Ponnambalam, S. Lindsey, N.S. Hickman, and T.M. Tritt. Sample probe to measure resistivity and thermopower in the temperature range of 300-1000 K. *Review of Scientific Instruments*, 77(7):073904, 2006.
- [173] W.H. Kettler, R. Wernhardt, and M. Rosenberg. Differential ac method of thermopower measurement. *Review of Scientific Instruments*, 57(12):3053–3058, 1986.
- [174] A.L. Pope, R.T. Littleton, and T.M. Tritt. Apparatus for the rapid measurement of electrical transport properties for both needle-like and bulk materials. *Review of Scientific Instruments*, 72(7):3129, 2001.
- [175] C. Wood, A. Chmielewski, and D. Zoltan. Measurement of Seebeck coefficient using a large thermal gradient. *Review of Scientific Instruments*, 59(6):951, 1988.
- [176] T. Dasgupta and A.M. Umarji. Apparatus to measure high-temperature thermal conductivity and thermoelectric power of small specimens. *Review of Scientific Instruments*, 76(9):094901, 2005.
- [177] L.R. Testardi and G.K. McConnell. Measurement of the Seebeck coefficient with small temperature differences. *Review of Scientific Instruments*, 32(9):1067, 1961.

- [178] J.E. Ivory. Rapid method for measuring Seebeck coefficient as ΔT approaches zero. *Review of Scientific Instruments*, 33(9):992, 1962.
- [179] C.N. Berglund. An automatic technique for accurate measurements of seebeck coefficient. *Review of Scientific Instruments*, 38(1):66, 1967.
- [180] F. Chen, J.C. Cooley, W.L. Hulst, and J.L. Smith. Low-frequency ac measurement of the Seebeck coefficient. *Review of Scientific Instruments*, 72(11):4201, 2001.
- [181] R.R. Heikes and R.W. Ure. *Thermoelectricity: Science and Engineering*. Interscience Publishers, 1961.
- [182] T.C. Harman. Special techniques for measurement of thermoelectric properties. *Journal of Applied Physics*, 29:1373, 1958.
- [183] T.C. Harman, J.H. Cahn, and M.J. Logan. Measurement of thermal conductivity by utilization of the Peltier effect. *Journal of Applied Physics*, 30:1351, 1959.
- [184] A.E. Bowley, L.E.J. Cowles, G.J. Williams, and H.J. Goldsmid. Measurement of the figure of merit of a thermoelectric material. *Journal of Scientific Instruments*, 38:433–435, 1961.
- [185] A.W. Penn. The corrections used in the adiabatic measurement of thermal conductivity using the Peltier effect. *Journal of Scientific Instruments*, 41:626, 1964.
- [186] *Model 2010 Multimeter User's Manual*. Keithley Instruments Inc., 2003.
- [187] *USER'S GUIDE Dynamic Measurement DC Source Agilent Model 66312A*. Agilent Technologies, 2004.
- [188] R. Bentley. *Handbook of Temperature Measurement Vol. 3: Theory and Practice of Thermoelectric Thermometry*. Springer, Singapore, 1998.
- [189] C.B. Vining. *CRC Handbook of Thermoelectrics*. CRC Press, 1995.
- [190] F. Dynys and A. Sayir. Self assemble silicide architectures by directional solidification. *Journal of the European Ceramic Society*, 25:1293, 2005.
- [191] PDF 01-072-6182 (ICDD, 2008).
- [192] PDF 04-006-2527 (ICDD, 2005).
- [193] A. Leineweber and E.J. Mittemeijer. Anisotropic microstrain broadening due to compositional inhomogeneities and its parametrisation. *Z. Kristallogr. Suppl.*, 23:117, 2006.

- [194] K.A. Jackson and J.D. Hunt. Lamellar and rod eutectic growth. *AIME MET SOC TRANS*, 236:1129–1142, 1966.
- [195] B. Vinet, L. Magnusson, H. Fredriksson, and P.J. Desr. Correlations between surface and interface energies with respect to crystal nucleation. *Journal of colloid and interface science*, 255:363–374, 2002.
- [196] S.V. Meschel and O.J. Kleppa. Standard enthalpies of formation of some 3d transition metal silicides by high temperature direct synthesis calorimetry. *Journal of Alloys and Compounds*, 267:128–135, 1998.
- [197] L.M. Levinson. Highly anisotropic columnar structures in silicon. *Applied Physics Letters*, 21:289–291, 1972.
- [198] Z. Zamanipour, J.S. Krasinski, and D. Vashaee. Comparison of boron precipitation in p-type bulk nanostructured and polycrystalline silicon germanium alloy. *Journal of Applied Physics*, 113:143715, 2013.
- [199] T. Nonomura, C. Wen, A. Kato, K. Isobe, Y. Kubota, T. Nakamura, M. Yamashita, Y. Hayakawa, and H. Tatsuoka. Thermoelectric properties of group vi metal silicide semiconductors. *Physics Procedia*, 11:110–113, 2011.
- [200] S.V. Faleev and F. Leonard. Theory of enhancement of thermoelectric properties of materials with nanoinclusions. *Physical Review B*, 77:214304, 2008.
- [201] B. Zhang, J. He, and T.M. Tritt. Size-selective high-yield growth of lead telluride (PbTe) nanocrystals using a chemical vapor deposition technique. *Applied physics letters*, 88:043119, 2006.
- [202] W. Kim, J. Zide, A. Gossard, D. Klenov, S. Stemmer, A. Shakouri, and A. Majumdar. Thermal conductivity reduction and thermoelectric figure of merit increase by embedding nanoparticles in crystalline semiconductors. *Physical Review Letters*, 96:045901, 2006.
- [203] R.M. Davis and C.C. Koch. Mechanical alloying of brittle components: silicon and germanium. *Scripta metallurgica*, 21:305–310, 1987.
- [204] B. Bokhonov, E. Ivanov, and V. Boldyrev. Nanocrystalline powder formation during mechanical alloying of W and Si. *Journal of alloys and compounds*, 199:125–128, 1993.
- [205] J.E. Callanan, R.D. Weir, and E.F. Westrum Jr. Thermodynamic properties of silicides. II. Heat capacity at temperatures T from 5.9 K to 341 K and derived thermodynamic properties to T=1200 K of tungsten disilicide: WSi_{2.06}. *The Journal of Chemical Thermodynamics*, 25:1391–1401, 1993.
- [206] J.K. Roberts and A.R. Miller. *Heat and Thermodynamics*. Interscience, 1954.

- [207] P.F. Qiu, R.H. Liu, J. Yang, X. Shi, X.Y. Huang, W. Zhang, L.D. Chen, J. Yang, and D.J. Singh. Thermoelectric properties of Ni-doped $\text{CeFe}_4\text{Sb}_{12}$ Skutterudites. *Journal of Applied Physics*, 111:023705, 2012.
- [208] PDF 01-071-4935 (ICDD, 2010).

APPENDICES

APPENDIX A

DEVICE DESIGN AND TESTING

Figure A.1 shows the build process for a two-couple device fabricated from powder processed $\text{WSi}_2\text{-Si/Ge}$ composites investigated in Chapter 8. Several routes of metalization for electrodes were studied including platinum ink (Fig. A.1), physical vapor deposited platinum, copper tape, nickel foil, silver paste, and a high temperature electrical epoxy (Pyro-duct 597). For oxidizing environments the copper tape was not a suitable choice for the hot shoe, but seemed to work well on the cold shoe. The other choices were found to make reasonable electrical contact but all choices were mechanically weak options. A further bonding or brazing study should be performed to build mechanically robust couples. Figure A.1a shows the hot and cold shoes coated with a platinum ink, which were then heat treated to cure the ink. The legs were then attached using an electrical epoxy (Fig. A.1b and c). N- and p-type legs were attached electrically in series and thermally in parallel, in the traditional design of a thermoelectric couple.

The couples were tested using a lab built test rig composed of a heater, cold plate, thermocouples, and a programmable electronic load. A couple is shown mounted for testing in Figure A.1d. A typical test consists of stabilizing a thermal gradient across the device then sweeping the electrical load from 0.1 Ohm to 100 Ohm.

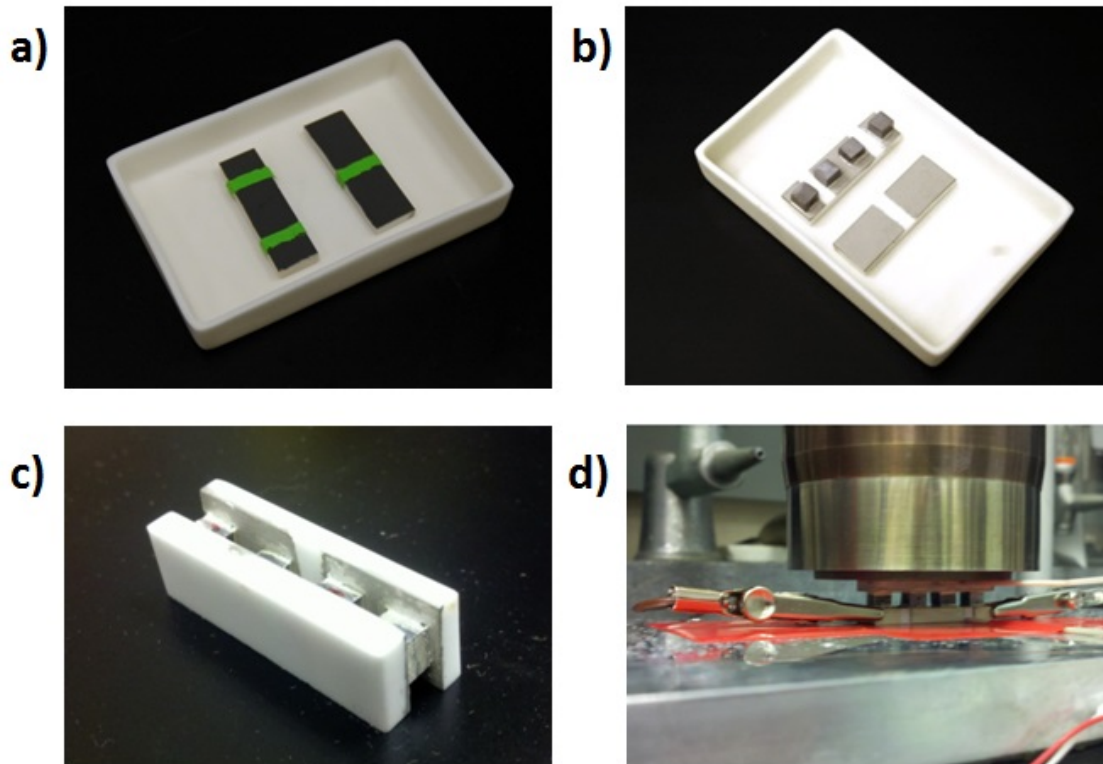


Figure A.1: Fabrication and testing of a two-couple device, a) hot and cold shoes painted with Pt ink b) two n- and two p-type legs mounted to shoes and electrodes c) complete device d) device mounted in test rig.

Figure A.2 top shows a set of typical voltage versus current curves (V-I plots are filled symbols) and power versus current curves (open symbols) of a device. Shown are three different thermal conditions, indicated in the plot key with delta temperature ΔT and average couple temperature T_{avg} , units are Celsius. The y-intercept of the V-I plots represent the open circuit voltage of the device, which increases as a function of delta temperature. The slope of the V-I plots represent the Thevenin resistance of the device, which is seen to increase as a function of temperature. The power versus current curves are typical of thermoelectric devices and increase up to a maximum power point before decreasing. The location of the maximum power point is coincident with a balance between the device electrical resistance and the load resistance. In practice the maximum efficiency operating point is the desired design point, rather than power. The modeling of Chapter 4 discusses optimization of maximum efficiency. An alternate presentation of the device characterization data is provided by Figure A.2 bottom. The device voltage, power, and electrical current is presented as a function of electrical load. In this presentation it is clear that the power maximizes around a load resistance of 0.4 Ohm, which is reasonably in the range of the device total resistance. A majority of the device resistance is attributed to the poor metallization and electrical contacts, as the resistance due to the legs is an order of magnitude less.

The devices were also subject to thousands of hours of continuous endurance testing in air. Figure A.3 shows time data over 2500 hours of Thevenin resistance, open circuit voltage, and maximum power. While the values are low, hindered by poor electrode and metallization of the thermoelectric legs, they are seen to be fairly stable

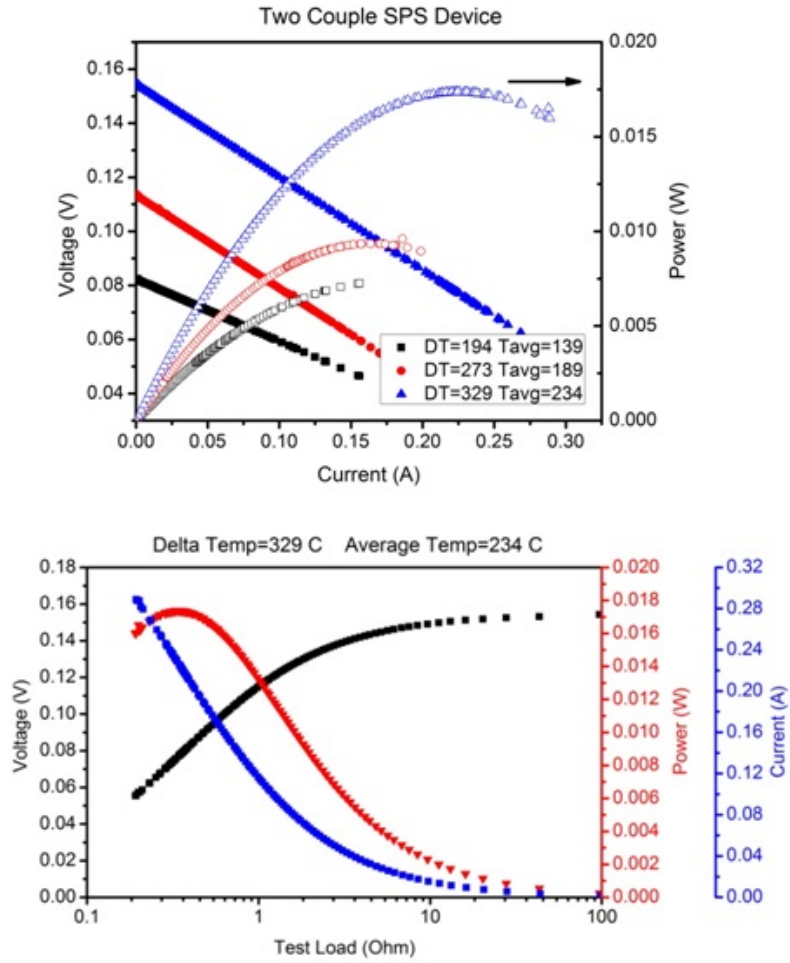


Figure A.2: Top) Voltage versus current plot of device under three different thermal conditions, Bottom) Voltage, Power, and Current as a function of test load.

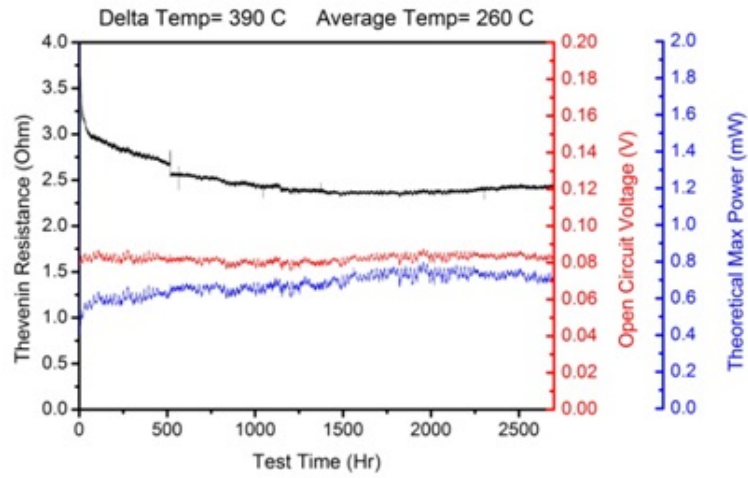


Figure A.3: Thevenin resistance, open circuit voltage, and maximum power as a function of test time during an endurance test in air.

in time. The endurance testing was performed on a device using copper electrodes, which quickly oxidized within the first half hour of operation then stabilized to a resistance of 2.5 Ohms.

APPENDIX B

UNCERTAINTY ANALYSIS DETAILS

The propagation of error through a measurement can be tracked by application of a Taylor series expansion. The series is truncated after the first correction for simplicity. The desired uncertainty U_y on a nominal measurement \bar{y} can be estimated from the uncertainty U_x of a nominal measured value \bar{x} , as

$$\bar{y} \pm U_y = f(\bar{x} \pm U_x) \approx f(\bar{x}) \pm \left. \frac{df}{dx} \right|_{x=\bar{x}} U_x. \quad (\text{B.1})$$

Using this method, uncertainty can be calculated for every source listed in tables 7.1 and 7.2. Since the sources of uncertainty introduced in this work are linearly independent, the result of each individual uncertainty may be combined into a total uncertainty using a common inner product generated norm. The uncertainties of the sources must be normalized into relative uncertainties before they are combined as

$$e_{y_x} = \frac{1}{\bar{y}} \left. \frac{\partial y}{\partial x} \right|_{x=\bar{x}} U_x, \quad (\text{B.2})$$

$$e_{Total} = \sqrt{e_{y_1}^2 + e_{y_2}^2 + e_{y_3}^2 + \dots} \quad (\text{B.3})$$

This final total relative uncertainty on y due to different sources can be reported as a percent error, or can be normalized using the nominal value \bar{y} . Both individual relative errors, due to each case listed in the tables 7.1 and 7.2, and the total absolute uncertainty for electrical resistivity, Seebeck coefficient, and power factor has been quantified as an example of uncertainty analysis in section 7.5. The calculated uncertainties vary with temperature. Additionally, the cold-finger uncertainty is an asymmetrical error which causes the power factor uncertainty to be asymmetrical.

As an example of the methods introduced, the uncertainty on power factor can be calculated in terms of the uncertainty on Seebeck coefficient and electrical resistivity as

$$U_{\text{P.F.}} = \frac{\bar{S}^2}{\bar{\rho}} \sqrt{\left(\frac{2U_S}{\bar{S}}\right)^2 + \left(\frac{U_\rho}{\bar{\rho}}\right)^2}, \quad (\text{B.4})$$

where the factor of 2 in the Seebeck term is introduced by the differentiation of power factor in terms of Seebeck coefficient. Equation B.4 can be applied separately to the positive and negative limits of the uncertainty, as the Seebeck uncertainty will be asymmetric because of the cold-finger effect.

Many of the cases highlighted in tables 7.1 and 7.2 follow a straight-forward procedure for determination of the uncertainty, using the error propagation method outlined in the previous section. In this section, the uncertainty due to thermocouple tip radius (table 7.1 case #1) is outlined in detail as an example. Following the example are the cases which require more detail.

The maximum uncertainty in probe spacing L due to the thermocouple tip radius is twice the tip radius, R

$$U_{L_{\text{Tip}}} = 2R = 0.5\text{mm}. \quad (\text{B.5})$$

Therefore the relative uncertainty on electrical resistivity due to this source on the variable L can be estimated using equations 7.4 and B.2. In the example calculation, the thermocouple tip radius of 0.25 mm and nominal probe separation of 8 mm were used

$$e_{\rho_{\text{Tip}}} = \left. \frac{1}{\bar{\rho}} \frac{\partial \rho}{\partial L} \right|_{L=\bar{L}} = \frac{1}{\bar{\rho}} \frac{\sum z_i \sum y_i - N \sum z_i y_i}{(\sum z_i)^2 - N \sum z_i^2} \frac{wD}{L^2} 2R = \frac{2R}{L} = \frac{0.5\text{mm}}{8\text{mm}} = 6.25\%. \quad (\text{B.6})$$

For sources #7 and #8 in table 7.1 (DAQ accuracy of voltage and current) the propagation of error due to each current measurement z_i and voltage measurement y_i can be calculated

$$\frac{\partial \rho}{\partial z_i} = \frac{[(\sum z_j)^2 - N \sum z_j^2] [\sum y_j - N y_i] - [\sum z_j \sum y_j - N \sum z_j y_j] [2 \sum z_j - 2N z_i]}{[(\sum z_j)^2 - N \sum z_j^2]^2} \frac{wD}{L}, \quad (\text{B.7})$$

$$\frac{\partial \rho}{\partial y_i} = \frac{\sum z_j - N z_i}{(\sum z_j)^2 - N \sum z_j^2} \frac{wD}{L}. \quad (\text{B.8})$$

Combining equations B.7 and B.8 with equation B.2 and the assumed uncertainty values found in table 7.1 provide a complete means of calculating uncertainty

due to the DAQ accuracy on the electrical resistivity measurement. Similarly, for Seebeck measurement the following relation is necessary to track error due to voltage y_i DAQ accuracy (table 7.2 Source #5)

$$\frac{\partial S}{\partial y_i} = \frac{\sum x_j - Nx_i}{(\sum x_j)^2 - N \sum x_j^2}. \quad (\text{B.9})$$

Table 7.2 source #6 (DAQ accuracy on temperature) requires a link from the voltage uncertainty y_i to the temperature uncertainty. This was solved by using standard high temperature thermocouple calibration curves.

$$U_{\text{Temp}} = \left. \frac{\partial T}{\partial y} \right|_{y=\bar{y}} U_{\text{Voltage}}, \quad (\text{B.10})$$

$$\begin{aligned} \left. \frac{\partial T}{\partial y} \right|_{y=\bar{y}} &= -1.86649 \times 10^{-7} y^5 + 4.4010965 \times 10^{-5} y^4 - 3.860286 \times 10^{-3} y^3 \\ &+ 0.16394193 y^2 - 3.292062 y + 48.3022 \text{ with } y \text{ thermocouple voltage in mV,} \end{aligned} \quad (\text{B.11})$$

$$\frac{\partial S}{\partial x_i} = \frac{[(\sum x_j)^2 - N \sum x_j^2] [\sum y_j - Ny_i] - [\sum x_j \sum y_j - N \sum x_j y_j] [2 \sum x_j - 2Nx_i]}{[(\sum x_j)^2 - N \sum x_j^2]^2}. \quad (\text{B.12})$$

Equation B.12 allows for the expression of the Seebeck uncertainty in terms of the probe to probe temperature difference x_i using equations B.2 and B.10.